Signal Integrity and Shielding Issues in Mixed Signal Circuits under Transient Electromagnetic Field Generated by High Power Pulsed Nd: Glass Lasers

By

M. S. Ansari

(Enrollment No. ENGG03200704003)

Raja Ramanna Centre for Advanced Technology, Indore

A thesis submitted to the

Board of Studies in Engineering Sciences

In partial fulfillment of requirements for the degree of

DOCTOR OF PHILOSOPHY

Of

HOMI BHABHA NATIONAL INSTITUTE

December, 2013

Homi Bhabha National Institute

Recommendations of the Viva Voce Board

As members of the Viva Voce Board, we certify that we have read the dissertation prepared by M. S. Ansari entitled "Signal integrity and shielding issues in mixed signal circuits under transient electromagnetic field generated by high power pulsed Nd: glass lasers" and recommend that it may be accepted as fulfilling the dissertation requirement for the Degree of Doctor of Philosophy.

______________________________ Date: April 24, 2015
Chairman – Prof. A. P. Tiwari

______________________________ Date: April 24, 2015
Guide/ Convener – Prof. S. V. G. Ravindranath

______________________________ Date: April 24, 2015
Member 1 – Prof. S. V. G. Ravindranath

A K Bhattacharjee
______________________________ Date: April 24, 2015
Member 2 – Prof. A. K. Bhattacharjee

______________________________ Date: April 24, 2015
Examiner – Prof. Arun K. Tangirala

Manmohan Singh
______________________________ Date: April 24, 2015
Co-guide – Prof. M. S. Bhatia

P. D. Gupta
______________________________ Date: April 24, 2015
Technical Advisor –Prof. P. D. Gupta

Final approval and acceptance of this thesis is contingent upon the candidate's submission of the final copies of the thesis to HBNI.

I hereby certify that I have read this thesis prepared under my direction and I recommend that it may be accepted as fulfilling the dissertation requirement.

Date: April 24, 2015

Manmohan Singh

Place: RRCAT, Indore. Guide: Prof. S. V. G. Ravindranath Co-Guide: Prof. M. S. Bhatia

STATEMENT BY AUTHOR

This dissertation has been submitted in partial fulfillment of requirements for an advanced degree at Homi Bhabha National Institute (HBNI) and is deposited in the library to be made available to browsers under rules of the HBNI.

Brief quotations from this dissertation are allowable without special permission provided that accurate acknowledgement of source is made. Requests for permission for extended quotation from or reproduction of this manuscript in whole or in part may be granted by the competent authority of HBNI when in his or her judgment the proposed use of the material is in the interest of scholarship. In all other instances, however, permission must be obtained from the author.

M. S. Ansari

DECLARATION

I hereby declare that the investigation in this thesis has been carried out by me. The work is original and has not been submitted earlier as a whole or in part for a degree/diploma at this or any other Institution/university

M. S. Ansari

List of Publications arising from the thesis

Journal

1. C. P. Navathe, M. S. Ansari, S. Nigam, N. Sreedhar, B. Singh and R. Chandra, "Control System for Bipolar Capacitor Bank of a High Power Nd:glass Laser Chain," *IEEE Transactions on Plasma Science,* vol. 40, no. 7, pp. 1898-1906, 2012.

2. M. S. Ansari, S. V. G. Ravindranath, M. S. Bhatia, R. K. Patidar and C.P. Navathe, "Application of Wavelet Transform for Analysis of Radiated Electromagnetic Interference in a High Power Terawatt Laser Setup," *Indian Journal of Science and Technology*, vol. 5, issue 11, pp. 3647-3650, 2012.

3. M. S. Ansari, M. S. Bhatia, S. V. G. Ravindranath, B. Singh and C. P. Navathe, " Investigation of Electromagnetic Interference from a Pulsed Solid State Laser Power Supply," *International Journal of Engineering Research and Applications,* vol. 3, issue 1, pp. 1577-1581, 2013.

4. M. S. Ansari, S. V. G. Ravindranath, M. S. Bhatia, B. Singh and C. P. Navathe, "Electromagnetic Coupling through Apertures and Shielding Effectiveness of a Metallic Enclosure Housing Electro-optic Pockels cell in a High Power Laser System," *International Journal of Applied Electromagnetics and Mechanics*, vol. 42, issue 2, pp. 191-199, 2013.

Conferences

1. M. S. Ansari, B. Singh, R. Chandra and C. P. Navathe, "Development of pulse forming network for large size disk amplifiers in Nd: glass laser chain," *Proceedings of seventh DAE-BRNS National Laser Symposium,* Vadodra, 2007.

2. M. S. Ansari, Bhupinder Singh and C. P. Navathe, "Timing jitter of ECL ICs under high clock frequency and pulsed electromagnetic fields," *10th International conference on Electromagnetic interference and compatibility*, Bangalore, 2008.

M. S. Ansari

3. M. S. Ansari, C.P. Navathe, S. V. G. Ravindranath and M. S. Bhatia, "Measurement of radiated electromagnetic interference in flash lamp power supplies for high power Nd: glass lasers," *Proceedings of DAE-BRNS National Laser Symposium (NLS-19),* Indore, 2010.

4. M. S. Ansari, S. V. G. Ravindranath, M. S. Bhatia, B. Singh, A. S. Joshi and C.P. Navathe, "Dependence of xenon flash lamp spectrum and pumping efficiency of Nd:glass laser amplifier on the power supply circuit parameters," *Proceedings of DAE-BRNS National Laser Symposium (NLS-21),* Mumbai, 2013.

5. Bhupinder Singh, M. S. Ansari and C.P. Navathe, "A 10 kV Flash lamp power supply for high power Nd: glass laser amplifier," *Proceedings of DAE-BRNS National Laser Symposium (NLS-21),* Mumbai, 2013.

M. S. Ansari

Dedicated to the loving memory

of my father

Dr. Muhammed Sharfuddin Ansari

ACKNOWLEDGEMENTS

I would like to express my deep sense of gratitude to the thesis supervisor Dr. S. V. G. Ravindranath for his guidance, keen interest and encouragement throughout the course of this work. I am grateful to the co-supervisor Dr. M. S. Bhatia for his expert comments and encouragements. My special thanks goes to Dr. P. D. Gupta, Director Raja Ramanna Centre for Advanced Technology, Indore and technical adviser for this dissertation, for excellent support and guidance. I am grateful to the monitoring committee chairman Dr. A. P. Tiwari and member Dr. A. K. Bhattacharjee for critically examining the work and for fruitful discussions. I am indebted to Mr. C. P. Navathe, Head, Laser Electronics Support Division, RRCAT, for the permission to pursue this work. I am grateful to Dr. P. A. Naik, Head, Laser Plasma Division, RRCAT, for useful suggestions. I am thankful to Dr. S. Mukhopadhyay for useful discussions on wavelet transformation. I am thankful to all members of LESD and LPD at RRCAT, especially to Mr. A. S. Joshi, Dr. J. A. Chakera, Dr. M. P. Singh, Mr. M. P. Kamath, Mr. Y. B. S. R. Prasad, Dr. A. K. Sharma, Mr. Bhupinder Singh, Mr. V. K. Singh, Mr. Abrat Verma, Mr. Rajendra Singh, Mr. Yogesh Sahu, Mr. S. R. Khade and Mr. Deepak Sharma for helping me in many ways. I have been supported and immensely encouraged at different stages of this endeavor by Mr. A. C. Thakurta, Mr. J. Dwivedi, Dr. Archana Sharma, Dr. M. P. Joshi, Dr. Arup Banerjee, Dr. Avijit Chowdhury, Mr. Sanjay Sethi and Mr. Abid Munshi. Many other colleagues and friends have directly and indirectly contributed towards completion of this work. Finally, I wish to acknowledge the understanding and fortitude of my wife Rehana, patience of my children Nida and Faisal, prayers of Ammy and unflinching support of my brother, sisters and their family members.

M. S. Ansari

CONTENTS

SYNOPSIS

This dissertation investigates the topic of signal integrity and shielding of electrical systems in flash lamp pumped high power solid state lasers operating under pulsed electromagnetic interference. From electrical point of view, components of a high power laser can be grouped into high voltage, high current stages and fast rise time high voltage, low current systems. Flash lamps and Faraday isolators belong to the former category. Whereas, Pockels cell based system is triggered by fast rise time high voltage and low current drivers. These are operated in pulsed, single shot mode, which results into generation of transient and non-stationary electromagnetic pulses. Electromagnetic emission or interference from each of these components is unique in terms of intensity, timing parameters and frequency contents. This research work is one of the few reported studies in optically pumped solid state high power laser chains towards characterization of electromagnetic interference through analytical and measurement techniques. Important highlights of this dissertation are,

a) Identification and characterization of electromagnetic interference from electrical components and interconnects in high power laser systems.
b) Analysis of field couplings and crosstalk in high power laser intra-system configurations.
c) Investigations of susceptibility and effects of pulsed electromagnetic interference on timing integrity of delay and synchronization circuits in multi-stage laser chains.
d) Analysis of electromagnetic shielding effectiveness for laser components exposed to transient electromagnetic fields.

Electromagnetic interference and extent of loss of signal integrity in a system depend on several factors such as, characteristics of interfering fields, type of components and their placements, timing parameters of high voltage and high current switching devices, printed circuit board design, cable routings, load terminations and shielding [Green, 1999]. Geometry and shape of power and ground networks play important role in maintaining signal quality. Wavelet transform, Finite Difference Time Domain (FDTD) and Transmission Line Matrix (TLM) methods are used for analysis of field emission and coupling problems in this work.

Noise couplings, crosstalk and shielding studies are carried out for two different types of laser chains namely 2-beam 400 J, 1.5 ns, Nd: phosphate glass [Joshi, 2011] and an ultra-high intensity (10^{18} W/cm^2) table top terawatt (TTT) laser chain based on Ti: Sapphire crystal [Naik, 2003]. These high power pulsed lasers operate in non-homogeneous and complex electromagnetic environment, where several stages are electrically triggered, controlled and time synchronized. Each of these laser systems has specific functional, timing and electromagnetic compatibility requirements. The two-beam laser chain consists of a low energy laser oscillator followed by successively increasing amplifier stages, optical isolators based on Faraday rotator and Pockels cells operated by high voltage fast switches. Xenon flash lamps of varying arc lengths operating at a maximum peak current of 6 kA are the optical pump source for amplifier stages. There are around 200 flash lamps, which are excited in several combinations by energy storage capacitor banks with total energy handling capacity of 500 kJ. Transfer of energy from capacitors to nonlinear flash lamp loads is accomplished by using critically damped second order *RLC* circuits. It operates under a centralized electronic control unit, which generates charge, trigger and fire commands for laser stages in specified sequences and sets relative delays for their triggering [Navathe, 2012]. Low voltage control and synchronization electronics have to function in tandem with high voltage, high current systems and electro-optical switching devices. Environment as seen by low voltage control, interface and synchronization circuits is polluted by electromagnetic noise from flash lamp, Faraday rotator and Pockels cell power supplies and trigger circuits. Timing jitter as low as two ns for relative delay between trigger circuits causes noticeable shot-to-shot variation in optical power because of changes in laser round trip and amplifier gain factors. Jitter is introduced by conducted and radiated noise generated by firing of flash lamps of laser amplifier stages at different instants of operation cycle. Development of low susceptibility trigger and delay circuits is one of the aims of this research work. Towards achievement of this goal, a delay generator circuit based on differential emitter coupled logic is developed, which has reduced the timing jitter significantly to 800 ps.

Large size of radiating structures, existence of nonlinear loads and impedance discontinuities caused by presence of interconnects in high power laser systems add to simulation and analysis complexities. A major portion of analysis in this work relies on time domain measurements. Extent of electromagnetic interference and its effects on signal integrity are estimated by in-situ measurements by near field probes and far field antennas. Although, the measurement results presented in this work are specific to flash lamp pumped solid state lasers, the proposed methodology and analytical techniques are applicable to other multi-scale intra system setups.

The thesis is organized into following chapters.

Chapter 1 provides introduction and dissertation outline. Theme of the research work is to identify and characterize electromagnetic interference sources and their effects on integrity of trigger signals in electrical systems of multi-stage flash lamp pumped solid state lasers. Investigations of electromagnetic interference are essential to achieve reliable laser operation with parameters conforming to designed values. From electrical system perspective, the two 2-beam high power laser chain and the table top terawatt laser setup have similar power supplies, interconnects and components. However, they differ in terms of overall size and functional requirements. Table top terawatt laser setup is more compact and uses regenerative amplifiers for which timing and delay parameters of trigger signals are stringent. Interference from operation of flash lamp circuits at earlier stages of laser cycle introduces jitter in set delays for subsequent laser amplifier stages. It has to be minimized and kept at an acceptable level through selection of less susceptible components and effective shielding techniques. Pulsed and transient nature of interference, entail time domain measurements and analysis. Wavelet transform is used in this work to characterize noise generated at different time instants during TTT laser operation cycle. Finite difference time domain and transmission line matrix methods are employed in later parts of the dissertation to analyze the problems of electromagnetic field emission and coupling. Transient voltages induced due to near and far end crosstalk in co-axial cables and wires are estimated by analytical technique and transmission line matrix method. Effects of finite ground planes on induced voltage are investigated. Analysis of shielding effectiveness of metallic enclosures with specific aperture requirements for electro-optical components is an important aspect of the presented work.

Chapter 2 discusses existing literatures relevant to the dissertation work. Topics on electromagnetic interference in high power laser systems with emphasis on signal integrity, field couplings, shielding and susceptibility against transient electro-magnetic pulses are reviewed. High power lasers are widely used for laser-plasma experiments and for industrial processes requiring localized and directed delivery of large peak power. These applications involve laser matter interaction at high temperature. Research papers and technical reports on electromagnetic interference and compatibility from high power laser laboratories address two different issues. First of these is generation of electromagnetic pulses and radio frequency interference due to arc discharge process in flash lamps and due to high energy particles in laser–matter interaction experiments [Mead, 2004]. Emphasis of this category of papers is to model electromagnetic pulse generation process and its propagation around target chambers in plasma experiments. Second group deals with studies and measurements of interference from flash lamp pulsed power supplies and high voltage fast switching devices with an aim to maintain electromagnetic compliance conformity [Anderson, 2003]. These are also linked to reliable operation and minimal variation in shot-to-shot laser energy and beam quality. High power lasers are typical examples of intra-system setups in which electromagnetic interference is concerned with self-compatibility of the system of interest. An intra-system noise analysis encompasses identification and characterization of radiating structures, field couplings in interconnects, transmission line crosstalk, and shielding against internally generated fields [Morgan, 2007]. Literature survey for this work includes reports from major high power laser laboratories such as National Ignition Facility (NIF), USA [Stathis, 1994] and Laser Mégajoule (LMJ) project, France [Cervens, 2009]. Standard mitigation techniques consisting of shielding, ground isolation and low impedance grounding are well researched and documented. However, there are not many reported work which attempts systematic modeling and mathematical analysis of source identification, field emissions, couplings and susceptibility studies in pulsed power systems of optically pumped solid state lasers.

Signal integrity in an electrical system has gained additional attention in recent times due to increase in clock speed, density of integrated circuits and strict requirements of adherence to electromagnetic emission standards. Analysis of degradation in timing parameters of propagating signals and means to reduce it has been a topic of active research in many subfields of electronics and electrical technology. Interconnect layouts, dimensions and characteristics of terminating impedances are important parameters which influence the nature of electromagnetic interference and their impact on signal integrity in a system [Young, 2001].

Flash lamp pumped high power laser systems based on multi-stage amplifiers employ metallic enclosures for housing electro-optical components. Shielding effectiveness of these enclosures is affected by presence of intentional apertures for laser transmission. Shielding effectiveness (SE) with apertures are calculated either by rigorous solution of electromagnetic boundary problems, numerical electromagnetic modeling or approximate formulations. Robinson [Robinson, 1998] has reported analysis of electromagnetic shielding effectiveness based on strip line equivalent circuit. Taflove [Taflove, 1988] has implemented finite difference time domain approach for calculation of SE.

There are several research papers on use of digital signal processing techniques for electromagnetic compatibility of power electronics circuits and switched mode power supplies. Measurements of transient noise and electromagnetic pulses are generally carried out in time domain. Fourier transform based post measurement analysis extracts frequency details but has limitation of losing time information. Relatively newer concept of wavelet transform has gained popularity for time-frequency decomposition of transient signals. It uses a finite energy function $\psi(x)$ which is scaled by a positive real number and translated by a real number to investigate transient and discontinuous signal. Wavelet transform has been applied for noise analysis in diverse areas such as, switched mode power supplies, power lines, electrostatic discharge and biomedical instrumentation [Antonini, 2001]. Development of accurate analytical and numerical techniques is an important topic of research in the field of electromagnetic compatibility. However, it is difficult to formulate and implement analytical methods to study electromagnetic problems in multi-scale and intra-system setups. Finite difference time domain and transmission line matrix are two widely used time domain numerical methods for solution of field equations in electromagnetic compatibility studies. FDTD method was initially proposed by Yee [Yee, 1966] as a numerical solution of Maxwell's curl equations. It approximates time and space derivatives with second order finite difference terms. Computational space is divided into grid of uniform unit cells. Electric field components in a volume space are calculated at a given time instant. Magnetic field is estimated at the incremented time from the values of previously calculated electric fields. Computational space is terminated by an absorbing boundary condition. Spatial and temporal resolutions depend on minimum wavelength λ and velocity of propagation c as $\Delta x = \lambda/10$ and $\Delta t = (\Delta x/2c)$ respectively. There is a rich repository of research papers on implementation of FDTD for electromagnetic wave propagation, radiation and shielding in electrical engineering applications. Gridding of computational space into fine mesh requires large computational resources. FDTD is resource intensive and it is difficult to model thin and long structures with this technique Transmission line matrix method is another widely used time domain numerical method for solving field interactions. It is based on equivalent circuit representation of Maxwell's field equations. Hoefer [Hoefer, 1985] summarizes earlier developments of TLM method. It evaluates electric and magnetic fields in terms of transmission line parameters and wave propagation.

Good amount of work on time domain modeling of electromagnetic interference is available in terms of research papers and textbooks. However, no significant research work is reported on specific application of time domain numerical techniques and wavelet transform for noise analysis in power supplies and electrical systems of multi-stage high power solid state lasers.

Chapter 3 discusses signal processing and numerical techniques for electromagnetic interference analysis. Mathematical techniques utilized for noise source analysis and characterization in this work are wavelet transform, finite difference time domain and transmission line matrix method. Wavelet transform is an effective frequency-intensity analysis technique for transient signals. It resolves a time domain signal in terms of scaled and dilated functions known as wavelets. This is to be contrasted against the conventional Fourier transform, which resolves a time domain function in terms of continuous sinusoidal waves of multiple frequencies. FDTD and TLM are time domain solutions of differential form of electromagnetic field equations. Finite difference time domain technique generates numerical solutions of electromagnetic problems from time and space discretized Maxwell equations. Whereas, TLM generates numerical solution by applying principle of equivalence between electromagnetic equations and transmission line network parameters. TLM analysis at time step k begins with assignment of incident and reflected voltages at a particular node j represented by ${}_kV_j^i$ and ${}_kV_j^r$ respectively. Total voltage at the node is given by ${}_kV_j = {}_kV_j^i + {}_kV_j^r$. Loop current at each node at the k^{th} time step, I_k, is calculated by considering equivalent circuits of the four neighboring branches. Electric and magnetic fields at k^{th} time instants are calculated from the voltage ${}_kV_j$, current I_k and space discretization *Δl.* Field at the next time instant, *k+1* is calculated by Huygenes Principle of wave propagation. This chapter forms theoretical background for work described in subsequent portions of the dissertation.

Chapter 4 is system description for laser units under investigation. It provides details of power supplies, control systems, synchronization circuits and flash lamp trigger circuits with emphasis on signal integrity issues for two different solid state high power laser chains that is, a 400 J, 1.5 ns, 2-beam laser chain and a table top terawatt laser system. Functioning and operational requirements of electro-optical and magneto-optical components such as high voltage and high current flash lamps, high voltage Pockels cells and Faraday isolator drivers used in these lasers are described. There are two different types of pulse forming networks for flash lamp discharge, namely, unipolar and bipolar. Flash lamp peak current, pulse width and optical emission spectra depend on pulse forming components comprising of energy storage capacitors, trigger transformer inductance and flash lamps. A high voltage, short duration trigger pulse, initiates current discharge through flash lamp, which is a strong source of radiated emission. Other notable sources of noise emission are electro-optic Pockels cells, which are driven by high voltage and high speed (~ 3 kV, 5 ns) pulsed voltage. Faraday isolators need high peak pulsed current to generate transient magnetic field of around 15 kG. It consists of a solenoid coil of few mH, driven by energy storage capacitor banks. Controlled discharge of capacitor banks into solenoid coil produces half sinusoid current of 3-5 ms flowing through 3-10 m long wires. Faraday isolator current generates crosstalk interference in nearby cables, which are studied in later part of this thesis.

Chapter 5 discusses radiated and conducted emissions from electrical circuits and systems in the laser setups. Conventional problem of electromagnetic emissions from an excited conductor is extended to analyze radiated and conducted emissions from two different types of flash lamp power supplies and Pockels cell driver circuits. Noise emissions are affected by various factors such as characteristics of cables, proximity to ground plane from radiating sections, type of shielding etc. Measurement results of radiated and conducted emissions from a single core and coaxial conductors, carrying flash lamp discharge current are presented. Effects of ground planes and layout geometry on emission characteristics of electrically long cables are looked into. Noise emissions and coupling in cables are frequency dependent with occurrence of several resonance peaks. Shielded coaxial cables such as RG58 [Appendix B.6] help to reduce noise emission by a factor of 2 to 6 dB as compared to unshielded, single core cable of equivalent length and core diameter. Bends in cable layout introduces parasitic impedances and increase the level of noise emission. Analysis of radiated emission from flash lamp circuits for peak current of 3 kA and pulse width of 600 μs are carried out in near and far field regions. Bipolar mode of flash lamp operation increases the discharge current path, which in turn results into increased radiated emission. Differences in amplitude of radiated emission due to unipolar and bipolar discharge paths are more significant in far field regions for frequencies greater than 300 MHz. Maximum deviation of 30 dB occurs at around 600 MHz. Conducted emission measured between 150 kHz to 30 MHz is reduced by approximately 30 dB in unipolar discharge as compared to bipolar configurations. Effect of cable shielding on attenuation of conducted noise is of the order of 2 dB. Current through Faraday isolator coil is half sinusoid of nominal peak amplitude 1.14 kA and pulse width 5 ms. Peak value of differential mode current in Faraday isolator cable is of the order of 30A.

Maximum noise emission due to Faraday isolator current occurs during falling edge of the current pulse, which coincides with commutation of silicon controlled rectifier in the pulse forming network. These measurement results suggest use of unipolar flash lamp discharge network for reduced noise emission and improved susceptibility.

Chapter 6 deals with noise analysis and signal integrity topics in the table top terawatt laser system. It is a relatively compact laser unit with stringent functional requirements of timing integrity of trigger signals for pulse selector and regenerative amplifier stages. The regenerative amplifier stage has functional requirements of low jitter injector and ejector trigger signals. Experimental results of development of a low jitter delay circuit with emitter coupled logic gates are described. Digital integrated circuits belonging to this logic family operate with differential signals and are less affected by common mode noise. Radiated emission in TTT laser unit is measured in time domain. Wavelet transform is applied on the measured data to analyze noise emitted by individual components. Daubechies and Morlet wavelet functions with scales limited to match the measurement antenna bandwidth of 1 GHz are compared with reconstructed interference signal.

Delay generators designed with emitter coupled logic mono-shots provide low jitter of the order of 800 ps. This is a significant improvement over circuits based on Transistor Transistor Logic (TTL) devices, for which typical jitter is 2 ns. Improvement in emitter-coupled logic circuits is due to reduction of differential mode noise. Wavelet decomposition of electromagnetic interference measured in time domain indicates strong emission during high voltage switching of Pockels cell drivers. Relative intensity of noise emission from flash lamp operation is half of the intensity from pulsed high voltage drivers for Pockels cells. This requires better isolation of the driver circuits.

Analysis of wavelet transformation of noise data during flash lamp discharge reveals strong emission during initial rising portions, which coincides with application of high voltage trigger pulse.

Chapter 7 presents analysis, simulations and measurement results of electromagnetic field couplings and shielding under pulsed excitations. Near and far end cross talk induced voltages in a victim cable due to propagation of a Pockels cell driver step voltage (dV/dt ~ -750 V/ns) at a lateral distance of 10 cm are analyzed by transmission line matrix method and experimentally measured. Peak amplitudes of near and far end induced voltage without a ground plane are -30 V and -25 V respectively. Existence of finite ground plane results into approximately ninety percent reduction of induced voltages. Frequency domain measurement of induced voltage in the range of 300 kHz to 1 GHz is carried out with S_{21} characterization. Amplitude of coupled voltage reduces by 20 to 30 dB due to presence of ground plane. Effects of intentional apertures for optoelectronic components on the shielding effectiveness are investigated. Analysis based on equivalent circuit (apertures modeled as strip lines) and finite difference time domain methods of shielding effectiveness of metallic enclosures with cross apertures have been carried out. Investigations of shielding effectiveness of an aluminum enclosure of size 170 mm x 130 mm x 175 mm with circular and rectangular apertures on two opposite faces and housing Pockels cell and the driver circuit are discussed.

Analysis of generation and interaction of pulsed electromagnetic fields, crosstalk analysis and effects of ground planes in electrically large laser systems are important contribution of this dissertation.

Chapter 8 concludes the dissertation by summarizing the research work. Related topics, which can be taken up as extension of this work, are pointed out. The thesis is focused on investigations of generation and interaction of electromagnetic fields produced by power supplies and trigger circuits in flash lamp pumped high power laser systems. Improvements in laser performance and reliability due to methodical investigations of the process of electromagnetic emissions and their interactions with nearby components are highlighted. Future work in this direction can be taken up to model and characterize the generation and propagation of electromagnetic pulses due to flash lamp arc discharge and high intensity laser-matter interaction process. Interaction of these electromagnetic bursts with electronic sensors, trigger and control circuits in near and far field regions can be investigated from electromagnetic compatibility point of view. This work can be extended to analyze the interaction and absorption of laser-plasma produced electromagnetic pulses with biological systems. Procedures based on advanced signal processing and optimization techniques such as multi resolution analysis and genetic algorithm can be further developed for investigation of spectral contents and time evolution of electromagnetic pulses in a multi scale laser unit.

Important contributions of this thesis are:

1. Analysis of electromagnetic interference is carried out for flash lamp power supplies, trigger circuits and high voltage pulsed switches. Radiating structures are identified and characterized by measurements in time and frequency domains. Comparative study is carried out for unipolar (+ve bank) and bipolar (± banks) designs for flash lamp discharge circuits. Radiated emission in a bipolar supply is found to be higher as compared to emission from unipolar power supply. These investigations have helped to formulate an optimum

design of flash lamp pulse forming network for reduced electromagnetic interference and better efficiency of optical pumping for solid state lasers.

2. Digital signal processing techniques such as wavelet transform are applied to time correlate the interfering sources. This has provided time-frequency correlation of electromagnetic interference resulting into source identification and has helped in mitigation of intra-system interference in high power laser setups.
3. Analysis of shielding effectiveness of metallic enclosures with apertures and housing electro-optical components are carried out using equivalent circuit models. Comparative studies of enclosure shielding effectiveness for circular and rectangular apertures excited by transient electromagnetic fields are done. These have resulted into improved design of shield geometry and optimization of aperture shape and area with a view to reduce noise couplings in Pockels cell trigger circuits.
4. Analysis and measurements of electromagnetic field couplings in multi-conductor systems are carried out. Aggressor conductors were excited by high peak pulsed current and low rise time step voltage. Crosstalk interference for cables of varying characteristics and load conditions are analyzed. Transmission line effects of co-axial cables commonly used in high power laser system are investigated. It involves extraction of distributed resistance, inductance, conductance and capacitance (*RLGC*) parameters. An assessment of these parameters has helped in analyzing crosstalk and noise couplings in flash lamp and Pockels cell driver cables.
5. Susceptibility of electrical signals for laser control and synchronization circuits operated under pulsed electromagnetic environment is looked into.

Electromagnetic interference affects the signal integrity which are manifested in terms of degradation of rise time, jitter in set delay between trigger signals, transient noise etc. Reduction of jitter in delay circuits is important as it improves the stability of laser energy and beam quality. Significant work on this aspect of signal integrity is carried out as part of this dissertation and delay circuits based on various logic families are compared. It has resulted into development of circuits with smaller delay jitter between trigger signals in regenerative amplifier stage of the table top terawatt laser unit. This in turn has led to improvement in laser performance in terms of predictable and stable gain parameters and laser energy.

These investigations have provided new and hitherto unreported information on frequency and time domain parameters of radiated and conducted electromagnetic transients generated in flash lamp pumped high power solid state lasers. Numerical and signal processing techniques in combination with measurement results have been applied to understand, estimate and mitigate electromagnetic interference and its effects on signal integrity in flash lamp pumped lasers. Apart from these contributions resulting into betterment of laser performance, the dissertation work has provided theoretical insight into related topics such as electromagnetic pulse coupling into different types of structures and cables. It has also resulted into development of less susceptible mixed signal circuits operating under transient electromagnetic fields.

The research work carried out for this thesis is published in peer-reviewed journals (4) and presented in national and international conferences (5).

LIST OF FIGURES

LIST OF TABLES

NOMENCLATURE

Symbol

ABC	Absorbing Boundary Condition
CMOS	Complementary Metal Oxide Semiconductor
CWT	Continuous Wavelet Transform
DWT	Discrete Wavelet Transform
ECL	Emitter Coupled Logic
EM	Electromagnetic
EMP	Electromagnetic Pulse
EMC	Electromagnetic Compatibility
EMI	Electromagnetic Interference
ESD	Electrostatic Discharge
FEM	Finite Element Method
FDTD	Finite Difference Time Domain
FEXT	Far End Crosstalk
FWHM	Full Width Half Maximum
IBIS	Input Output Buffer Information Specification
IC	Integrated Circuit
ICEM	Integrated Circuit Electromagnetic Model
IGBT	Insulated gate bipolar junction transistor
LECCS	Linear Equivalent Circuit and Current Source
LEMP	Lightning Electromagnetic Pulse
LIL	Ligned’ Integration Laser
LISN	Line Impedance Stabilization Network
LMJ	Laser Magajoule
MOM	Method of Moments
MOPA	Master Oscillator Power Amplifier
NEMP	Nuclear Electromagnetic Pulse
NEXT	Near End Crosstalk
NIF	National Ignition Facility
OATS	Open Area Test Site
PCB	Printed Circuit Board

PWM	Pulse Width Modulation
PFN	Pulse Forming Network
PML	Perfectly Matched Layer
RLGC	Resistance Inductance Conductance and Capacitance
RFI	Radio Frequency Interference
SE	Shielding Effectiveness
STFT	Short Time Fourier Transform
TEM	Transverse Electromagnetic
TLM	Transmission Line Matrix
TTL	Transistor Transistor Logic
TTT	Table Top Terawatt
VNA	Vector Network Analyser
VSWR	Voltage Standing Wave Ratio

NOTATIONS

$\vec{B}$	Magnetic flux density
$\vec{D}$	Electric flux density
db	Daubechies wavelet function
dB	Decibels
$\vec{E}$	Electric field
$\vec{H}$	Magnetic field
$\vec{J}$	Electric current density
$L^2(\mathbf{R})$	Space of square integrable functions over $\mathbf{R}$
$\vec{M}$	Equivalent magnetic current density
σ	Electric conductivity (Siemens / m)
$\overset{*}{\sigma}$	Magnetic conductivity (Ω / meter)
μ_0	Permeability of free space
ε_0	Permittivity of free space
$\psi(t)$	Wavelet function
$\mathbf{R}$	Real vector space
ω	Angular frequency
$\mathbf{Z}$	Integer vector space

Chapter 1

Introduction

The research work presented in this dissertation investigates electromagnetic interference in electrical systems for flash lamp pumped high power solid state (Nd: glass) lasers. It is focused on analysis and characterization of noise from different laser components which form a multi-scale, intra-system configurations. Effects of the interference on time integrity of trigger signals for critical components are analyzed and various circuit options are looked into. Flash lamp pumped high power Nd: glass laser chains are intense and coherent source of light in infrared regime of electromagnetic spectrum. These are important tools for a variety of laser-plasma interaction experiments such as fusion studies, equation of states and electron acceleration under intense electric field. High intensity of laser beam and finite damage threshold of laser materials lead to Master Oscillator Power Amplifier (MOPA) type of design for the laser chains. MOPA configuration consists of a master oscillator followed by several laser amplifiers of successively increasing gain. Apart from laser oscillator and amplifiers, there are other components such as electro-optical Pockels cells and magneto-optical Faraday rotators in a typical high power laser chain. Each of these components works in synchronization with each other and has unique requirements of power supply, control and trigger signals. Optical amplifiers are pumped by flash lamps which work on the principle of arc discharge through an inert gas such as xenon (Xe) or krypton (Kr). Pockels cells are electro-optical devices which rotate plane of polarization of incident light under externally applied electric field. The required electric field is generated by applying a high voltage (several kV) and fast rise/fall time (few ns) pulses to Pockels cell electrodes. Faraday rotators are magneto-optical devices which rotate plane of polarization of incident light under the influence of magnetic field. The required magnetic fields are generated by high peak current pulse (several kA) flowing through an inductive coil. From electrical point of view, the high power laser chains are pulsed, single shot systems powered by controlled discharge of large capacitor banks. Each stage is fired in synchronism and with certain fixed and pre-determined delays. It has multiple electromagnetic interference sources such as power supply discharge networks and high voltage, high current switches with potential to cause single event upsets and disturbances in control signals which may in turn result into loss of synchronization, increase in timing and delay jitter and consequent loss of reliability and stability of laser energy. This entails a systematic and quantitative study of noise source identification, mechanisms of Electro Magnetic Pulse (EMP) generation, their propagation, interactions with cables, interconnects, shielding enclosures and the influence on integrity of low voltage control and synchronization circuits.

More specifically this work looks into following aspects of electromagnetic interference in high power laser systems:

- Analytical calculations and measurements of transient electromagnetic fields generated by cables of different types, carrying pulsed flash lamp currents.
- Calculation and measurement of coupled induced voltage on and effects on the low voltage control and trigger signals.
- Studies on optimization of electronic components for improved susceptibility to the interfering electromagnetic transients.
- Effects of finite ground planes on field interaction and crosstalk.

- Interaction of EMPs with electromagnetic shields and enclosures.
- Use of wavelet transform and time domain numerical techniques for identification and characterizations of noise sources.

1.1 Motivation and objectives

Raja Ramanna Centre for Advanced Technology, Indore, India, has several high power laser chains aimed towards laser plasma interaction studies. These lasers are optically pumped by Xe flash lamps of varying arc lengths and are fired at very low repetition rate. For practical purposes these lasers are considered as single shot events. Electrical power supplies, drivers for high voltage switches and control circuits are locally developed for delay settings and synchronizations of different stages of the laser chains which are configured as MOPA system. Laser systems for which signal integrity and shielding issues were looked into, as part of the dissertation work are,

i) A 2-beam Nd: glass high power laser chain developed for fusion related studies. Rated energy of the laser system is 400 J in one of the arms and optical pulse width is specified as 1.5 ns [Joshi, 2011].

ii) A table top terawatt laser system which generates intense laser pulses of femtosecond duration for laser-plasma interaction studies at ultra-high intensities (10^{18} W/cm^2) [Naik, 2003].

Objectives of this research work are to analyze the laser power supplies, cabling, interconnect and shield enclosures from EMC and EMI perspective. This is to ensure reliability of control and trigger signals by reducing jitter in set delays, conforming to signal rise and fall time as per designed specifications, reduction of crosstalk and reflection induced voltages. Final aim of these studies and measurements is to increase reliability of electrical systems such that shot to shot variations in laser parameters are minimized.

1.2 Accomplishment and approach

High power solid state laser chains are complex multistage and electrically large systems. Main tasks of the electrical power supply and control systems for these lasers are to energize large number of energy storage capacitor banks and to discharge them through optical pump sources (flash lamps) in a controlled and synchronized manner. Different stages and components in a high power laser chain are fired in synchronization and with certain specified delays in the range 100 ns to 500 μs. Trigger signals for different stages are generated by computerized control systems and hard wired digital circuits. Some of the stages which are fired prior to other stages generate electromagnetic interference which disturbs the delay and timing parameters of trigger signals for subsequent stages. Signal integrity in this dissertation refers to consistency of set delays, rise time and pulse shapes of trigger and clock signal during entire cycle of laser operation. Pulsed and transient voltages and currents generated to excite flash lamps, Faraday coils, Pockels cells, power semiconductor devices and electromechanical relays also generate interfering fields which introduce jitter in set delays and timing parameters. This dissertation aims towards identification of noise sources, which are cause of signal distortion and their characterization. General approach followed in the presented work is to analyze the field generation, propagation and interaction through analytical and numerical techniques such as Finite Difference Time Domain (FDTD) and Transmission Line Matrix (TLM) methods. Continuous wavelet transform (CWT) is used for identification of noise source from time-frequency analysis. Although, there are good numbers of research papers on de-noising and image processing applications of wavelet transforms, its use for noise source identification and characterization in multistage high power laser systems has not been reported yet. Crosstalk analysis is carried out by modeling parallel conductors with coupled transmission line equations. Impedance parameters of cables under different conditions are estimated by scattering parameter measurements. Electromagnetic shielding of optoelectronics components has to deal with presence of intentional apertures for optical transmission. This dissertation analyzes field couplings through a pair of circular and rectangular apertures.

1.3 Contribution of the thesis

Important contributions of this thesis are:

i. Theoretical analysis and measurements for electromagnetic interference from flash lamp power supplies, trigger circuits and high voltage pulsed switches are carried out in time and frequency domains. Flash lamp discharge networks have two different configurations namely, unipolar (+ve bank) and bipolar (+ve and –ve banks). Comparative study is done for electromagnetic interference from these configurations. Radiated emission in a bipolar supply is found to be higher as compared to the emission due to unipolar power supply. Increased emission in bipolar circuit is due to larger area of flash lamp current loop. Re-routing with an aim to decrease the loop area and improvement in cable shields results in reduction of noise interference. Investigations in this area have helped to select an optimum design of flash lamp pulse forming network for flash lamp discharge.

ii. Wavelet transform is applied to time correlate the interfering sources in laser electrical systems consisting of power supplies, discharge and trigger networks.

This represents an intra-system multi-scale setup where several sources within the system generate interference noise. This has provided insight into time-frequency correlation of EMI and helped in source identification. Analysis based on wavelet transform has increased the level of noise prediction which has in turn improved the mitigation procedures.

iii. Studies of shielding effectiveness of metallic enclosures with apertures and housing electro-optical components have resulted into improved design of shield geometry and optimization of intentional aperture shapes and areas with a view to reduce noise couplings in Pockels cell trigger circuits.

iv. Investigations of signal integrity of delay generators and digital ICs for laser control and synchronization circuits operating under pulsed electromagnetic environment, have resulted into design of circuits with lesser jitter in set delay between trigger signals in a table top terawatt laser system. This has improved laser performance in terms of predictable and stable regenerative amplifier gain parameter and laser quality.

v. Analysis of crosstalk induced voltages due to propagation of pulsed currents from flash lamp and Faraday coil discharge circuits and effects of finite ground plane.

These investigations have provided new and hitherto unreported information on frequency content and types of radiated and conducted electromagnetic transients generated in flash lamp pumped high power solid state lasers. Application of computational electromagnetics and signal processing techniques in combination with measurement results have been applied to understand, estimate and mitigate electromagnetic interference and its negative effects on signal integrity in flash lamp pumped lasers. Apart from these contributions resulting into betterment of laser performance, the dissertation work has provided theoretical insight into related topics such as electromagnetic pulse coupling to different types of structures and cables and susceptibility studies of mixed signal ICs under transient electromagnetic fields. The investigations and measurements are specific to operational requirements of flash lamp pumped high power laser systems. However, the theoretical and analytical approach is applicable to other intra system setup as well.

1.4 Organization of the thesis

Rest of the thesis is organized as follows:

Chapter 2 discusses existing literature relevant to the dissertation work. Topics on analysis, modeling and measurement techniques for signal integrity, signal processing techniques, electromagnetic noise emission, field couplings, shielding and susceptibility against transient electro-magnetic pulses are reviewed. Current approach towards these topics and methods used in earlier works are described.

Chapter 3 discusses wavelet transform and electromagnetic numerical techniques namely, finite difference time domain and transmission line matrix methods. These signal processing and mathematical tools are used to address the noise and EMI issues in high power laser systems. Descriptions provided in this chapter form theoretical background for subsequent sections of the dissertation.

Chapter 4 is system description for power supplies, control systems, synchronization circuits and flash lamp trigger circuits with emphasis on signal integrity issues of two different solid state high power laser chains. These are a 400 J, 2-beam high power laser chain and a high intensity ultra-short table top terawatt laser unit. Functioning and operational requirements of electro-optic and magneto-optic components used in these lasers i.e. high voltage and high current flash lamps, high voltage Pockels cells and Faraday isolators are described in detail.

Chapter 5 discusses the phenomena of radiated and conducted emissions. Conventional problem of electromagnetic emissions from an excited conductor is extended to analyze electromagnetic emissions from different types of flash lamp power supplies and Pockels cell driver circuits. Noise emissions are affected by various factors like characteristics of cables, proximity to ground plane from devices and cables, type of shielding etc. Results for measurements of radiated and conducted emissions from a single core and a coaxial conductor of length 2m carrying flash lamp discharge current is presented. It is observed that shielded coaxial cable (RG-58) reduces noise level by at least 2 dB as compared to unshielded single core cable. Effects of ground planes and bents on emission characteristics from electrically long cables are looked into. Differences in noise emissions for unipolar and bipolar flash lamp supplies and driver circuits for Pockels cells are analyzed and compared.

Chapter 6 deals with noise analysis and signal integrity topics in the table top terawatt laser system, which is a relatively compact laser unit with stringent functional requirements of timing integrity of trigger signals for various stages. Experimental results of development of low jitter delay circuit with emitter coupled logic gates are described. ICs belonging to this logic family are observed to be less affected by radiated EMI. Electromagnetic interference in this laser unit is measured in time domain. Wavelet transform is applied on the measured data to analyze noise emitted by individual components. Results of the time-frequency analysis on EMI are presented.

Chapter 7 presents analysis, simulations and measurement results of electromagnetic field couplings and shielding under pulsed excitations. Effects of ICs and PCB terminations on the coupled noise are analyzed. Effects of intentional apertures for optoelectronic components on the shielding effectiveness are investigated. Analysis based on equivalent circuit (apertures modeled as strip lines), transmission line matrix and finite difference time domain methods of shielding effectiveness of metallic enclosures with cross apertures have been carried out and results of investigations of shielding effectiveness of an aluminum enclosure of size 170 mm x 130 mm x 175 mm with circular and rectangular apertures on two opposite faces and housing Pockels cell and the driver circuit are discussed.

Chapter 8 concludes the dissertation by providing outline of the research work. Related topics which can be taken up as extension of this work are pointed out. This chapter highlights improvements in laser performance and reliability due to methodical investigations and simulation of the process of field emissions from different types of structures and their interactions with other components.

Appendix A describes the design of a pulse selector circuit for table top terawatt laser and EMC modeling of integrated circuits.

Appendix B discusses specifications and types of antennas for time domain EMI measurements.

Chapter 2

Literature survey

From the perspective of signal integrity and electromagnetic interference, flash lamp pumped high power solid-state lasers represent a class of multi scale and intra-system setup. Major high power laser facilities around the world have EMC assessment programs aimed towards mitigation of electromagnetic interference, smooth operation and conformity vis-à-vis EMC standards. This chapter reviews existing reports and literatures on EMC analysis of high power lasers and also on interrelated topics of signal processing techniques, electromagnetic emissions from cables and interconnects, field couplings, crosstalk, electromagnetic shielding and signal integrity. Some of the unique features of electromagnetic interference analysis in high power laser systems are due to being single shot events and because of the interconnected stages being spread over larger areas with varying degree of geometrical dimensions. Single shot event refers to short duration and very low repetition rate of the laser operation. Multi scale feature puts extra and quite often prohibitive requirements on computational resources. Furthermore, electromagnetic noise generated by the laser components are non-stationary and transient in nature. Low voltage electronics circuits and control units in these systems are prone to single event upsets. Time domain analysis suits this type of transient electromagnetic events in comparison to frequency domain analysis for repetitive interference. Research literature available on the topic of signal integrity and electromagnetic interference in flash lamp pumped solid-state lasers can be divided into two categories. First category deals with electromagnetic pulses and radio frequency interference generated by arc discharge process in flash lamps and by physical processes in laser–matter interaction experiments [Kelly, 1980]. Focus of this category of papers is to model the process of electromagnetic pulse generation and its propagation around target chambers in plasma experiments. Second category of literature addresses the issues of electromagnetic interference generated by pulsed power supplies, trigger circuits and high voltage switches for lasers. Research papers in this category are aimed towards measurement methods and characterization of interference from compliance, component susceptibility and personnel safety point of view [Anderson, 2003], [Bhatia, 2002]. Conformity to compliance standards, component susceptibility and field coupling are linked to reliable laser operation and minimal variation in shot-to-shot laser energy and better beam quality. High power laser units are typical examples of intra-system setups in which the requirement of electromagnetic compatibility is concerned with susceptibility of the system of interest. Investigations of electromagnetic interference for an intra-system unit such as high power laser systems encompasses proper selection of signal processing and numerical analysis tools, identification and characterization of radiating structures, field coupling and crosstalk in signal transmission lines and shielding against internally generated electromagnetic fields [Morgan, 2007].

Fourier transform has been conventionally used as a signal processing tool to extract frequency information from time domain measurements of electromagnetic interference. Krug et al. [Krug, 2002] reports fast Fourier transform algorithm for time domain measurement data in frequency range 30 MHz to 1 GHz. Post measurement spectrogram is obtained by Bartlett and Welch techniques. Bartlett spectrogram [Bartlett, 1948] averages segments of non-overlapping sampled data whereas, Welch spectrogram [Welch, 1967] uses windowed data segments overlapping in time. Fourier transform provides useful information of spectral content in a measured signal. However, it is not adequate for analysis of transient and non-stationary signals. Noise analysis in intra-system setups such as multi stage high power lasers can be more informative and predictable by utilizing time windowed signal processing tools such as short time Fourier transform and wavelet transform, which are capable of simultaneously generating time and frequency information.

Short time Fourier transform (STFT) was introduced by Dennis Gabor for time-frequency analysis of non-stationary speech data [Gabor, 1946]. It applies Fourier transform on localized data obtained by multiplying fixed duration window with the signal. The analysis window is translated in time to cover the entire signal length. This technique discerns spectral contents of a signal vis-à-vis time information. Short time Fourier transform has been used to map time and frequency parameters of electromagnetic interference measurements data from several noise sources [Russer, 2011]. However, fixed window size in STFT is not able to provide uniform resolution for both time and frequency parameters. Wavelet transformation resolves the problem of time and frequency resolution encountered in STFT by adopting analysis windows of varying scales. Wavelet co-efficient are generated by correlating the time domain signal with scaled and translated version of a mother wavelet $\psi(t)$. This enables wavelet transformation to be localized both in time and in the frequency. At lower scales the signal is analyzed with compressed version of wavelet function. Whereas at higher scales a signal is analyzed with dilated wavelets, which results into correlation with low frequency components. Wavelet transforms are broadly classified into continuous wavelet transformation (CWT) and discrete wavelet transformation (DWT). In continuous wavelet transform, the wavelet coefficients are calculated by linear translation and scaling of mother wavelet function whereas, in discrete wavelet transformation the translation and scaling is dyadic i.e. spaced at interval of 2^j for j level of decomposition. Wavelet functions satisfy admissibility criteria of zero mean value and have important properties of compact support, vanishing moments, regularity and symmetry. These enable temporal localization for analysis of signals with discontinuity. Orthogonal class of wavelets are characterized by similarity in decomposition and reconstruction equations. Some of the popularly used wavelet functions are proposed by Haar, Meyer and Daubechies [Kaiser, 1994]. An important criterion in selection of a wavelet function is the similarity with the signal under analysis such that correlation between reconstructed wavelet and the original signal is optimum. Choice of a wavelet depends on the support size of the mother wavelet and the number of vanishing moments.

Signal decomposition by wavelet transform is applied to diverse fields such as signal processing, de-noising, data compression and solution of differential equations. However, application of wavelet transform for analysis of electromagnetic interference in laser systems is still limited. There are several research papers on its use for noise analysis in related areas of power electronics, electrostatic discharge and high voltage systems. Coppola et al. [Coppola, 2005] have applied continuous wavelet transform with complex Morlet basis function to analyze noise events due to switching of IGBT modules in a chopper circuit. The analysis provides time evolution of signals with specific frequency contents due to triggering of the power semiconductor switches and identifies conducted noise sources in the frequency range 5 to 15 MHz. Time duration of switching transients is of the order of 1 μs. Maximum frequency content of a noise event during specific time duration is estimated by taking norm of a sub-matrix formed by the coefficients of the wavelet transform. Wavelet analysis was able to associate maximum interference frequencies during turn on and turn off processes of 13.5 and 7.5 MHz respectively. Masugi [Masugi, 2003] has investigated interference from electrostatic discharge current with multi resolution discrete wavelet analysis. Electrostatic discharge current and the resulting interference is a good example of transient and non-stationary signal. Discrete wavelet transform executes iterative low and high pass filtering and thereby decomposes a time domain signal into approximate low frequency terms A_j and detail high frequency terms D_j. Thus the time domain signal is expressed as sum of low and high frequency components A_j and $\Sigma D_j(t)$ respectively. Masugi has used wavelet decomposition to quantify the important parameters of electromagnetic interference such as rise time and maximum amplitude. Energy contents in low and high frequency components are evaluated as squared terms $A_j(t_i)^2$ and $D(t_i)^2$. This paper also discusses chaos attractors to investigate the variations in measured data. Kumar et al. [Kumar, 2007] presents a methodology based on multi resolution analysis of current and voltage waveforms to evaluate power loss at different frequency bands. Antonini et al. [Antonini, 2001] have used an extension of wavelet transformation known as wavelet packet decomposition for feature extraction, de-noising, compression and classification of interference signals. Unlike DWT in which a discrete signal $x(n)$ is decomposed by iterative filtering of the low pass filtered approximate components, wavelet packet decomposition filters both the approximate and detail components. Wavelet packet decomposition offers more flexible coding and reconstruction as compared to discrete wavelet transformation. The paper by Antonini [Antonini, 2001] analyzes transient noise generated on a low voltage line due to operation of an air insulated switch and short circuit current on a nearby high voltage power line. In this work, wavelet packet decomposition uses Daubechies wavelet function of order 5. The chosen method provides a good differentiation of frequencies associated with switch operation and short circuit currents. Keshwani et al. [Keshwani, 2010] has applied the techniques of short time Fourier transform and wavelet transform to investigate spatial distribution of noise signals in a control room environment. This paper highlights the application of modern signal processing tools for real time noise processing in multi-source environment.

From systems point of view, main contributors of EMI in optically pumped solid state high power lasers are,

a) Pulsed power supplies for flash lamps.

b) High voltage and fast rise time switches for electro-optic devices.

c) Generation of electromagnetic pulses from arc discharge in flash lamps and from laser matter interaction experiments.

National ignition facility (NIF) at Lawrence Livermore National laboratory, USA, is the largest flash lamp pumped solid state laser system consisting of 192 beams, capable of delivering 1.8 MJ of optical energy at 351 nm in 3 ns [Moses, 2009]. There are several papers and reports on the topic of EMI/EMC at NIF. Results and methodology of EMI measurements for flash lamp pulsed power supplies and plasma electrode Pockels cell are reported by Anderson [Anderson, 2003]. Electromagnetic noise in NIF power conditioning systems are mainly due to switching of spark gap and impedance discontinuity attributed to transition from coaxial geometry to flash lamps through termination interconnects. Flash lamp main current pulse is preceded by a fast rise time pre ionization conditioning pulse. Rise time of pre ionization current is of the order of 10^{11} A/sec. Laser pulse occurs after peak of the flash lamp main current. Thus, major portion of electromagnetic interference due to flash lamp excitation is initiated several hundred micro-seconds prior to occurrence of the laser pulse. Radiated noise from switching of plasma electrode Pockels cell (PEPC) is of low amplitude but has broader frequency content in comparison to interference signals generated by flash lamp pre-ionization current. Low impedance grounding, isolation and shielding practices are adopted to minimize the EMI effect. Fields intensities were obtained by numerically integrating the experimental data from E-dot and B-dot probes of 100 MHz bandwidth. Measured field intensities show resonant behavior, which are attributed to physical dimensions of switching elements and their placement with respect to ground. Characterization of electromagnetic pulses generated near target chamber due to laser-target interaction in NIF is reported by Stathis [Stathis, 1994]. Short time EMPs encountered in high power laser systems have potential to cause signal integrity problems in laser plasma diagnostic instruments. The technical report by Stathis analyzes noise coupling in cables and electrical circuits due to electromagnetic pulses (EMPs) generated by laser plasma interaction effects. Electromagnetic interference in plasma chamber scales linearly with neutron and gamma flux. Estimated peak value of the electric field outside NIF plasma chamber is of the order of 1.5 MV/m. The study provides useful data for characterization of several cables such as RG-213/214 under EMP excitation. On a 1.9 MJ NIF shot the noise voltage induced in RG-213 cable is of the order of 30 V. A typical laser plasma experimental set up consists of several sensitive plasma and x-ray diagnostic instruments. Electromagnetic noise generated by neutron detectors and X-ray imaging systems at NIF and their effects on other instruments has been analyzed by Brown et al. [Brown, 2012]. There are scientific reports and research papers from other high power laser systems such as Laser Mégajoule (LMJ), Orion and Ligned' Integration (LIL), which provide useful insights into electromagnetic interference aspects. Mead et al. [Mead, 2009] have investigated generation of electromagnetic pulses and their characterization in Orion laser systems. Polarized (Horizontal and Vertical) radiated emission in the frequency range 1 kHz to 1 GHz is measured using standard EMC measurement equipment. Measured value of peak radiated field in the Orion laser is of the order of 600 V/m. The paper also outlines useful techniques like shielding, use of fiber cables, reversal of current flow and single point grounding implementation to minimize the effect of electromagnetic interference. Technical challenges posed by requirements of controlled energy, precision timing and positioning of targets under harsh electromagnetic environments for the Laser Mégajoule project is discussed by de Cervens et al. [Cervens, 2009]. The authors have discussed low impedance grounding system from EMC perspective for the 1.8 MJ LMJ laser project. EMC aspects of fast diagnostic design at Ligned' Integration Laser are discussed by Raimbourg [Raimbourg, 2007]. This paper analyses the generation of electromagnetic noise due to interaction of 60 kJ laser with a solid target. The laser plasma interaction results into pulsed electric field of the order of few kV/m outside the target chamber. A surge immunity test generator is used to simulate the induced current from capacitor bank discharge circuit. Electromagnetic field with rise time as low as 100 ps and frequency contents exceeding 1 GHz is characterized with a magnetic loop based on Moebius design. Effects of single and multi-point groundings on interference voltage induced on a digital oscilloscope are compared.

Topic of signal integrity, which concerns with faithful propagation of signals over transmission lines, has seen renewed research activities in recent times due to increase in component density, clock speed development of systems based on nano-materials and strategic applications of EMPs [Caignet, 2001]. Interfering fields have different types of effects on functionality of electronic systems. It varies from causing permanent damage in semiconductor components to upsets and false triggers in digital circuits and software glitches in embedded systems. In a multistage high power laser system signal integrity is an important topic from the point of view of synchronization of trigger signals for various stages. Timing jitter between the master clock and trigger signals has to be as low as possible for stable laser operation. Signal integrity analysis for PCB tracks, cables and interconnects depend on solution of transmission line equations and extraction of *RLGC* (Resistance, Inductance, Conductance and Capacitance) parameters. Signal integrity in digital circuits and systems also depends on parasitic impedance in transmission lines, cables and interconnect. A detailed characterization requires modeling and analysis based on solution of transmission line equations and parameter extraction. Interconnect parameters namely *RLGC* can be extracted either by 3-D electromagnetic solver or by *S* parameter measurements [Young, 2001], [Kao, 2001].

Reliable and stable laser operation depends to a great extent on immunity level of ICs and power electronics components. Research on electromagnetic compatibility of power electronic circuits and systems is driven by increase in use of high frequency PWM technology in power supply designs and motor drives [Marlier, 2012], [Redl, 1996]. Determination of noise immunity of semiconductor ICs is an important aspect of EMC assessment of a system. Boyer et al. [Boyer, 2007] present electromagnetic interference susceptibility characterization and testing methods for integrated circuits. Susceptibility test is carried out by applying a localized near field disturbance with a near field magnetic probe for frequency range 1 MHz to 2 GHz. The authors present a case study in which susceptibility of a 16-bit microcontroller is tested for different functionalities under inductive coupling.

There are several pioneering papers on prediction of device performance under external electromagnetic fields. Tront [Tront, 1985] has discussed SPICE models for predicting radio frequency upsets of digital ICs. Laurin [Laurin, 1995] has investigated the effects of radiated EMI on operation of digital systems by simulating the response of logic circuits to incident plane wave. Electromagnetic simulations of semiconductor devices are carried out by combining linear moment-method model of wire structure with non-linear circuit models. Noise induced timing and delay jitter are important aspects of EMC assessment of multi-stage synchronization circuits. Accurate jitter analysis depends on availability of reliable device models. Magnitude and frequency content of signal deterioration also depends on electrical characteristics and geometry of interconnects, surrounding materials and shields. Noise induced jitter has statistical spread in time and frequency domains. Results of several research works suggest that high frequency interference signals introduce less jitter as compared to low frequency interfering signals. A method to predict Radio Frequency Interference (RFI) induced delays in CMOS inverter is proposed by Laurin [Laurin, 1995]. The analysis proposes mathematical expressions for radiated and capacitive/inductive coupled noise. Robinson et al. [Robinson, 2003] have suggested a theoretical model to explain high frequency immunity behavior of digital integrated circuits based on switching parameters of logic gates. It results into quantification of dynamic immunity level of digital ICs under pulsed interfering signal in terms of time width of the interference pulse and the low pass filter time constant. Model proposed by Robinson to calculate immunity level for digital logic families matches with specified immunity levels of respective logic families. CMOS logic family has highest noise immunity as compared to variants of TTL ICs. This paper also evaluates statistical distribution of the timing jitter variations from knowledge of probability distribution function of interfering signals.

Electromagnetic noise dealt in this dissertation is transient and non-repetitive. Time domain measurements and analysis are best suited for this class of EMC problems. Analytical methods for EMI solution in large-scale systems under transient noise exposure are not always possible to formulate. There are several accurate and relatively easy to implement numerical solutions for the investigated EMI/EMC topics. Computational electromagnetics for EMC applications with emphasis on accuracy, speed and resource utilization is an evolving subject. Burrus et al. [Burrus, 1998] provide comprehensive information on development of numerical electromagnetics in recent past. Finite difference time domain method is one of the most used techniques. It is based on differential form of Maxwell's equations. It uses staggered grids for electrical and magnetic fields in time and space, which was introduced by Yee [Yee, 1966]. Maxwell's curl equations for electric and magnetic fields are converted from derivative form to a set of difference equations. It discretizes a problem domain in time Δt and space Δx, Δy and Δz. The electric field at time step $(n+1)\Delta t$ is calculated from the electric field at time $n\Delta t$ and magnetic field at the time step $(n+0.5)\Delta t$. This is illustrated in Figure 2.1 and further elaborated in chapter 3 of this thesis.

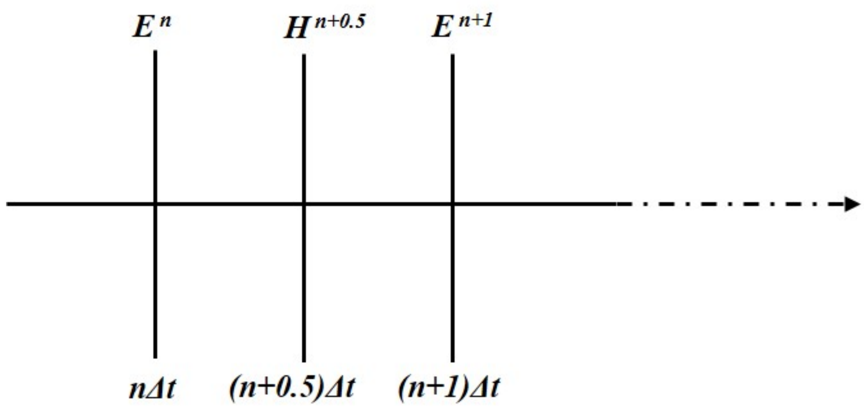

Figure 2.1: Time staggering of electric and magnetic field components [Bruns, 2007]

Maximum time step in FDTD method is limited by Courant-Freiedrich-Lewy criterion, which for a cubic unit cell is equal to the time taken by electromagnetic field to travel the distance between two diagonal grids. A perfectly matched layer truncates finite difference time domain computational space. Transmission line matrix method utilizes the analogy of electromagnetic wave propagation and propagation of impulses in transmission lines networks [Johns, 1980]. It consists of a 3-D network where electric and magnetic fields are modeled by voltages and currents. Space discretization unit in

TLM method is typically of $\lambda/10$, where λ represents the minimum wavelength of interest. There are several recent publications on computational electromagnetics for EMI applications. Muot et al. [Muot, 2012] have applied a hybrid approach consisting of finite difference time domain and transmission line methods to calculate lightning induced electromagnetic effects on interconnected buildings. It is an example of application of FDTD and TLM methods for electrically larger systems. Finite difference time domain modeling method is a frequently applied numerical technique for EMI/EMC applications [Lin, 2001], [Liu, 2005] and [Taflove, 2005]. However, it is not well suited for problem features, which requires smaller time steps, has sharp resonance points or applications with large unbounded spaces.

Electromagnetic noise in an electrical system is generated either by radiation or conduction mechanism. Modeling of emission mechanism is an essential step in EMC assessment and analysis. Dominant factor that affects the EMI and radiated emission in a system is the current return path. Measurement and analysis zones for radiated emission are divided into near field and far field [Balanis, 2005]. Distance greater than $2(D^2/\lambda)$, where D is dimension of radiating element and λ is the wavelength, is considered as far field region. Far field measurements are affected by scattering in surrounding medium and are conventionally carried out in controlled environment like open area test sites (OATS), anechoic chambers and transverse electromagnetic (TEM) cells. In contrast, near field measurements are less expensive as it can be carried out in normal laboratory conditions. Presence of scattering elements around radiating elements does not affect the near region measurement results. For far field emission analysis, a current carrying conductor is modeled either as a uniform current dipole in which case it is assumed that current amplitude and phase are constant throughout the cable with a non-zero current at end points or a long dipole antenna with a non-uniform current distribution [Paul, 2006]. For uniform current dipole models, far field calculation is based on emissions from an elemental dipole. Practical current carrying conductors are modeled as long dipole antennas for which calculation is carried out by superposition of contributions from small sections along the radiator. Each of the smaller section is assumed to carry a constant current which depends on element position and current distribution along the line. Contribution of common mode current in far field emission is more than the contribution of differential mode current [Paul, 2005]. Analytical formulations and models for far field emissions are reported for both common mode and differential mode currents [Balanis, 2005], [Paul, 1984]. Conducted emission measurement is specified in frequency band 150 kHz to 30 MHz and measurement setup includes a line impedance stabilization network (LISN) [CISPR, 1997]. Several modeling and analytical techniques have been reported in recent publications for investigation of conducted noise in power supplies and inverters [Yazdani, 2011]. Contributions due to common mode and differential mode currents are also to be taken into account for investigations of conducted interference [Stahl, 2010].

Laser power supplies, control and synchronization circuits utilize various types of conductors to carry high voltages and control signals. Electromagnetic interference, field couplings and crosstalk between cables affect the overall laser performance. Coupling of an external electromagnetic field with electrical cables depends on a number of factors such as time and frequency parameters, intensity of incident field, system geometry, proximity to ground planes, shielding and cable characteristics [Sali, 1982]. Roy et al. [Roy, 2008] have investigated electromagnetic coupling and crosstalk induced voltages in multi-conductor cables by electromagnetic modeling and validation with 3-D field solver software package. Liu et al. [Liu, 2010] have reported a FDTD and multi-conductor transmission line analysis for prediction of time domain response of transient electromagnetic field to shielded twisted pair cables. Proposed model divides the coupling of external fields to transmission lines into two systems namely external and internal systems. The external coupling is solved by finite difference time domain method, whereas the internal coupling between sheath and inner conductor is solved by multi-conductor transmission line model. For field coupling and crosstalk analysis a shielded cable can be considered to consist of two systems coupled through transfer impedance. Exterior of cable shield and ground is one of the systems whereas shield interior and inner wires form the second system [Paul, 1994]. There are several recent papers, which aim to simplify analysis and modeling techniques for crosstalk in cable systems [Liu, 2013]. Field couplings between two cables have been traditionally solved by transmission line equations. Commonly employed techniques for crosstalk prediction in multi-conductor cables are based on transfer impedance technique [Sali, 1979], modal decomposition [Benson, 1992] and eigen value method [Tealby, 1987]. Li et al. have used a numerical technique known as equivalent cable bundle method for cross talk analysis in multi-conductor system [Li, 2012].

Electromagnetic shielding of noise sources and victim circuits are important aspects of EMI investigations in intra-system setups. Shielding effectiveness (SE) as represented by ratio of field intensity at a point in absence of shield to field intensity at the same point in presence of shield [IEEE Standards, 1997] is commonly used to quantify an electromagnetic enclosure. Geetha et al. [Geetha, 2009] have reviewed basic theory of electromagnetic shielding. This paper provides a detailed survey of metals, conducting plastics and conducting polymers for the control of electromagnetic emission. In multistage amplifier based high power laser systems, electromagnetic shielding enclosures for electro-optical components such as Pockels cells contain intentional apertures for optical transmission. Certain aspects of shielding problems in this area are similar to conditions existing in commonly studied electro-optical units which have feed-through and apertures for coupling fiber cables and light. Presence of apertures in electromagnetic enclosures reduces overall shielding effectiveness due to decrease of counteracting eddy currents. Shielding effectiveness is calculated either by rigorous solution of electromagnetic boundary problems, numerical electromagnetic modeling or approximate formulations [Thomas, 2001]. There are several research papers which estimate the level of deterioration in shielding due to presence of apertures. Masterson et al. [Masterson, 2001] have reported measurement techniques and theoretical analysis to estimate shielding effectiveness of metallic enclosures in presence of different types of fiber optic feed-through. It estimates shielding effectiveness in terms of transmission cross sections which is defined as ratio of power coupled into an enclosure through an aperture to incident power per unit area. Mendez [Mendez, 1978] is one of the original researchers to present theoretical analysis of electromagnetic radiation from metallic enclosures with apertures. He has adopted the approach of treating metallic enclosures as resonant cavity. Bethe's theory of diffraction [Bethe, 1944] is a highly cited classical approach to determine electromagnetic emissions attributed to apertures. It implies that fields in vicinity of openings may be represented by sum of original fields at aperture location and fields due to electric and magnetic dipoles located at center of apertures. Robinson et al. in a later paper [Robinson, 1998] have formulated an analytical methodology based on equivalent transmission line model for shielding effectiveness of an enclosure with apertures. In this approach, apertures are represented by a co-planar strip-line short-circuited at both ends. Electromagnetic field coupled inside a cavity gets modified by presence of PCBs, components and wires. Thomas [Thomas, 2001] extended the method of strip line equivalent circuit by considering impedance of conducting plane and dielectric slab representing a practical PCB inside metallic enclosures.

2.1 Summary and conclusion

This chapter presents a brief literature survey on the topics of electromagnetic interference and compatibility for multi-stage high power lasers. Research papers and technical reports on this topic available in public domain point towards the need for smooth functioning and electromagnetic compatibility of diagnostic instruments as prime motivation. Two different sources of electromagnetic interference, their measurement techniques and treatment of the topic are clearly identified. One of the sources of interference is the pulsed power supply, which consists of charging circuit for large capacitor banks and discharge network for flash lamp load. The second source is interaction process of high intensity laser beams with solid matters. In the former case, the investigations are based on conventional techniques such as measurement in time domain with standard antennas and probes. Most of the reported measurements are carried out for radiated emissions in far field regime. For the case of EMI from laser matter interaction, there are reports of development of new probes and measurement setups as the resulting electromagnetic pulses are characterized by high intensity and fast rise time in sub nanosecond domain. The work in this thesis carries forward, earlier work on this topic in terms of identification of recent signal processing techniques such as wavelet transform, computational electromagnetics and their applications in interference analysis of high power flash lamp pumped solid-state laser chains. Measurements are carried out in both near and far field regimes of radiating structures in the laser systems. Bulk of the investigations described here relates to flash lamp pumped high power chains. However, some of the studies such as analysis of crosstalk induced voltages in cables and wires, field coupling through rectangular and circular apertures and time-frequency noise source characterization with wavelet transformation can be applied to EMI/EMC investigations in more generic electrical and electro-optical systems.

Chapter 3

Signal processing tools and numerical techniques for EMI analysis

Analysis of electromagnetic interference deals with identification and characterization of noise generating sources, calculation of propagation of electromagnetic field, interaction of electromagnetic field with cables and subsequent effects on integrity of critical signals which are responsible for system operation. These endeavors need specific mathematical tools, transforms and numerical techniques. Interference signals analyzed in this dissertation are specific to the high power laser chains and in general, these are non-stationary and transient. Literature survey points towards applications of various mathematical modeling and transforms for identification and characterization of noise sources in power electronics setups [Tesche, 1997]. Wavelet transform is suitable for time frequency decomposition of transient and non-stationary signals. Wavelet transform with Morlet and Daubechies functions is used for characterization and identification of noise sources from power supplies and high voltage semiconductor switches in a table top terawatt laser system and described in chapter 6.

Electromagnetic interference problems quite frequently reduce to solution of Maxwell's equations under certain boundary conditions. However, it is complicated for large scale systems to be accurately described by continuous linear functions and the corresponding Maxwell equations are difficult to solve by analytical techniques. There are several numerical methods in time and frequency domain to handle this class of problems. Frequency domain numerical solutions approximate the integro-differential equations and solve large matrix equations. Finite element methods (FEM) and method of moment (MoM) are two examples of frequency domain techniques.

Time domain techniques on the other hand are implemented by finite difference, time stepping algorithms. Finite Difference Time Domain (FDTD) and Transmission Line Matrix (TLM) methods are examples of time domain techniques. Time domain methods are better suited to handle transient interference and non-linear loads such as spark gaps and flash lamps. In time domain analysis, the calculation time is mesh dependent. Accuracy and computational stability of numerical methods are essential for useful and reliable solutions. Accuracy refers to closeness of approximate solution to the exact values. Stability refers to the requirement that computational resources do not increase with time. To some extent, reducing mesh size increases accuracy. However, from computational point of view it is not possible to reduce the mesh size beyond a certain point. Aggregate numerical errors associated with each calculation step become dominant with increase in step size. Time domain techniques are adopted to solve specific EMI problems of crosstalk and shielding for transient, impulsive and broad band interference in laser systems. Following sections of the dissertation describe wavelet transform, finite difference time domain and transmission line matrix methods as background information for the work presented in rest of the chapters of this dissertation. Analysis and modeling of fields due to conductors and interconnects of various shapes and sizes are carried out with the help of these techniques at different stages of this research work.

3.1 Wavelet transform

Wavelet transform is a mathematical tool used in signal processing for two dimensional, time-frequency-intensity analysis. It decomposes a time domain signal into a set of basis functions called wavelets. Wavelet concept includes multi-resolution decomposition of signals into orthogonal and bi-orthogonal functions [Daubechies, 1988]. It is particularly suited to investigate non-stationary and intermittent signals in which frequency does not remain constant over a defined time interval. Interfering signals produced in flash lamp pumped high power laser systems are non-stationary in nature and belong to a class of problems appropriate for analysis with wavelet transform. Classical technique of Fourier transform of a signal misses the time information which is an essential parameter for source identification in inter-system setups. Short time Fourier transform (STFT) retains the time information of original signal by using fixed windows to localize the region of analysis. STFT of a signal *x(t)* is given by the following expression:

$$STFT\left\{x(t)\right\}\left(\tau,\omega\right)=X\left(\tau,\omega\right)=\int_{-\infty}^{\infty}x(t)\omega\left(t-\tau\right)e^{-j\omega t}dt \tag{3.1}$$

ω(t) is the window function which is normally taken to be Hann or Gaussian. Time windowing of a non-stationary signal with widow *ω(t)* translated by factors *a* and *b* is shown in Figure 3.1.Time and frequency resolutions of STFT are determined by size and shape of window. Shorter time interval windows provide better resolution for time parameter at the cost of frequency resolution. Lower frequencies are missed as time interval becomes shorter. On the other hand increasing time interval will not accurately pin point occurrence of an event in time domain. It is on this issue of time vs. frequency resolution that wavelet transform differs remarkably from STFT.

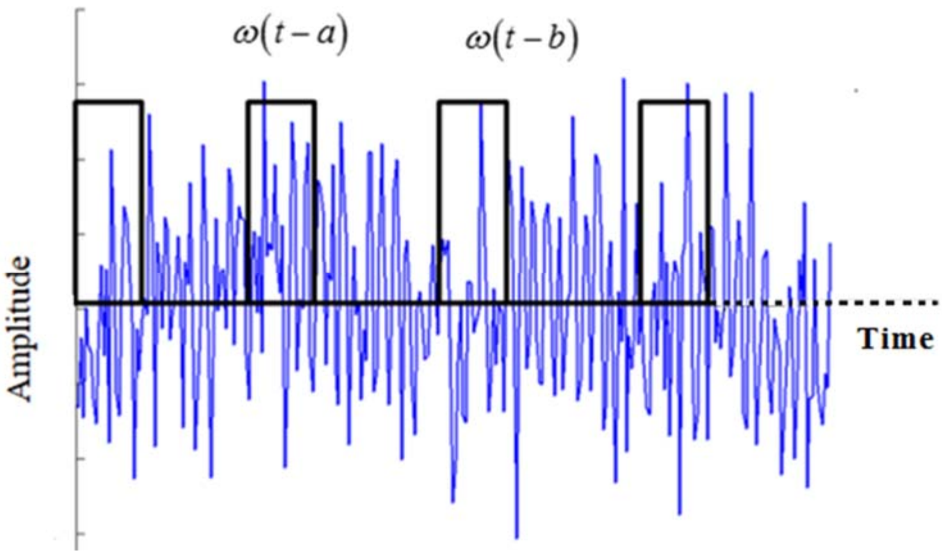

Figure 3.1: Time windows for short time Fourier transform

In contrast to fixed size of window in case of short time Fourier transform, wavelet transform has provision for variable size windows. Continuous wavelet transform (CWT) of a signal *x(t)* is given by,

$$W(s,\tau) = \frac{1}{\sqrt{|s|}} \int x(t)\psi^{*}\left(\frac{t-\tau}{s}\right)dt \tag{3.2}$$

Ψ(t) is known as mother wavelet. Wavelet functions *W(S, τ)* are derived from mother wavelet through translation and scaling. Parameter *τ* is translation parameter of wavelet function as it shifts through the signal. Term *s* is the scaling parameter. $\Psi^{*}(t-\tau/s)$ is conjugate of translated and scaled wavelet function. Larger scales correspond to low frequencies and it dilates the signal to reveal detailed information. At smaller scales the signal is compressed. Each scaling and shifting operation results into scaling of the mother wavelet by a factor of *1/s* and translation by *τ* to produce the wavelet co-efficient *W (s, τ)*. Thus, the wavelet transform decomposes a 1-D time-amplitude signal into 2-D time-scale amplitude information. Each wavelet function is associated with a periodic signal corresponding to a central frequency. The wavelet central frequency F_c connects scale to pseudo frequency and sampling rate as per following equation [Abry, 1997].

$$F_a = \frac{F_c}{a.\Delta} \tag{3.3}$$

where, Fa is the pseudo frequency, Fc is the central frequency, Δ is sampling period and a refers to scale. Necessary conditions for mother wavelets are that the set of discrete translations and dilations forms an orthonormal basis for $L^2(\mathbf{R})$ which is Hilbert space. $\boldsymbol{R}$ represents real numbers and L^2 is set of functions with bounded energy [Mallat, 1989]. It implies that wavelet functions have finite energy $\int |\psi|^2 \, dt < \infty$ and are band-limited $\int_{-\infty}^{\infty} \frac{|\psi(\omega)|^2}{\omega} d\omega < \infty$. Second condition of band limitation is known as admissibility criterion and it also implies that $\psi(0)=0$ for smooth $\psi(\omega)$ function. This is to be contrasted with short term Fourier transform where no orthonormal basis is generated. Function $x(t)$ can be recovered from the continuous wavelet coefficients with the following inverse wavelet transform.

$$x(t) = \frac{1}{W_\psi} \iint \frac{W(s,\tau)\psi_{a,b}(t)}{s^2} ds.d\tau \tag{3.4}$$

where, W_ψ is a function of Fourier transform of the mother wavelet $\Psi(t)$ and is represented by,

$$W_\psi = \int_{-\infty}^{\infty} \frac{|\psi(\omega)|^2}{\omega} d\omega \tag{3.5}$$

Discrete wavelet transformation is obtained by dyadic scaling and translation of the wavelet function to generate a set of orthogonal basis function [Daubechies, 1990]. It implies that the scaling and translation parameters s and τ for DWT take the form of 2^n and $m.2^n$ respectively, where n and m are integers. For a series of sampled data $x(n)$ the set of discrete wavelet transform coefficients are generated by the following expression.

$$DWT(2^n, m.2^n) = \frac{1}{\sqrt{2^n}} \sum_n x(n) \psi\left(\frac{n - m.2^n}{2^n}\right) \tag{3.6}$$

It is implemented by a cascade of low pass filter (coarse approximation) and high pass filter (detail information). In this way the sampled signal is decomposed into a number of sub-bands. Realization of filter bank with Mallat algorithm [Burrus, 1998] for two level decomposition is shown in Figure 3.2. The term $X(n)$ represents the sampled signal which is band limited to Nyquist frequency of $fs/2$, where fs is the sampling frequency. In the first stage it is passed through a half band high and low pass filter. Post filtering requirement of the sampling frequency reduces successively by half. This results into good time resolution at higher frequencies and good frequency resolution at lower frequencies. After filtering and sub sampling to desired level the DWT is obtained by concatenating the approximation and detail coefficients.

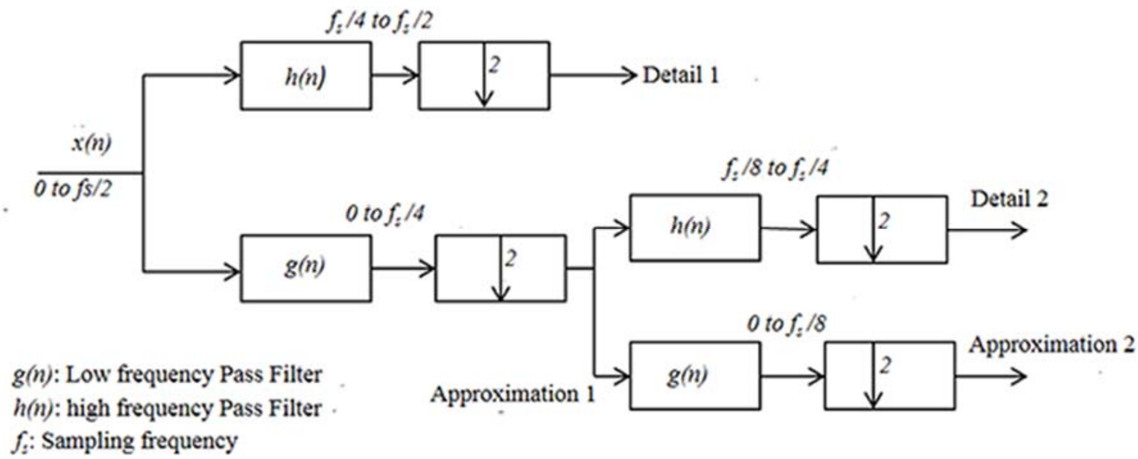

Figure 3.2: Mallat algorithm for two level discrete wavelet transformation

There are several orthogonal and non-orthogonal wavelet functions in use. Each of the wavelets has a characteristics shape, which depends on its frequency contents. Non-orthogonal wavelets are used for CWT analysis where continuous variation is expected. Wavelet functions are also classified as complex and real functions. Complex wavelets are needed for both phase and amplitude analysis. Some of the well-known wavelet functions are shown in Figure 3.3. Choice of the wavelet function for a particular application depends on shape and parameters of the time domain signal under analysis. Haar is the simplest orthonormal wavelet function and it resembles a step function. Mathematically, a Haar function is expressed as,

$$\psi(t) = \left| \begin{array}{ll} 1 & 0 \le t < 0.5 \\ -1 & 0.5 \le t < 1 \\ 0 & elsewhere \end{array} \right. \qquad (3.7)$$

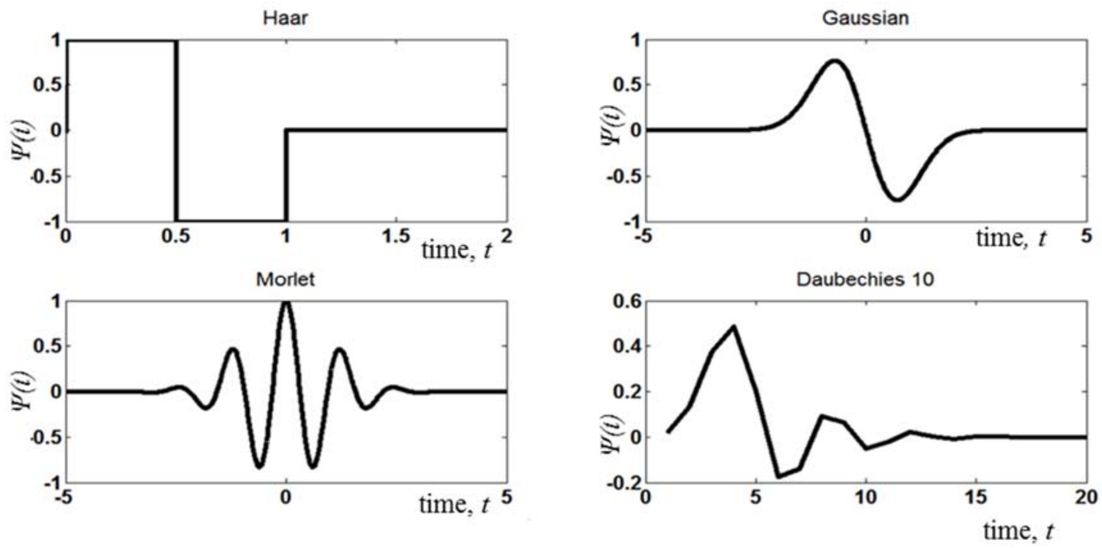

Figure 3.3: Wavelet functions

Haar function generated by discrete translation and dilation is mathematically represented as,

$$\psi_{m,n}(t) = 2^{-m/2}\psi(2^{-m}.t-n) \qquad m,n \in Z \tag{3.8}$$

It constitutes an orthonormal basis for $L^2(\mathbf{R})$. It is to be noted that Haar function is not continuous. It resembles a step function with the Fourier transform decaying as $1/\omega$. Gaussian functions by themselves are not proper wavelets as they do not have compact support. However, differentiated wavelets exhibit limited support and are used as wavelet function. First order differentiated Gaussian wavelet function is expressed as,

$$\psi(t) = a\sqrt{2\pi}\left(t-b\right)\exp\left[\frac{-\left(t-b\right)^2}{2a^2}\right] \tag{3.9}$$

Terms a and b are scaling and time shifting parameters respectively. A Gaussian wavelet is indefinitely derivable and is commonly used for analysis of biomedical signals. Morlet wavelet is a non-orthogonal function [Torrence, 1998] given by,

$$\psi(t) = \frac{1}{\sqrt[4]{\pi}}\left(e^{j\omega_0 t} - e^{-\omega_0^2/2}\right)e^{-t^2/2} \tag{3.10}$$

Term ω_0 is known as central frequency. For $\omega_0 > 5$ second term of expression (3.10) can be neglected. This results into simplified expression of Gaussian modulated sinusoid expressed as,

$$\psi(t) = \frac{1}{\sqrt[4]{\pi}} e^{j\omega_0 t} e^{-t^2/2} \tag{3.11}$$

Fourier transform of the Morlet wavelet is given by,

$$\psi(\omega) = e^{-(\omega - \omega_0)^2/2} - e^{-(\omega^2 + \omega_0^2)/2} \tag{3.12}$$

For the Morlet function the property $\psi(\omega)=0$, *for* $\omega=0$, provides better frequency localization. It is also marked by smoothness and periodicity, which makes it suitable for functions without sharp discontinuity. Phase plot of wavelet transform of a real signal with complex Morlet function is used to analyze singularities [Lee, 1994].

Daubechies wavelets also known as Maxflat belong to a family of orthonormal wavelets which are compactly supported. Compact support is due to specific selection of scaling function ϕ, which is represented as,

$$\phi(t) = \sum \alpha_k \sqrt{2}\phi(2t-k) \tag{3.13}$$

Where α_k for $k,m,N \in Z$ exhibit following properties,

$$\alpha_k = 0 \qquad 2N < k < 0 \tag{3.14}$$

$$\sum_{k=-\infty}^{\infty} \alpha_k \alpha_{k+2m} = \delta_{0m} \tag{3.15}$$

$$\sum_{k=-\infty}^{\infty} \alpha_k = \sqrt{2} \tag{3.16}$$

Based on $\phi(t)$ and α_k as defined above, the Debauchies wavelet function is,

$$\psi(t) = \sum_{k=-\infty}^{\infty} (-1)^k \alpha_{-k+1} \sqrt{2}\phi(2t-k) \qquad (3.17)$$

A wavelet function $\psi(t)$ has N vanishing moments if the condition $\int t^m \psi(t) dt = 0$ holds for $m=0, 1, 2, \ldots N-1$. Suitability of a mother wavelet for analysis of EMI due to laser power supplies in this work is judged by frequency decomposition and correlation of the reconstructed wave. Approximation error of a wavelet transform varies with the number of vanishing moment 'L' as 2^{-L}. Thus it is preferred to utilize a wavelet function having larger vanishing moment. Use of wavelet transform for noise characterization in a table top terawatt laser unit is reported in chapter 6.

3. 2 Finite difference time domain method

Finite difference time domain method provides a time-domain solution of Maxwell's equations in differential form by discretizing both the physical region and time interval with a uniform grid. It was introduced by Yee [Yee, 1966] and is a widely used method for investigations of electromagnetic behavior in cellular phones, mobile computing, EMI/EMC, lasers and photonic circuits. It is a conceptually simple technique as the calculation does not require formulation of integral equation. However, its implementation necessitates modeling of objects as well as its surroundings, which increases the execution time. Another drawback of FDTD is that computational meshes are rectangular in shape. They do not conform to objects with curved surfaces, as is the case of the cylindrical or spherical boundary. Maxwell's equations for electric and magnetic fields in rectangular co-ordinates are written as,

$$\varepsilon \frac{\partial E_x}{\partial t} = \frac{\partial H_z}{\partial y} - \frac{\partial H_y}{\partial z} - \sigma E_x - J_x \qquad (3.18)$$

$$\varepsilon \frac{\partial E_y}{\partial t} = \frac{\partial H_x}{\partial z} - \frac{\partial H_z}{\partial x} - \sigma E_y - J_y \tag{3.19}$$

$$\varepsilon \frac{\partial E_z}{\partial t} = \frac{\partial H_y}{\partial x} - \frac{\partial H_x}{\partial y} - \sigma E_z - J_z \tag{3.20}$$

$$\mu \frac{\partial H_x}{\partial t} = \frac{\partial E_y}{\partial z} - \frac{\partial E_z}{\partial y} - \overset{*}{\sigma} H_x - M_x \tag{3.21}$$

$$\mu \frac{\partial H_y}{\partial t} = \frac{\partial E_z}{\partial x} - \frac{\partial E_x}{\partial z} - \overset{*}{\sigma} H_y - M_y \tag{3.22}$$

$$\mu \frac{\partial H_z}{\partial t} = \frac{\partial E_x}{\partial y} - \frac{\partial E_y}{\partial x} - \overset{*}{\sigma} H_z - M_z \tag{3.23}$$

Where,

$\vec{E}$: Electric field (V/m)

$\vec{D}$: Electric flux density (Coulomb/m^2)

$\vec{H}$: Magnetic field (A/m)

$\vec{B}$: Magnetic flux density (Webers/m^2)

$\vec{J}$: Electric current density (A/m^2)

$\vec{M}$: Equivalent magnetic current density (V/m^2)

σ : Electric conductivity (Siemens/m)

σ^* : Magnetic conductivity (Ω / meter)

FDTD based on Yee's algorithm discretizes the physical region and time interval of differential form of the three dimensional Maxwell's equations on uniformed grids. Electromagnetic fields are updated on each time step by values calculated in previous steps in adjacent cells. Thus, the differential equations (3.18) to (3.23) are simulated by a 3D physical model as illustrated in Figure 3.4. Terms i, j and k denote the points with co-ordinates $i\Delta x$, $j\Delta y$ and $k\Delta z$. Components of electric field *(E)* and magnetic field (*H)* are interlaced, so that each *E* component is surrounded by four *H* components and each *H* component in turn is surrounded by four *E* components. For example, H_x component located at point (*i, j+1/2, k+1/2*) is surrounded by four circulating $\vec{E}$ components, two E_y components and two E_z components matching to the electromagnetic equation, which states that H_x component increases directly in response to a curl of $\vec{E}$ components in x direction with a constant magnetic permeability of material μ at the location of this unit cell. Similarly, $\vec{E}$ components increase directly in response to curl of $\vec{H}$ components with a constant proportional to electrical permittivity ε of the material at the present location. Interlacing of $\vec{E}$ and $\vec{H}$ components is represented in Figure 3.5. Components of $\vec{E}$ are updated at $N\Delta t$ and all the $\vec{H}$ components are updated at $(N/2)\Delta t$. In other words, $\vec{E}$ components in the *N*th time step are updated and stored in memory using previously stored $\vec{H}$ data. The corresponding $\vec{H}$ components in the (*N* /2)th time step are updated and stored in memory using the calculated $\vec{E}$ data.

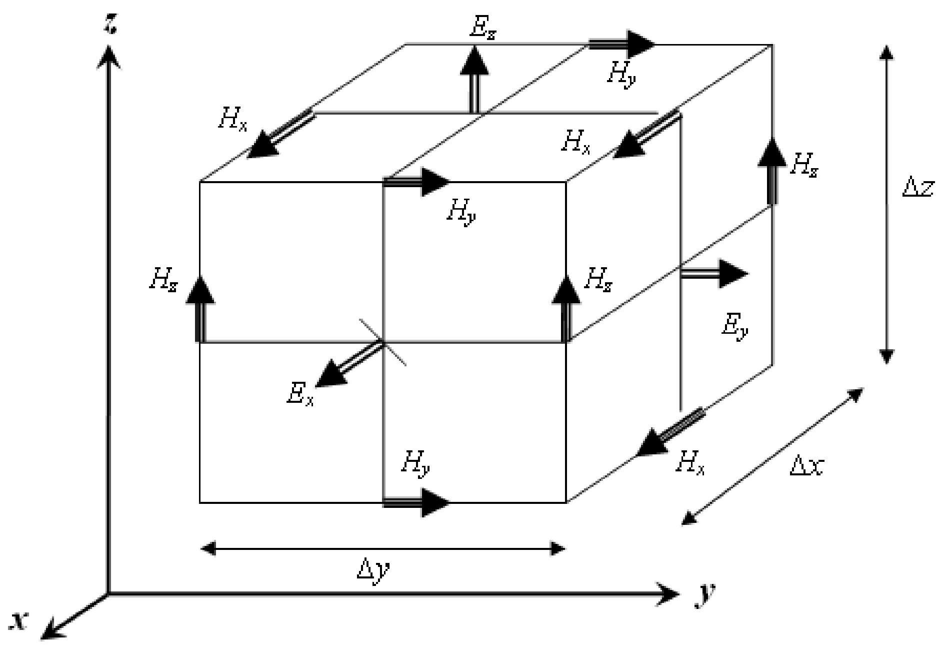

Figure 3.4: Geometrical representation of Yee cell

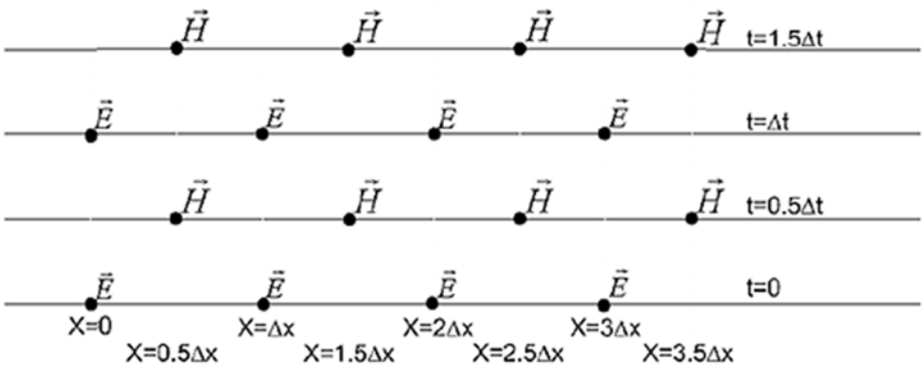

Figure 3.5: Interlacing of $\vec{E}$ and $\vec{H}$ components

This calculation is iterated through time steps so that field values can be updated at any time interval. Electric component E_z at co-ordinate ($i\Delta x, y\Delta y, (k+1/2)\Delta z$) and at *nth* time step is represented as $E_z^N\ (i, j, K+1/2)$. Magnetic components are placed on a half time step i.e. $H_x^{N+1/2}\ (i, j+1/2, K+1/2)$. A difference approximation based on Taylor series expansion of space and time derivatives is used to discretize differential form of Maxwell's equations as represented below.

$$\frac{\partial f\left(x_0\right)}{\partial x} = \frac{f\left(x_0 + \Delta x\right) - f\left(x_0 - \Delta x\right)}{2\Delta x} + O\left[\left(\Delta x\right)^2\right] \qquad (3.24)$$

The term $O[(\Delta x)^2]$ denotes remainder term, which approaches zero as the square of space increment. In conclusion, the discretized Maxwell’s equations are derived from Maxwell’s differential and the difference equations. For single electromagnetic components in Maxwell's equations, for example H_x, averaging of two consecutive time step value is applied in discretized equation as,

$$\frac{\mu\left(i,j+1/2,k+1/2\right)}{\Delta t}\left[H_x^{n+1/2}\left(i,j+1/2,k+1/2\right)-H_x^{n-1/2}\left(i,j+1/2,k+1/2\right)\right]$$
$$=\frac{1}{\Delta z}\left[E_y^{n}\left(i,j+1/2,k+1\right)-E_y^{n}\left(i,j+1/2,k\right)\right]$$
$$-\frac{1}{\Delta y}\left[E_z^{n}\left(i,j+1,k+1/2\right)-E_z^{n}\left(i,j,k+1/2\right)\right]$$
$$-\frac{\sigma_m\left(i,j+1/2,k+1/2\right)1}{2}\times$$
$$\left[H_x^{n+1/2}\left(i,j+1/2,k+1/2\right)+H_x^{n-1/2}\left(i,j+1/2,k+1/2\right)\right]$$
$$-M_x^{n}\left(i,j+1/2,k+1/2\right)\frac{1}{\Delta z}\left[E_y^{n}\left(i,j+1/2,k+1\right)-E_y^{n}\left(i,j+1/2,k\right)\right] \quad (3.25)$$

Equations for the magnetic fields H_y, H_z and electric fields E_x, E_y and E_z can be written on similar pattern. Algorithm represented by the above equation is accurate and easy to implement. Major mathematical operations are addition, subtraction and multiplication which are easier and cost effective to implement on hardware. Structures of the six equations for electric and magnetic fields are equivalent, making it possible to apply various methods such as custom hardware implementation and parallel computing to speed up the calculations.

Finite difference time domain computational space is bounded to achieve a converging solution. When, the scattered or the radiated fields arrive at the boundary they are reflected back into the computational space unless appropriate preventive measure is taken. In a conventional FDTD formulation field components at the boundaries cannot be updated because some of the nearest-neighbor field components needed to evaluate the finite difference curl enclosing it lie outside the problem space. Usual method is to estimate the missing field components just outside the problem space. An absorbing boundary is created by assuming that a locally plane wave is propagating out of the space and the field on the boundary is estimated by looking at the fields just within it. An early attempt at implementing such an absorbing material boundary condition was reported by Holland [Holland, 1983]. It utilizes a conventional lossy and dispersion-less absorbing material. Such an absorbing layer is matched only to normally incident plane waves. Oblique incident waves are partially reflected back into computation region and tend to corrupt the solution. This raised the need for a different scheme to accomplish a more efficient absorbing boundary layer. In this context the Perfectly Matched Layer (PML) introduced by Berenger is the most widely used absorbing boundary layer in FDTD applications [Berenger, 1994]. Flow chart for implementation of FDTD algorithm for each time step is shown in Figure 3.6. Model space is first of all divided into appropriately sized unit cells, each having electrical permittivity ε and magnetic permeability μ. Electromagnetic field components are initialized and parameters affiliated to each cell are set up. Excitation or power source in model space is defined in the next step. These steps are iterated updating the computations for each time step. Since $\vec{E}$ and the $\vec{H}$ components of the fields are interlaced in time domain, $\vec{E}$ components are updated first followed by the $\vec{H}$ components. Boundary condition part of the algorithm deals with unit cells located on boundary of the model space.

3. 3 Transmission line matrix method

Transmission-line matrix method is a time domain numerical technique for solving electromagnetic field parameters by modeling the problem space as intersecting transmission lines. It is based on Huygens' model of propagation that simulates the time evolution of electromagnetic fields. Voltage impulses are scattered by transmission line nodes (junctions) and travels to the adjacent nodes. This discretizes the problem in time and space. TLM provides equivalence between Maxwell's equations for electric and magnetic fields and transmission line equations for voltages and currents [Johns, 1980].

Each constitutive block of the system under analysis is replaced by physical network of transmission lines connected to form constitutive nodes in space [Christopoulos, 1995].

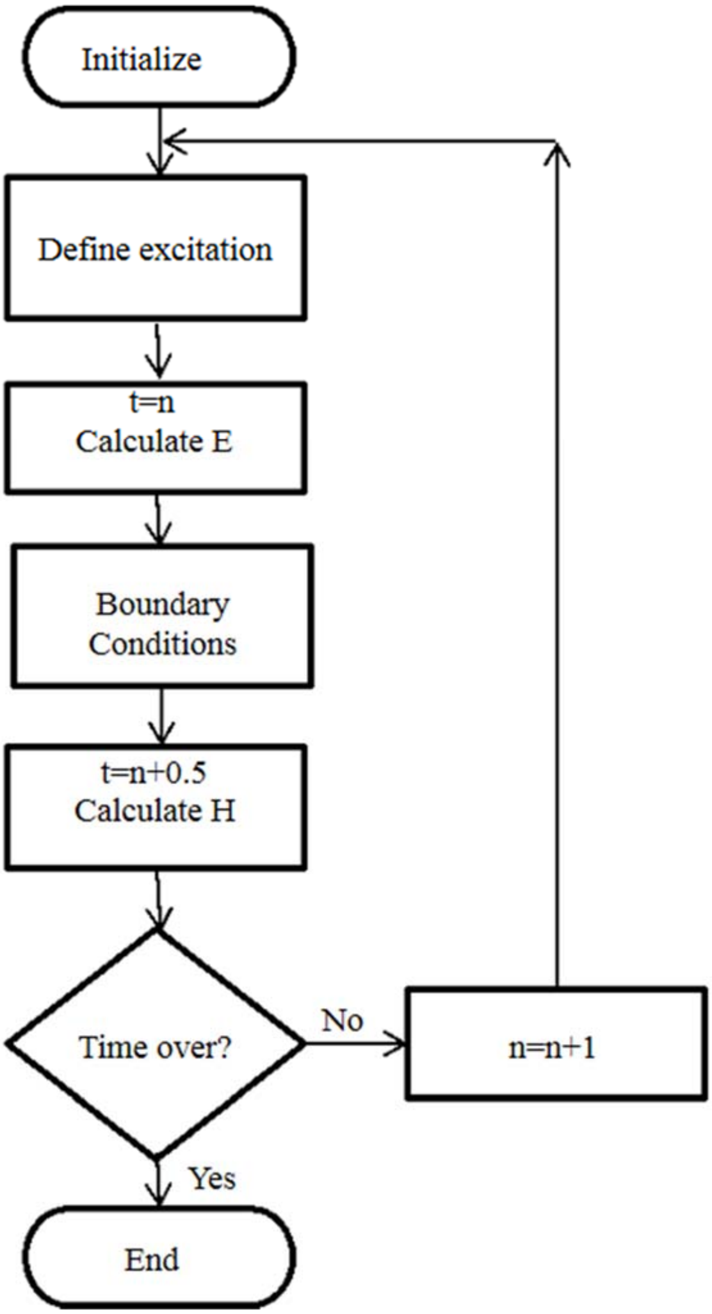

Figure 3.6: Finite difference time domain method flow chart

A section of the transmission line mesh in two dimensional Cartesian space with a voltage impulse V incident on the central node A is shown in Figure 3.7a. Figure 3.7b shows scattering to adjacent nodes on lines 1 to 4. The time step for temporal discretization is $\Delta t = \Delta l/V$, where V is velocity of propagating wave. For node A in the Figure 3.7, reflected voltages at a time step $(k+1)\Delta t$ due to incident impulses at a previous time step $k\Delta t$ is given by following expression,

$$\begin{bmatrix} V_1 \\ V_2 \\ V_3 \\ V_4 \end{bmatrix}_{k+1}^{r} = \frac{1}{2}\begin{bmatrix} -1 & 1 & 1 & 1 \\ 1 & -1 & 1 & 1 \\ 1 & 1 & -1 & 1 \\ 1 & 1 & 1 & -1 \end{bmatrix} \cdot \begin{bmatrix} V_1 \\ V_2 \\ V_3 \\ V_4 \end{bmatrix}_{k}^{i} \tag{3.26}$$

Discretization in space follows from the observation that an impulse emerging from a node becomes incident impulses on neighboring nodes.

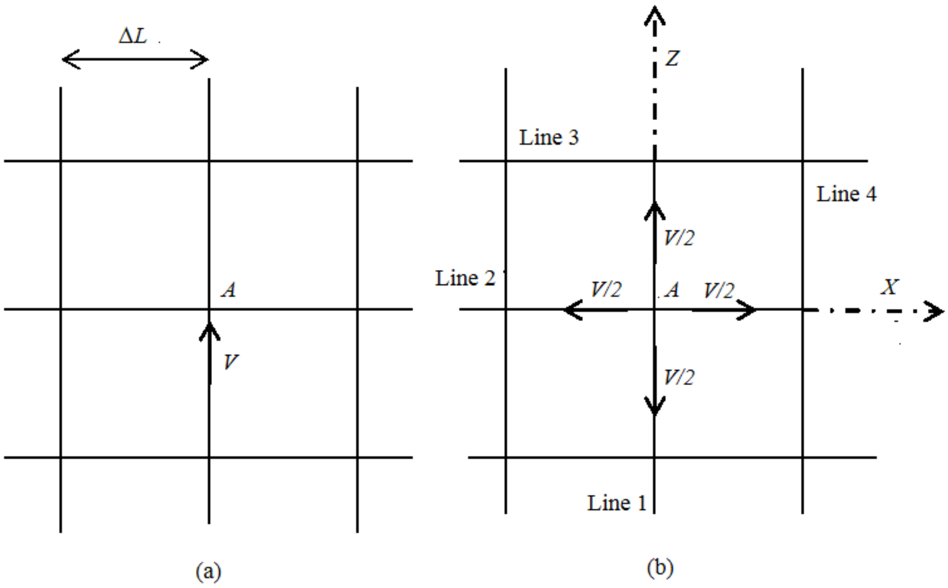

Figure 3.7: Two dimensional TLM Cartesian mesh

Spatial steps of TLM algorithm are governed by following set of equations

$$ {}_{k+1}V_1^{i}(z,x) = {}_{k+1}V_3^{r}(z,x-1) \tag{3.27}$$

$$ {}_{k+1}V_2^{i}(z,x) = {}_{k+1}V_4^{r}(z-1,x) \tag{3.28}$$

$$ {}_{k+1}V_3^{i}(z,x) = {}_{k+1}V_1^{r}(z,x+1) \tag{3.29}$$

$$ {}_{k+1}V_4^{i}(z,x) = {}_{k+1}V_2^{r}(z-1,x) \tag{3.30}$$

Equations (3.27) to (3.30) are used to calculate impulse response from initial conditions by incrementing time and space variables. Building blocks of TLM method is the equivalent circuit of a transmission line [Christopoulos, 1995] as shown in Figure 3.8.

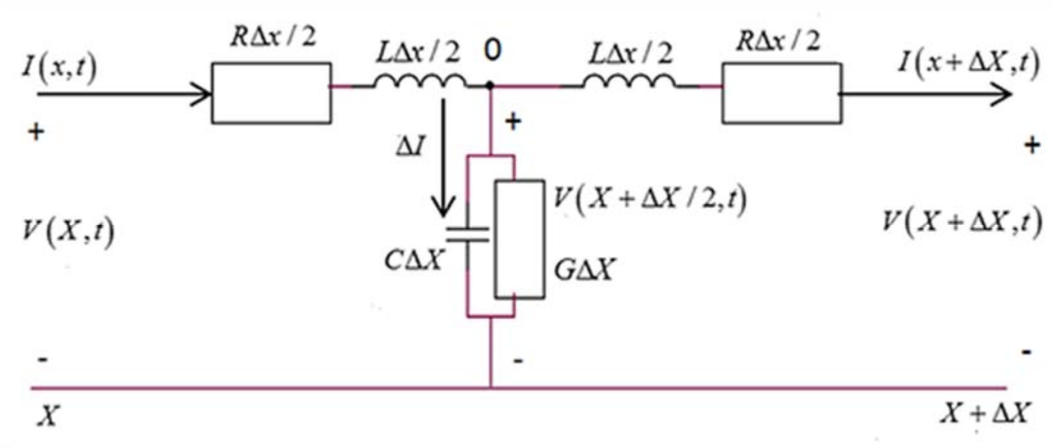

Figure 3.8: Equivalent circuit of a transmission line

The terms *R* and *G* are series resistance and shunt conductance, *L* and *C* are series inductance and shunt capacitance per section of length *Δx*. Voltage and current along the transmission line in terms of *RLGC* parameters are expressed by following equations.

$$\frac{\partial^2 V}{\partial X^2} = LC\frac{\partial^2 V}{\partial t^2} + \left(RC + GL\right)L\frac{\partial V}{\partial t} + RGV \tag{3.31}$$

$$\frac{\partial^2 I}{\partial X^2} = LC\frac{\partial^2 I}{\partial t^2} + \left(RC + GL\right)\frac{\partial I}{\partial t} + RGI \tag{3.32}$$

These expressions can be generalized into the following Telegrapher's equation and implies an analogy between transmission line and wave propagation,

$$\nabla^2\phi = LC\frac{\partial^2\phi}{\partial t^2} + RC\frac{\partial\phi}{\partial t} \tag{3.33}$$

Figure 3.9 shows discretization in time domain for an arbitrary node *n* of a transmission line at time-step *k*. Incident and reflected voltages at each node are shown.

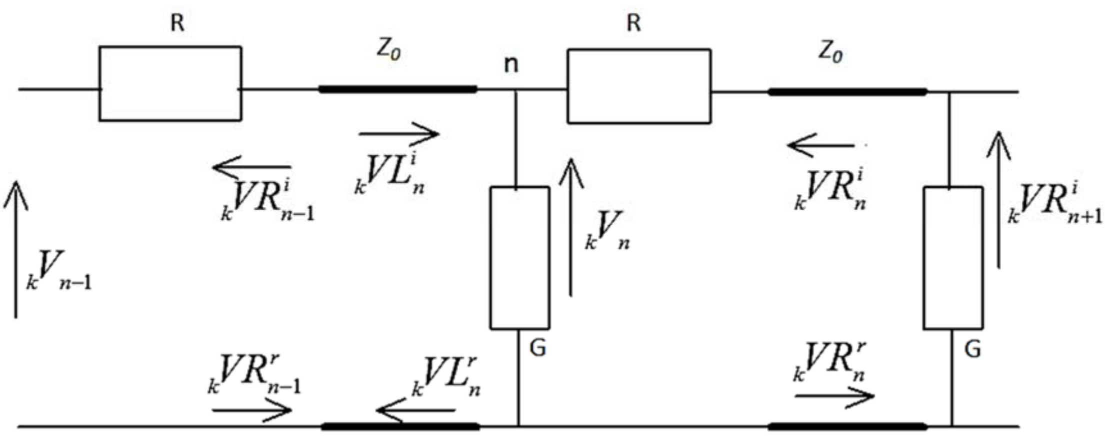

Figure 3.9: Nodal analysis of a transmission line section

At node n, total voltage $_kV_n$ at time-step k is result of incident voltages from left ($_kVL^i_n$) and from right ($_kVR^i_n$). Lines to left and to right of node n may be replaced for duration of time-step k by equivalents circuit as shown in Figure 3.10.

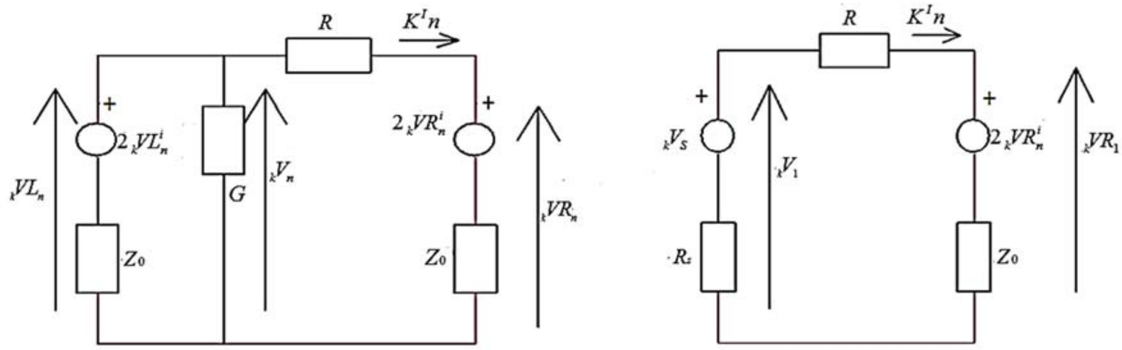

Figure 3.10: Equivalent circuit of TLM section

Voltages $_kV_n$ and currents $_kI_n$ can be obtained from Thevenin's equivalents by basic circuit principles. Reflected voltages from left and from right of node n are calculated as,

$$_kVL^r{}_n = {_kVL_n} - {_kVL^i{}_n} \tag{3.34}$$

$$_kVR^r{}_n = {_kVR_n} - {_kVR^i{}_n} \tag{3.35}$$

Voltage incident from left on node *n* at time step *k*+1 is what was reflected from right of node *n*-1 at the previous time step *k*. New incident voltages are given by,

$$_{k+1}VL^{i}_{n} = {}_{k}VR^{r}_{n-1} \tag{3.36}$$

$$_{k+1}VR^{i}_{n} = {}_{k}VL^{r}_{n+1} \tag{3.37}$$

Computational domain in a 3-D TLM procedure is divided into cells and terminated by an absorbing boundary condition (ABC). Each cell is represented by twelve voltages referring to adjacent faces. The nodal voltage and current terms which are equivalent to electromagnetic field parameters as given below,

$$\begin{aligned}
&Electric\ \ Field:\ E_y \equiv V_y \\
&Magnetic\ \ Fields:\ -H_z \equiv \left(I_{x3} - I_{x1}\right) \\
&\qquad\qquad\qquad\quad -H_x \equiv \left(I_{z3} - I_{z4}\right) \\
&Material\ \ \mathrm{Pr}operties:\ \mu \equiv L\ \ and\ \ \varepsilon \equiv 2C \\
&Transmissionline\ \ characteristic\ \ impedance, Z_0 = \sqrt{\frac{L}{C}}
\end{aligned}$$

Flowchart for a 1D TLM algorithm is shown in Figure 3.11. It is based on mathematical formulation represented by equations (3.34) to (3.37).

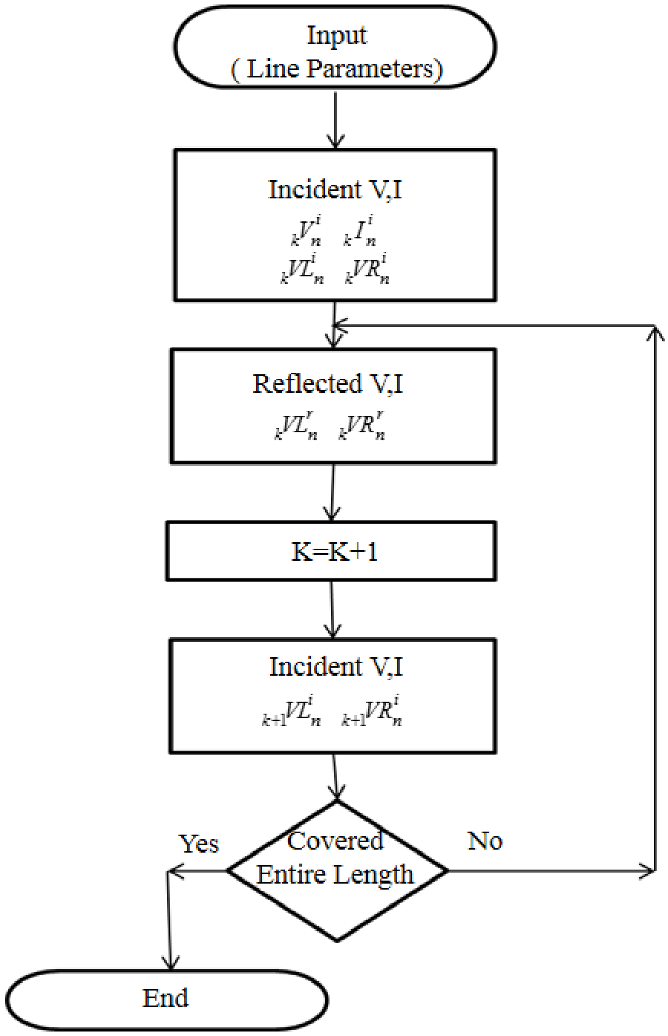

Figure 3.11: Transmission line matrix method flow chart

3.4 Summary and conclusion

This chapter provides theoretical background for signal processing tool and electromagnetic numerical techniques for noise source identification, field calculations and crosstalk analysis in this dissertation. Continuous and discrete wavelet transform, finite difference time domain method and transmission line matrix method are discussed in detail. Wavelet transform is a relatively newer technique for time-frequency analysis of transient and non-stationary signals. It is a mathematical transformation that represents a signal in terms of shifted and dilated forms of a single function called mother wavelet. It is possible with wavelet transformation to resolve a signal on time and frequency scales. It has proven to be effective for feature extraction and classification of the electromagnetic interference sources in an intra-system setup. This chapter discusses mathematical formulation of continuous and discrete wavelet transforms. Several types of wavelets such as Haar, Gaussian, Morlet and Debauchies are explained and their properties are discussed.

Finite difference time domain and transmission line matrix method are widely used numerical techniques for calculation of EM fields inside a finite volume. The computational space is enclosed by Absorbing Boundary Conditions (ABC) in TLM and Perfectly Matched Layer (PML) in FDTD. Main differences between these two time domain numerical techniques are that Finite difference time domain technique handles the electromagnetic fields and discretizes the Maxwell equations whereas, TLM deals with incident currents and voltages on equivalent nodes and uses analogy between transmission line networks and electromagnetic parameters. Furthermore, in FDTD method there is a separation of half a space step and half time step between electric and magnetic fields. In TLM method, electric and magnetic fields are solved at the same time instant at the center of the TLM cell. Wavelet transform is applied in this work for post measurement analysis and characterization of noise sources in a high intensity table top terawatt laser setup from flash lamp discharge current and synchronized switching of high voltage semiconductor devices. Computational electromagnetic techniques of FDTD and TLM are applied to simulate electromagnetic shielding effectiveness and crosstalk induced voltage respectively in chapter seven of this thesis.

Chapter 4

System description

Electromagnetic interference and integrity of control signals are analyzed in this work for two different types of flash lamp pumped solid state lasers. From electromagnetic compatibility point of view, both these lasers fall under the category of intra-system setup, where sources of noise lie within the system itself. First of these lasers is a two-beam high power Nd: glass laser and the second is a femtosecond table top terawatt laser. The two-beam high power laser chain is housed in a hall of dimensions 46 m by 10 m. Electrical power supplies are located in ground floor which is connected through long cables of several meter length to the laser system. Control system is located in a separate cabin with isolated ground. On the other hand, table top terawatt laser unit is a relatively compact unit in which the laser stages, power supplies, control system and several other electro-optical units are housed in a single hall and linked with interconnects consisting of cables, wires and termination blocks. Main blocks in these systems are flash lamp based laser amplifiers, pulse selector, pulse injector and Faraday rotator. Each of these stages has different functional requirements and is powered by pulsed voltage of timing parameters varying from several nanoseconds to hundreds of microseconds. There are relative delays between activation of these stages. Propagation of pulsed current for operation of any one of these stages, radiate electromagnetic noise and interact with control signals of components which are triggered at later stages. Noise interaction and coupling may disturb set delays, timing parameters and synchronization, which in turn affect the laser quality. Flash lamps, Faraday isolator coil, Pockels cell drivers are some of the high voltage and high current devices whose operation generates considerable amount of transient and pulsed electromagnetic noise. Following sections in this chapter describe the electrical and elctro-optical components in detail.

4.1 Nd: glass high power laser chain

One of the systems for which EMI studies were carried out is a two beam Nd: glass high power laser chain developed at Laser Plasma Division, Raja Ramanna Centre for Advanced Technology, Indore. Rated energy of the each beam is 400 J with pulse width specified as 1.5 ns. Thus, the laser is capable of delivering around 266 GW of pulsed optical power per beam. There is an additional option to deliver 25 J of energy in short pulses of 500 fs using optical parametric chirped pulse amplification (OPCPA) technique in one of the laser arms. Limitations of material damage threshold and the need to achieve a better beam quality dictate that high power lasers be designed as Master Oscillator and Power Amplifier system, which consists of a low energy master oscillator and several power amplifier stages. Figure 4.1 shows the laser block diagram.

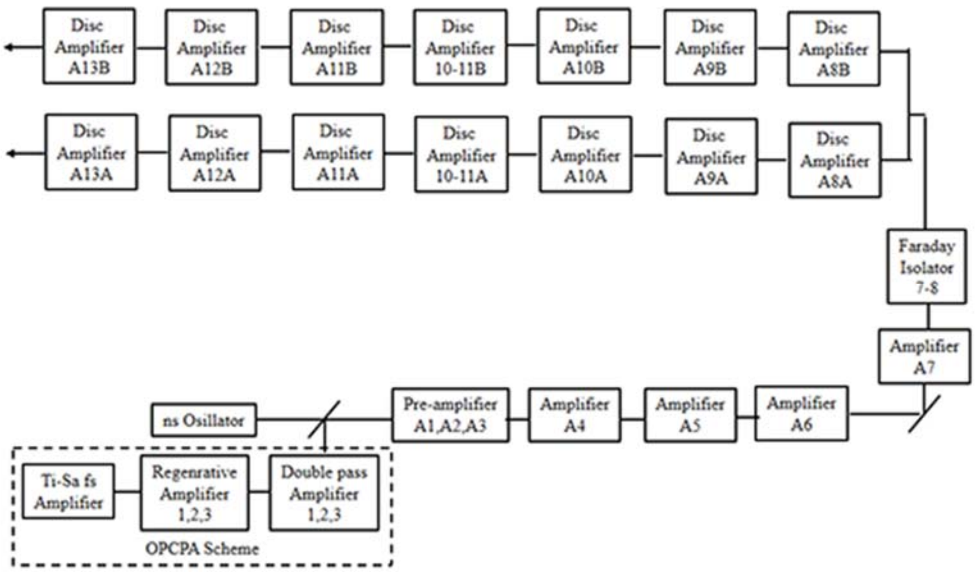

Figure 4.1: High power laser chain

Oscillator of the laser chain is based on Nd: YLF active medium. It provides energy of 40 mJ in 15 ns. This is sliced by an electro-optical Pockels cell based pulse slicer to a pulse width of 1.5 ns duration. Nd: glass laser amplifiers are optically pumped by xenon filled flash lamps of varying arc lengths (150 to 900 mm). Amplifier power supply consists of a charging circuit which energizes multiple capacitor banks and a trigger circuit which generates high voltage pre-ionization pulse for flash lamps. Voltage levels to which capacitor banks are charged depend on pumping energy and gain specifications of a laser amplifier stage. There are a number of possible circuit schemes for charging of capacitor banks and discharging them through flash lamps in controlled manner [Bhadani, 1989], [Souda, 1999]. Charging circuit implemented in the laser system under present study is based on a 50 Hz series resonant constant current scheme [Jennings, 1961]. Charging current depends on ratio of line voltage and impedance of resonating element in the mains transformer primary circuit. Constant current charging of large capacitor banks has advantage of improved efficiency and reduced charging time. This can be compared with conventional *RC* charging circuits where efficiency is never better than fifty percent and it takes approximately five time constants to fully charge a capacitor bank. Energy stored on capacitor bank is discharged through a flash lamp pair by generating a 25 kV, 5 μs trigger voltage with the help of a SCR and pulse transformer circuit. The laser chain also includes two Faraday isolators for protecting low power optics from back reflected light. This stage optically isolates low power section from higher stage amplifiers. Faraday isolators work on the principle of rotation of a plane polarized light passing through magneto-optical material placed in a magnetic field. Electrical power supply requirements for Faraday isolator is to generate a pulsed magnetic field of the order of 15 kG and 4 ms duration by discharging the energy stored in 1000 μF capacitor bank through a coil of inductance 1.4 mH. Current flow through Faraday coil is initiated by triggering a SCR connected in series with energy storage capacitors and the coil. This results into half sinusoid current of peak value of the order of 1.5 kA. Amplifier stages from A4 onwards are charged by a bipolar power supply consisting of positive and negative capacitor banks. Considering the complete laser unit, there are a total number of 300 capacitor banks corresponding to 188 flash lamps of different lengths. Total electrical energy handled by the power supply is of the order of few MJ and maximum peak current flowing through a flash lamp pair is approximately 6 kA. Desirable current pulse width is 300 μs, which corresponds to fluorescence life time of laser glass. This laser operates under a central control system. Control system operation involves setting up of the capacitor voltage in accordance with required energy, setting up of delays for firing of flash lamps, SCRs and the Pockels cell drivers. Firing sequence is started by a master pulse. Faraday isolator coils are excited first to generate a safe level of pulsed magnetic field. This is followed by triggering the oscillator and amplifier flash lamps. Laser energies are measured at certain key points along the chain. Table 4.1 lists power supplies for different stages in the laser chain. Photographs of laser chain and power supply hall are shown in Figures 4.2 and 4.3 respectively.

4.2 Table top terawatt (TTT) laser setup

Another high power laser setup for which electromagnetic interference analysis is carried out as part of this work is a table top terawatt laser system [Naik, 2003]. It generates intense ultra-short laser pulse for laser-plasma interaction studies at ultra-high intensities (10^{18} W/cm^2). The setup consists of a mode locked master oscillator operating at 100 MHz repetition rate, a pulse selector circuit which selects a single laser pulse from the 100 MHz train in synchronization with an external trigger, a flash lamp pumped regenerative laser amplifier, a pulse injector, a pulse ejector electro-optic switch and a delay generator circuit.

Figure 4.2: Two beam high power laser chain

Figure 4.3: Laser power supply hall

Table 4.1 List of laser power supplies

Laser Stage	Type of PFN	No. of flash lamps	Arc length (mm)	Bore Dia (mm)	Total capacitance (µF)	Operating voltage (V)	Operating Energy (J)
Oscillator [Coherent make]							
Regenerative amplifier	Unipolar	2	76	7	100	1000	50
Double pass amplifier-1	Unipolar	4	180	12	400	3000	1800
Double pass amplifier-2	Bipolar	6	280	19	450	6500	9500
Double pass amplifier-3	Unipolar	4	150	10	400	2500	1250
Oscillator [Ekspla make]							
Amplifier-1	Unipolar	4	150	10	400	3500	2450
Amplifier-2	Unipolar	4	150	10	400	3500	2450
Amplifier-3	Unipolar	4	150	10	400	3500	2450
Amplifier-4	Bipolar	6	280	16	450	6500	9500
Faraday Isolator 4-5	Unipolar	-	-	-	1000	3000	4500
Amplifier-5	Bipolar	12	280	16	900	6500	19000
Amplifier-6	Bipolar	12	280	16	900	6500	19000
Faraday Isolator 6-7	Unipolar	-	-	-	1000	2500	3125
Amplifier-7	Bipolar	12	280	16	900	6500	19000
Amplifier-8A	Bipolar	16	280	16	1200	7000	29400

Faraday Isolator 8-9A	Unipolar	-	-	-	1300	3000	5850
Amplifier-9A	Bipolar	16	280	16	1200	7000	29400
Amplifier-10A	Bipolar	20	280	16	1500	7000	36750
Amplifier-D1A	Bipolar	10	600	20	1500	8000	48000
Amplifier-D2A	Bipolar	12	750	20	1800	8000	57600
Amplifier-D3A	Bipolar	12	900	20	1800	8000	57600
Amplifier-8B	Bipolar	16	280	16	1200	7000	29400
Faraday Isolator 8-9B	Unipolar	-	-	-	1300	3000	5850
Amplifier-9B	Bipolar	16	280	16	1200	7000	29400
Amplifier-10B	Bipolar	20	280	16	1500	7000	36750
Amplifier-D1B	Bipolar	10	600	20	1500	8000	48000
Amplifier-D2B	Bipolar	12	750	20	1800	8000	57600
Amplifier-D3B	Bipolar	12	900	20	1800	8000	57600

Pulse selector and delay generator circuits in TTT laser chain achieve following tasks:

1. Selection of a single pulse from 100 MHz pulse train generated by the laser oscillator.
2. Single pulse injection into regenerative amplifier after fixed delay.
3. To generate an adjustable delay that corresponds to a required number of round trips in the regenerative amplifier.

Basic setup consisting of these blocks is followed by a single pass and a double pass flash lamp pumped laser amplifiers for further gain enhancement. Pulse selector, pulse injector and pulse ejector stages consist of electro-optic switches, which are built around Pockels cells and in turn are biased by high voltage and high speed semiconductor switches [Becker, 1994]. Main stages of the TTT laser system i.e. the regenerative amplifier, pulse selector, pulse injector and pulse ejector are shown in Figure 4.4. Flash lamp power supplies and trigger circuits of these stages are main sources of electromagnetic interference. Charge and trigger commands for flash lamp power supplies are generated by a centralized control system [Singh, 2006]. Pulse selector stage consists of a double Pockels cell and two crossed polarizers. Input polarizer is parallel to polarization of oscillator pulse and output polarizer is perpendicular to it. A 5 ns pulse of 3.5 kV pulse generated by a MOSFET switch drives Pockels cell to rotate polarization and allow a single laser pulse to pass through output polarizer for injection into the amplifier stage. Rregenerative amplifier consists of Nd: phosphate glass rod as an amplifying medium, which is pumped by two flash lamps. Function of the injector stage is to inject a single laser pulse into regenerative amplifier. It consists of a polarizer and a Pockels cell. Pulse injection process begins with application of a high to low going step of quarter wave voltage (3.5 kV) through a MOSFET switch on the Pockels cell. It injects the laser seed pulse in regenerative stage for several round trips for energy amplification.

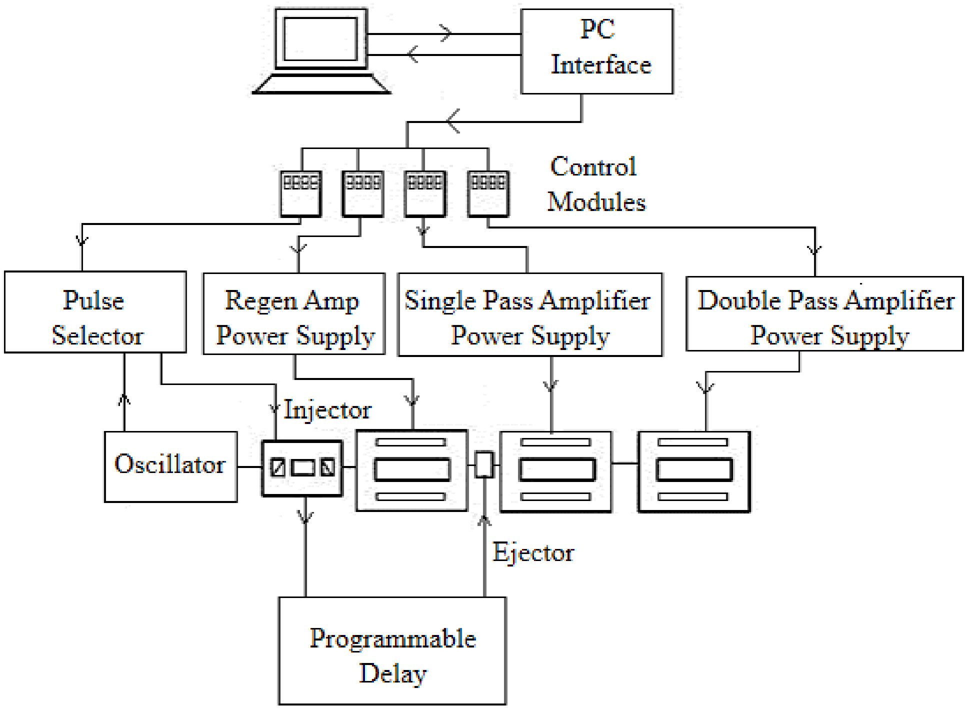

Figure 4.4: Block diagram of TTT laser chain

Ejector stage consists of a Pockels cell and a plate polarizer. A fast rising (5-10 ns) step pulse of 3.5 kV is applied to the Pockels cell, which rotates the plane of polarization resulting into ejection of amplified pulse. Signal integrity and EMI issues in TTT laser system deals with synchronization of the pulse selector stage with a 100 MHz free running signal, generation of precise and jitter free delays in the range of 5 to 800 ns and electromagnetic shielding of the electro-optic Pockels cell. Delay time is set in accordance to round trip time of seed pulse and corresponding amplification factor in the regenerative amplifier stage.

4. 3 Flash lamp: Physical and electrical characteristics

Optical amplifiers in laser systems under investigation i.e. high power two-beam chain and table top terawatt setup are based on pulsed xenon flash lamps. Flash lamp power supply and trigger circuits are high voltage, high current systems and potential sources of electromagnetic interference. Flash lamps for laser application are electric arc lamps designed to produce incoherent white light for short durations. These lamps consist of sealed glass tubing with electrodes at either end and filled with noble gas xenon or krypton at low pressure. A fast rising high voltage trigger applied between electrodes ionizes the filled gas and conducts pulsed current to produce intense and broad band light. Major portion of flash lamp optical emission is due to electron-ion recombination and transitions between excited states of the filled gas atoms and ions [Marshak, 1984]. In high power lasers under present investigations, flash lamps are used as optical pump sources to excite energy levels of Nd: glass laser medium. Trigger voltage initiates discharging of electrical energy stored in capacitor bank through a pulse forming network (PFN) comprising of energy storage capacitors, a series inductance and non-linear flash lamp impedance. Number of excited ions available for stimulated emission in a lasing medium depends on the pump energy, current density and the current rise time, which in turn depend on the PFN components [Dishington, 1974]. Optical emission from a flash lamp is broadband in nature and encompasses the regime from blue to infrared. However, only certain specific bands in the emission spectrum are absorbed by the laser medium and contribute towards the lasing process. Major portion of flash lamp emissions in smaller wavelength regime ends up as thermal heating after being absorbed by the active medium [Gusinow, 1975]. Pump energy and discharge current rise time affect the optical spectrum. Flash lamp current peak and timing parameters depend on circuit values namely capacitance C, inductance L, flash lamp constant K_0 and charging voltage V_c. Power supply consists of a charging circuit, a capacitor bank and a trigger circuit. Application of a high voltage flash lamp trigger pulse initiates discharge of capacitor bank into flash lamps resulting into a pulsed current through interconnects. Full width at one third of the current maximum is maintained in the range of (300-500 μs) and the current peak varies from 1 to 6 kA. Important steps in powering a flash lamp pumped solid state laser are shown in Figure 4.5 [Gagnon, 2008].

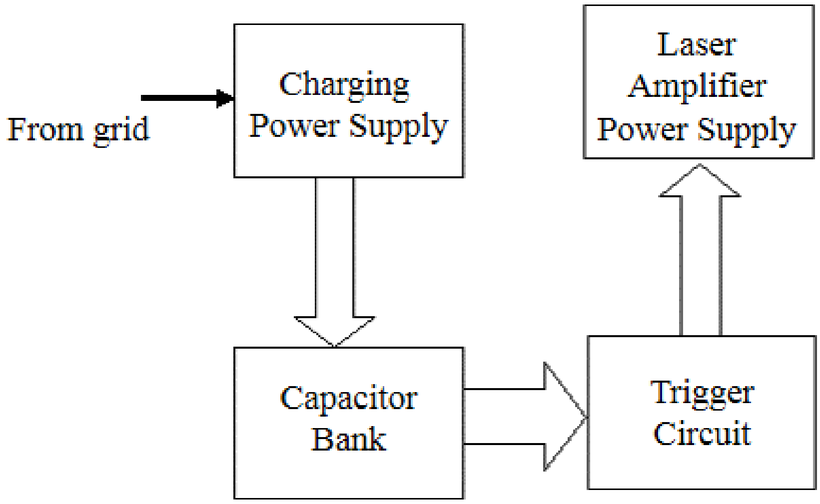

Figure 4.5: Laser amplifier power supply scheme

Energy is extracted from power grid over a period of 60 to 120 seconds and converted to capacitor voltage (5 to 10 kV) by charging circuit. Once, capacitors are charged to the desired energy level, a semiconductor switch in trigger circuit is turned ON and capacitor bank discharges into the flash lamps in around 600 μs. Transfer of energy from capacitor bank to flash lamp is accomplished using critically damped *RLC* circuit [Koechner, 2006]. Single flash lamp configuration under the present study is energized by 300 μF of capacitors. There are a number of possible circuit schemes for charging of energy storage capacitor banks and discharging them through flash lamps in controlled manner. Typical value of the inductor L is 70 μH. Arc lengths of the flash lamps used in the lasers vary from 150 mm to 900 mm and the lamp current density is maintained between 2.5 to 3 kA per cm^2. Equivalent circuit diagram of a flash lamp pulse forming network, flash lamp current and corresponding optical signal measured with a photo diode are shown in Figure 4.6. Measurements consisted of recording the flash lamp current with a Rogowski coil, optical output was recorded with a Si avalanche photo diode (Perkin Elmer make, Si-APD, 30902E). Oscilloscope traces of the photodiode and current sensor voltage output is shown on right side of the diagram.

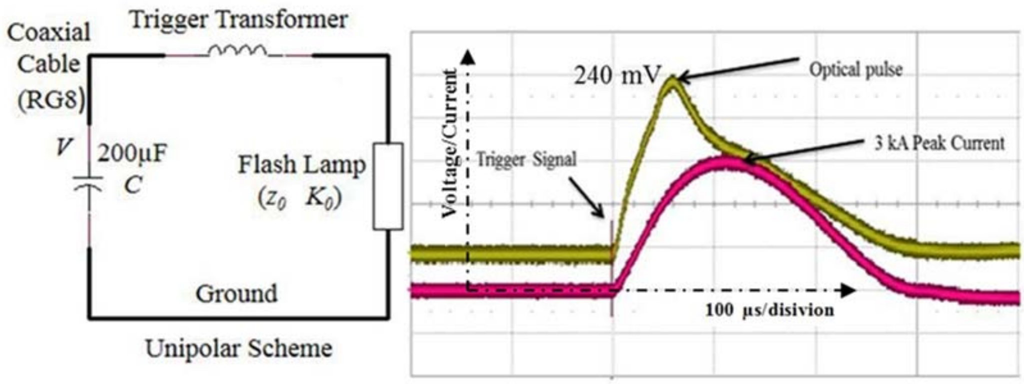

Figure 4.6: Flash lamp pulse forming network, optical output and current profile

Resistivity 'ρ' of arc discharge plasma in a flash lamp is given by [Marshak, 1984].

$$\rho = (N / n)\rho_0 + \rho_i \tag{4.1}$$

where, N is neutral atom density and n is electron density. Terms ρ_0 and ρ_i represent resistivity due to electron-atom and electron-ion collisions respectively. ρ_0 and ρ_i in turn depend on Maxwellian electron temperature as $T^{5/2}$ and $T^{-3/2}$ respectively. Relationship between electrical energy pumped to flash lamp plasma and optical radiation represented by plasma temperature is given by [Mead, 2009], [Robinson, 1998] as,

$$vJ^2\rho = \left[nK\tau / \left(1 + nK\tau\right)\right]\varepsilon\sigma A T^4 \tag{4.2}$$

Terms v and A represent inside volume and surface area of lamp, J is current density, ε and T are plasma emissivity and temperature respectively. K is average collisional electron de-excitation constant, τ is average self-absorbed radiation life time and σ is

Stefan–Boltzmann constant (5.67×10^{-8} W m^{-2} K^{-4}). Voltage-current (*V-I*) relation of flash lamps displays non-linear characteristics. Temporal characteristics of flash lamp voltage and current are shown in Figure 4.7. Experimental set-up for this measurement consists of a 300 μF capacitor bank charged to 4 kV and then discharged through a 280 mm arc length xenon flash lamp. Current flow starts with onset of trigger signal. Region I exhibits negative resistance characteristics where voltage decreases despite rise in current. Region II marks stabilized portion of the discharge process. Voltage current parameters in the stabilized region marked by II in the diagram are given by the following equation [Markiewicz, 1966].

$$V = K_o\sqrt{i} \tag{4.3}$$

K_0 is flash lamp constant dependent on lamp dimensions and fill pressure of the gas expressed as,

$$K_o = 1.28\left(\frac{l}{d}\right)\left(\frac{p}{g}\right)^{1/2} \tag{4.4}$$

where, l is arc length, d is inner diameter and p is fill pressure in torr. The term g is flash lamp constant and depends on the type of filled gas. Its value for xenon is 450. Thus, calculated value of K_0 for xenon flash lamp of arc length 280 mm, bore diameter 16 mm and fill pressure 400 Torr is 21 V/√Amp.

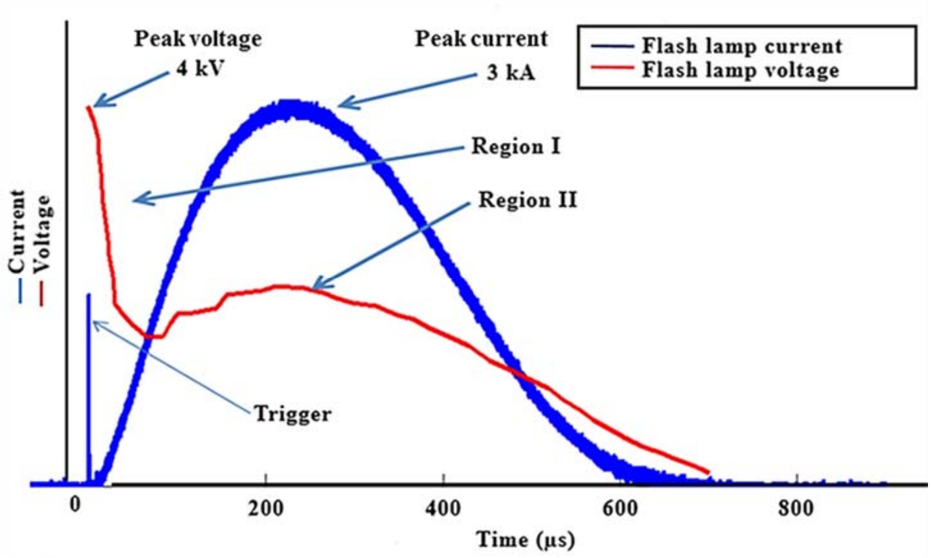

Figure 4.7: Flash lamp temporal V-I characteristics

Lamp resistance is dependent on arc length *l*, internal diameter *d* and discharge current *i(t)* as represented by the following equation,

$$R_{FL} = \frac{1.28l}{d}\left(\frac{p}{g}\right)^{1/2}\left[i(t)\right]^{-1/2} \tag{4.5}$$

From electromagnetic interference point of view a flash lamp discharge current with increased rise time is desirable because of lower frequency content as compared to circuit parameters which generate low rise time current pulse. As a part of this thesis, a study was carried out to observe emission spectrum from flash lamp with respect to different rise time of the lamp current. The flash lamp emission spectrum in the range 200 to 1100 nm was recorded with a fiber optic spectrometer. Spectrometer fiber cable tip was kept at an axial distance of 1 m from flash lamp. Typical flash lamp emission consists of a continuum spectrum band associated with bound-free transition in high temperature plasma and discrete lines due to bound-bound transitions [Brown, 1981]. Variations in flash lamp spectra under different circuit conditions, pump energy and discharge current parameters are investigated. In first set of experiments, flash lamp was excited by a capacitor bank of 300 μF. Series inductance comprised of trigger transformer secondary with a value of 70 μH. This results in current pulse width of around 500 μs. Capacitor voltage was set in the range 1 kV to 3.5 kV leading to electrical pump energy variation of 150 J to 1.8 kJ respectively. Peak currents and corresponding flash lamp spectra are shown in Figure 4.8. Pumping efficiency, represented by ratio of flash lamp emission contributing to lasing process to thermal heating in shorter wavelength region is smaller as compared to portions represented by longer wavelengths. Thus, an efficient pumping scheme should tend to minimize shorter wavelength spectrum (< 400 nm). It is observed that increase in peak current shifts the continuum spectrum towards shorter wavelength region. Increase in current peak density deteriorates the flash lamp envelope and electrodes. This reduces the flash lamp life time. Also at higher peak current continuum spectra dominates as compared to discrete spectra. In second set of experiments changes in emission spectra are observed for different values of flash lamp current pulse widths and rise times for fixed current density (peak current ~ 1.8 kA). This is done by manipulating the values of C and the series inductance L.

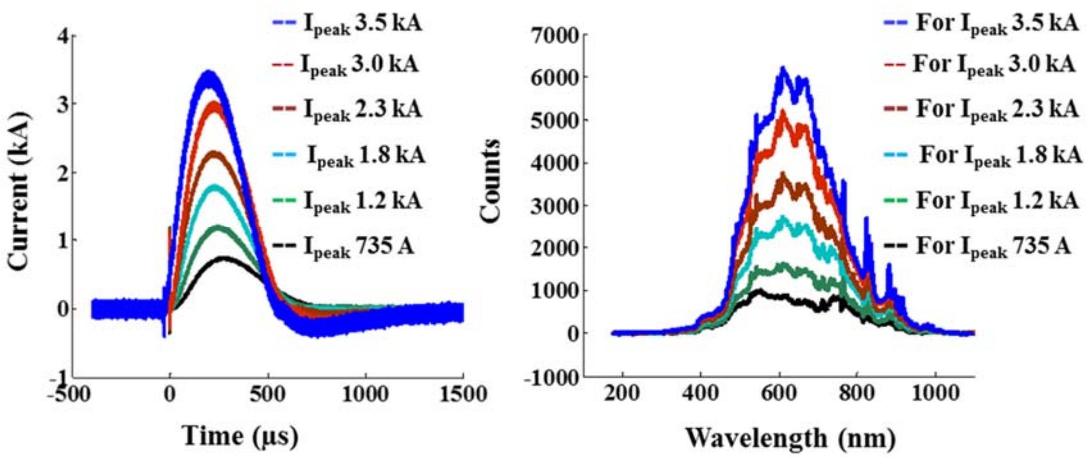

Figure 4.8: Flash lamp current profiles and emission spectra

Keeping the current density constant, a higher pulse width and higher rise time current shifts the spectrum towards ultra violet region. Optical emission in this regime are absorbed by flash lamp jacket resulting into increased heat dissipation. Also, the continuum spectra dominate as compared to the discrete lines with increase in the current pulse width (PW) as shown in Figure 4.9. Current pulse width is measured between 10% to 10% points of the peak value. Term T_r in the diagram refers to current rise time (10 to 90 % points of the peak value). This analysis points to an optimum flash lamp current pulse width of 200 µs duration.

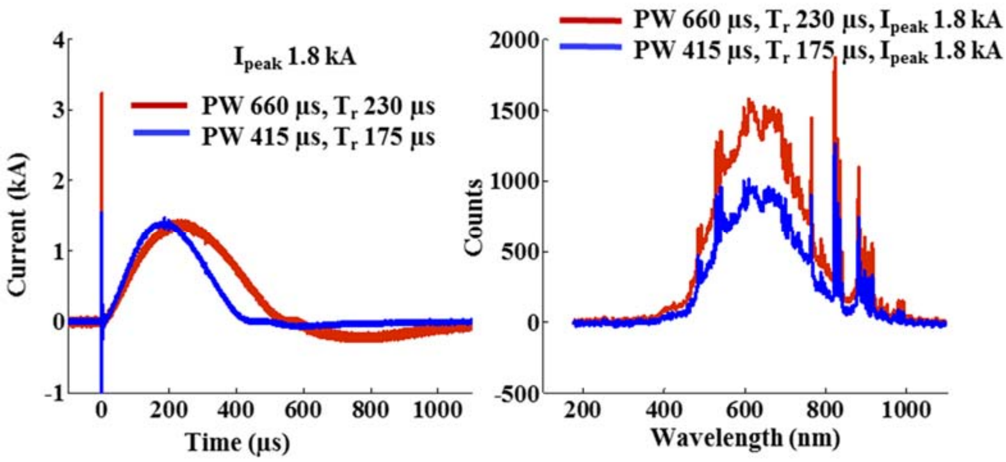

Figure 4.9: Current pulse width and flash lamp emission spectra

4.4 Flash lamp power supply

Block diagram of a flash lamp power supply is shown in Figure 4.10. It depicts a pulse forming network configured in bipolar mode which has two capacitor banks namely (+ve & -ve). This arrangement doubles the voltage applied across flash lamp load. Main parts of power supply are charging circuit, control circuit, isolation circuit and flash lamp pulse forming network. Constant current capacitor charging scheme is preferred to the conventional constant voltage (*RC*) charging because of increased charging efficiency (~ 90%). Charging process based on *RC* network has maximum efficiency of 50 %. As such it is not suitable for high power laser systems which have to handle total stored electrical energy of several Mega Joules. Charging circuits are discussed in detail in the following section. Control circuit initiates capacitor charging by triggering a solid state relay (*SSR*). Feedback circuit consists of a potential divider and an isolation amplifier to separate the high voltage ground from control ground. Galvanic isolation between common reference points in capacitor and control circuits is of the order of 100 dB and it substantially reduces the conducted electromagnetic interference. It is achieved through various means, such as by commercial optically coupled isolation amplifiers or by a voltage to frequency converter and an opto-isolator setup. On completion of charging of capacitor banks to required voltage the control system generates a trigger signal for flash lamps. It is to be noted that in the two beam high power laser chain, capacitor banks and flash lamps are placed in two different halls. Length of co-axial cables connecting capacitor bank and trigger transformer mounted near flash lamp assembly is of the order of 5 m. Figure 4.11 shows physical locations of capacitor banks and flash lamps. The interconnects, which represent impedance discontinuities consist of lugs on capacitor terminals, shielded co-axial cable (*RG8*) and lugs on flash lamp electrodes. Long co-axial cables carry linearly charging capacitor voltage to trigger transformers and flash lamps. Flash lamp assembly and trigger transformers are shown in Figure 4.12. Longer cable lengths, high voltage signals and impedance discontinuities at interconnect lead to electromagnetic emissions.

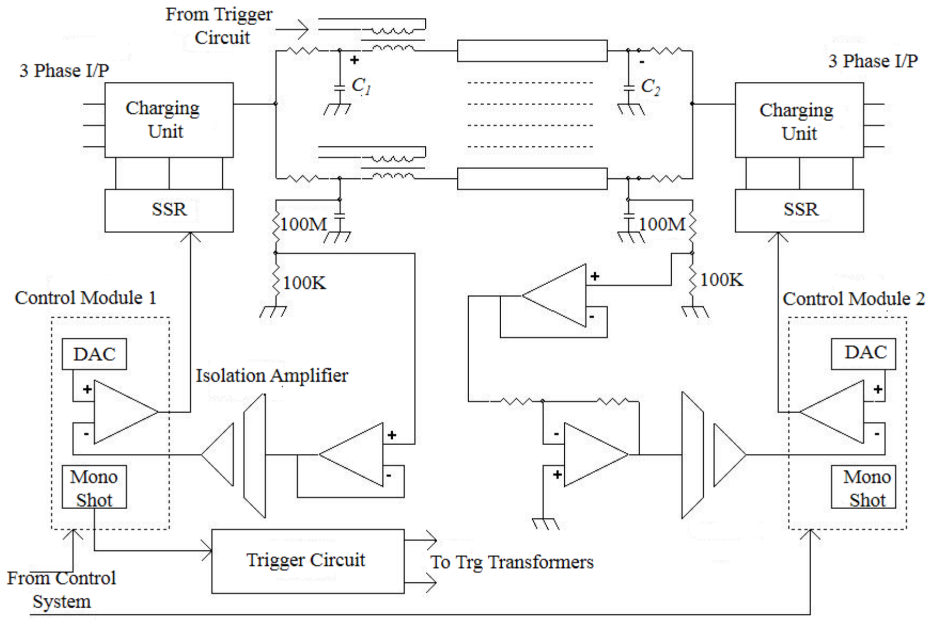

Figure 4.10: Flash lamp power supply

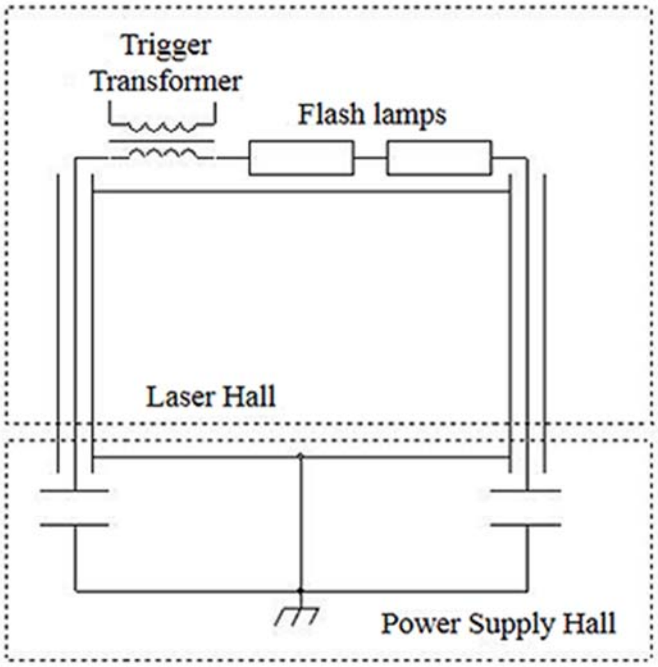

Figure 4.11: Location of capacitor banks and flash lamps

4. 4. 1 Charging circuit and pulse forming network

Constant current charging technique is implemented for the capacitor banks because of better efficiency (~ 90%) and reduced timings. The charging circuit is shown in Figure 4.13. Capacitor charging circuit consists of an LC network on primary side of the mains 50 Hz transformer. Inductance L is built in the transformer as leakage inductance whereas capacitance C is an additional series capacitor. Under the condition that L and C are tuned at supply frequency, the load current i.e. the capacitor charging current becomes constant [Jennings, 1961] and is represented by following equation. I_{rms} is the capacitor current, V_{rms} is input voltage and ω is angular frequency.

$$I_{rms} = \frac{V_{rms}}{j\omega L} = \frac{V_{rms}}{(1/j\omega C)} \tag{4.6}$$

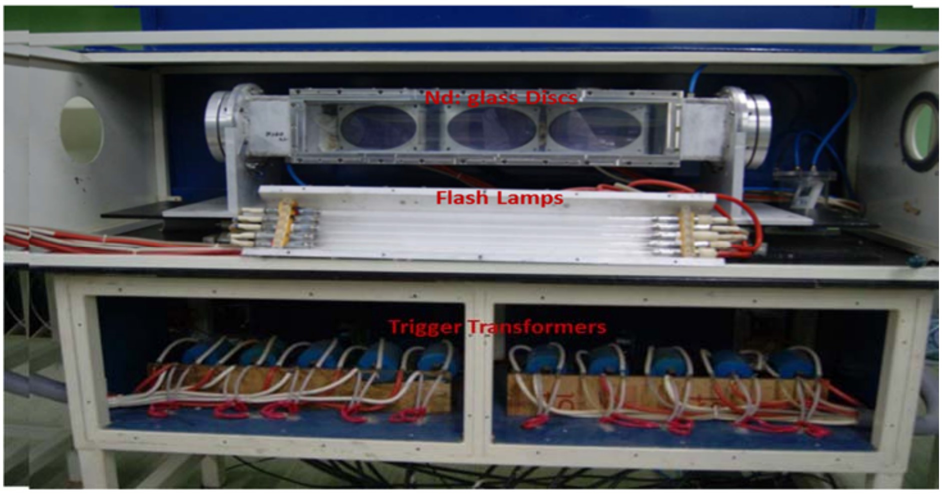

Figure 4.12: Trigger transformer and flash lamp assembly

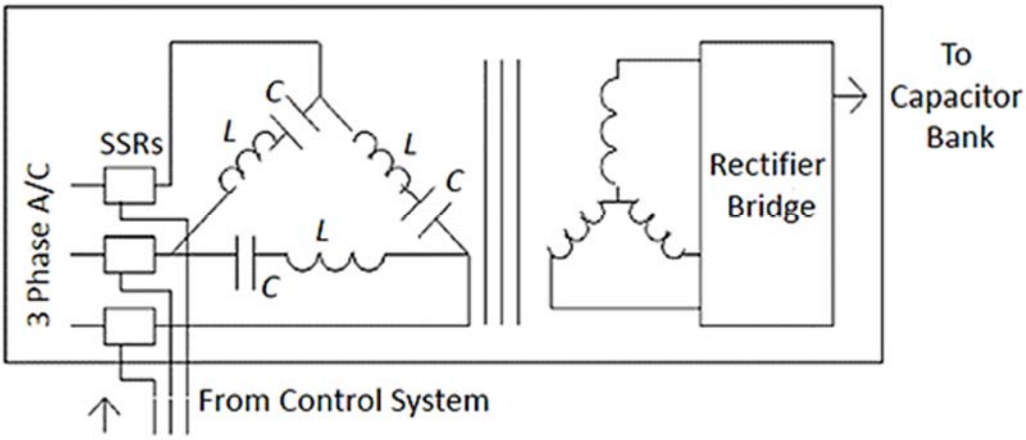

Figure 4.13: Capacitor bank charging circuit

After the capacitor bank is charged to set voltage the stored energy is discharged to flash lamp on application of a high voltage trigger impulse. Loop current of the pulse forming network is governed by the following equation,

$$L\frac{di}{dt}+\frac{1}{C}\int_0^t idt+R_{FL}i=V_c \tag{4.7}$$

Where, L is the series inductance, R_{FL} is the flash lamp impedance and V_c is capacitor voltage. Damping of flash lamp current depends on circuit impedance and capacitor voltage. Markiewicz [Markiewicz, 1966] has simplified the solution of flash lamp equation (4.7) by introducing the substitutions, $Z_0=\sqrt{L/C}$ and the damping parameter, $\alpha=K_0/\sqrt{V_c Z_0}$. For lower values of α, the flash lamp current remains underdamped. For damping parameter of 0.75, the circuit becomes critically damped. Whereas, for higher values of α, the circuit becomes over-damped. Other parameters remaining constant, at lower capacitor voltages the circuit becomes over-damped as compared to higher voltages. Similarly increasing the value of L results into underdamped conditions whereas, a low inductance circuit results into over-damped conditions. From efficiency point of view, it is desirable to operate a flash lamp under critically damped circuit conditions [Brown, 1981]. Variation in capacitor voltage changes the critically damped operating conditions of flash lamp pulse forming networks. There are two different PFN configurations namely unipolar and bipolar as shown in Figure 4.14. In unipolar scheme the capacitor bank is charged to positive voltage which is connected to one end of the flash lamp through trigger transformer secondary. On the other hand, in bipolar configuration there are two sets of capacitor banks charged to positive and negative voltages respectively. In this configuration none of the flash lamp terminals are grounded. In bipolar network, two capacitor banks form series combination which results into doubling the voltage and reducing the capacitance to half. This has advantage of quadrupling the pumped energy without increasing voltage ratings of capacitors, cables and interconnects. The pulse width can be reduced and voltage can be doubled by retaining the same value of capacitance. EMI from both these networks is analyzed as part of this dissertation.

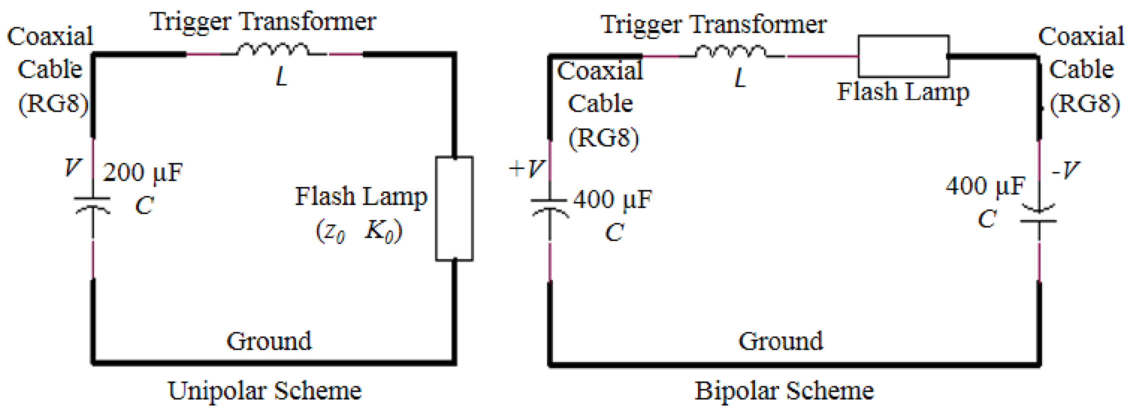

Figure 4.14: Unipolar and bipolar pulse forming networks

4.5 Faraday isolator

Faraday isolators are magneto-optical devices used in high power laser chains to provide optical isolation to prevent any plasma back reflected beam from entering high gain laser amplifiers. When high power short pulse lasers are focused to create plasma, a sizable fraction (10-30%) of laser energy is back reflected at intensity levels of around 10^{15} W/cm^2.This gets amplified during back propagation. At some stage the power density may exceed the damage threshold resulting into break down of optical components. Faraday isolators offer an attenuation of 1000:1 for back reflected beams while insignificant attenuation for the forward beam. These are incorporated at several locations in the laser chain, and are driven by high peak (1-2 kA) pulsed currents. Faraday isolators work on the principle of rotation of a plane polarized light passing through a transparent material placed in magnetic field. Angle of rotation is proportional to the applied magnetic field *H* and length *l* of the material and given by $\theta = v.L.H$, where ν is material constant known as Verdet constant. The Faraday active medium is mounted inside a solenoid magnet. A half sinusoid current passing through the Faraday coil generates magnetic field suitable for rotation of plane of polarization of the incident light by 45^o. Two polarizers are mounted on either side of the solenoid. These are oriented at 45^0 with respect to each other. There are four Faraday isolators in the 2-beam high power laser chain. These are named according to their locations as, FI4-5, FI6-7, FI8-9A and FI8-9B. Faraday isolator power supplies charge a unipolar capacitor bank, which is discharged into a solenoid coil to generate a pulsed magnetic field of the order of 15 kG. Figure 4.15 shows schematic of Faraday isolator power supply. It consists of a pair of Silicon Controlled Rectifiers (SCRs) connected in series which are switched to discharge capacitor bank through Faraday coil. Voltage across the SCRs is equalized by shunt resistors. Capacitance and coil inductance are chosen such that they together generate a current pulse of half sinusoidal shape to provide required pulsed magnetic field. Figure 4.16 shows time profile of Faraday isolator coil for stage FI 45 in the two beam laser chain. Pulsed current through Faraday coil is measured with a Rogowski coil.

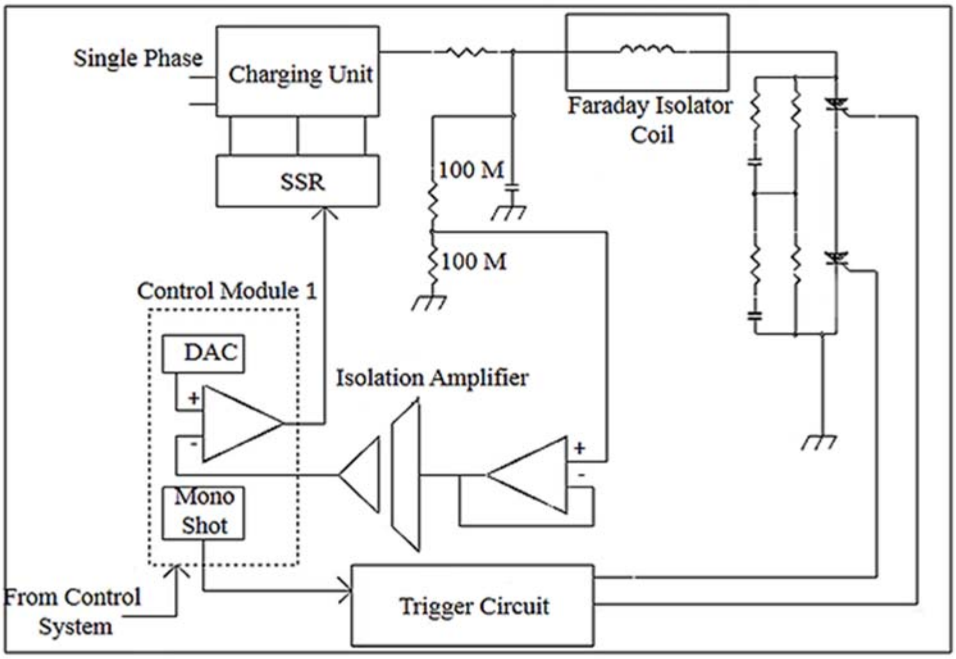

Figure 4.15: Faraday isolator power supply

Typical data for the Faraday isolators used in the chain is given in Table 4.2.

Table 4.2 Faraday isolators

Faraday Stage	**Inductance (mH)**	**Capacitance (µF)**	**Magnetic field (Tesla)**	**Peak current (A)**
Faraday Isolator 4-5	2.5	1000	1.52	962
Faraday Isolator 6-7	4.2	1000	0.76	1200
Faraday Isolator 8-9A	4.0	1300	0.76	1200
Faraday Isolator 8-9B	4.0	1300	0.76	1200

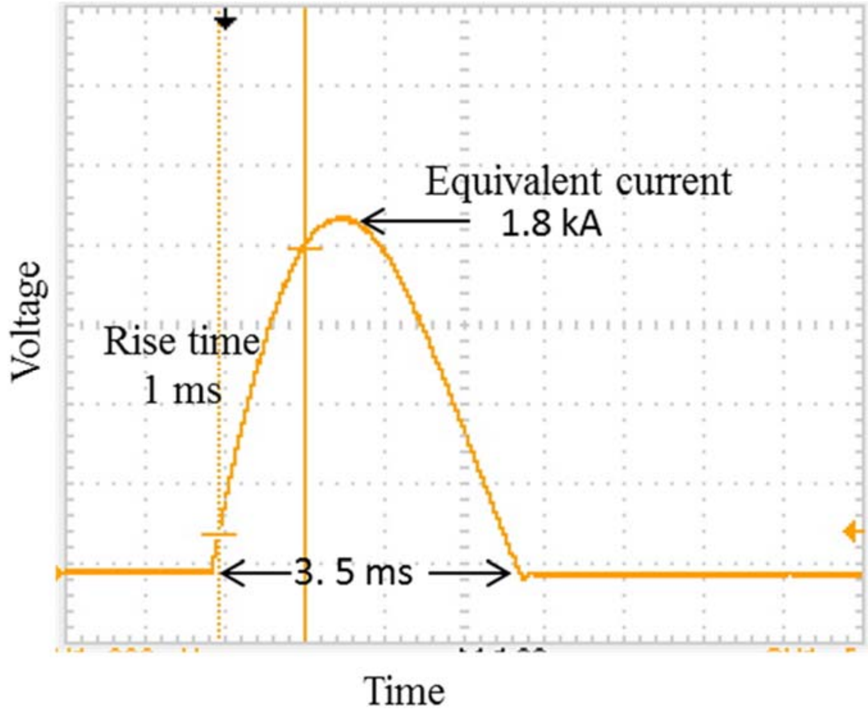

Figure 4.16: Faraday isolator current pulse (Rogowski sensor response)

4.6 Pockels cell and driving circuits

Pockels cells are electro-optical components in a solid stage high power laser chain. These devices are biased by pulsed or step voltages (~3 kV) to modulate laser propagation. It consists of a crystal through which a light beam can propagate and the phase delay can be changed by applying longitudinal or transverse electric field. Pockels cells thus act as a voltage-controlled optical switch and modulator which alters the plane of polarization of light propagating through it. Amount of rotation in electric vector of propagating light depends on birefringence of the material, which is electrically controlled. Some of the crystal compounds used in construction of Pockels cells are ammonium di-hydrogen phosphate (ADP), potassium di-hydrogen phosphate (KDP) and deuterated potassium dihydrogen phosphate (KD^*P). Figure 4.17 shows time profile of bias voltage for a (KD^*P) Pockels cell for which noise analysis is carried out in this dissertation work. Some of the applications of Pockels cells in high power laser systems are Q-switching, pulse selection and coupling to regenerative amplifiers. Electrically, Pockels cells represent capacitive load varying from 2 to 30 pF depending upon the aperture dimension. Typical amplitude and rise time of Pockels cell switching voltage are 3-3.5 kV and 1-5 ns respectively. Driver voltage is fed to Pockels cell through co-axial cable. High voltage and fast rise time drive signal is a potential source of EMI to other components. Its own operation is also susceptible to external electromagnetic interference. Noise free operation of Pockels cell is critical to laser quality and stability. Typical aperture of Pockels cell used in the present work is 9.5 mm with 8 pF capacitance value. For a step input from the source, voltage wave shape across a Pockels cell can be approximated to $1-e^{-t/\tau}$ [Carder, 1978]. Time constant τ is $Z(C/2)$, where Z is terminating impedance and C is capacitance. For typical capacitance value of 8 pF and terminating impedance of 50 Ω, calculated value of τ is 0.2 ns.

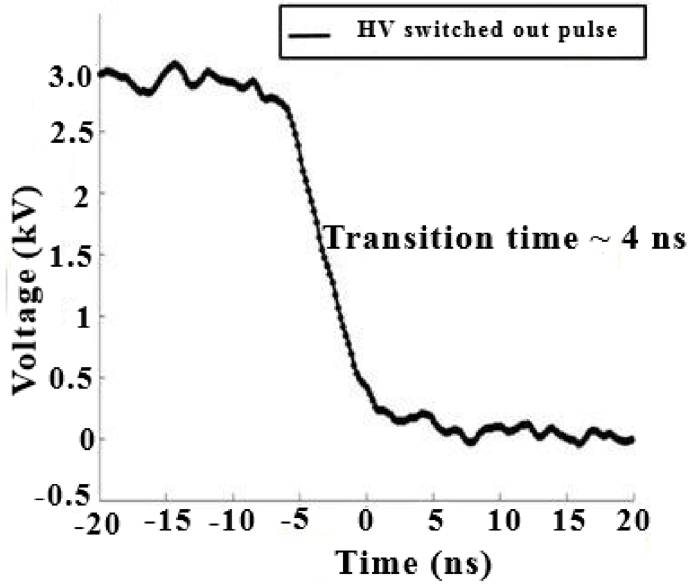

Figure 4.17: Pockels cell bias voltage

Several techniques based on spark gaps, krytrons and avalanche transistors are used for generation of high voltage and low rise time pulses for Pockels cell applications

[Houtman, 1985], [Matsushima, 1981]. More recently MOSFETs have been increasingly used in Pockels cell driver circuits [Arnold, 2007]. As a part of this dissertation, EMI generated by BJT (avalanche break down mode) and MOSFET based Pockels cell drivers are measured and analyzed.

Electromagnetic interference from power electronics semiconductor switching devices depends to a great extent on the rate of switching (*dv/dt, di/dt*) and the parasitic impedances (stray capacitance and inductance). Switching characteristics which play important role in EMI such as ringing frequency and overshoots are functions of the device input impedance. For MOSFET based switches the gate loop and switched current loop contribute to the overall stray inductances [Chen, 2010]. Reverse recovery time and amount of charge involved during switching off process are other two parameters which influence the noise emission and susceptibility. Equivalent circuit model of a MOSFET switch from EMI perspective is shown in Figure 4. 18.

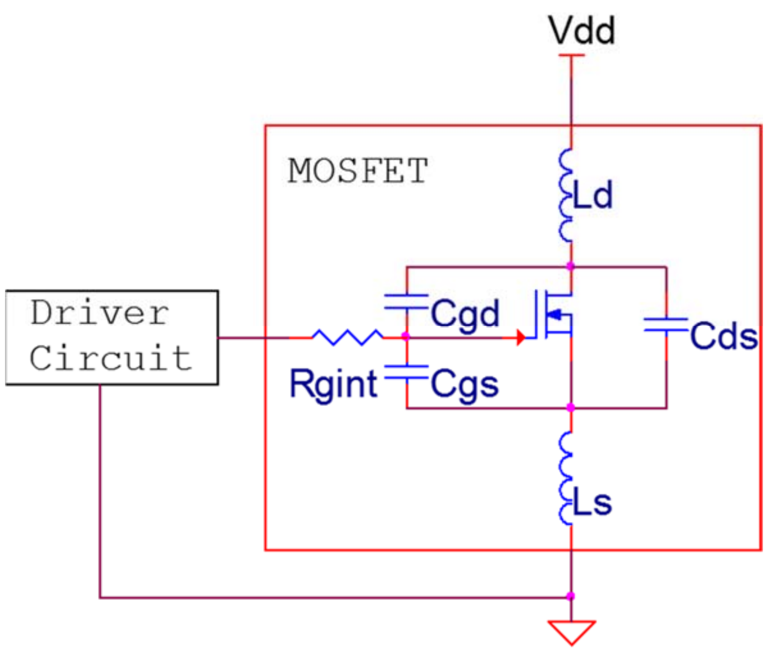

Figure 4.18: Equivalent circuit of power MOSFET switch [Wang, 2013]

The gate-source, gate-drain and drain-source capacitances are represented by C_{gs}, C_{gd} and C_{ds}. respectively. L_s and L_d are parasitic inductances associated with source and drain loops. Internal gate drive resistance is represented by R_{gint}. Typical value of internal gate resistance is 1 Ω. The freewheeling diode is modelled by a junction diode with reverse recovery characteristics in parallel with its parasitic capacitance. Turn on time of the MOSFET is affected by the parasitic capacitances. Switching transients of the MOSFET are essentially the charging process of its parasitic capacitances. Critical stray inductances for power MOSFETs are the gate-loop, switching-loop, and the common-source inductances. These affect the switched out waveform ringing, switching loss, device stress, and electromagnetic interference. Interference noise is directly proportional to the voltage overshoot and oscillations during turn-on and turn off transients. The response to electromagnetic interference varies between a MOSFETs and BJT switches due to different input impedances. MOSFET switches are more prone to EMI due to high input impedance. Bipolar junction transistors (BJTs) are current driven devices. Switches based on BJTs operating in avalanche mode have different noise characteristics as compared to MOSFET switches. In avalanche mode, transistors operate near the collector emitter voltage breakdown (BV_{ceo}) region. Noise Figure for transistors operating in avalanche mode increases considerably. Equivalent circuit model of a bipolar junction transistor, operating in avalanche breakdown mode is shown in Figure 4.19.

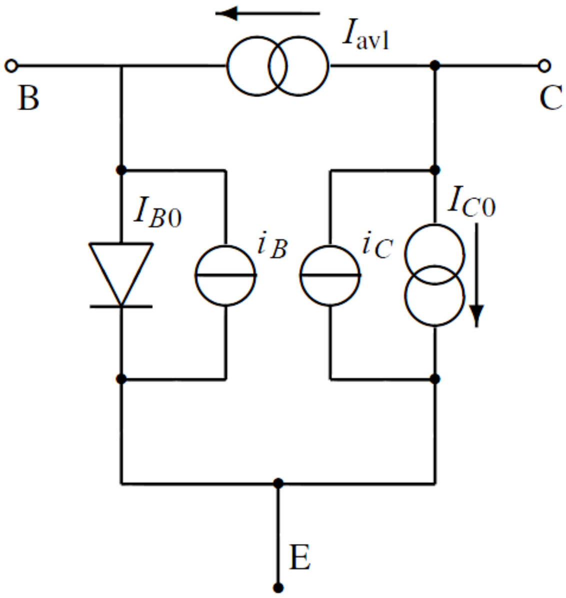

Figure 4.19: Equivalent circuit of BJT switch [Paasschens, 2004]

I_{BO} and I_{CO} are DC base and collector currents respectively. I_{avl} is the avalanche current, which depends on multiplication factor M as $I_{avl} = (M-1)I_{CO}$. In avalanche mode of operation two separate effects lead to noise generation. These are the effects of impact ionization and amplification of the avalanche based shot noise. Figure 4.20 shows a fast transition Pockels cell driver circuit based on bipolar junction transistor operating in avalanche break down mode. It utilizes the current mode second breakdown in a BJT for fast and high voltage switching [Baker, 1991], [Oak, 1991]. Transistors (Q7 to Q19) are cascaded for high voltage operation.

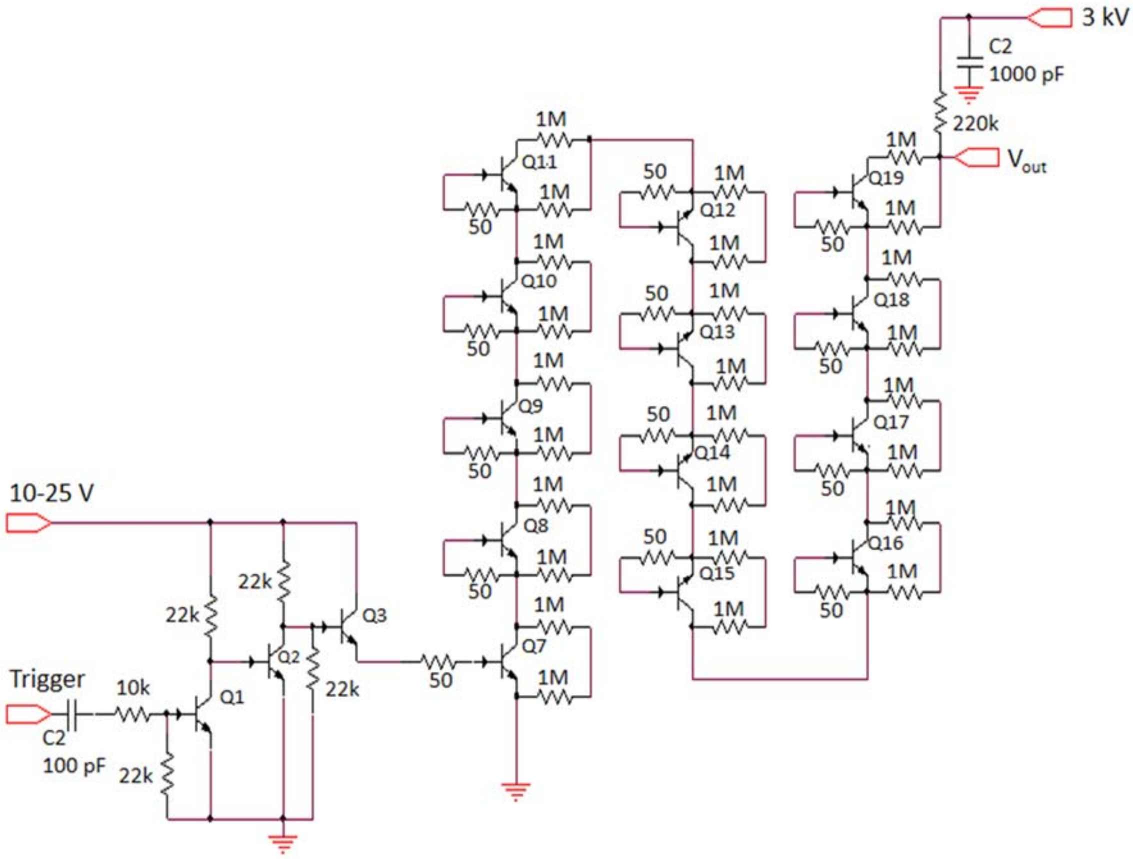

Figure 4.20: Pockels cell driver circuit

Another circuit used in this work is a commercial Pockles cell driver based on MOSFETs. Both driver circuits are optimized to switch 3 kV in 4 ns as shown in Figure 4.17. Measurement results indicate larger EMI for avalanche transistor based Pockels Cell drivers in comparison to MOSFET based switches. Results of EMI measurements for the two class of switches are shown in Figure 4.21. It is to be noted that under similar loading, shielding and operating conditions the radiated noise from MOSFET based switch reduces by 14 dB as compared to the switch based on BJT operating in avalanche mode.

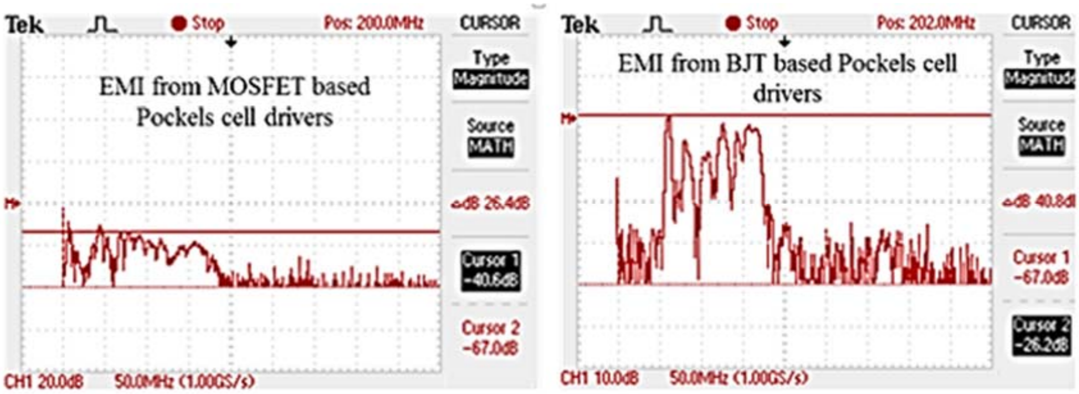

Figure 4.21: Fourier transform of noise measurements from MOSFET and BJT based Pockels cell drivers

4.7 Laser control system

A separate module controls each of the power supply stage. Control signals for charging and triggering of flash lamps are generated by a microprocessor-based system, which is connected to control modules through a proprietary parallel bus [Navathe, 2012]. Figure 4.22 shows the laser control system. Data pertaining to selection of a particular power supply stage, charging voltages and delays between various amplifier stages are entered through a graphical user interface front end. These data are routed from PC to microprocessor through serial bus which is then loaded in respective modules. The charging and firing operations, safety checks and monitoring of status of all power supplies is carried out through a control program. Safety checks include common problems associated with capacitor banks and flash lamps, such as short circuiting of capacitors, overcharging, self-firing of flash lamps, etc. The control system is interfaced to the nanosecond oscillator, which operates in repetitive mode. All the succeeding amplifiers and Faraday isolators are operated in single shot. Minimum gap between two shots taken at low energy with only initial amplifiers is about 5 minutes, while the same at full energy is about 30 minutes. The low repetition rate of about 30 minutes is based on cooling profile of the laser medium. It is necessary to ensure that the firing of all amplifiers and Faraday isolators in the laser chain is synchronized with a selected pulse of this oscillator.

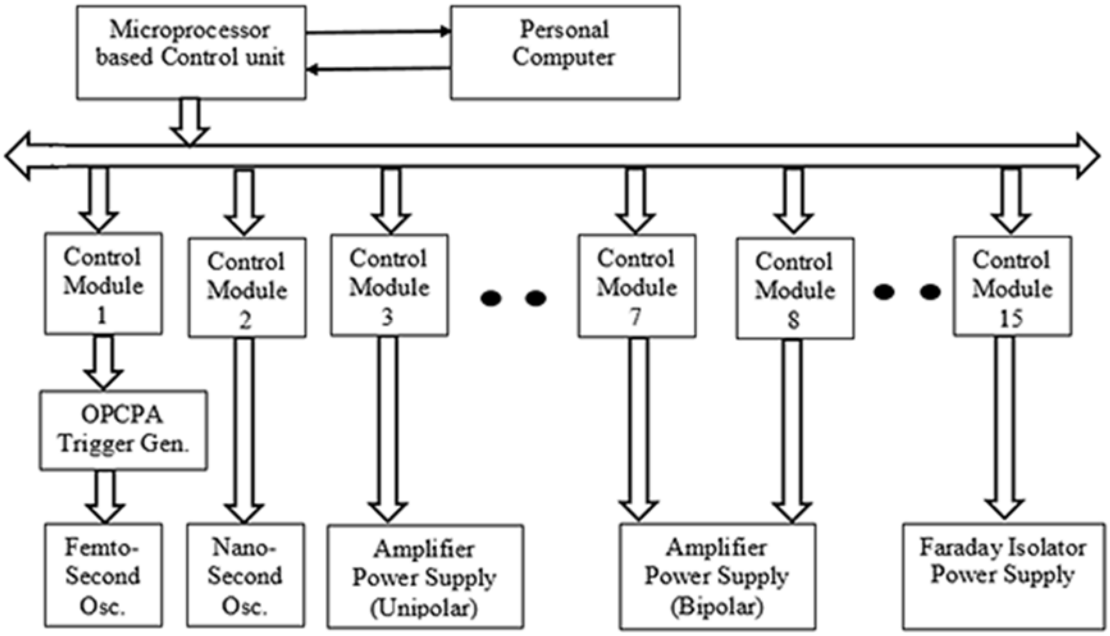

Figure 4.22: Laser control system block diagram

For this purpose, the oscillator is triggered in repetitive mode at 0.25 Hz by the control system. When chain has to be fired, then control system initiates charging of all capacitor banks as per the settings entered by the operator. After about 30 seconds to 1 minute, when charging of all banks is over, the firing sequence is initiated. The laser oscillator has an external trigger input for synchronization. The trigger signal is to be provided 1500 µs prior to the laser oscillator pulse. As laser amplifiers driven by flash lamps take time to reach peak gain they are fired 360 µs prior to the oscillator pulse. It ensures that low energy oscillator pulse enters the amplifier stage at the time of maximum gain. Similarly, the Faraday isolators are fired so that the current pulses (and hence the magnetic field) in them reach their peaks at the time of arrival of the laser pulse. Approximate delay between the trigger pulses to the Faraday isolators and laser pulse vary from 2000 to 3500 μs, depending on actual coil inductance and energy storage capacitance of that stage. Thus the control system fires all the stages at appropriate delays so that the laser pulse sees maximum gain in all amplifier stages. These delays are generated by a clock based on crystal oscillator, with an accuracy of 100 ppm. The timing sequence of this operation is shown in Figure 4.23.

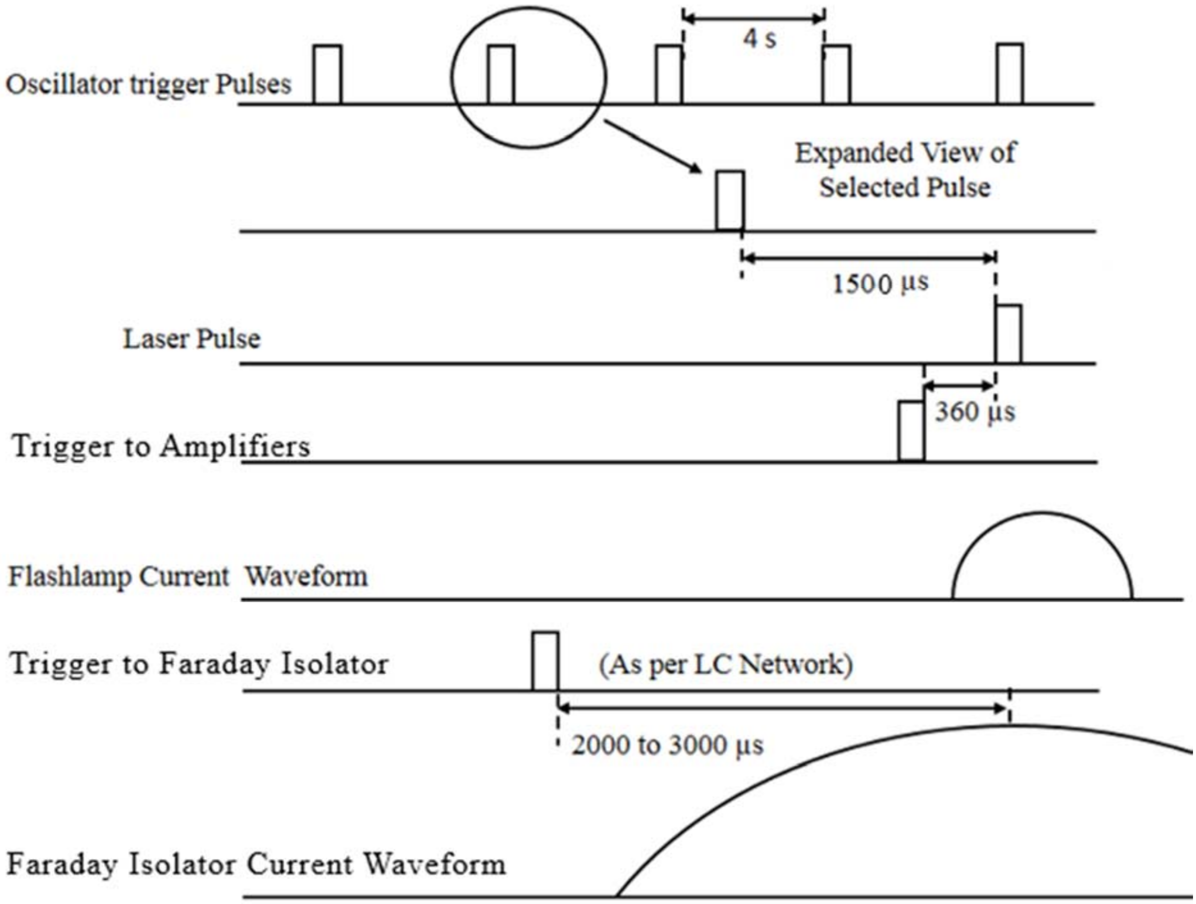

Figure 4.23: Timing diagram of laser chain (Not to scale)

4.8 Signal integrity in high power laser electrical circuits

As mentioned in earlier sections of this chapter, some of the high voltage and high current impulses travel through long cables (5-10 m) in laser power supply stages. In other cases like switching of Pockles cells, the cable lengths are not very long but signal rise time is fast (~ 5 ns). There are different types of connectors and interconnects which create impedance discontinuity. These conditions generate significant amount of crosstalk and noise emissions, with potential to disturb integrity of control and trigger signals. Important signal integrity parameters which are dealt in subsequent sections of this dissertation are, rise time deterioration, ringing which result in false triggering of critical devices and reflections through un-matched and nonlinear loads. Following types of electrical signals are encountered in the laser systems under discussion.

Pulsed and non-periodic: These are dominant sources of EMI generated by,

a) Triggering and discharge of capacitor banks through flash lamps.
b) Low voltage (5-12 V) trigger signals from laser control systems.
c) 3 kV/5 ns rise time switching of high voltage BJT and MOSFET switches for operation of electro-optic devices like Pockels cells.
d) Operation of electromechanical relays.

Continuous pulses: These are free running clock signals for synchronization of different stages of laser unit. For example, in the case of table top terawatt laser there is a 100 MHz signal occurring in synchronization with laser pulses. This is taken through a RG 58 co-axial cable of around 5 m length to pulse selector circuit.

These may be compared with some of the standard test pulses and the mode of characterization as defined by International Electro-Technical Commission (IEC) [IEC, 2004]. Figure 4.24 shows timing parameters of a test pulse defined by IEC 61000 (4-4) and (4-5) standards for EMI pulses in the context of electrical fast transient/surge immunity tests. Temporal profile of the test pulse in terms of the rise time (T_r) and FWHM can be compared with high voltage trigger signal for Pockels cells. Figure 4.25 shows frequency spectrum of the IEC 61000 standards test pulses. The term *x/y* refers to a pulse of rise time (10-90 %) of x and FWHM of y. EFT refers to electrical fast transients which define 15 ms bursts of pulses with rise time of 5 ns and pulse width of 50 ns at a repetition rate of 300 ms.

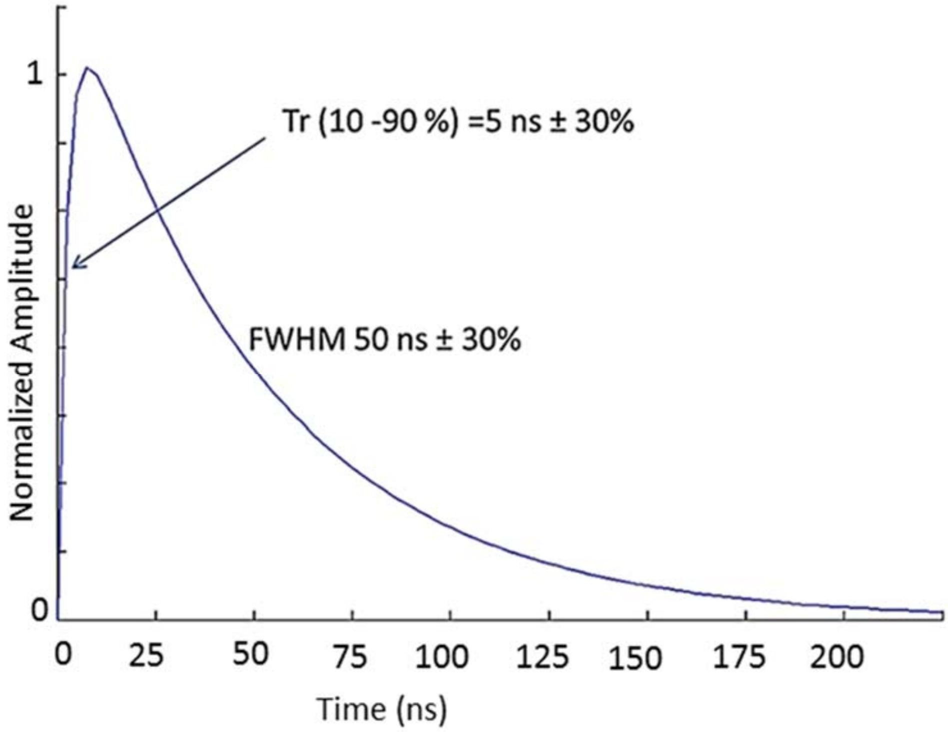

Figure 4.24: Test pulse for electrical fast transients [IEC, 2004]

Laser and other diagnostics operate in presence of the interfering noise. Some of the preventive steps taken to eliminate the EMI effects are,

a) The digital signals controlling the amplifier power supplies are connected through opto-couplers.
b) Analog signals are connected through isolation amplifiers.
c) A fiber optic cable is used to generate trigger signals.
d) Conducted noise is reduced by taking the mains power through an isolation transformer.

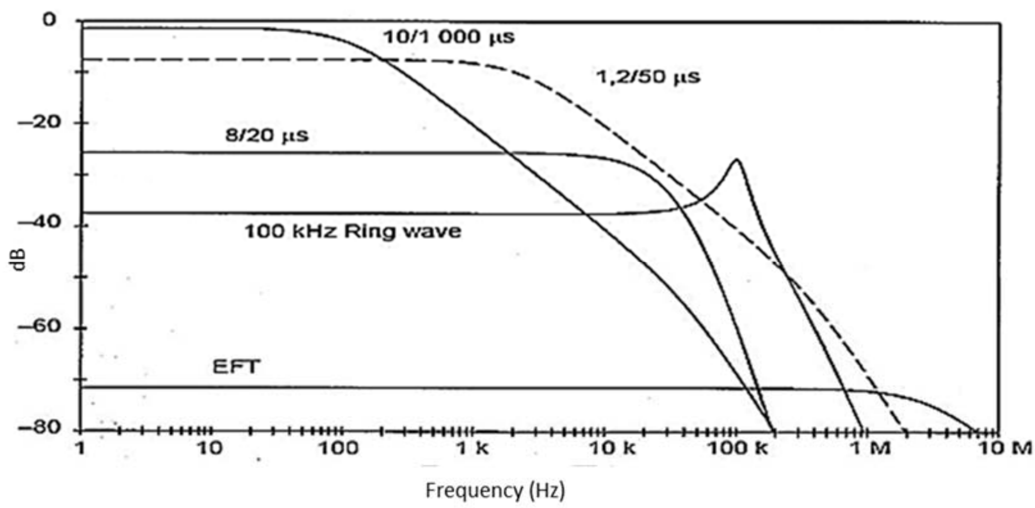

Figure 4.25: Frequency spectrum of EMC test pulses [IEC, 2004]

4.9 Summary and conclusion

This chapter describes the high power laser systems, electro-optical components and pulsed power supply units under investigations. These components produce transient and non-stationary electromagnetic pulses. One of the laser systems under investigations is a 2- beam high power Nd: phosphate glass laser chain. Second set up under study is the ultra-high intensity table top terawatt laser. Both of these lasers are single shot solid-state systems pumped by Xenon filled flash lamps. These lasers are developed at Raja Ramanna Centre for Advanced Technology, Indore for research in the field of laser plasma interaction leading towards inertial confinement fusion related studies. Cables and interconnects carrying pulsed high voltage and current generate transient electromagnetic interference, which affect the integrity of low voltage control and diagnostic signals. Analysis of electromagnetic interference and noise susceptibility is important for reliable operation of the laser systems.

Flash lamps are arc discharge tubes and from electrical point of view these are non-linear, loads excited in controlled manner by energy stored in capacitor banks. A high voltage trigger pulse initiates the main discharge current of peak value of several kA and duration of 400 to 600 μs through a pulse forming network. Values of peak current and pulse duration are decided by pumping requirements of the lasing medium, which forms the basic guideline for selection of pulse forming network components. Profile of flash lamp current consists of an initial fast rise time and oscillatory trigger portion followed by a critically damped and smooth discharge. There are two different power supply configurations used in the laser systems for flash lamps. These are configured in unipolar and bipolar modes and have different electromagnetic behavior which in general depends upon current/voltage rise time, area and path of current loop. Amplitude of EMI becomes more pronounced due to several unavoidable impedance discontinuities in current path and large cable lengths.

Other high voltage and high current components producing electromagnetic interference and crosstalk in the laser systems are Faraday isolators based on magneto-optic effect and Pockels cells based on electro-optical effects. The table top terawatt laser system has Pockels cells at injector and ejector stages of the regenerative amplifier. These are driven by high amplitude (~ 3 kV) and few ns rise time pulsed voltages. Delay in trigger signals for the two cells controls the number of round trips in amplifier stage and consequently the amplification factor.

The investigated high power laser chains are multi-stage units and belong to the class of intra system setup. Radiating structures are of different geometrical scales ranging from few centimeter long digital clock carrying PCB tracks to 5 m long cables, which carry high peak pulsed currents for flash lamps and Faraday coils. Subsequent portions of this thesis discuss time domain measurements, characterization and time-frequency analysis of the radiated and conducted interfering noise. Measurements of the radiated noise are carried out in near and far field regions with E probe, H probe and antennas. Measurement bandwidth of the radiated emission is limited to 1 GHz. Conducted noise measurement bandwidth is up-to 300 MHz. EMI measurements in two different types of flash lamp power supply configurations are compared.

Chapter 5

Electromagnetic interference in flash lamp pumped laser systems

This chapter presents the analysis and measurements of radiated near and far fields, and conducted emissions due to interconnects in the laser power supplies and other electrical systems. Impedance, terminating loads and shielding characteristics of cables are important factors, which determine the amplitude, time and frequency parameters of interfering signals. The laser systems employ different types of cables such as *RG8* for pulsed flash lamp current, *RG58* for trigger and clock signals, eight core multi-conductor cables for control signals, parallel wires for Faraday isolator solenoid current and high voltage cables for Pockels cell biasing. Ground plane, cable layout and bends affect the electromagnetic interference. Near field measurements are carried out with *E* and *H* probes of 1 GHz bandwidth. Far field measurements are carried out by a bi-conical and a dipole antenna covering the frequency range from 20 MHz to 300 MHz and 330 MHz to 1 GHz respectively. Line impedance stabilization network (LISN) of bandwidth 30 MHz is used for measurement of conducted emission. Laser power supplies under study consist of a charging circuit, which energizes 200 μF of energy storage capacitor bank to maximum voltage of 5 kV. Stored electrical energy is discharged through a 280 mm arc length, 16 mm bore diameter xenon flash lamp in form of pulsed current. Trigger and discharge current loops through flash lamp network and impedance discontinuities at interconnects result into conducted and short time, broad band, radiated noise. Faraday isolator power supply consists of a charging circuit which energizes 1000 μF of energy storage capacitor bank to 3 kV. Stored electrical energy is discharged through a 4 mH Faraday coil with the help of a silicon controlled rectifier switch. Electromagnetic emission takes place during initial triggering of SCR and during the main discharge current. Power supplies for flash lamps and Faraday isolators are pulsed with typical repetition rate of once in five minutes. EMI produced as a result of triggering of flash lamps and semiconductor devices have a certain degree of randomness and statistical variations. Each measurement data consists of averaged value of ten readings.

Measurements of the pulsed electromagnetic interference are carried out in time domain. Post storage transient EMI signals are converted to frequency domain with the help of fast Fourier transform and Welch mean square spectrum estimate [Welch, 1967]. Investigations of EMI generation and susceptibility in solid state laser power supplies and synchronizing circuits have become significant with growing sophistication in optics and opto-electronics components driven by high power handling and fast switching devices. Under broad band pulse excitations, the connectors, wires and cables have significant inductance/capacitance and behave as transmission lines. This leads to signal integrity effects such as reflection, overshoot, undershoot and crosstalk [Achar, 2001]. Longer wires in power supply and control systems behave as transmitting/receiving antennas. Modeling of transmission line effects and radiation properties is a multidisciplinary topic encompassing electromagnetics, circuit theory, transmission line and antenna theory. Quantitative measurements and characterization are helpful to understand the noise characteristics, to mitigate the noise related effects and to validate for electromagnetic compatibility compliance standards. Radiated emissions from an electrical system are attributed to differential and common mode currents in cables and interconnect [Paul, 1989]. Differential current flows through load and return path. There is 180^{o} phase shift between currents flowing through main conductor and the return conductor. As such, fields generated by components of differential currents in forward and return paths tend to cancel out. On the other hand, common mode current flows in the same direction in forward and return paths and resulting fields add up. Common mode current is coupled to reference (earth) plane through parasitic capacitances. Despite smaller magnitude, field contribution by common mode current is significantly higher than that of differential mode current and normally dominates the analysis of electromagnetic interference [Paul, 2006].

5.1 Near field and far field measurements

Electromagnetic emissions from a radiating source are divided in different regions [Balanis, 2005] characterized by distance of observation r, wavelength λ and dimension of the radiating element D. Two distinct regions are identified as 'Near' and 'Far' fields. In terms of electromagnetic behavior, the difference lies in energy transport and wave impedance. In near field region reactive component of the power density $\left(\overline{E}\times\overline{H}\right)$ dominates. Whereas, in far field region the real part of the power density i.e. radiating component is prominent. In the near field region, wave impedance E_θ / H_ϕ varies widely and depends on source characteristics. In far field region, the wave impedance is constant to a value of 377 Ω and is not influenced by source characteristics. Figure 5.1 illustrates variation of wave impedance in near and far field regions, which depends on emitted wavelength λ. Compared to far-field measurements, near-field measurements have advantages in terms of accuracy, reliability and costs [Fan, 2010]. Since, near field measurement probes and EMI sources are placed in close proximity, uncertainty factors due to scattering and medium conditions are reduced. Near field measurements are able to provide information about radiating source. On the other hand far-field measurements are direct measurement of radiation patterns where the data are not influenced by presence and dimensions of probes [Balanis, 2005]. Far field measurement by itself is not able to provide source diagnostic or identification.

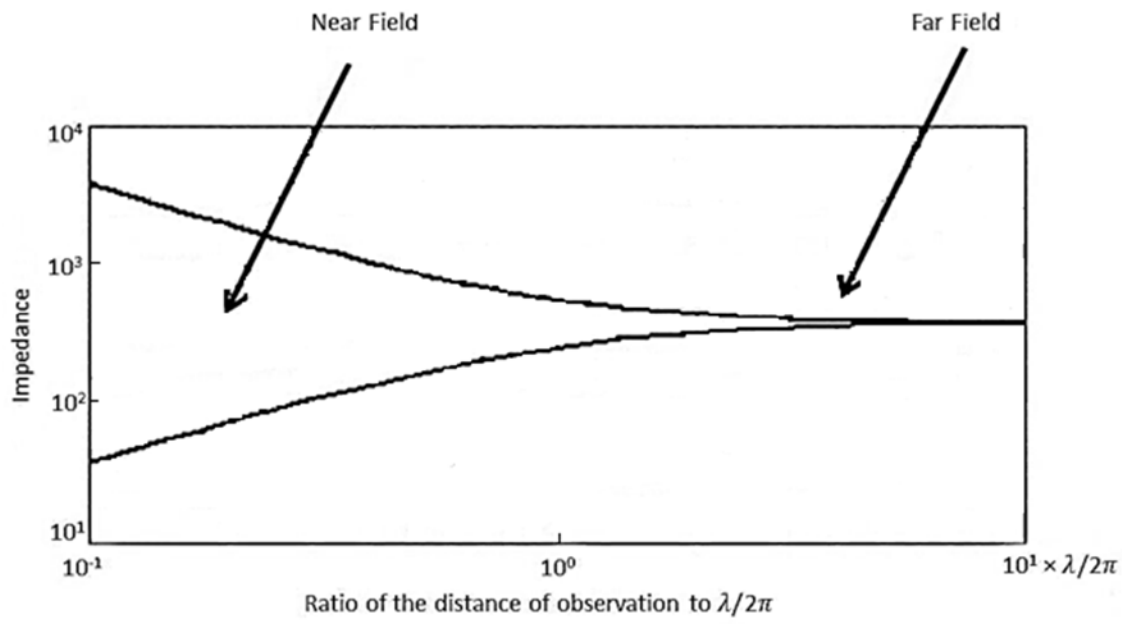

Figure 5.1: Wave impedance for near and far fields

5.2 Analytical solutions for field calculations

Analytical techniques are classical methods for characterization of interfering electromagnetic field emissions. It depends on rigorous formulation of current distribution in critical parts of the system. Field characterizations based on analytical solutions provide accurate results, however, this approach is difficult to formulate in a large scale intra-system setup. Following sections describe uniform current and Hertzian dipole techniques for solution of radiated fields from wires and interconnects**.**

a) Uniform current dipole: This model assumes that the current amplitude and phase throughout the radiating structure are constant. Thus it considers the entire radiating geometry as a single Hertzian dipole. Far region electric fields due to differential and common mode currents under the above mentioned assumptions for two conductor system are given respectively by following set of equations [Paul, 1989].

$$E_{D,\max} = \frac{120\pi I_d l d f^2}{c_0^2 R} \tag{5.1}$$

$$E_{C,\max} = \frac{120\pi I_c l f}{c_0 R} \tag{5.2}$$

where, E_D is electric field due to differential mode current, E_C is electric field due to common mode current, I_d is amplitude of differential mode current, I_c is amplitude of common mode current, l is the conductor length, d is separation distance between two conductors, R is distance of observation point, f is operating frequency and c_0 is speed of light in free space. Equations (5.1) and (5.2) above assume that separation between the conductors are much less than the conductor length. In presence of a ground plane, total electromagnetic field is vector sum of a radiated wave that travels directly to the observation point from the forward and return paths and a ground reflected wave. Ground plane affects the field due to common mode current. Correction factor to common mode field due to presence of ground plane is [Paul, 1984]

$$F = \left| 1 - \frac{R}{\sqrt{R^2 + 4h^2}} e^{-j\frac{2\pi}{\lambda}\left(\sqrt{R^2+4h^2}-R\right)} \right| \tag{5.3}$$

It is to be noted that the correction factor depends on height of conductor h above ground plane, and the wavelength λ.

b) Hertzian Dipole Technique: Hertzian dipole model is the most commonly used analytical technique for calculation of electromagnetic field emission. It treats a radiating structure to be composed of small size dipoles. Total radiated electromagnetic field is summation of contributions from individual dipoles. It is also assumed that distance between the observation point and dipole is larger than the dipole size. Typically the radiating conductor is divided into sections of length 0.1λ. Hertzian dipole model is more accurate evaluation of far field with a known current distribution. This approach is suitable when current distribution along conductor length cannot be assumed to be uniform and constant. Wire sections are short enough to have a uniform current along its length and are considered to behave as a Hertzian dipole. Electric field in time domain due to a current elements in *Z* direction is given by [Thomas, 1994],

$$E_z(t) = \frac{lz^2}{4\pi\varepsilon_0 R^2}\left[\frac{3i\left(t-\frac{R}{c_0}\right)}{c_0 R^2} + \frac{3\int_0^t i\left(\tau-\frac{R}{c_0}\right)d\tau}{R^3} + \frac{1}{c_0^2 R}\frac{\partial i\left(t-\frac{R}{c_0}\right)}{\partial\left(t-\frac{R}{c_0}\right)}\right]$$

$$-\frac{1}{4\pi\varepsilon_0}\left[\frac{i\left(t-\frac{R}{c_0}\right)}{c_0 R^2} + \frac{\int_0^t i\left(t-\frac{R}{c_0}\right)d\tau}{R^3} + \frac{1}{c_0^2 R}\frac{\partial i\left(t-\frac{R}{c_0}\right)}{\partial\left(t-\frac{R}{c_0}\right)}\right] \tag{5.4}$$

The term c_0 is speed of propagation in free space, $i\left(t-\frac{R}{c_0}\right)$ is current at the retarded time and *R* is distance of observation point from the actual dipole position placed at origin. Total radiated fields from a transmission line of length *L* above a ground plane is calculated as integral of each infinitesimal dipole element.

5.3 Emission characteristics of cables and terminations

Straight wire pairs such as tracks on printed circuit board (PCB), ribbon cables etc. are commonly used interconnects in power electronic systems. In laser setups under study, a pair of parallel straight wires is used to carry control signals and part of the capacitor discharge current. Radiated emission is attributed to differential and common mode currents through interconnects. For systems which are connected with a pair of wires, the conducting ground plane provides a return path for common mode current, whereas, differential current flows through load and return path. In such systems, the conducting ground plane provides a return path for common mode currents and acts as an image plane [Dockey, 1993]. Signal propagation along a transmission line consisting of a pair of parallel wires above a ground plane is shown in Figure 5.2. Voltages V_1, V_2 and currents I_1, I_2 are de-composed into differential mode as V_d, I_d and common mode components denoted by V_c and I_c. Differential mode currents through a pair of conductors are equal in magnitude and phase but flowing in opposite directions, whereas common mode currents flow in the same direction.

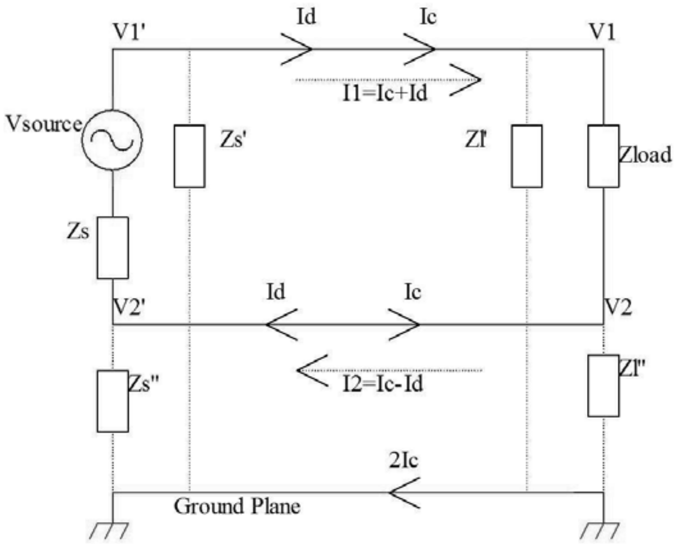

Figure 5.2: Equivalent circuit model for common mode current

Voltage and current on each wire are related to common and differential parameters through a transformation matrix [S] as

$$\begin{bmatrix} I_1 \\ I_2 \end{bmatrix} = [S] \begin{bmatrix} I_d \\ I_c \end{bmatrix} \tag{5.5}$$

$$\begin{bmatrix} V_1 \\ V_2 \end{bmatrix} = \left[S^T \right]^{-1} \begin{bmatrix} V_d \\ V_c \end{bmatrix} \tag{5.6}$$

For multi-conductor transmission lines, voltage and current are defined by the matrix equations

$$\frac{\partial[V(x)]}{\partial x} = -[Z][I(x)] \tag{5.7}$$

$$\frac{\partial[I(x)]}{\partial x} = -[Y][V(x)] \tag{5.8}$$

[V] and [I] are voltage and current matrices on the conductors, [Z] is transmission line impedance matrix and [Y] is transmission line admittance matrix. For a lossless transmission line, [Z] and [Y] are formed by inductance matrix [L] and capacitance matrix [C] as,

$$[Z] = j\omega[L] \tag{5.9}$$
$$[Y] = j\omega[C] \tag{5.10}$$

Analytical solution for per unit length [L] and [C] matrices of a two wires system above ground plane is given by [Christopoulos, 2007].

$$L = \frac{\mu_0}{2\pi}\begin{bmatrix} \ln\frac{2h}{a} & \ln\frac{D}{d} \\ \ln\frac{D}{d} & \ln\frac{2h}{a} \end{bmatrix} \tag{5.11}$$

where, μ_0 is the permeability in free space, d is the wire separation, h is the wire height above ground, a is the wire radius and $D=\sqrt{(4h^2+d^2)}$.

Corresponding capacitance matrix is,

$$C = \frac{2\pi\varepsilon_0}{\left(\ln\frac{2h}{a}\right)^2 - \left(\ln\frac{D}{d}\right)^2}\begin{bmatrix} \ln\frac{2h}{d} & -\ln\frac{D}{d} \\ \ln\frac{D}{d} & \ln\frac{2h}{d} \end{bmatrix} \tag{5.12}$$

where, ε_0 is the free space permittivity. Terminations and bends introduce impedance discontinuities in transmission line parameters of a cable and contribute to the overall emission characteristics. In the transmission line equivalent circuit diagram shown in Figure 5.3, discontinuities are represented by an extra impedance Z_p.

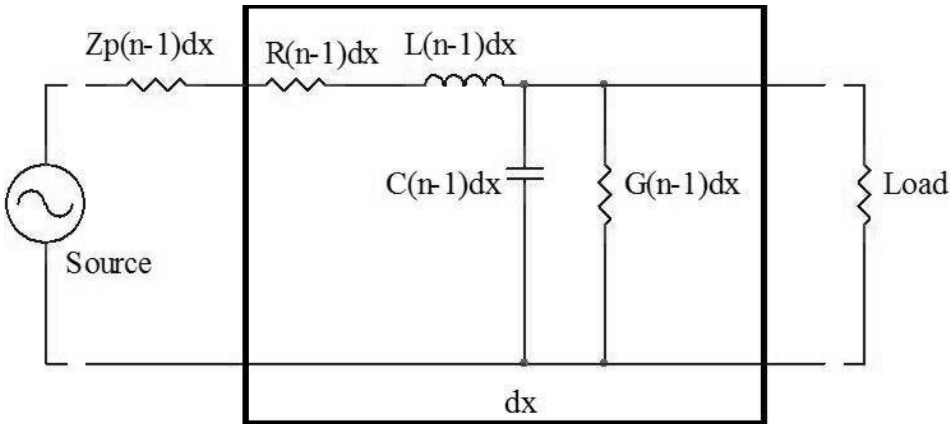

Figure 5.3: Equivalent circuit of impedance discontinuity in a transmission line

Radiation loss by a bent transmission line is calculated in terms of *S* (scattering) parameters. For an incident power of P_{in} and the radiated power of P_{rad} the radiation loss is defined in terms of the scattering (S) parameters S_{11} and S_{21} as [Lee, 2001],

$$\frac{P_{rad}}{P_{in}} = 1 - \left|S_{11}\right|^2 - \left|S_{21}\right|^2 \quad (5.13)$$

Figure 5.4 illustrates the experimental setup for measurement of radiation loss due to layout geometry in a co-axial line. It involves *S* parameter measurements with a vector network analyzer (VNA). Results of the radiation loss from a two meters long RG8 cable for layout angles of 15°, 45° and 90° respectively are shown in Figure 5.5. Radiated emission increases with increase in layout angles due to introduction of extra parasitic impedances as illustrated in Figure 5.3.

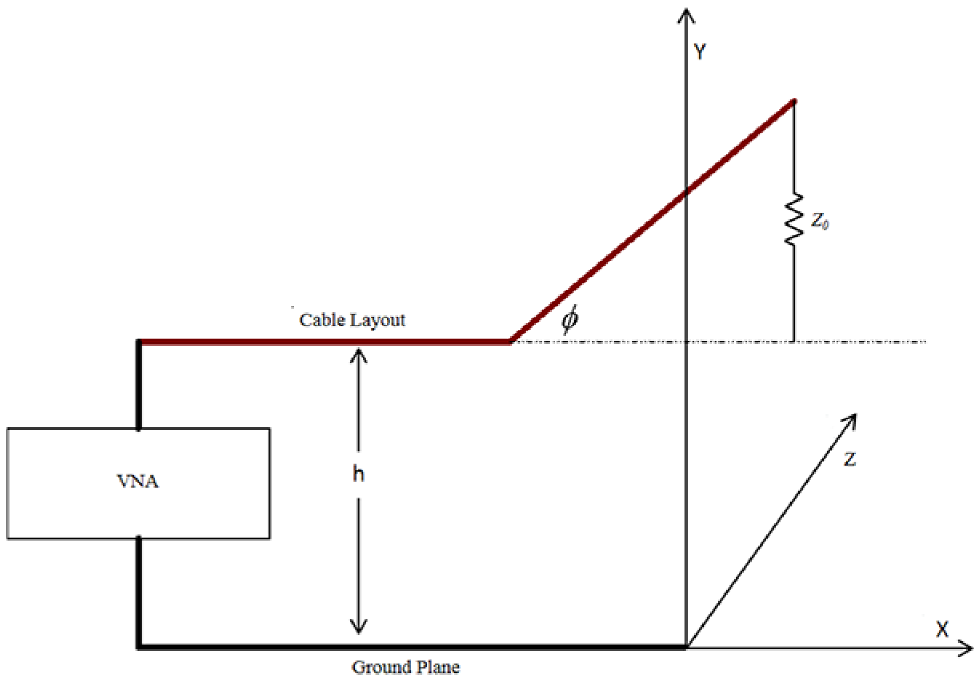

Figure 5.4: Experimental setup for EMI measurement due to transmission line layout

5.4 Laser power supplies and EMI

Electromagnetic interference studies were carried out for laser power supplies in both unipolar and bipolar set ups. Flash lamp current and optical pulse for which studies were carried out is shown in Figure 5.6. It shows oscilloscope trace of photodiode and current sensor outputs. Signals obtained from both these sensors are in terms of voltage which are calibrated for optical output and current respectively. Current peak and pulse width are of the order of 3 kA and 600 µs respectively. A high *dV/dt* trigger voltage pre-ionizes the flash lamps. This initial portion of flash lamp excitation is a strong source of electromagnetic interference. Photograph of power supply, flash lamp assemblies and cable placement is shown in Figure 5.7.

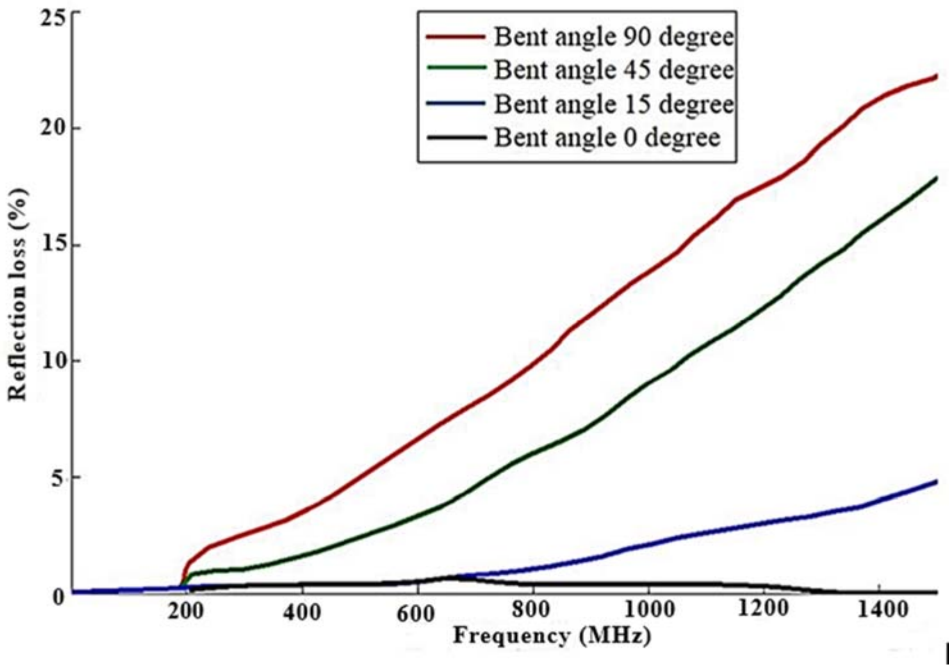

Figure 5.5: Emission due to transmission line layout geometry

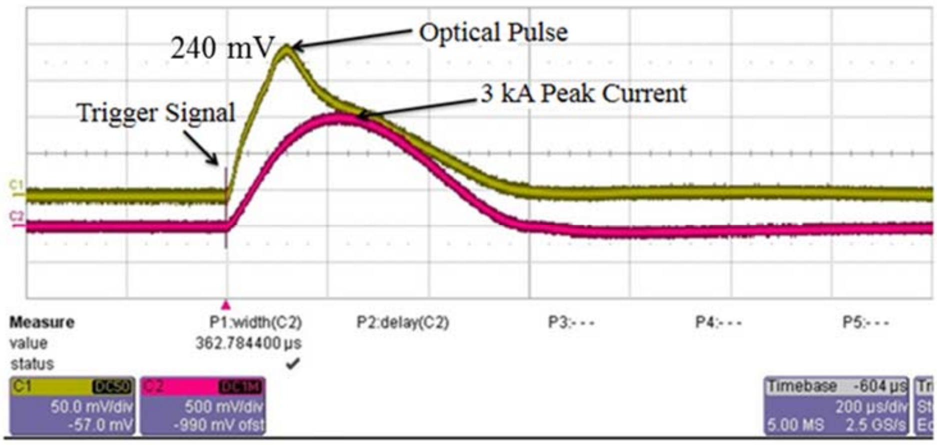

Figure 5.6: Snap shot of oscilloscope trace (voltage vs. time) for flash lamp optical pulse and current profile

Capacitor banks and charging power supplies are housed in a common chassis whereas flash lamps are placed in a separate enclosure. Far field measurement setup consists of bi-conical and dipole antennas to cover frequency range of 1 GHz [Kanda, 1994]. Antenna for far field measurements was placed at a distance of 3 m from capacitor discharge cable. Near field probes were kept at 20 cm from the discharge cables. For study of conducted emission in flash lamp power supply, AC mains were connected through a LISN (line impedance stabilization network). Flash lamp current is measured by a Rogowski probe. Experimental procedure consisted of charging the capacitor bank to 3 kV, generating a 15 kV/10 μs flash lamp trigger signal and discharging the stored energy through a flash lamp. EMI measurement setup is shown in Figure 5.8.

5.4.1 EMI in flash lamp power supply configurations

Power supply, interconnect, flash lamp location and current path in a unipolar power supply are shown in Figure 5.9. Energy storage capacitor bank, *C* is charged to the required voltage by a constant current charging circuit. *L* represents secondary coil of trigger transformer. *T1* to *T6* are termination blocks implemented with aluminum lugs of 6 mm diameter and mounted on Perspex sheet. *I1* and *I2* are forward and return currents through co-axial cable (RG8) which is around 3 m long. Charging circuit and flash lamp are mounted in two different enclosure assemblies. Flash lamp forward and return currents flow through central conductor and sheath of the co-axial cable respectively, thereby reducing the overall current loop area.

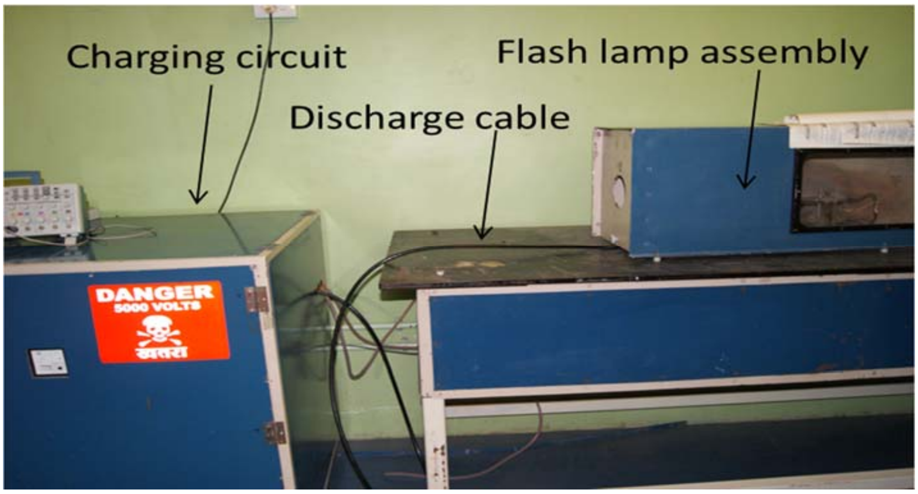

Figure 5.7: Power supply and flash lamp assembly

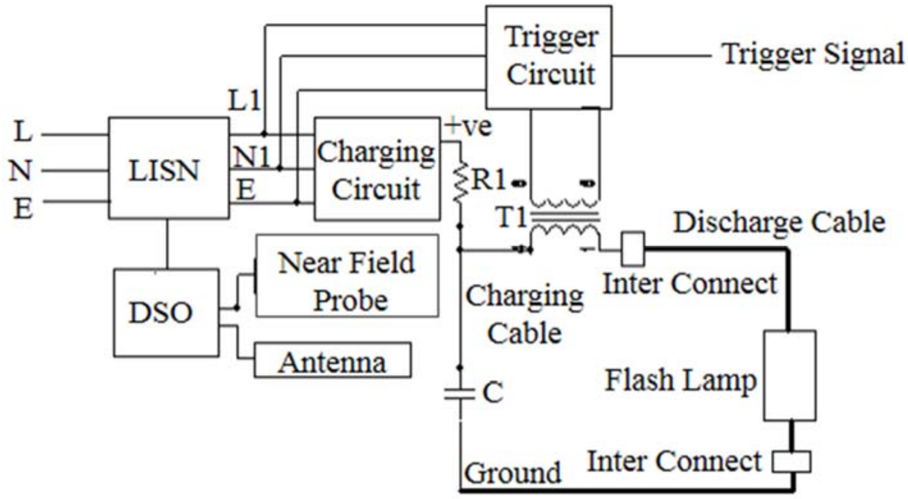

Figure 5.8: Flash lamp EMI measurement setup

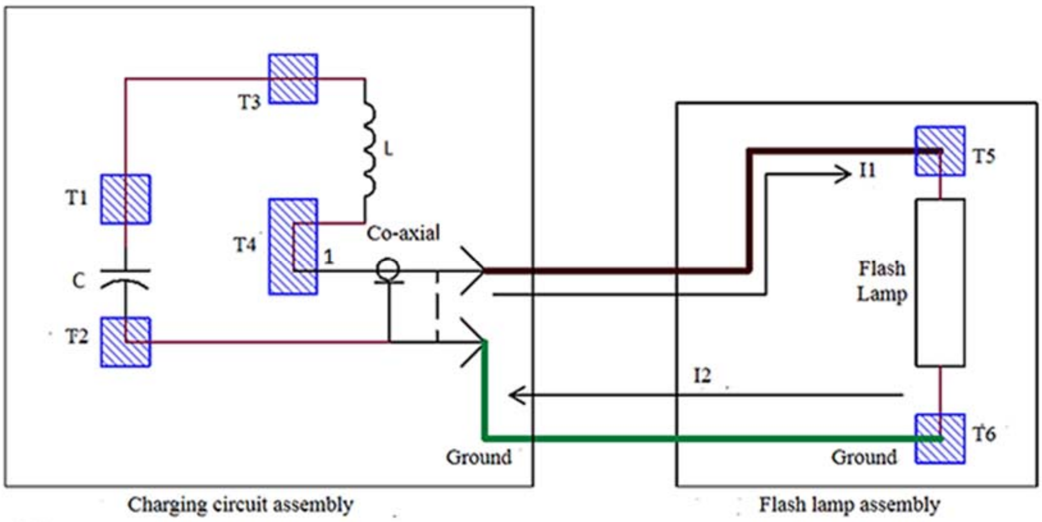

Figure 5.9: Unipolar flash lamp power supply

Bipolar power supplies for flash lamps consist of two capacitor banks charged to +ve and –ve voltages respectively such that net voltage across flash lamp doubles. Important aspects from EMI point of view in bipolar power supply are,

i) Both ends of flash lamps are floating.

ii) Overall current loop area increases as compared to unipolar scheme.

EMI measurements for both configurations are carried out under similar conditions of capacitance and charging voltage such that flash lamp current peak, rise time and pulse width remains the same. Schematic of bipolar power supply, flash lamp location and current path are shown in Figure 5.10. C1 and C2 are positive and negative capacitor banks charged to voltage ±V. *L* represents secondary winding of a trigger transformer as in unipolar configuration. T1 to T8 are termination points consisting of aluminum lugs. I1 and I2 are forward and return currents flowing through cables 1 and 2, which are around 3 m long. Average separation between cables is 300 mm. Charging circuit and flash lamp are mounted in two different chassis/assemblies.

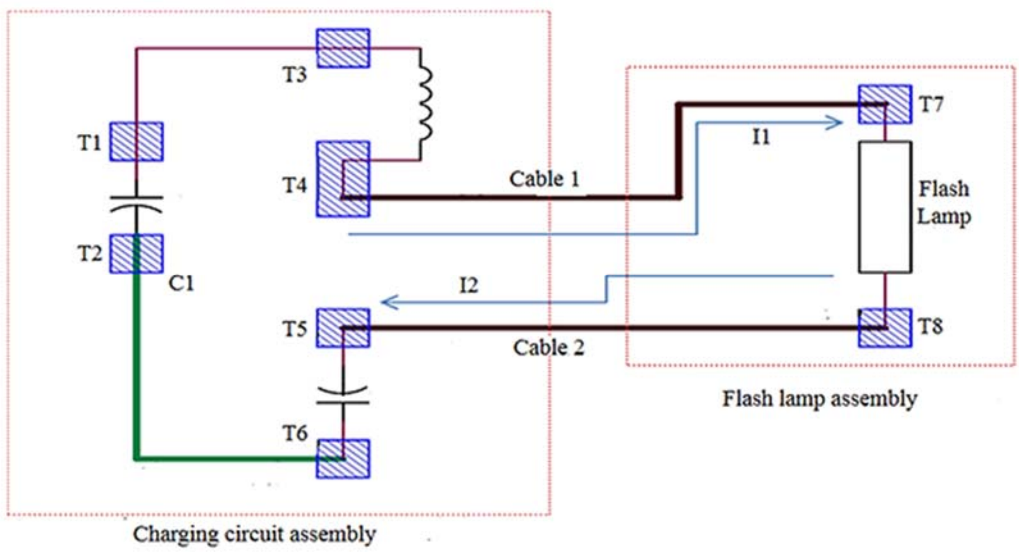

Figure 5.10: Bipolar flash lamp power supply

Termination blocks form impedance discontinuities, which along with emission from discharge cable are major sources of radiated EMI. Significant differences with respect to unipolar supply are increase in number of termination blocks and variation in flash lamp forward and return current paths.

5.4.2 Measurement of radiated emission

Measurements of noise emitted by capacitor discharge cables in unipolar and bipolar configurations are compared in the following sections. Power spectrum is calculated by Welch's method of spectral density function [Welch, 1967]. Figures 5.11 and 5.12 show the radiated near field noise *E* and *H* in unipolar and bipolar flash lamp power supplies. It is to be noted that the near field noise emitted in bipolar power supply is 2-10 dB higher than those emitted by unipolar configuration. Difference in resonance frequencies in unipolar and bipolar configurations is because of increase in cable length and introduction of extra impedance discontinuities in the second case. Far field is measured by two different types of antennas. A Bi-conical antenna is used in the frequency range 20 MHz to 300 MHz and a dipole antenna is used in the frequency range 330 MHz to 1 GHz. Antennas are placed at a distance of 1 m from the radiating cable. Far field measurement results for unipolar and bipolar supplies are shown in Figures 5.13 and 5.14. In lower frequency range 20 MHz to 300 MHz, difference in far field emissions for unipolar and bipolar supplies is not very significant. Whereas, in higher frequency range i.e. between 330 MHz to 1 GHz difference in emission is of the order of 30 dB.

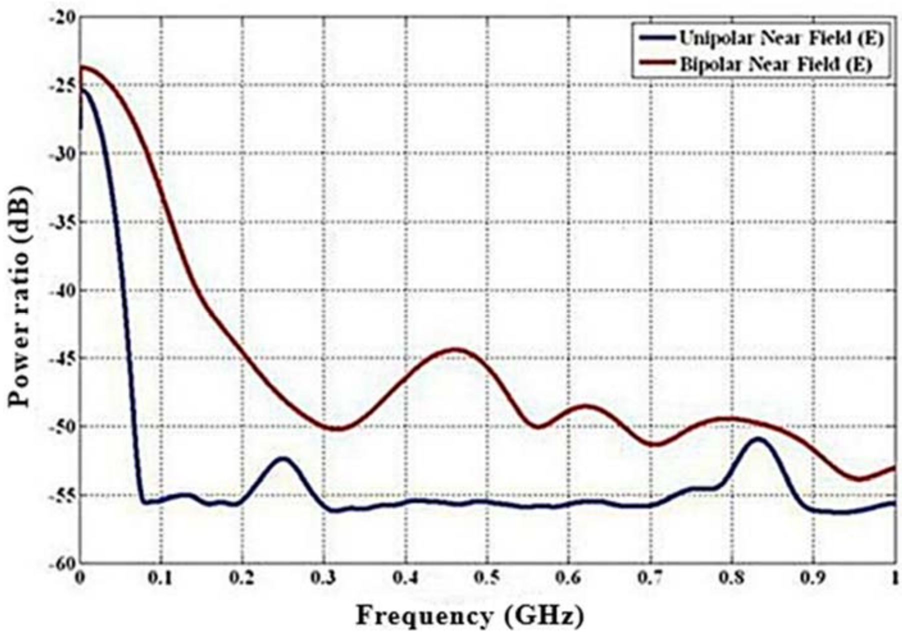

Figure 5.11: Near field E for unipolar and bipolar configurations

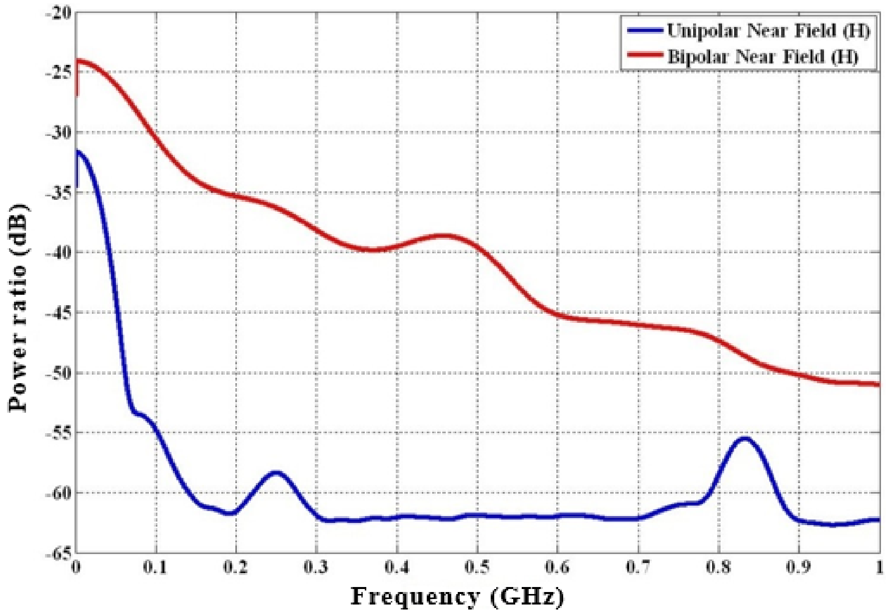

Figure 5.12: Near field H for unipolar and bipolar configurations

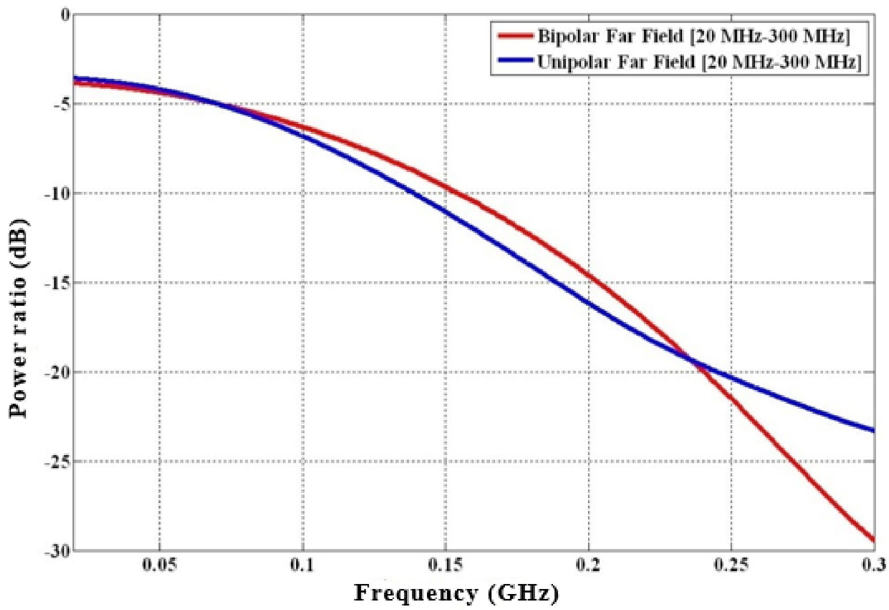

Figure 5.13: Far field measurement [20 - 300 MHz] unipolar and bipolar configurations

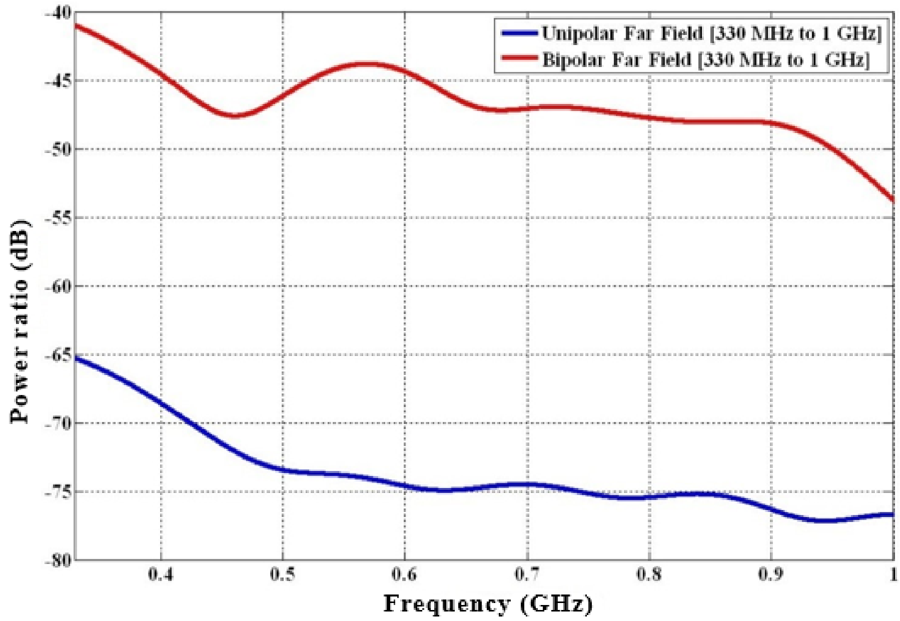

Figure 5.14: Far field measurement [330 MHz - 1 GHz] unipolar and bipolar configurations

5.4.3 EMI from single core and co-axial cables

Figures 5.15 and 5.16 show the near field emissions under two different conditions i.e. when capacitor is discharged into flash lamp through a single core cable and secondly through a co-axial cable. In low frequency range (less than 200 MHz) near field shielding effectiveness of coaxial cable is lower. In the frequency range 200 MHz to 1 GHz, average attenuation of RG8 co-axial cable is 3 dB more than that for a single core cable. Figures 5.17 and 5.18 compare far field emissions from single core and coaxial cables in frequency ranges [20 - 300 MHz] and [330 MHz - 1 GHz] respectively. With reference to Figure 5.18, peak emission in co-axial cable is observed at around 580 MHz. This point marks resonance effects, which is a function of cable dimensions. Cables of length 1 to 2 m are selected for these observations.

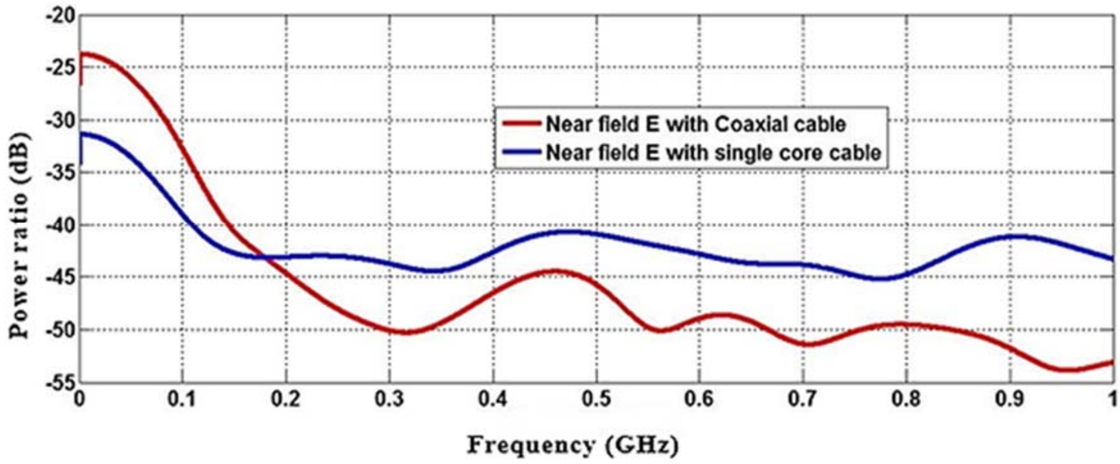

Figure 5.15: Near field E with single core and coaxial cable

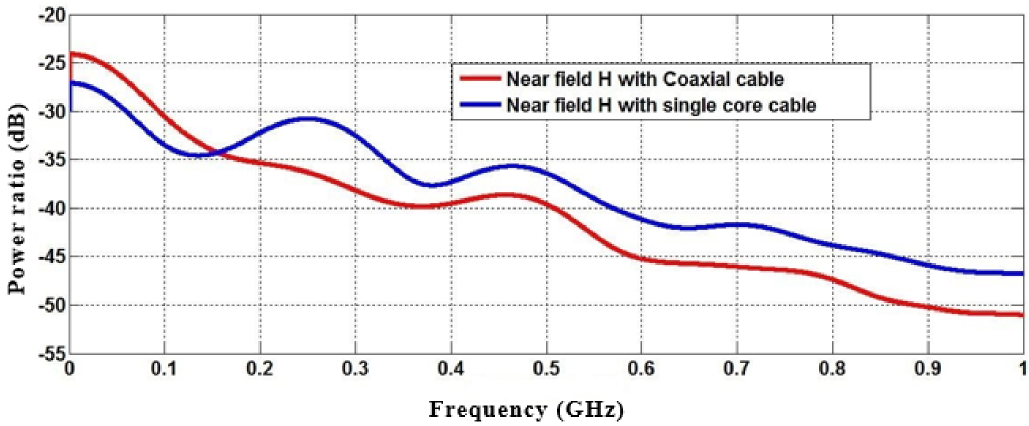

Figure 5.16: Near field H with single core and coaxial cable

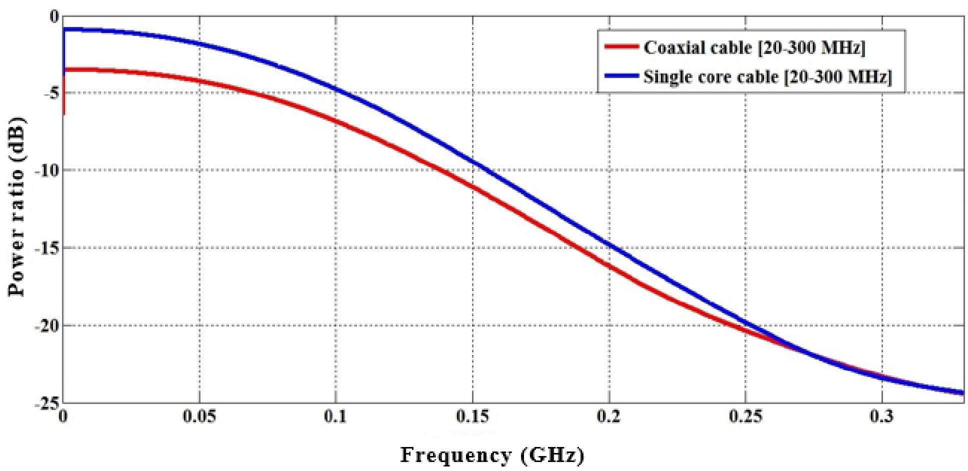

Figure 5.17: Far field measurements [20 - 300 MHz] single core and coaxial cable

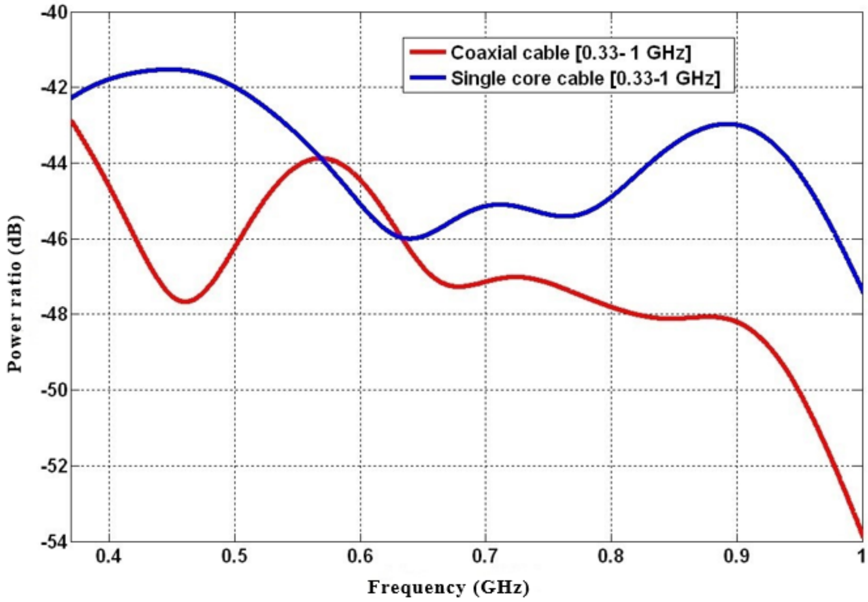

Figure 5.18: Far field measurements [330 MHz -1 GHz] single core and coaxial cable

Conducted emissions in flash lamp power supplies were measured over frequency range 150 kHz to 30 MHz, as per CISPR 22 standards [CISPR, 1997]. Conducted emission test setup includes a line impedance stabilization network which is placed between AC power and power supply circuit. Measured values of line conducted noise in bipolar and unipolar supplies are shown in Figure 5.19. Noise generated by bipolar supply is about 30 dB higher as compared to unipolar supply.

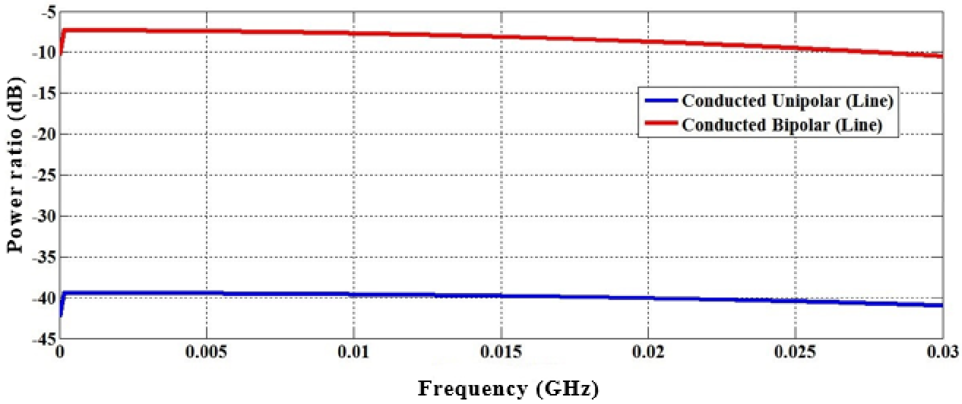

Figure 5.19: Conducted EMI in unipolar and bipolar power supply configurations

Conducted emission measurements were also carried out with a shielded co-axial cable and a pair of single core cables. Figure 5.20 compares conducted EMI in a coaxial and single core cable. Average reduction of conducted noise due to co-axial cable is of the order of 2 dB.

5.4.4 EMI from Faraday isolator power supplies

Faraday isolator stage in the laser chain consists of a solenoid for generation of pulsed magnetic field. Capacitor banks are discharged through a SCR into Faraday coil resulting into a half-sinusoid current pulse as shown in Figure 5.21. For analysis of radiated emissions, the forward current I_1 and the return current I_2 are resolved in terms of common and differential modes I_c and I_d respectively. Differential and common mode currents are estimated in terms of measured values of I_1 and I_2 as $I_d = (I_1 - I_2)/2$ and $I_c = (I_1 + I_2)/2$. Cable layout with respect to the ground plane is represented in Figure 5.22. Cables I and II are forward and return multi-strand conductors for the Faraday coil (load). Cross sectional area of the cable is 1.7 sq mm and approximate length is 5 m. These are laid 10 cm apart at a height of 5 cm from the ground conductor which is made up of 20 mm wide copper strip.

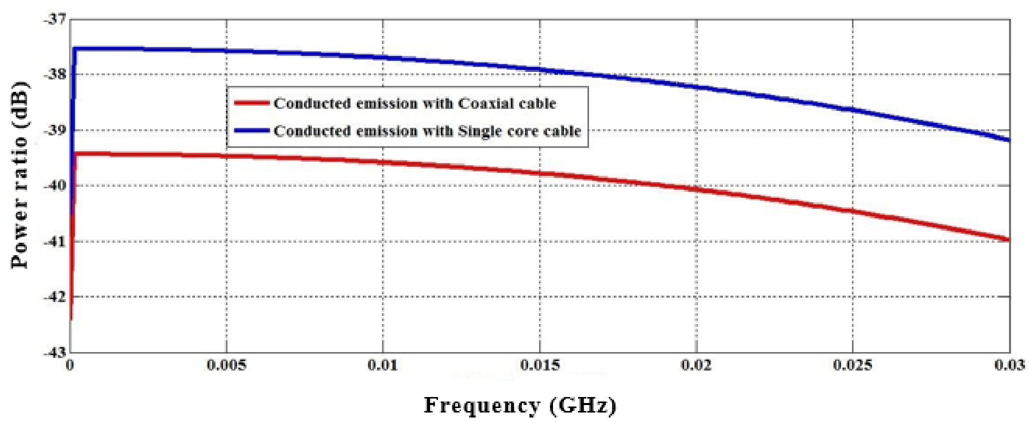

Figure 5.20: Conducted EMI in single core and coaxial cable

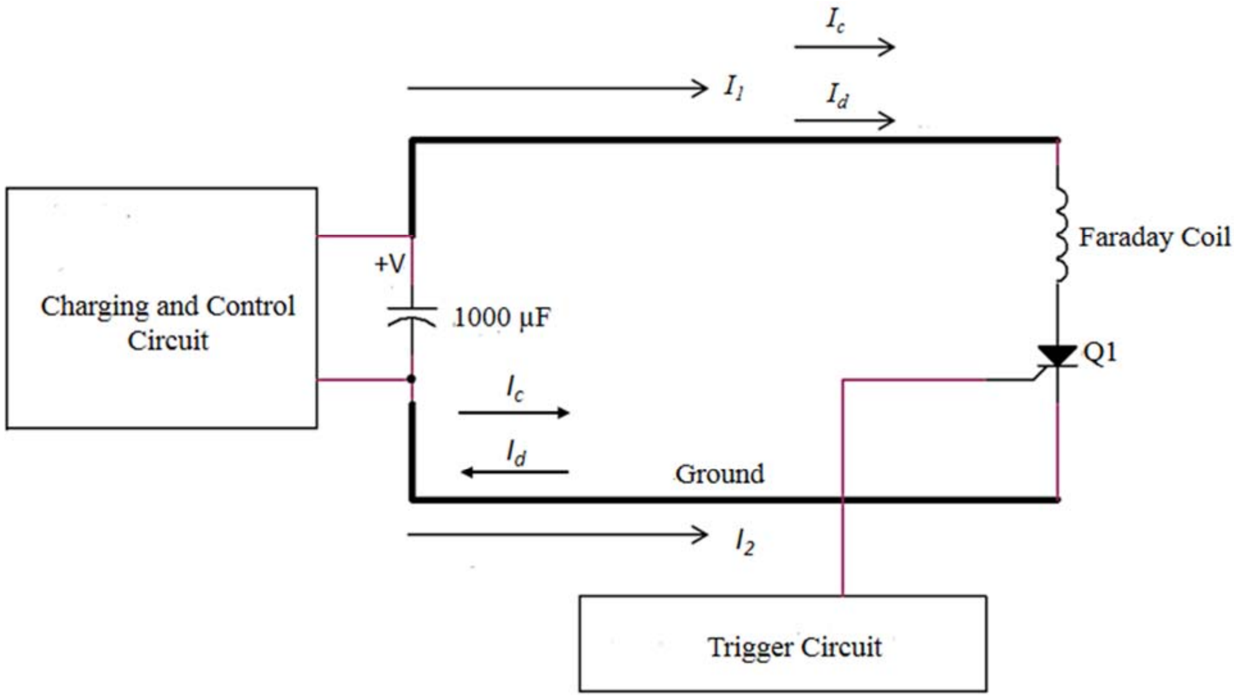

Figure 5.21: Currents in Faraday isolator PFN

$$I_1 = I_c + I_d \tag{5.14}$$
$$I_2 = I_c - I_d \tag{5.15}$$

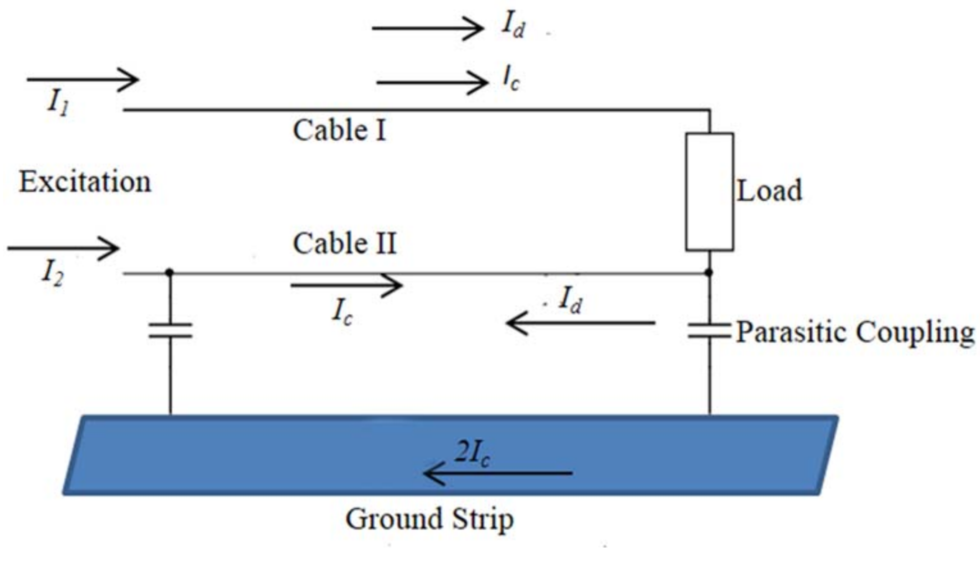

Figure 5.22: Faraday isolator power supply layout

Common mode current $2I_c$ flows in ground strip through parasitic capacitive coupling.

Measured values of differential and common mode currents are shown in figure 5.23.

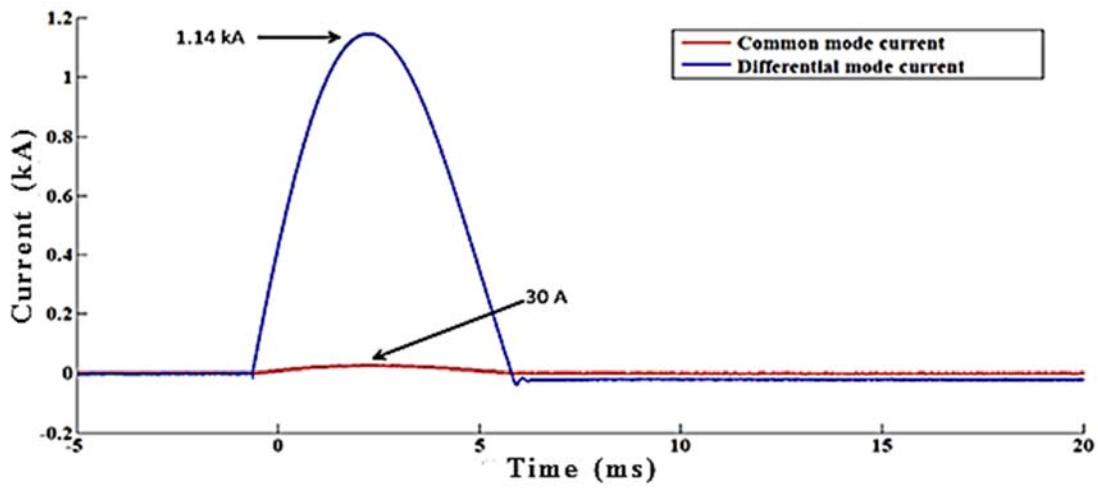

Figure 5.23: Common mode and differential mode currents due to Faraday coil excitation

Near region E and H fields in proximity to Faraday isolator discharge cable are shown below in Figure 5.24.

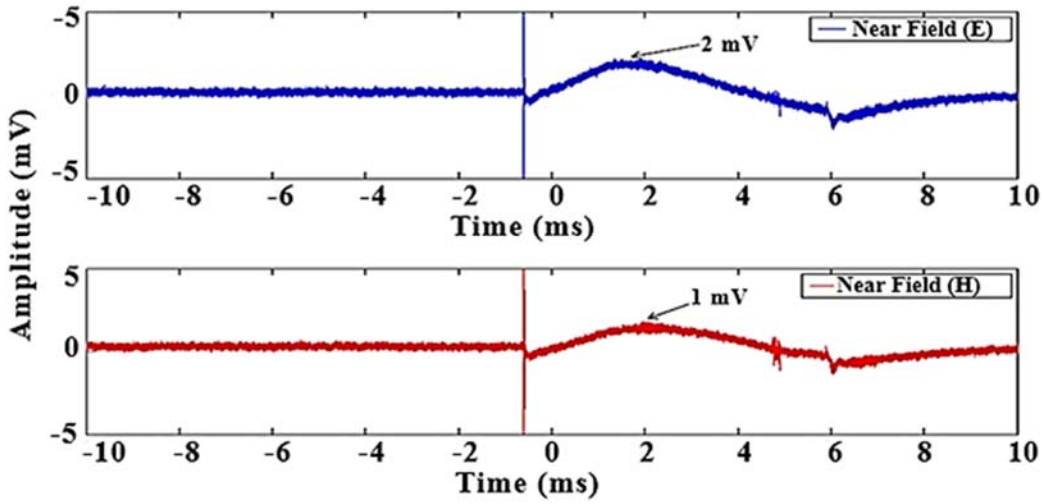

Figure 5.24: Near field (*E* and *H*) in Faraday isolator network

Dipole and bi-conical antennas of bandwidth 20 MHz to 1 GHz were used for far field measurements. Figure 5.25 shows the result of far field measurements at a distance of 1m from the discharge cable.

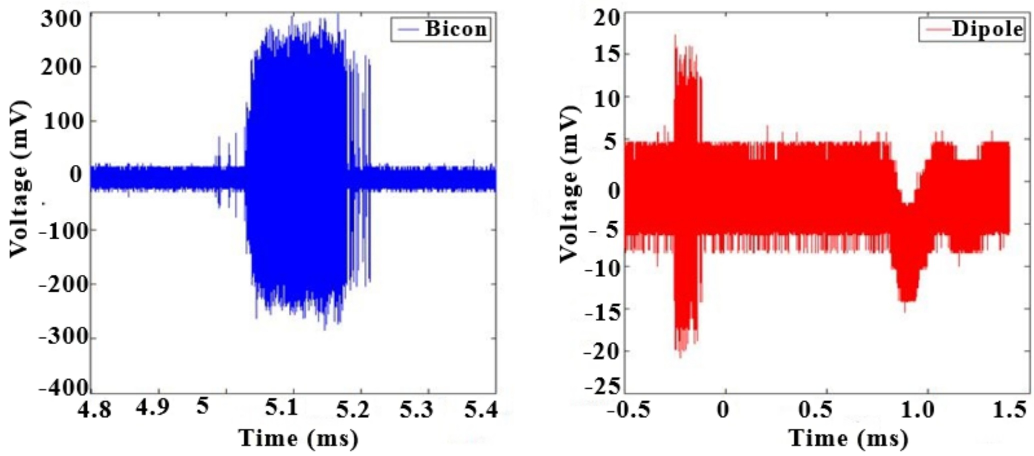

Figure 5.25: Far field emission measurement in Faraday isolator network

Far field measurements as shown above estimate the frequency components of radiated emission from Faraday isolator power supply. Radiated emission is due to triggering of SCR and due to long conductors (> 3 m) carrying pulsed current for Faraday coil. It is observed that the dominant portion of radiated emission lies in the frequency range 300 MHz to 1 GHz. It also indicates a large value of common mode current flowing through ground plane due to parasitic capacitance.

5.5 Summary and conclusion

This chapter presents characterization of near and far field emissions from flash lamp and Faraday isolator pulsed power supply circuits. The investigations are based on analytical formulation and measurement results. Flash lamp power supply consists of a 300 µF capacitor bank which is charged to maximum voltage of 5 kV. A high voltage trigger signal results into controlled discharge of capacitor bank through a flash lamp. Peak amplitude and width of the current pulse are of the order of 3 kA and 600 µs respectively. Main discharge current is preceded by a high voltage flash lamp trigger pulse. Interferences from two different flash lamp power supply configurations namely unipolar and bipolar are compared. Faraday isolator configuration consists of a capacitor bank of 1000 μF discharged through a coil of 4 mH to generate a pulsed magnetic field. Discharge process in Faraday isolator coil is initiated by triggering of silicon controlled rectifier. Current shape is half sinusoid of 1. 2 kA peak amplitude and pulse width of 6 ms. Trigger voltage for flash lamps, firing of SCR, flash lamp discharge currents and impedance discontinuities due to interconnects result into radiated and conducted emissions. Interference voltage due to differential and common mode currents in discharge cables for flash lamps and Faraday isolator coil are separately analyzed and compared with measured values. Radiated emission loss is strongly dependent on cable construction and layouts. Bend angles introduce parasitic inductance and capacitance in transmission lines. This effect is quantified for the types of cables and wires used in the laser units with *S* parameter measurements. Co-axial cables exhibit narrow band resonance effects, where shielding effectiveness of cable sheath deteriorates resulting into increased emission. Results of the analysis and measurements presented in this chapter have provided systematic insight into the phenomenon of generation of electromagnetic interference. Chapter 6 looks into time-frequency analysis of the interference signals from different sources in the table top terawatt laser setup.

Chapter 6

Signal integrity and noise analysis in table top terawatt laser

Table top terawatt laser system is a compact unit with power supplies, trigger circuits, cables and interconnects located in close proximity. Some of the stages are activated earlier and generate interfering fields which interact with nearby cables and affect set delays and timing parameters of trigger signals for later stages. Extent of field interaction and consequent signal distortions depend on a number of factors like shielding effectiveness of metallic enclosures housing critical components, EM field leakage from cables due to finite transfer impedances, cable layout and terminations. The TTT laser system has a free running oscillator operating at 100 MHz with a synchronous clock which is carried through a 3 m long shielded co-axial cable to synchronization and delay circuits. Trigger signals for later stages of the laser unit consisting of pulse selector, injector and ejector circuits in regenerative amplifier are generated in synchronization with the clock signal. Functional requirement of delay between Pockels cell driver circuits in injector and ejector stages in regenerative amplifier varies from 5 to 800 ns. Interaction with EMI generated fields introduce jitter in the set value of delays which alters the laser gain stability. Following sections discuss the results of development of a low jitter (~800 ps) delay circuit and its performance under radiated emission. Timing jitter under transient field for emitter coupled ICs having differential I/Os are found to be lower than for ICs with CMOS logic family. This is despite the fact that ECL family ICs have low noise margin.

The classical technique of time domain noise measurements followed by Fourier transform analysis is not adequate to correlate noise spectrum with specific noise sources or the time instants in this type of a multi stage system as it loses time information. Relatively new technique of wavelet transform, as described earlier in chapter 3 is applied to determine time-frequency relationship of the noise emission and to identify the sources of interference. There are numerous research papers on application of wavelet transform and its variants to analyze EMI in switched mode power supplies, electrostatic discharges etc. [Coppola, 2005]. However, no significant work is reported on application of wavelet transform for noise analysis in high power laser systems, which contain multiple noise emitters triggered at different instants of time. In this work, electromagnetic noise emitted by flash lamp trigger circuits and high voltage MOSFET switches in a terawatt laser is sampled in time domain by a digital oscilloscope. Wavelet transformation is applied on the sampled signal to generate time-frequency-intensity information. Electromagnetic interference analysis is carried out under following operating conditions.

a) Flash lamp trigger signal is followed by pulse selector event after an interval of around 360 μs. This in turn, is followed by pulse injector and pulse ejector triggers with an interval of 200 ns each. One round trip in the regenerative amplifier stage takes 10 ns. Thus, 200 ns delay means 20 round trips, which corresponds to power gain of 60 dB.
b) Flash lamp trigger signal is followed by a pulse selector trigger after 360 μs as in the first case above. However, time delays between pulse selector-injector and injector-ejector stages are set to 100 ns each. This corresponds to laser amplification gain factor of 30 dB.

6.1 Synchronization circuit in TTT laser chain

Table top terawatt laser system consists of a commercial mode locked laser oscillator operating at 100 MHz. Out of this train of laser pulses, one pulse is selected by a locally developed pulse selector stage. After a fixed delay the selected pulse is fed to a regenerative stage for amplification. Selected laser pulse makes several round trips in regenerative amplifier. It is ejected out after desired amplification is achieved. Laser pulse selection, its injection into the regenerative stage and ejection after amplifications are carried out by synchronized switching of Pockles cell. Electronics circuit for this task consists of a master trigger generator, which generates main trigger pulse in synchronization with the 100 MHz pulse train, a fixed delay generator for injection of selected pulse into regenerative amplifier stage and a variable delay generator which sets the delay corresponding to required number of round trips and gain.

From signal integrity perspective the important system requirements are,

a) To process 100 MHz clock train from laser oscillator and to generate a master trigger which is synchronized with the 100 MHz pulse train as well as a manually generated trigger signal.
b) Synchronized trigger signals should have lowest possible timing jitter and propagation delay.

The 100 MHz clock signal is carried through a shielded co-axial cable (RG 58) of 3 m length and terminated on both ends by 50 Ω characteristic impedance. Time domain measurements of clock signal and frequency spectrum of radiated emission at a distance of 1 meter are shown in Figures 6.1. It is a snap shot of spectrum analyzer display for frequency content of radiated emission from the TTT laser clock signal. Peak strength of the radiated emission at around 100 MHz is -60 dBm. The clock signal (100 MHz) is synchronized with laser pulses from oscillator section. It is used to select one single laser pulse for further amplification by laser amplifier stages. It is also used to generate low jitter trigger signals for the regenerative amplifier stage. A co-axial cable of approximately 5 m length carries the clock signal to the synchronization circuit. Spectrum analysis of the radiated field from cables carrying the clock signal gives an estimate of leakage from the cable and frequency-amplitude estimate of the noise expected near synchronization circuit. It is an important measurement considering the requirement of low jitter trigger signals to be generated from the synchronization circuit.

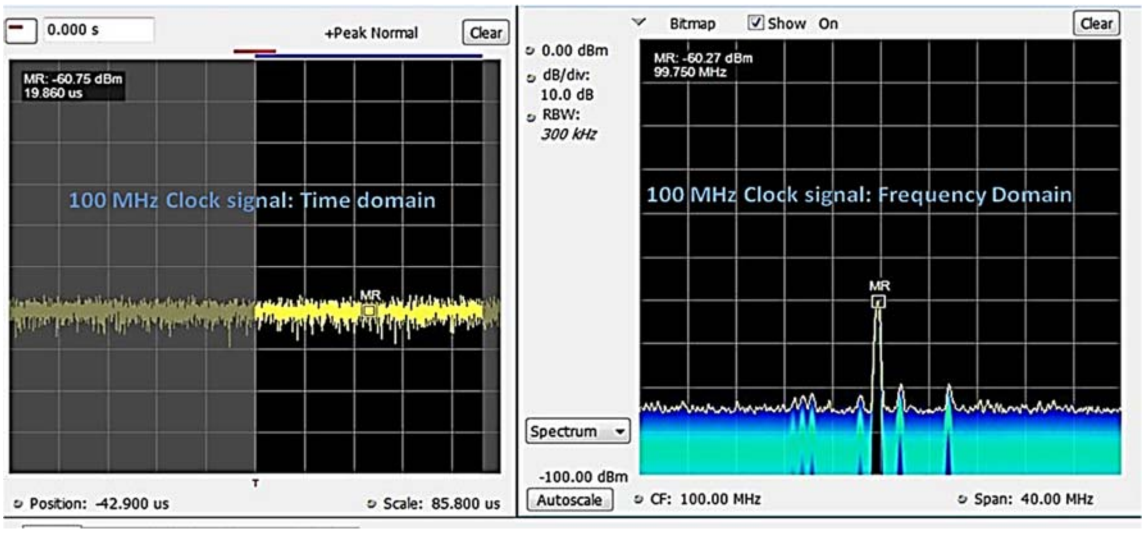

Figure 6.1: Snap shot of spectrum analyzer display of clock signal for laser pulse selection and synchronization

6.2 Pulse selector circuit and delay generator

Pulse selector circuit generates a trigger signal, which is synchronized with 100 MHz clock and with a trigger pulse, which is generated manually through external control system. Emitter coupled logic ICs with propagation delay of the order of picosecond are used for selector circuit to process 100 MHz clock signal. This family of ICs has differential output signals with capability to drive longer cables and maintain signal integrity. Schematic and other details of the pulse selector circuit and the delay generator are provided in appendix A. To maintain a fixed gain by the regenerative amplifier and thereby to ensure stability in laser energy, it is essential that the number of round trips in the regenerative amplifier remains constant for a particular setting. It means that jitter in delay between the pulse injection and ejection should be negligible. Several dedicated delay generator ICs and circuits based on mono-shots were investigated to design a low jitter delay stage. In most of the dedicated digitally programmable delay generator ICs, delay is set as input bits of a digital to analog converter section. These ICs have precision linear ramp generator whose slope is set by an external network of resistor and capacitor. Ramp generator signal is compared with DAC output to generate a fixed delay. Delay error or jitter is dependent on linearity and stability of ramp generator, which depends on tolerance and precision of external components namely resistance R and capacitance C. Full scale delay range for these ICs depends on values of the components and to achieve maximum delay, RC time constant is to be increased. Stability of the slope of ramp signal deteriorates at higher values of delay range i.e. at higher values of components. On the other hand, delay generators built around discrete mono-shots with ECL ICs show considerably improved performance in terms of the delay jitter. Figure 6.2 shows oscilloscope trace for measurement of delay jitter of 2.24 ns for the set delay of 800 ns for the designed programmable delay generator [Ansari, 2006]. Channel 2 shows the trace of delayed pulse with oscilloscope put in persistence display mode. It is delayed with respect to a trigger signal on channel 1. The low jitter value is achieved with tighter tolerance of resistors (0.5% Metal Film) and capacitors (1% Film). Timing jitter improved considerably for delay circuit implemented with a discrete mono-shot MC10198 [MECL, 1993]. It is to be noted that the type of passive components (R and C) are of same tolerances as used with earlier circuits. Circuit diagram of delay generator designed with discrete ECL ICs and the corresponding timing jitter in set delay are shown in Figures 6.3 and 6.4 respectively. Jitter in time delay is measured by measuring thickness of trace on channel 2 for the oscilloscope set under persistence display mode.

The oscilloscope is set in NORM trigger mode to be triggered by a signal on channel 1. Delay *Td* is determined by pulse width of signal *B* generated at output *Q* of the first mono-shot. Peak jitter in set delay reduces to 800 ps, which results into stable gain in regenerative amplifier stage and improvement in laser beam quality.

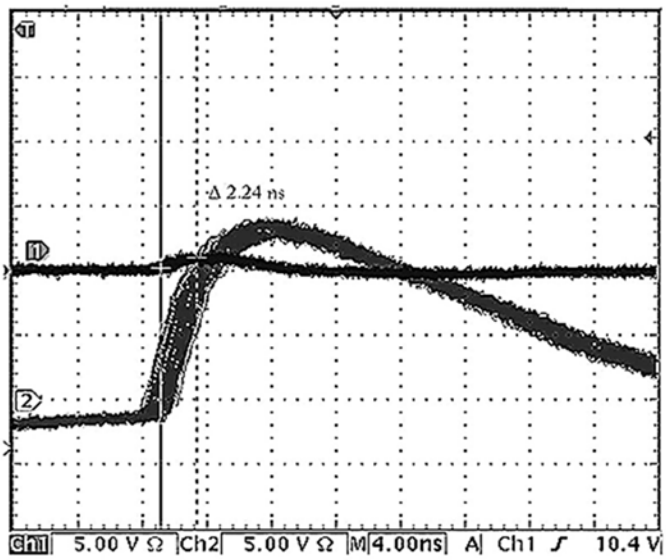

Figure 6.2: Timing jitter for programmable delay generator

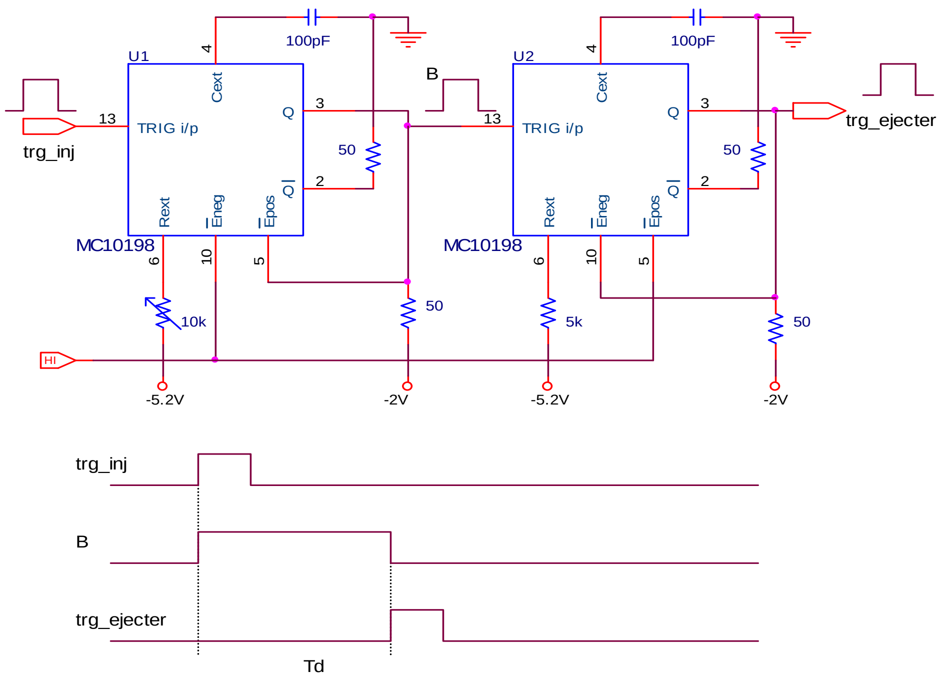

Figure 6.3: Delay generator based on ECL mono-shot

6.3 Time domain EMI measurements in TTT laser system

Table top terawatt laser unit selects a single laser pulse from a free running 100 MHz oscillator and amplifies the selected pulse in single shot operation mode. Complete cycle of pulse selection, injection, amplification and pulse ejection takes place in around 600 μs. Interference noise generated by various components in laser system is transient in nature and occurs at different instants of time. Flash lamp power supplies and high voltage drivers for electro-optical switches generate random and non-stationary interference signals. Time domain measurement is most suitable measurement technique for this type of interference signal. Data obtained by time domain measurements is digitized by high sampling rate ADC, usually a part of digital storage oscilloscope.

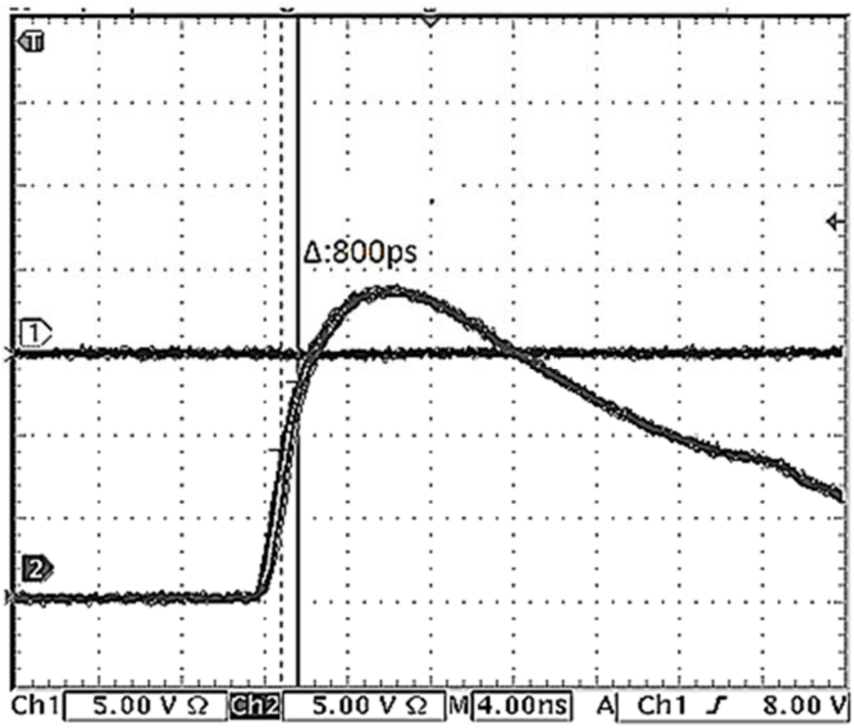

Figure 6.4: Timing jitter for delay generator based on ECL mono-shot

Traditionally, the frequency information of the measured signal is extracted by Fourier transform on post storage data [Braun, 2006]. Set up for a time domain measurement system for transient electromagnetic noise is shown in Figure 6.5. Measurement of transient electromagnetic pulses needs broad band antennas to cover entire frequency spectrum. Results presented in following sections are based on measurements by a dipole and a bi-conical antenna. Together these antennas cover maximum frequency up-to 1 GHz. Physical layout of main sources of EMI (i.e. the regenerative amplifier, pulse selector switch, pulse injector switch and pulse ejector switch) of the table top terawatt laser is shown in Figure 6.6. Figure 6.7 shows measurement setup for radiated EMI. A calibrated bi-conical antenna is used to measure the radiated emission. Measured signal is sampled by a digital storage oscilloscope with a sampling rate of 10^{10} samples per second. Mathematical techniques like FFT and wavelet decomposition can be applied on sampled data for frequency domain conversion and analysis. Wavelet based analysis described in following section, extracts time information of interference signal from various laser components as well as the respective frequency contents.

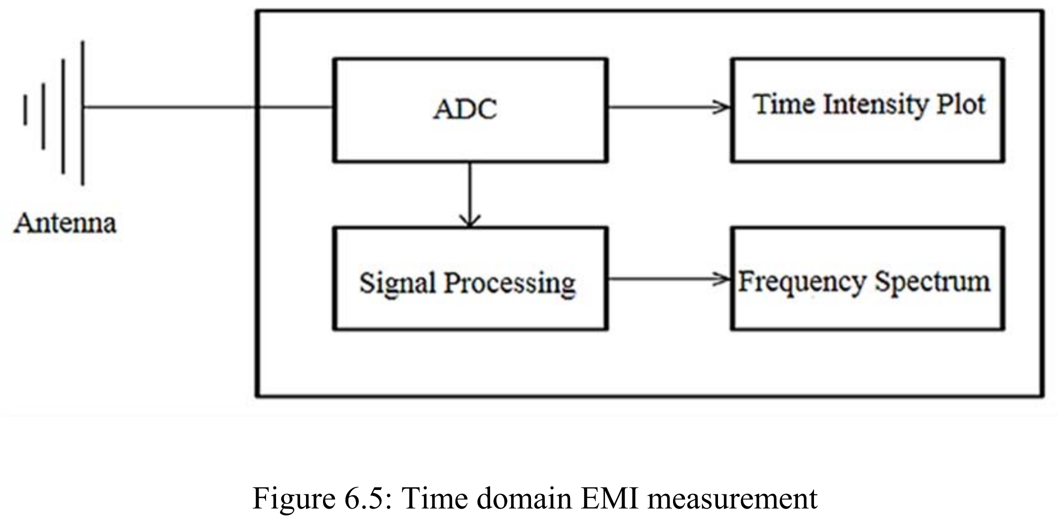

Figure 6.5: Time domain EMI measurement

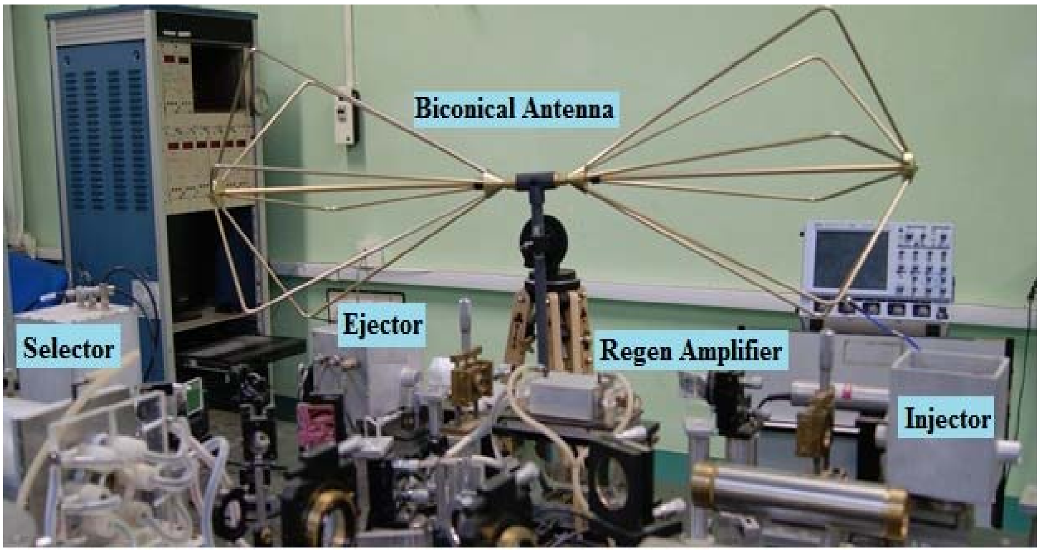

Figure 6.6: Photograph of bi-conical antenna and table top terawatt laser

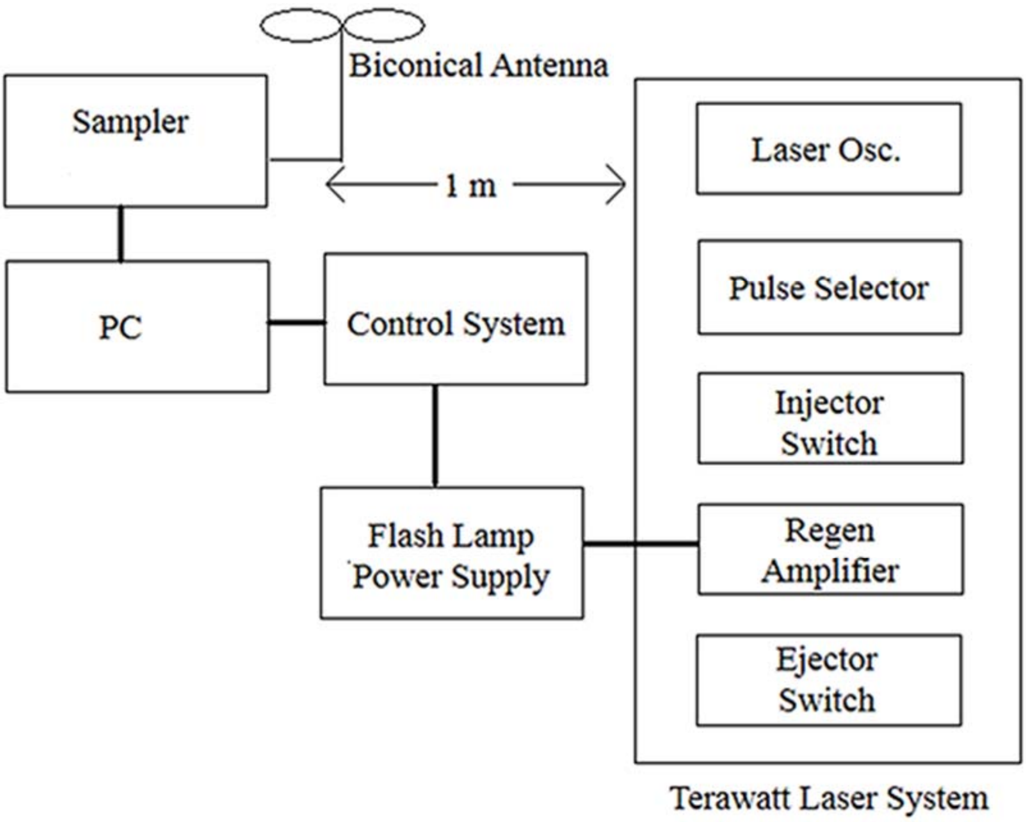

Figure 6.7: EMI measurement setup for TTT laser chain

Table top terawatt laser operation cycle starts with charging of energy storage capacitor banks of regenerative amplifier power supply and triggering of flash lamps to initiate gain build up in the amplifier stage. Timing diagram of the operation sequence is shown in Figure 6.8. Time instant *A* marked on the diagram shows triggering of flash lamps with a high voltage (10 kV) signal of 5 µs duration. Weak arc discharge through flash lamp during initial high voltage trigger signal generates a damped oscillatory current as shown in Figure 6.9. This event initiates discharge of energy stored in power supply capacitor banks through the flash lamps. Main discharge current through flash lamp is shown in Figure 6.10. Time instant *B* represents triggering of Pockels cell in laser pulse selector stage by switching a high voltage (~ 3 kV) and fast rise time (~ 5 ns) solid state (MOSFET) device. This instant coincides with peak of the flash lamp current and also marks the first burst of high frequency interfering signal due to activation of high voltage, high speed solid state switch.

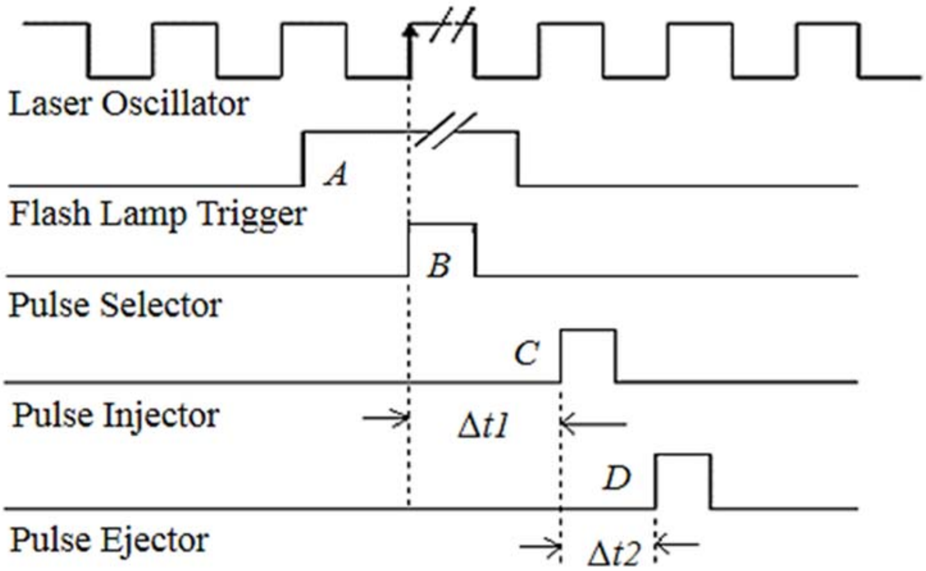

Figure 6.8: Timing diagram of laser trigger signals

Instant *C* indicates switching of Pockels cell in the laser pulse injector stage with a high voltage step switch. The switch at this stage has fast initial rise time of the order of 5 ns and slow fall time of the order of 100 µs. It is because of the slow fall time that this switch is referred to as a step switch. Point *D* refers to switching of Pockels cell by a pulsed type of high voltage switch for laser ejector stage. The high voltage switch at this stage has nanosecond switching for both rising and falling edges. There are specified set delays marked by *Δt1* and *Δt2* between triggering of these switches. Initial high voltage flash lamp trigger signal is a strong source of radiated electromagnetic interference. Pulse selector circuit in the laser chain is activated after the flash lamp trigger signal to coincide with peak of the amplifier gain. Each of these events is accompanied by radiated noise of varying magnitude and frequency.

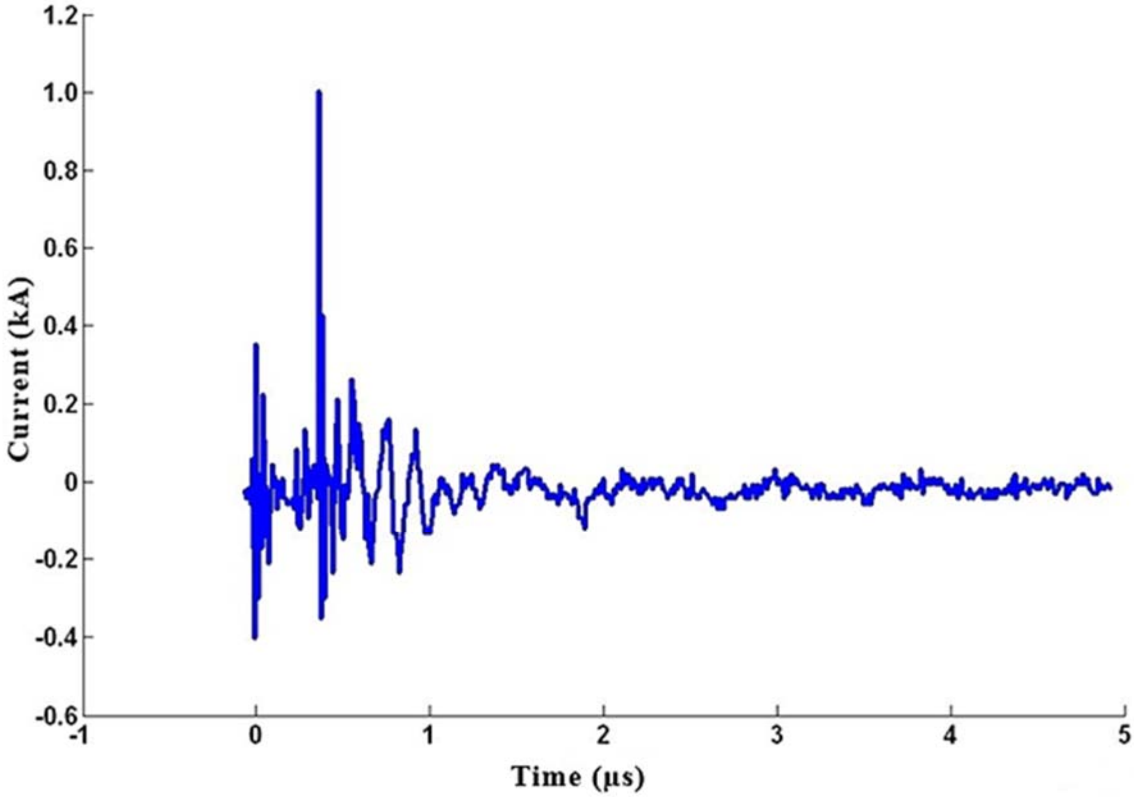

Figure 6.9: Flash lamp trigger current

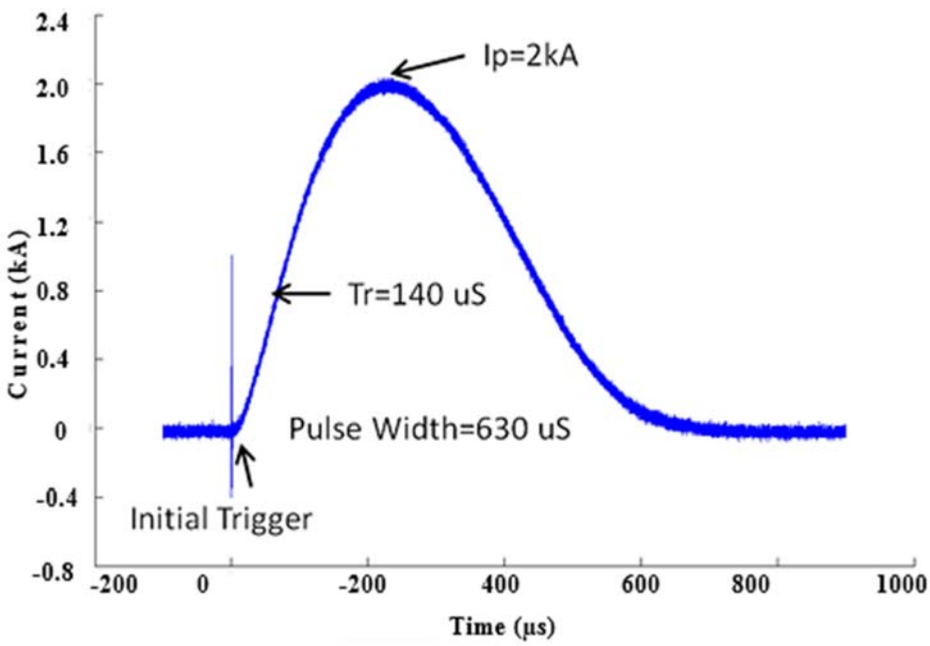

Figure 6.10: Flash lamp main discharge current

Figure 6.11 shows far field radiated electromagnetic interference measurement in time domain. It is generated by triggering of a flash lamp and switching of three high voltage MOSFET devices at different instants. It is to be noted that there is no main discharge of the flash lamp current. Triggering of MOSFET switches are time separated by 100 to 200 ns. Instant *A* marked on the diagram represents switching of SCR and electromechanical relays for flash lamp trigger generation circuits. Instants *B, C*, *D* and *E* marks the onset of flash lamp arc discharge and operation of three high voltage Pockels cell drivers in sequence.

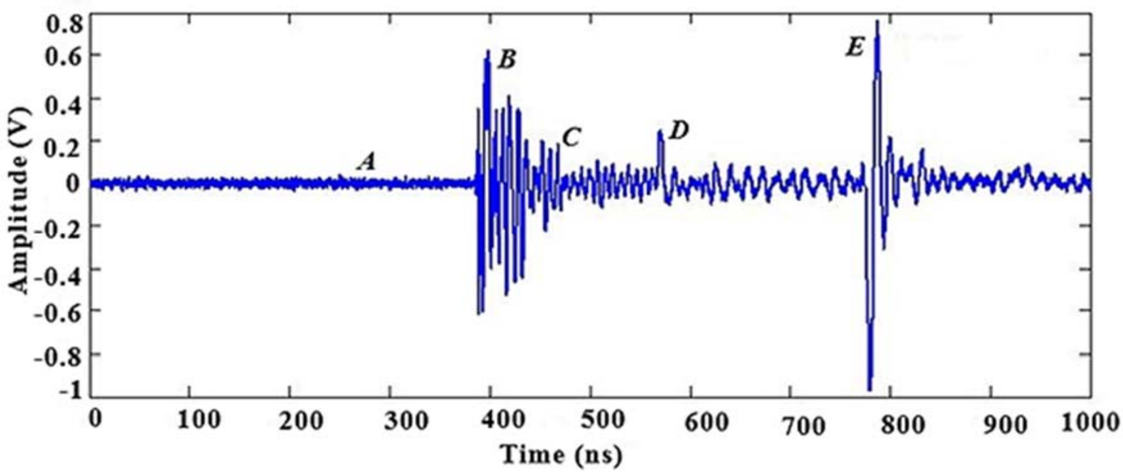

Figure 6.11: Radiated interference due to flash lamp trigger and Pockels cell drivers

6.4 Time-frequency analysis of EMI in TTT laser

The table top terawatt (TTT) laser unit has multiple sources of electromagnetic noise emitter such as fast rise time switching of high voltage semiconductor devices, flash lamp pre-ionization by high voltage trigger pulse, flash lamp main discharge current, operation of Faraday isolator coil and operation of high voltage relays. Each of these processes and components has distinct time and frequency features of electromagnetic noise emission. However, overall the system noise consists of transient impulse and oscillatory components with multiple sharp peaks. Figure 6.12 shows Fourier transform of the noise signal. It is to be noted that the signal is non-stationary in terms of frequency content and Fourier transform does not provide information on time evolution of the frequency components.

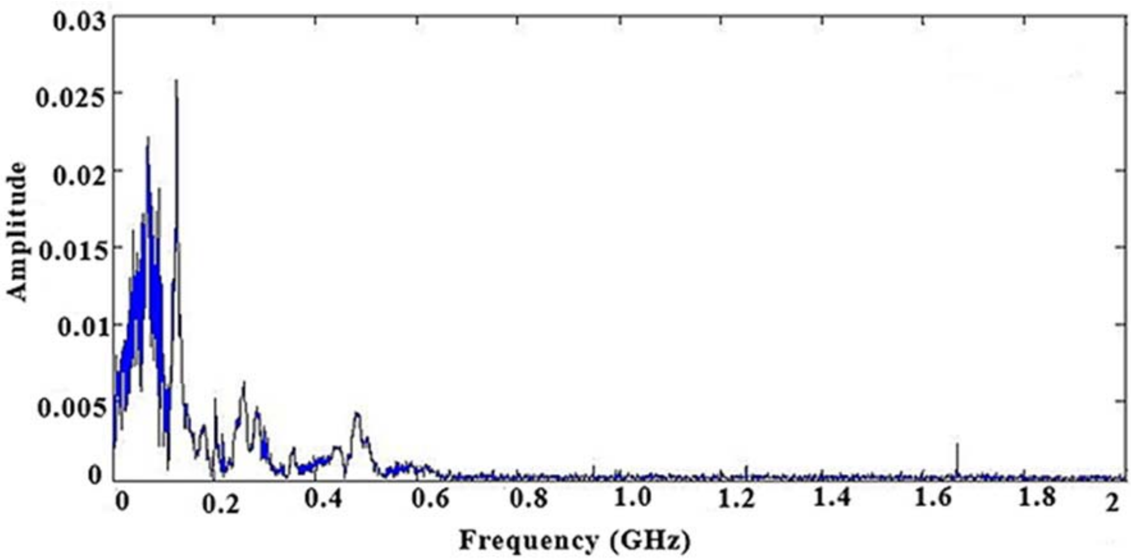

Figure 6.12: FFT of radiated interference from flash lamp trigger and Pockels cell drivers

From noise mitigation point of view it is imperative that a time-frequency analysis is carried out for the interfering signal. Algorithms based on time window convolution such as short time Fourier transform (STFT) and wavelet transform are appropriate tools for time-frequency analysis of this category of signals. Figure 6.13 shows short time Fourier transform of the noise signal. The STFT is based on Gaussian window. Width of the STFT window is 1, 10 and 100 ns respectively with 50 percent data overlap in each case. It is observed that low frequency components occurring between 600 to 700 ns duration are better resolved by larger window size of 100 ns. High peak of noise signal of 200 to 300 MHz frequency is observed at around 400 to 500 ns. Inherent drawback of STFT in terms of poor frequency resolution when analyzed with shorter time width window is obvious in this analysis. Wavelet transformation is more suitable technique to find out time evolution of frequency bands present in this type of noise signal. Starting point of a wavelet transformation based analysis is estimation of frequency components in the signal and selection of an appropriate wavelet function. There are several functions which meet the wavelet admissibility criteria. Selection of a wavelet functions for an application is primarily guided by the characteristics of orthogonality, symmetry, and compact support [Daubechies, 1992]. It also depends on optimum correlation with the signal under observation. An orthogonal wavelet is suitable for signal decomposition into non-overlapping frequecncy bands. Symmerty property is useful for linear phase filter design. Haar wavelet function is suitable for signal edge detection especially in image processing application. Wavelets with compact support and vanishing moments are more efficient to represent signals that have localized features such as power supply transients [Safavian, 2005].

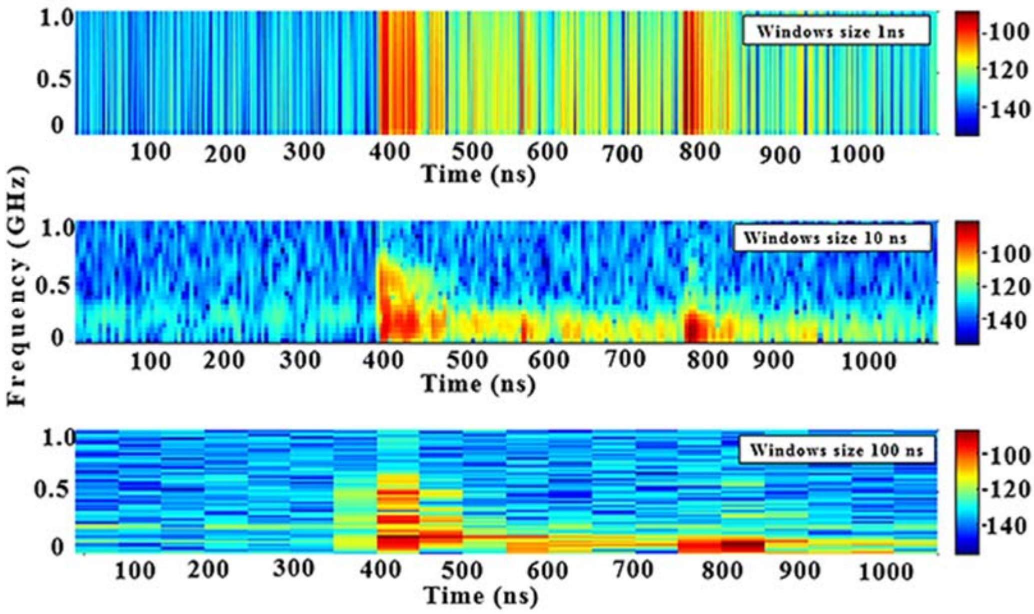

Figure 6.13: STFT of flash lamp trigger and Pockels cell driver noise

Daubechies wavelet function 4 (db4) is suitable for analysis of transients in power supply systems [Gargoom, 2004]. Morlet wavelet function, which is Gaussian modulated sine wave matches with oscillatory nature of the electromagnetic noise signals. Furthermore, it provides finer resolution in time and scale. Daubechies wavelet 4 and Morlet wavelet functions are used for analysis of transients in power supply systems [Gargoom, 2004], [Huang, 1999]. Daubechies and Morlet wavelet functions are chosen in this work due to better correlation with the type of EMI signals dealt in this work. Discrete wavelet transformation analysis based on Daubechies 2 (db2) and Daubechies 4 (db4) functions are carried out for the time-frequency analysis.

Discrete wavelet transform decomposes the signal in approximation and detail coefficients corresponding to sub-band low and high pass filtering. For n level decomposition the frequency bands for approximation (An) and detail (Dn) coefficients are given by $\left[0, \frac{f_s}{2^{n+1}}\right]$ and $\left[\frac{f_s}{2^{n+1}}, \frac{f_s}{2^n}\right]$ respectively. Where f_s is the sampling frequency. Sampling rate for the time domain measurement shown in Figure 6.11 is 10^{10} samples per second. Frequency bands corresponding to four level DWT approximation and detail coefficients at this sampling rate are shown in Table 6.1.

Table 6.1 Wavelet coefficients frequency bands

Wavelet Coefficients	**Frequency**
A1	0 to 5 GHz
A4	0 to 312.5 MHz
D1	2.5 to 5 GHz
D2	1.25 to 2.5 GHz
D3	625 MHz to 1.25 GHz
D4	312.5 to 625 MHz

Figures 6.14 and 6.15 show decomposition of the noise signal by Daubechies wavelet functions of order 4 and 2 respectively. An approach based on minimum error between the original and reconstructed signal is adopted to judge suitability of a wavelet function. Reconstruction is carried out with the help of approximate and detail coefficients generated by discrete wavelet transformation. Figure 6.16 shows

reconstructed signals from the db4 and db2 functions. Figure 6.17 shows the absolute error between reconstructed and the original signal.

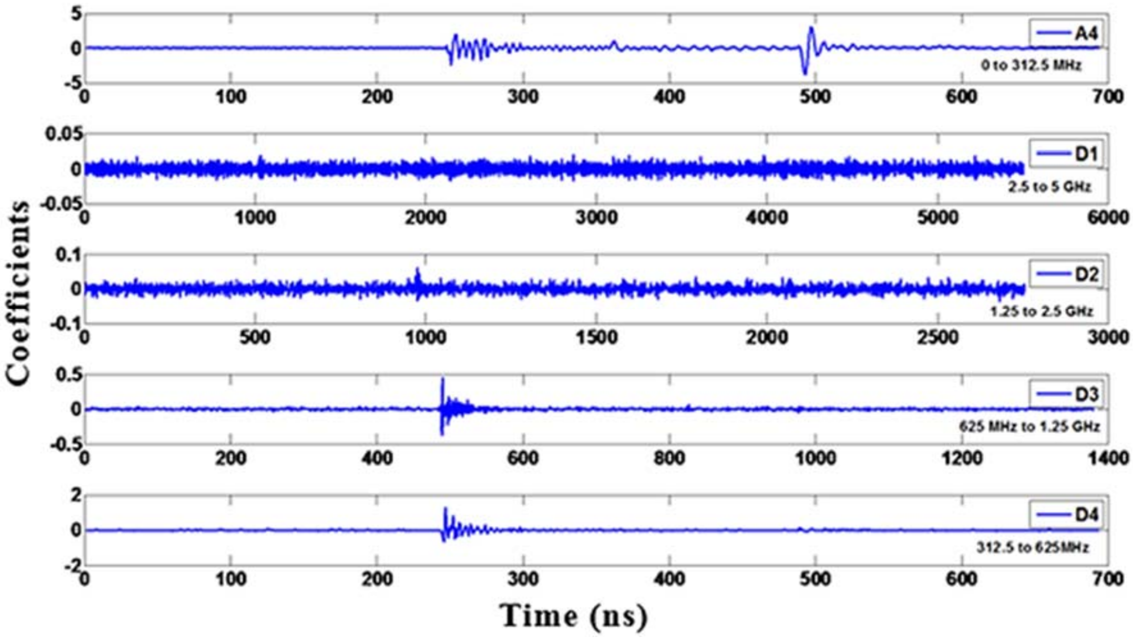

Figure 6.14: Approximation and detail coefficients for DWT with db4 function

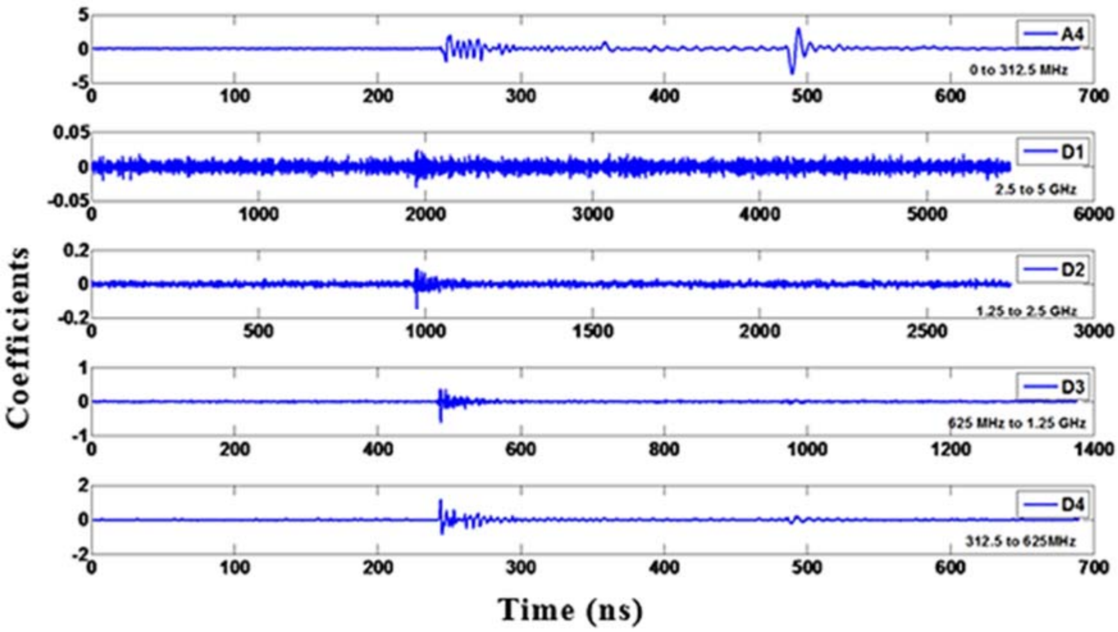

Figure 6.15: Approximation and detail coefficients for DWT with db2 function

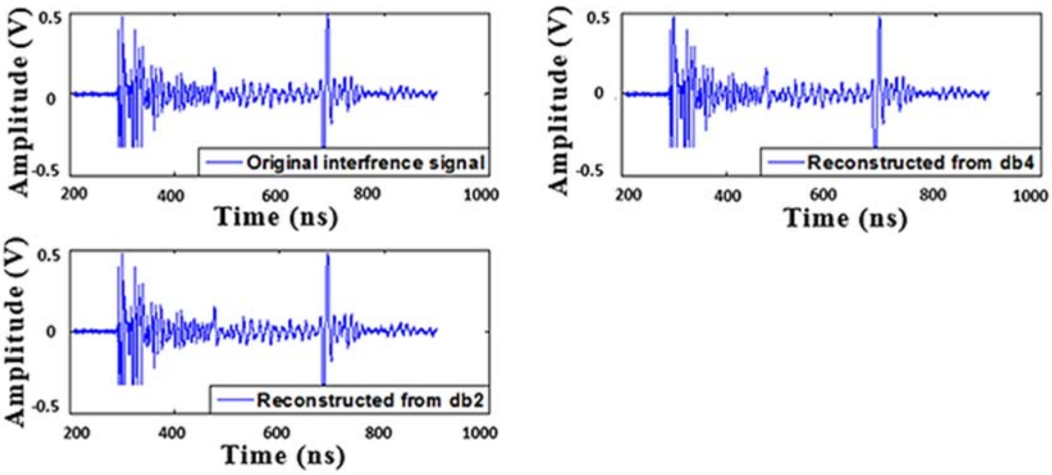

Figure 6.16: Interference signal reconstructed from db4 and db2 coefficients

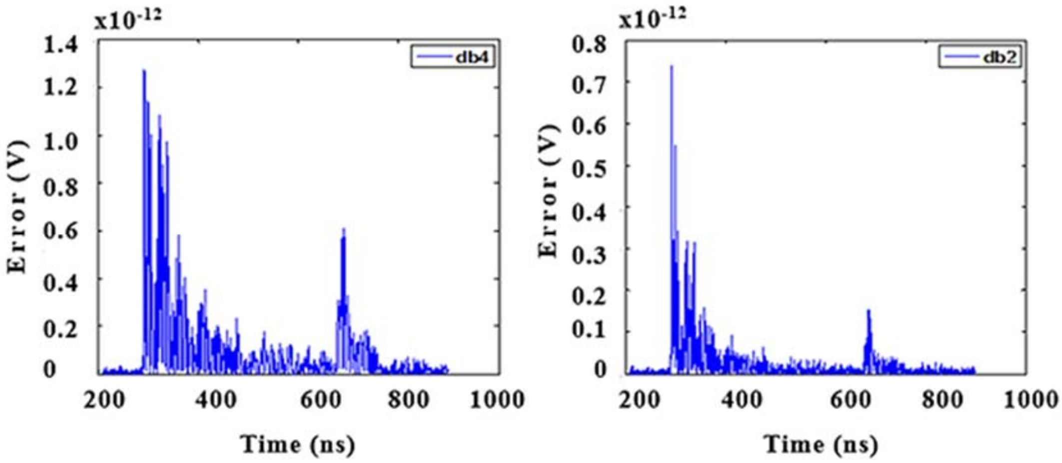

Figure 6.17: Error between original and signal reconstructed with db4 and db2 functions

It is to be noted that error between original and reconstructed waveforms is relatively lesser for Daubechies wavelet function of order 2 (db2) as compared to Daubechies wavelet function of order 4 (db4).

The noise signal is also analysed with continuous wavelet transform based on db2 and Morlet functions. Spectrogram and scalogram of the noise signal are generated with continuous wavelet transformation based on these two functions. Spectrogram is a plot between wavelet scales-time and intensity. Scalogram of a wavelet transform represents energy distribution of the signal in time-scale plane in terms of percentage energy for each coefficient. Mathematically it is defined as mean of the squared wavelet coefficients ($W_{j,k}$) computed over the data samples i.e. $\frac{1}{n_j}\sum_{k=1}^{n_j} W_{j,k}{}^2$ Results of the analysis based on Morlet and Daubechies 2 and functions are shown in Figures 6.18 to 6.21.

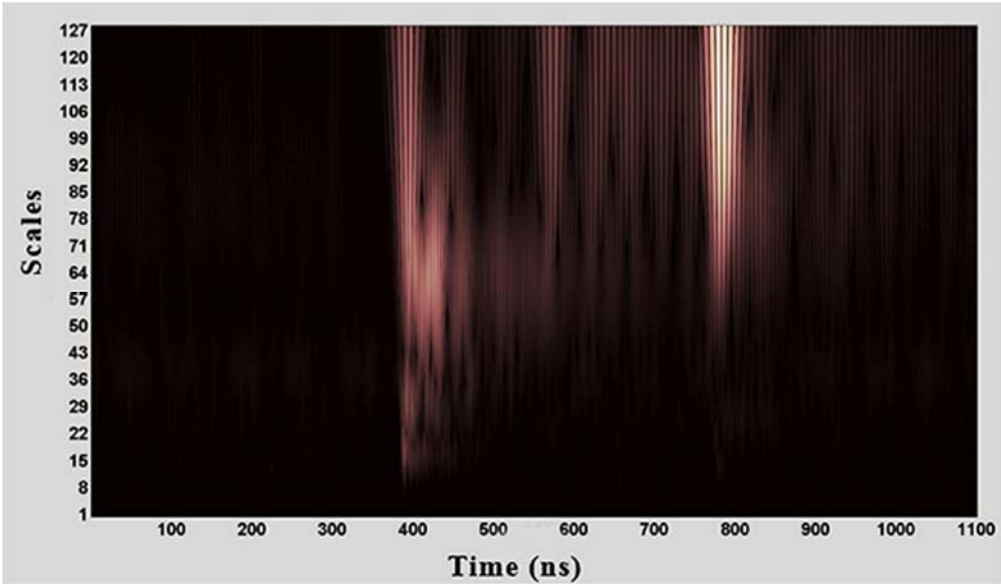

Figure 6.18: Spectrogram of scale from Morlet function

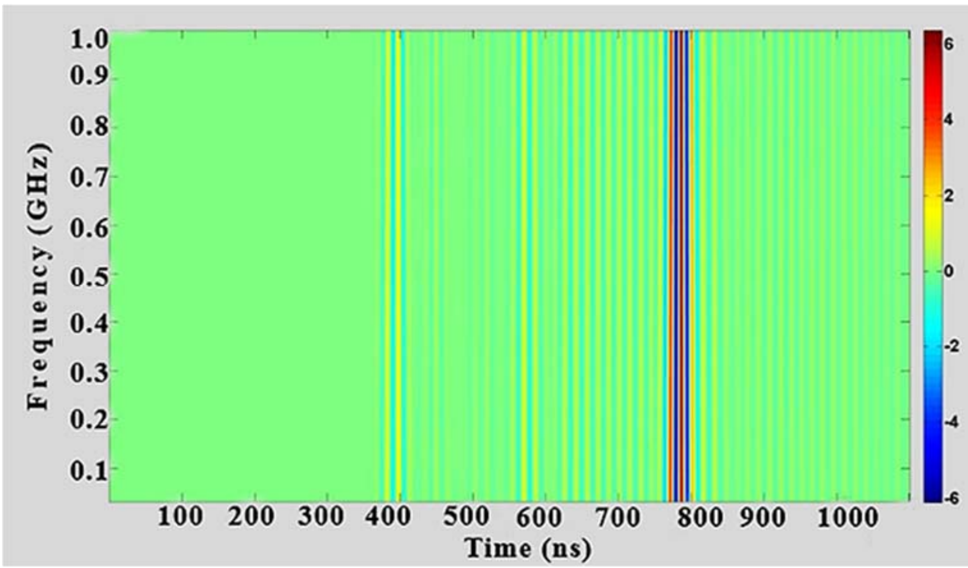

Figure 6.19: Spectrogram of frequency from Morlet function

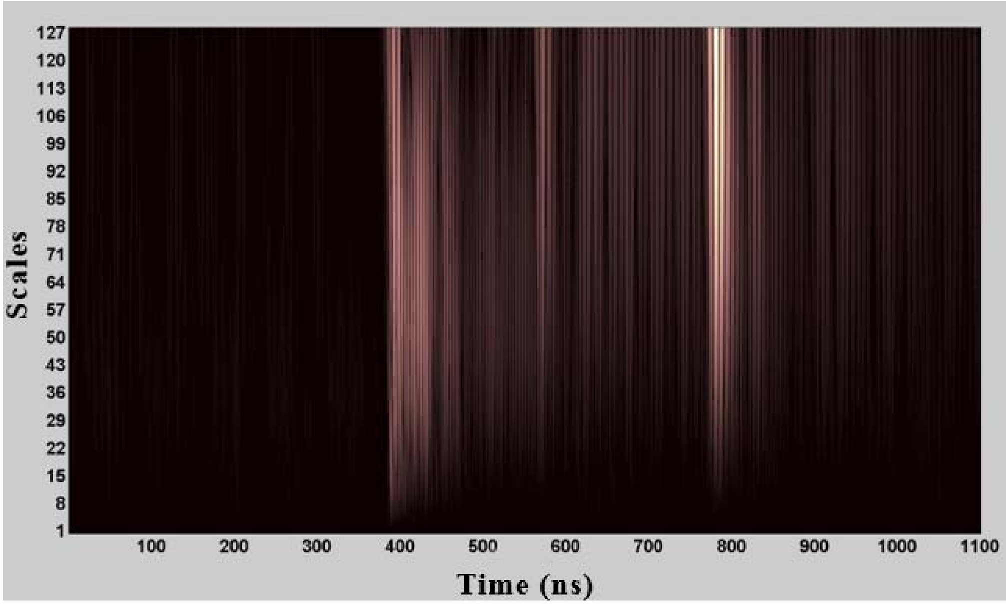

Figure 6.20: Spectrogram of scale from db2 function

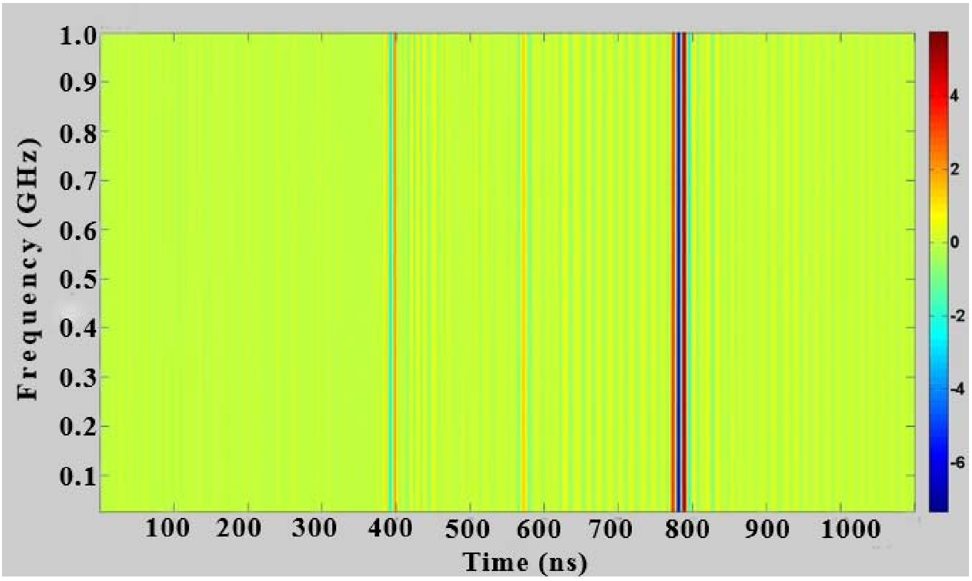

Figure 6.21: Spectrogram of frequency scale from db2 function

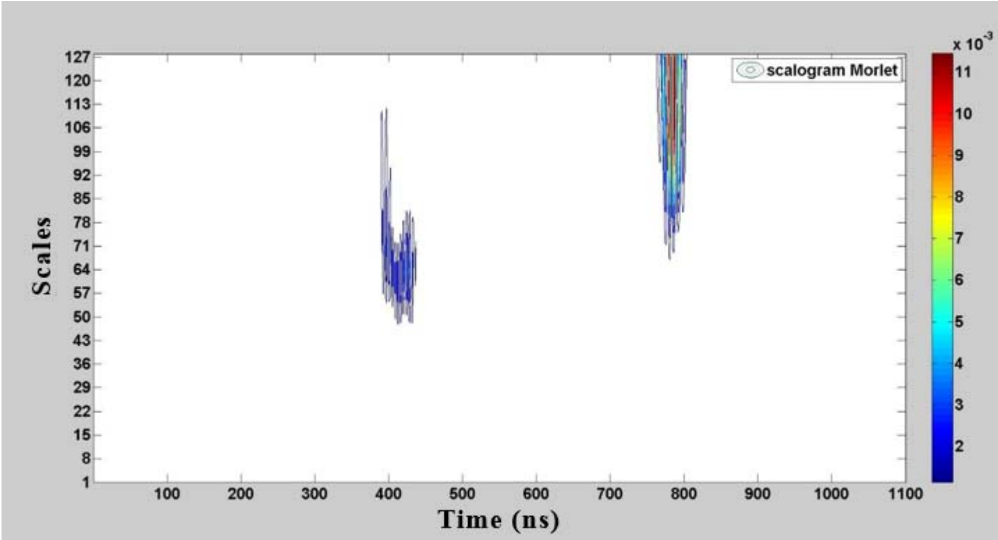

Figure 6.22: Scalogram from Morlet function

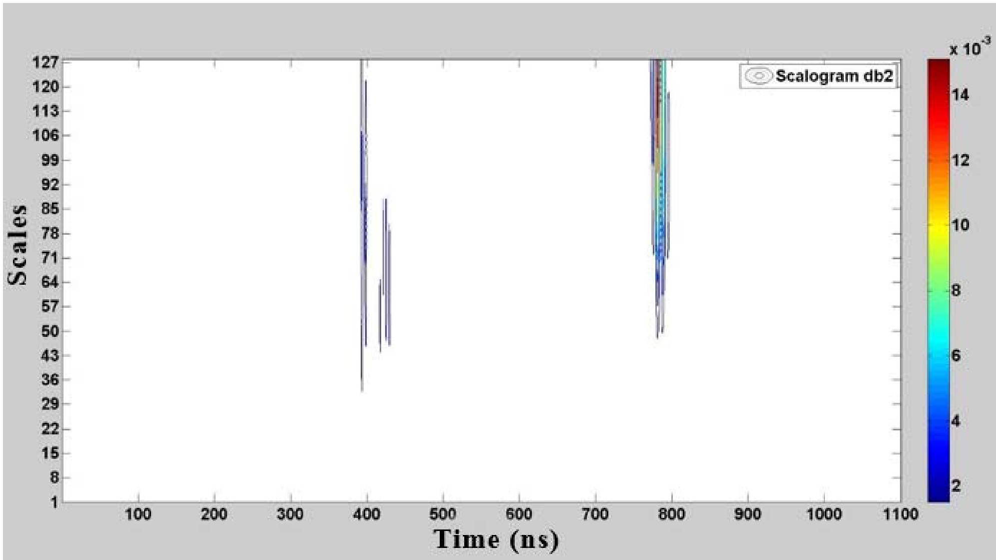

Figure 6.23: Scalogram from db2 function

Discrete wavelet transformation of the signal in Figures 6.14 and 6.15 represent time evolution of the radiated noise signal. It is useful for extracting frequency band of interest from a noisy signal. Wavelet decomposition shown in the Figures indicates that a large noise amplitude lies between 312.5 to 625 MHz at time duration 200 to 300 ns. Higher frequency components between 1.25 to 2.5 GHz is observed at 1 μs. Figures 6.18 to 6.23 indicate presence of low frequency noise at 800 ns coinciding with switching of one of the high voltage MOSFET devices. At around 400 ns first MOSFET device is switched on. This event falls in mid frequency range represented by scales 50 to 113. The wavelet analysis gives a clear picture of the frequency content of interference signal present at different point of time.

Second set of analysis is carried out with the setup as described above but with additional component of flow of flash lamp main discharge current, as shown in Figure 6.10. Figure 6.24 shows wavelet transform of radiated electromagnetic noise analyzed with Morlet function in the presence of main discharge of flash lamp current when time delay between pulse selector, injector and ejector stages (*Δt1* and *Δt2*) are set to 200 ns. Low frequency components of the order of few MHz, in the interference signal are due to flash lamp whereas, the higher frequency components are due to emissions from high voltage fast switches. Analysis of high frequency component is limited to 1 GHz due to bandwidth limitations of measuring antenna. Lower and upper limits of wavelet scales are fixed at 4 and 5000, which correspond to pseudo frequency range of 812 kHz to 1 GHz for Morlet function, which has central frequency of 0.81 Hz. The lower scale is changed to 3 for analysis with Daubechies function, which has central frequency of 0.66 Hz. This corresponds to upper frequency of 1.1 GHz.

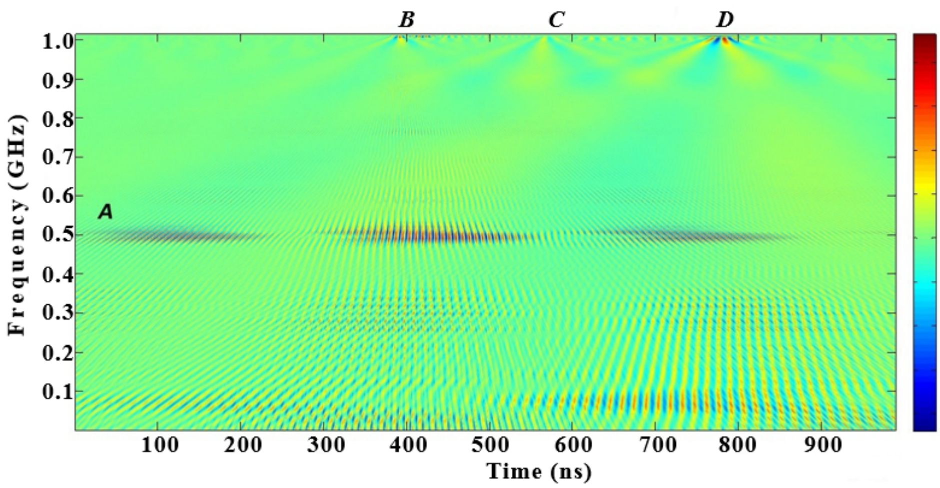

Figure 6.24: Wavelet transform with Morlet function of interference signal generated by flash lamp main discharge current

Region of interference from flash lamp is marked by *A*. These are low frequency emissions concentrated at around 500 MHz. Triggering of high voltage switches are marked by points *B*, *C* and *D*. Emission at point *C* is due to step switching of a high voltage solid state switch. Intensity of emission for this device is lower as compared to the emission at point *D* which is due to pulsed switching. Figure 6.25 shows wavelet transformation of the interference signal with Daubechies function of order 2.

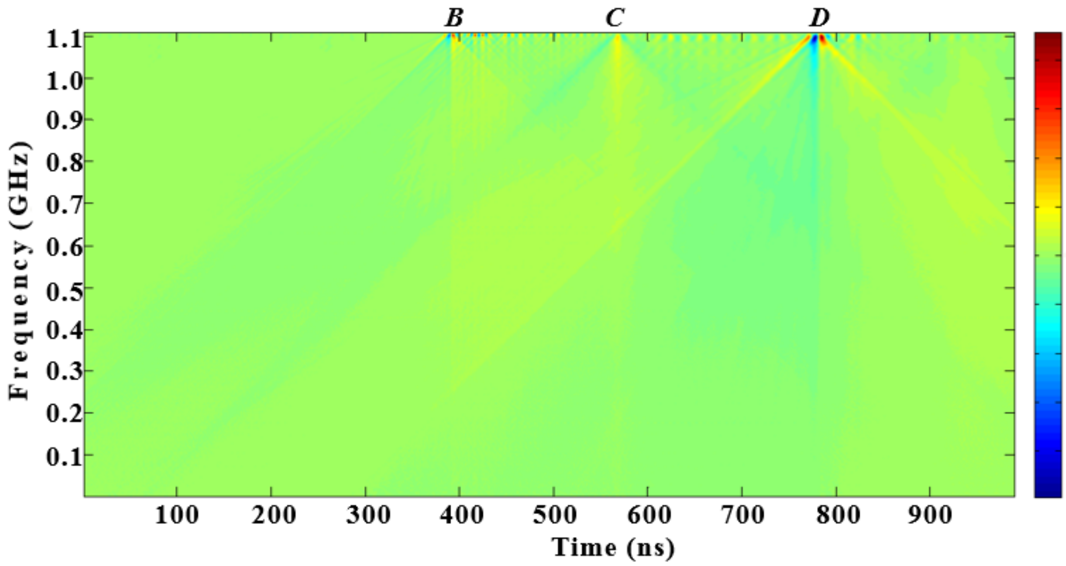

Figure 6.25: Wavelet transform with db2 function of interference signal generated by flash lamp main discharge current

Profiles of the high frequency components shown by db2 wavelet function, due to switching of high voltage MOSFET devices marked at instants *B*, *C* and *D* is sharper as compared to the profile by transformation based on Morlet function. However, it is not able to discern the low frequency oscillatory interference signals due to flash lamp main current discharge.

6. 5 Summary and conclusion

This chapter discusses signal integrity and noise analysis in a compact table top terawatt laser setup. Details of the laser unit are provided in chapter 4 of this thesis on system description. Electrical components of the laser unit generate pulsed electromagnetic interference of varying power and timing characteristics. Interfering fields have potential to disturb normal functioning of active components in trigger circuits. The laser unit consists of delay generator circuits for precision triggering of several stages in specific time sequence. Delay generator circuits based on unipolar mode CMOS/TTL and differential mode ECL logic are compared for susceptibility to transient electromagnetic fields generated by pulsed power supplies of flash lamp trigger. Design based on emitter-coupled integrated circuits, which have differential logic levels is found to be less susceptible to the transient interference noise in table top terawatt laser setup. A delay generator based on differential signal emitter coupled components is designed, which exhibits low timing jitter of 800 ps under pulsed EMP environment generated by flash lamp discharge current and switching of high voltage Pockels cells.

Interference from multiple noise sources in the laser chain are analyzed by wavelet transformation of the time domain signal. Noise emissions are due to high voltage triggering and pulsed current discharge through flash lamps and high voltage switching of MOSFETs in pulse selector, pulse injector and pulse ejector stages. Triggering of these devices are synchronized in time.

Suitability of a wavelet function for analysis of pulsed interference signals encountered in the laser system is estimated by decomposing the signal in approximate and detail coefficients, reconstruction of the signal from the coefficients and analyzing the error profile between original and the reconstructed signals. Signals decomposed and reconstructed with Daubechies wavelet function of order two, closely resemble the original profile. However, it is not able to resolve the low frequency components of interference signals attributed to flash lamp current. Wavelet transform with Morlet basis function provides better representation of low frequency oscillatory signal and is able to distinguish between switching transients due to operation of flash lamps and due to the semiconductor switches. Scales are chosen to limit the frequency to 1 GHz as dictated by the antenna bandwidth.

Time evolution of interference signal due to triggering of flash lamp and operation of high voltage MOSFET switches are studied with DWT signal decomposition. Spectrogram and scalogram analysis are carried out with CWT based on db2 and Morlet wavelet functions. Analysis is carried out for two different operating conditions of the flash lamp i.e. one with high voltage trigger only and another with discharge of main current. Wavelet based analysis of interference noise generated by the laser system provides the following information,

a) Radiated EMI from initial high voltage triggering of flash lamps is centered on 500 MHz and appears as bursts of few hundred ns durations. Low frequency bursts of smaller intensity and shorter durations are present throughout the discharge cycle.
b) Interference from pulse selector, pulse injector and pulse ejector stages have different characteristics, depending upon timing parameters of high voltage switches used for Pockels cell driver in the particular stage.
c) Noise emission is more intense in ejector stage where high voltage switch is of pulsed type and has lower rise time.
d) Noise from injector stage is less intense as it is generated from a step type of MOSFET switch having larger rise time.
e) Intensity interference from selector stage is of intermediate magnitude.

Time domain measurement of electromagnetic interference from various stages of flash lamp pumped high power laser chains is described in chapter 5 of this thesis. Wavelet transform is applied on the measured data to effectively identify and characterize noise sources in an intersystem setup consisting of various stages of a terawatt laser unit. It provides an overview of electromagnetic noise generated by triggering of flash lamps and high voltage Pockels cell drivers. This analysis is helpful towards attaining better electromagnetic compatibility of multistage high power lasers.

Chapter 7

Field coupling and shielding issues in high power lasers

Flash lamp pumped high power laser systems are based on pulsed power supplies consisting of capacitor discharge through electrically long cables into non-linear loads. These result into multiple pulsed electromagnetic sources of varying characteristics. Electromagnetic fields generated by high peak current sources like electrical systems of flash lamp and Faraday isolator power supplies are coupled to co-axial cables carrying low voltage control and synchronization signals. Analysis of noise couplings and crosstalk carried out in this chapter comprises of calculation of fields generated by pulsed current sources, coupling of incident fields into co-axial cables, estimation of spatially distributed induced voltage and current and crosstalk in multi-conductor systems. Several studies on this topic have been carried out for electromagnetic pulses (EMPs) generated due to lightning (LEMP) [Rachidi, 2001], nuclear reactions (NEMP) [Uman, 1982] and electrostatic discharge (ESD) [Berghe, 1998]. These events are characterized on the basis of intensity, temporal and spatial profiles. Fields due to lightning, high altitude nuclear explosion and ESD are normally modeled as double exponential of the form $E(t)=E_0[e^{-\alpha t} - e^{-\beta t}]$. Flash lamp current pulse is marked by an initial sharp trigger region followed by a near critical discharge of capacitor bank through an inductor and a non-linear flash lamp load. Faraday isolator current discharge is half sinusoid of around 5 ms duration. Apart from flash lamps and Faraday rotator high peak current sources, there are drivers for high speed switching of Pockels cells and operation of electromechanical relays which contribute to generation of pulsed and transient electromagnetic fields. Generation of interference field due to Faraday isolator current and its coupling to a shielded co-axial cable is evaluated and compared with measurement results. Analytical solutions in the present work assumes TEM mode of field propagation in cables because of smaller cross-sectional dimensions. Evaluation of EMP coupling to cables involves the development of appropriate models for interference source and victim cable. The analysis also needs determination of following parameters,

a) Series voltage and shunt current distributed along the cable shield. These are computed by solving single conductor transmission line equation where the voltage and current sources are derived from the EMP to shield coupling.
b) Coupling from shield to inner conductor which generates core wire voltage and current. These are obtained by solving single-conductor transmission line equations, which include distributed series and shunt source terms. The impressed sources are related to the shield current and voltage through surface transfer impedance and admittance respectively.
c) Currents and voltages at inner conductor and cable shield.

Crosstalk in the context of EMC/EMI studies refers to unintended electromagnetic coupling between wires and conductors. It is a major factor in maintaining signal integrity in high clock frequency, low rise time and densely placed systems. Crosstalk depends on signal rise time, transfer impedance and admittance of cables and is usually represented in terms of near-end or backward crosstalk (NEXT) and far-end or forward crosstalk (FEXT). Near end crosstalk refers to the induced voltage on victim line at the end closer to the driver, whereas far end crosstalk refers to the induced voltages at a point farthest from the driver [Hall, 2000]. Conventional electromagnetic compatible design steps minimizes crosstalk coupling by lowering the mutual inductance and capacitance by increasing the separation between adjacent signal lines, introducing electric field screens and implementation of wide area plane to minimize the overall ground impedance.Work presented in this thesis looks into time and frequency domain analytical and measurement aspects of crosstalk voltages induced in transmission lines due to pulsed switching of electro-optical (flash lamps and Pockels cells) and magneto-optical (Faraday rotator) components. In the laser systems under study the aggressor signals are generated from flash lamp discharge circuits which switch large peak current (~ 6 kA of pulse durations of the order of 500 μs), Pockels cell driver circuits which switch high voltage (~ 3 kV with rise time less than 5 ns), TTL and CMOS level control signals transmitted through multi-conductor cables and connectors and high frequency (100 MHz) synchronization signals. This chapter deals with the analysis and measurements of couplings due to these aggressor signals through mutual capacitance and inductance into various types of cables and connectors.

7. 1 Analytical solutions of field coupling

Electromagnetic field coupling is expressed in terms of time and space partial-derivatives of induced voltages and currents along the line and the source terms. Differences among the classical treatments of this topic are essentially in representation of source terms. Taylor et al. [Taylor, 1965] have calculated the source terms as functions of both the electric and magnetic fields. Agrawal et al. [Agrawal, 1980] have calculated the source terms as functions of only electric field. Rachidi [Rachidi, 1993] has calculated the source terms as functions of magnetic fields. Figure 7.1, represents an electrical conductor placed at a height of h above infinite ground plane. It is exposed to electromagnetic field and terminated with impedances Z_s and Z_L at the two ends respectively.

Interfering fields from an aggressor cable are caused by flow of current pulses through electrical interconnects. The electric and magnetic fields due to a fixed current wave shape through a straight vertical channel is given by [Uman, 1975].

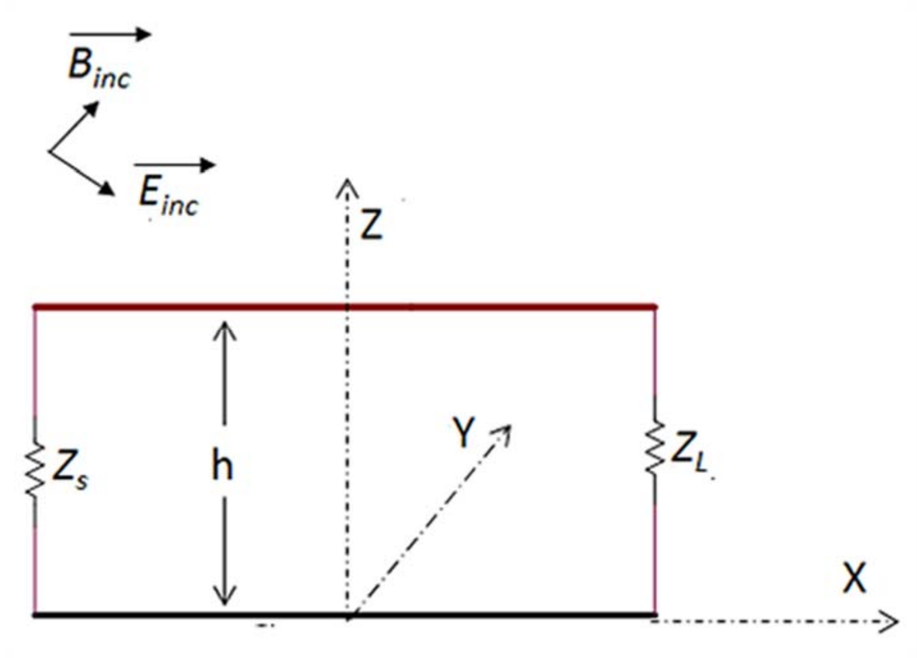

Figure 7.1: Field to transmission line coupling

$$E(D,t) = -\frac{\mu_0 v}{2\pi D} i(t - D/c)\vec{a}_z \tag{7.1}$$

$$B(D,t) = \frac{\mu_0 v}{2\pi c D} i(t - D/c)\vec{a}_\phi \tag{7.2}$$

where, *i(t)* represents the propagating current, *v* is velocity of propagation of current pulse, *D* is horizontal distance from the channel to the point of observation, *c* is speed of light, μ_0 is permeability of free space, *z* and *φ* are vertical and azimuthal coordinates respectively. Induced voltage and current in co-axial core are calculated from field parameters incident at the shield, cable *RLGC* parameters and the transfer impedance.

7. 2 Faraday isolator current induced crosstalk

Faraday isolators in high power lasers utilize magneto-optic effects to rotate plane of polarization of incident light. These stages operate on pulsed magnetic fields generated by discharging energy stored on capacitor bank (typically 1000 μF) through inductive coils placed around Faraday rotor material. Current peaks vary between 1 to 3 kA depending upon capacitance value and charging voltage. As mentioned in the previous sections, Faraday isolator solenoid produces pulse magnetic fields to rotate plane of polarization of incident lasers. This section analyses generation of electrical field due to conductors carrying Faraday isolator pulsed currents of 1.2 kA peak and 5 ms duration. It is followed by calculation of induced voltage and current in a victim coaxial cable which carries low voltage trigger signals for synchronization circuits and comparison with measurement data. Half sinusoid current through Faraday coil is mathematically represented as,

$$I = I_0 \sin 2\pi 100t \qquad t \leq 5ms \tag{7.3}$$

Radiated fields at the victim cable is calculated from equations (7.1) and (7.2). Current pulse in aggressor cable and the calculated electric field at a distance of 3 m are shown in Figure 7.2. Time domain expression for induced voltage and current at *z=0* for a transmission line which is exposed to electric field is given by [Ari, 1988],

$$V(0,t) = h.\frac{\rho_1 + 1}{2}.E(t) \tag{7.4}$$

$$I(0,t) = h.\frac{\rho_1 - 1}{2.Z_L}.E(t) \tag{7.5}$$

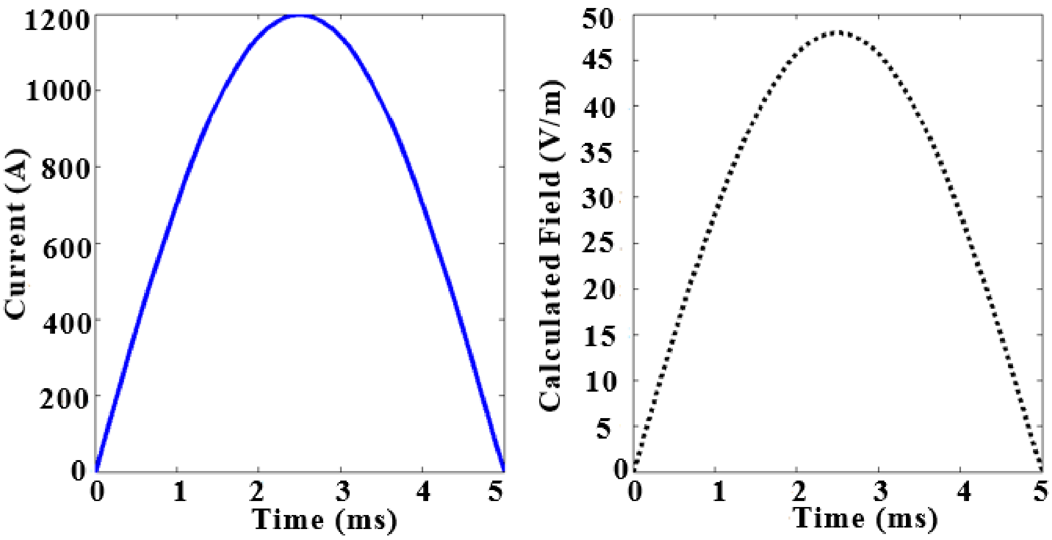

Figure 7.2: Faraday isolator current and electric field

The electric field $E(t)$ is a function of incident field E^{inc}, polarization angle θ, elevation ψ and azimuth angle φ,

$$E(t)=W.E^{inc}(t)-\sum_{n=0}^{\infty}(\rho_1\rho_2)^n\left\{\rho_2\left(W^{+}-\rho_1 W^{-}\right)E^{inc}(t-t_{1,n})-\left(\rho_2 W^{+}-W^{-}\right).E^{inc}(t-t_{2,n})\right\} \quad (7.6)$$

$$W^{\pm}=\frac{\cos\theta.\cos\psi.\sin\phi-\sin\theta.(\cos\phi\mp sin\psi)}{\pm 1-\sin\psi.\cos\phi} \quad (7.7)$$

where h represents the height of the ground plane in victim cable. Reflection coefficients ρ_1 and ρ_2 depend on termination resistors Z_1, Z_2 and characteristic impedance Z_0. These are represented respectively, by

$$\rho_1=\frac{Z_1-Z_0}{Z_1+Z_0} \quad (7.8)$$

$$\rho_2=\frac{Z_2-Z_0}{Z_2+Z_0} \quad (7.9)$$

For matched conditions of source and load impedances i.e. $Z_1=Z_2=Z_0$ the reflection co-efficient $\rho_1 = \rho_2 = 0$. Terms $t_{1,n}$ and $t_{2,n}$ in equation (7.6) depend on length of victim conductor.

$$t_{1,n} = \frac{2l}{c_0}(n+1) \tag{7.10}$$

$$t_{2,n} = \frac{l}{c_0}(2n+1+\sin\psi.\cos\phi) \tag{7.11}$$

For the case of polarization angle $\theta = 0^0$, azimuth $\varphi=90^0$ and cable length 5 m the incident electric field is,

$$E(t) = -\left[E^{inc}(t) + E^{inc}(t-1.7\times10^{-8})\right] \tag{7.12}$$

Induced voltage and current in a 5 m long co-axial cable with grounded sheath due to plane wave incident field generated by half sinusoid Faraday isolator current is shown in Figure 7.3. Cable sheath at a separation distance of 1mm is considered as ground plane. Calculated induced voltage is compared with measured values.

7. 3 Cable geometry and layout

Cross talk and field coupling analysis are carried out for two different types of cables namely, single core and co-axial, of length 1.2 m and 5 m. Single core cable consisted of 19 strands of copper wires of overall diameter 2.3 mm. Rated resistance per unit length is 7 mΩ. Co-axial cable is of type *RG58* for which the constructional details are given in Figure 7.4.

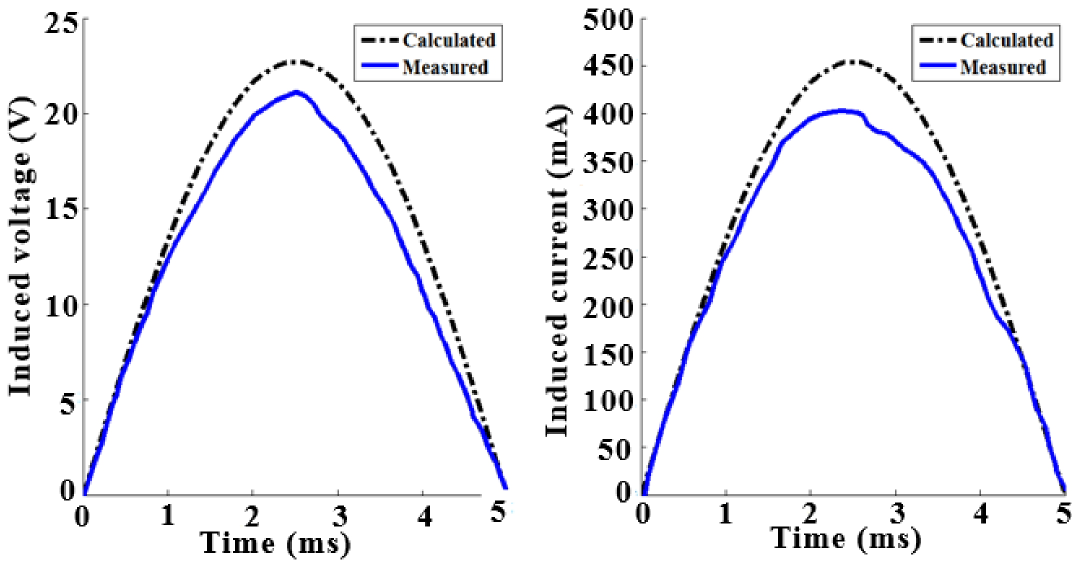

Figure 7.3: Induced voltage and current

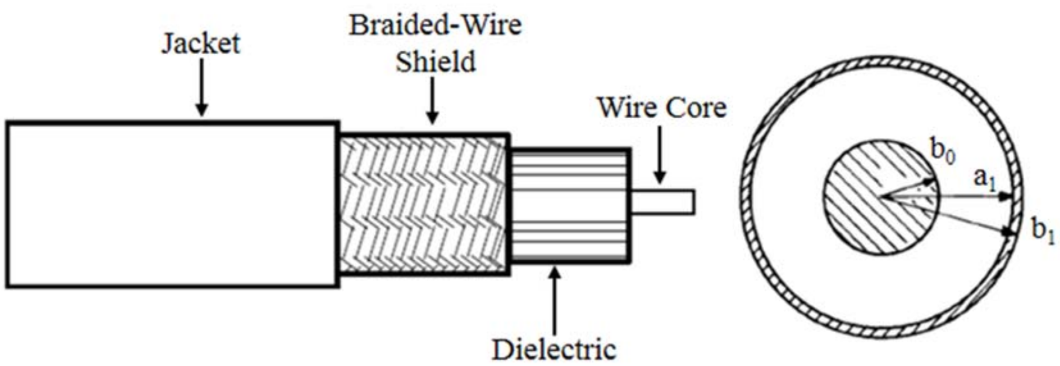

Figure 7.4: Constructional details of co-axial cable

Cable dimensions are, b_0 (Copper core 0.451 mm), a_1 (1.397 mm) and b_1 (1.524 mm). Shield (braid) parameters are important in determining the transfer impedance. Weave pattern of the braid is shown in Figure 7.5.

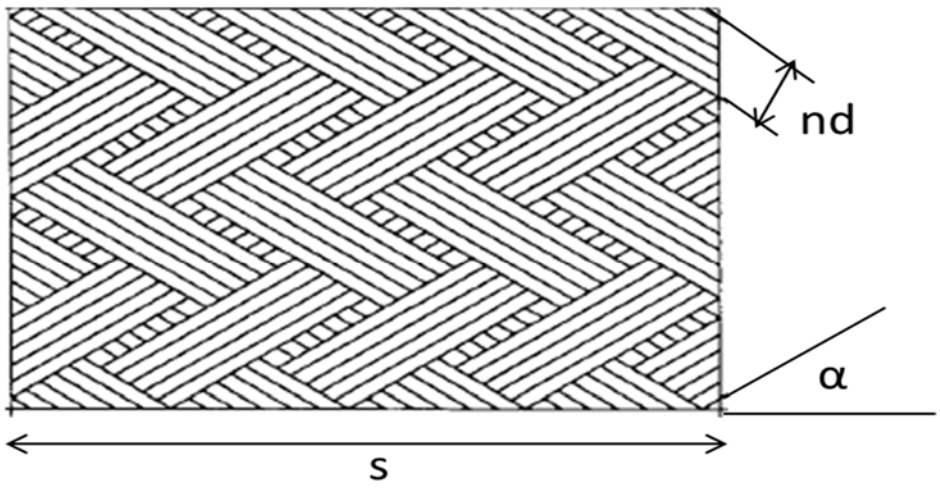

Figure 7.5: Shield weave pattern [Kley, 1993]

Dimensional parameters of cable braid are given by [Vance, 1978],

Average braid diameter: $D_m = D_0 + 2.5d$

Braid angle: $\alpha = \arctan\left(\pi D_m / s\right)$

Filling factor: $G = mnd / (2\pi D_m \cos\alpha)$

Optical coverage: $G(2-G)$

Where, m is the number of carriers, n is number of wires in each carrier, d is wire diameter, D_0 is braid diameter and s is lay length. For co-axial cable used in this work the shield strand diameter is 0.127 mm, number of strands is 12, braid angle is 27.7^0, fill factor is 0.746, and optical coverage is 0.9355 [Vance, 1978]. Crosstalk analysis is carried out with an avalanche transistor based high voltage switch (3 kV, $t_r \sim 4$ ns), as shown in Figure 4.18. It generates a step pulse that drives the line from one end with a Pockels cell connected as load at the other end. Pockels cell used in the experimental set-up (Inrad make PKC 21) can be electrically considered as a capacitive load of 8 pF in parallel with a terminating 50 Ω resistor. Figure 7.6 shows layout for aggressor, victim and reference cables. Victim cable carrying synchronous clock signal runs parallel to the aggressor cable at a separation of 10 cm. An identical cable for carrying synchronous clock signal runs parallel to the aggressor cable at a distance of 10 cm. Reference wire is routed below the generator wire at a vertical distance of 2.5 cm. Diagonal distance between the victim wire and the reference wire is approximately 10.3 cm. Radius of generator, victim and reference wires are 0.15 mm. Crosstalk voltage at near and far end are analysed and measured under different conditions of terminations and ground planes.

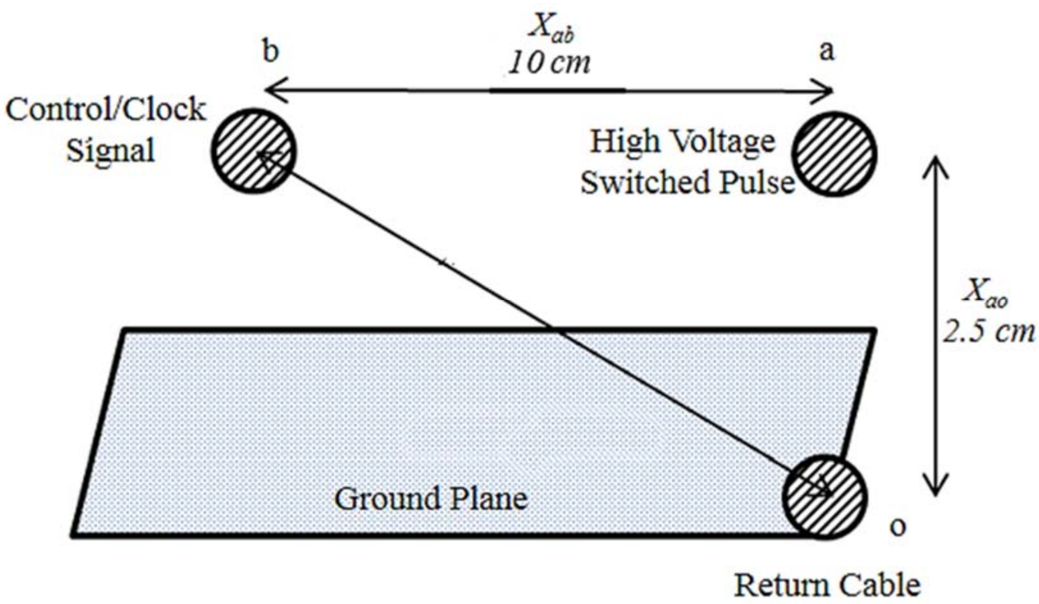

Figure 7.6: Cable layout for cross talk analysis

7. 4 Crosstalk analysis under transient excitation

Crosstalk in multi-conductor systems is attributed to mutual inductance and mutual capacitance of victim and aggressor lines. Equivalent circuit of a pair of parallel conductors consisting of an aggressor line carrying high voltage step and a victim line is shown in Figure 7.7. A high voltage switched out pulse is launched on one of the lines. Terms Z_1, Z_1', Z_2 and Z_2' represent termination impedances. R, L and C are per unit length transmission line parameters. C_m and L_m are mutual capacitance and inductance respectively. Far end crosstalk (FEXT) affects the signal integrity at receiver end and is more problematic as compared to near end cross talk. It is proportional to time delay required to travel from near end to far end of the cable. Equivalent circuit of a three conductor transmission line system is shown in Figure 7.8 [Paul, 1978].

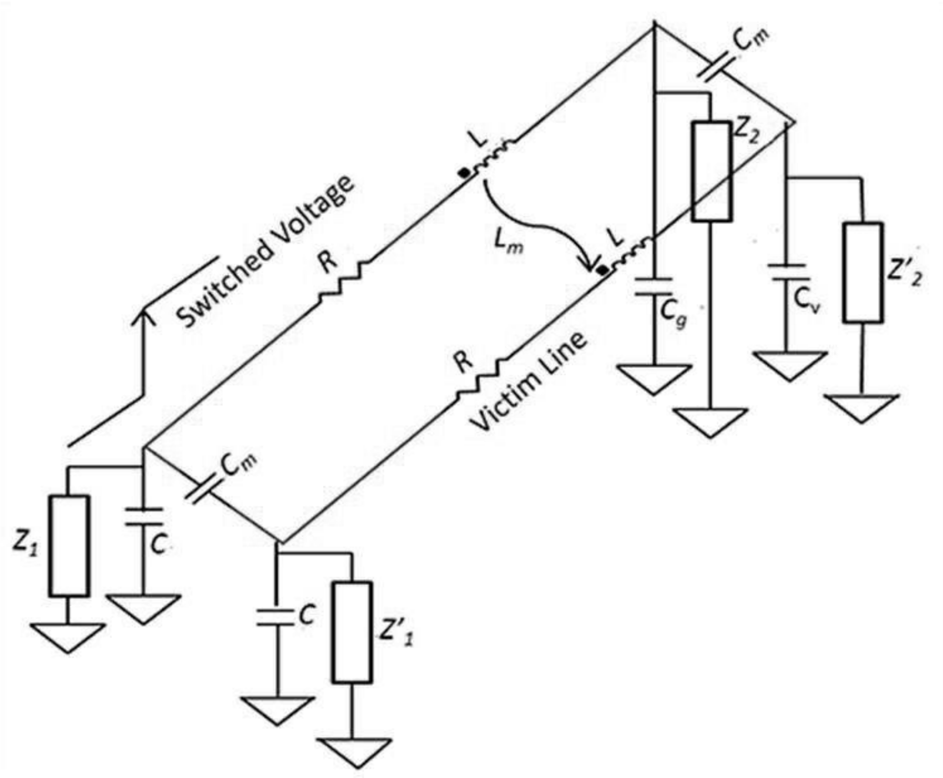

Figure 7.7: Equivalent circuit of parallel conductors

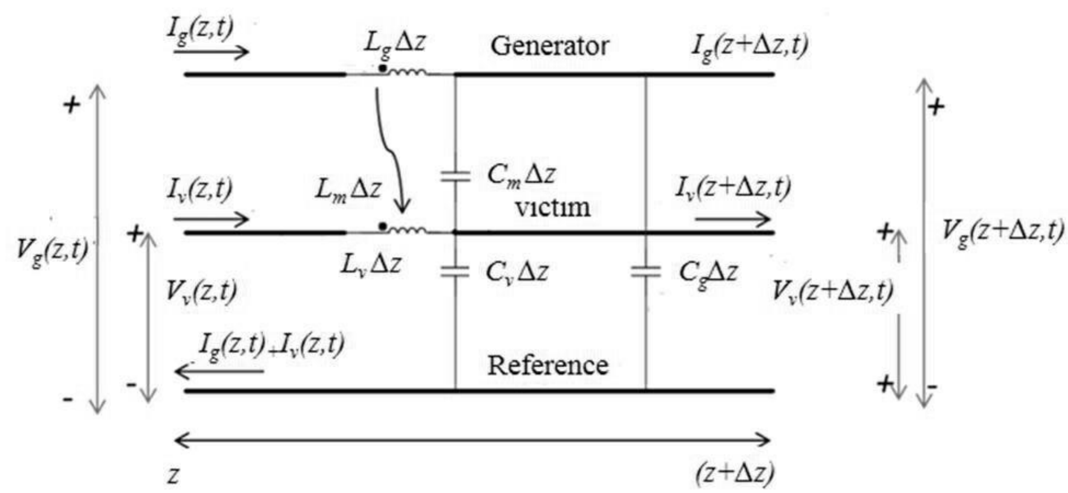

Figure 7.8: Transmission line equivalent circuit

V_g and V_v are voltages impressed on generator and victim lines. I_g and I_v represent currents through corresponding conductors. L_g, L_v, C_g, and C_v represent self-inductance and capacitances respectively. L_m and C_m are mutual inductance and mutual capacitance between the generator and victim cables. Multi-conductor transmission line (MTL) equation for the equivalent circuit is given by [Muot, 2012], [Paul, 1984],

$$\frac{\partial V_g(z,t)}{\partial z} = -L_g \frac{\partial I_g(z,t)}{\partial t} - L_m \frac{\partial I_v(z,t)}{\partial t} \tag{7.13}$$

$$\frac{\partial V_v(z,t)}{\partial z} = -L_m \frac{\partial I_g(z,t)}{\partial t} - L_v \frac{\partial I_v(z,t)}{\partial t} \tag{7.14}$$

$$\frac{\partial I_g(z,t)}{\partial z} = -\left(C_g + C_m\right) \frac{\partial V_g(z,t)}{\partial t} + C_m \frac{\partial V_v(z,t)}{\partial t} \tag{7.15}$$

$$\frac{\partial I_v(z,t)}{\partial z} = C_m \frac{\partial V_g(z,t)}{\partial t} - \left(C_v + C_m\right) \frac{\partial V_v(z,t)}{\partial t} \tag{7.16}$$

These are represented in matrix form as,

$$\frac{\partial}{\partial z}\left[V(z,t)\right] = -[L] \frac{\partial}{\partial t}[I(z,t)] \tag{7.17}$$

$$\left[V(z,t)\right] = \begin{bmatrix} V_g(z,t) \\ V_v(z,t) \end{bmatrix} \tag{7.18}$$

$$\left[I(z,t)\right] = \begin{bmatrix} I_g(z,t) \\ I_v(z,t) \end{bmatrix} \tag{7.19}$$

Transmission line inductance and capacitances are represented by,

$$\left[L\right] = \begin{bmatrix} L_g & L_m \\ L_m & L_v \end{bmatrix} \tag{7.20}$$

$$\left[C\right] = \begin{bmatrix} \left(C_g + C_m\right) & -C_m \\ -C_m & \left(C_v + C_m\right) \end{bmatrix} \tag{7.21}$$

Self-inductances of generator conductor (L_g), victim conductor (L_v) and mutual inductance (L_m) with respect to a reference cable depend on conductor geometries and mutual separation with reference conductors. Under the conditions of larger separation distance in comparison to cross sectional dimensions the self and mutual inductances of a cable pair is given by,

$$L_g = \frac{\mu_0}{2\pi} \ln\left(\frac{X_{a0}^2}{r_g r_0} \right) \qquad H/m \tag{7.22}$$

$$L_m = \frac{\mu_0}{2\pi} \ln\left(\frac{X_{a0} X_{b0}}{X_{ab} r_0} \right) \qquad H/m \tag{7.23}$$

The terms r_g and r_0 represent radii of the generator and reference cables. X_{a0} and X_{b0} are separation distances between reference cable with aggressor and victim cables respectively. X_{ab} is mutual separation between the aggressor and victim cables. For cable lengths of 1.2 m and radii 1.1 mm the inductances are calculated as L_m =0.61 μH/m, L_g=1.23 μH/m and L_v=1.8 μH/m**.** Since the medium surrounding the cables is homogeneous, the corresponding capacitance matrix is calculated from inductance matrix [**L**] as,

$$\begin{bmatrix} C_g & C_m \\ C_m & C_v \end{bmatrix} = \mu\varepsilon \begin{bmatrix} L_g & L_m \\ L_m & L_v \end{bmatrix}^{-1} = \frac{1}{C_0^2} \left[L \right]^{-1} \tag{7.24}$$

Calculated L and C parameters of the cable layout in Figure 7.6 are,

$$\left[L \right]_{calc} = \begin{bmatrix} 1.23 & 0.61 \\ 0.61 & 1.80 \end{bmatrix} \qquad \mu H/m \tag{7.25}$$

$$\left[C\right]_{calc} = \begin{bmatrix} 7.18 & 3.68 \\ 3.68 & 3.74 \end{bmatrix} \quad pF/m \tag{7.26}$$

Near and far end crosstalk are analysed and measured for step excitation of a single core aggressor cable. Excitation is a step voltage from a fast rise time switch as shown in Figure 7.9. Near and far end crosstalk induced voltages depend on terminating loads [Paul, 2006]. Cross talk transfer functions based on transmission line equivalent model are represented by

$$M_{NE}^{L} = \frac{R_{NE}}{R_{NE}+R_{FE}} \cdot \left(\frac{L_m}{R_s+R_L}\right) l \tag{7.27}$$

$$M_{NE}^{C} = \frac{R_{NE}R_{FE}}{R_{NE}+R_{FE}} \cdot \left(\frac{R_L C_m}{R_s+R_L}\right) l \tag{7.28}$$

Corresponding expressions for far end coupling are,

$$M_{FE}^{L} = -\frac{R_{FE}}{R_{NE}+R_{FE}} \cdot \left(\frac{L_m}{R_s+R_L}\right) .l \tag{7.29}$$

$$M_{FE}^{C} = \frac{R_{NE}R_{FE}}{R_{NE}+R_{FE}} \cdot \left(\frac{R_L C_m}{R_s+R_L}\right) .l \tag{7.30}$$

Where, M_{NE}^{L}, M_{NE}^{C}, M_{FE}^{L} and M_{FE}^{C} represent crosstalk transfer functions i.e. the ratio of induced to excitation voltages due to inductive and capacitive effects at near and far end. R_{NE} and R_{FE} are near and far end termination impedances of the victim cable. R_S is source impedance, R_L is load impedance, l is the cable length. Load on the aggressor line is an electro-optical device, Pockels cell, which is equivalent to a capacitor in parallel with a 1 MΩ resistor. Excitation source, which causes crosstalk induced interference is shown below in Figure 7.9.

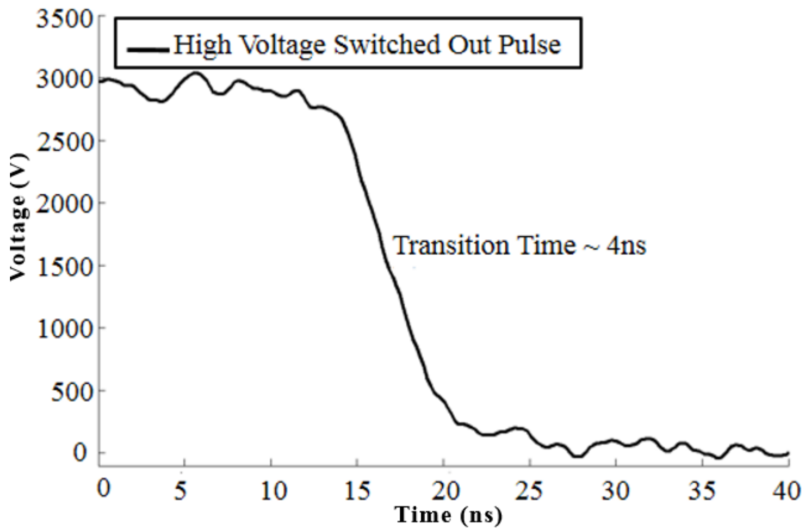

Figure 7.9: Excitation source

Figure 7.10 shows the calculated and measured induced voltages at near and far ends of a single core cable under the termination conditions of R_L = 1 MΩ, R_{NE} = 50 Ω, R_{FE} = 50 Ω and R_s = 50 Ω due to pulsed excitation in a nearby wire.

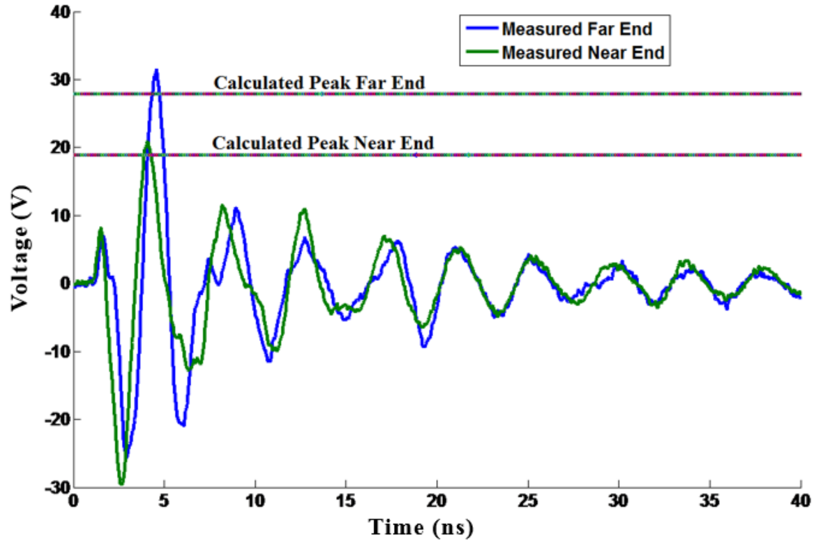

Figure 7.10: Near and far end induced voltage under pulsed excitation without ground plane

Ground plane provides a low impedance path to the return current. Mutual inductance and capacitance reduces due to closer return path for coupled currents. Spatial distribution of the return path is a function of height of the cable from ground plane [Jhonson, 1993] as shown in Figure 7.11. Overall effect is the reduction in the cross talk amplitude. Self and mutual inductance of the generator wire placed above ground plane at a height *h* are represented respectively, by

$$L_{gg} = \frac{\mu_0}{2\pi} \ln\left(\frac{2h}{r_g}\right) H/m \tag{7.31}$$

$$L_{mg} = \frac{\mu_0}{2\pi} \ln\left(\frac{\sqrt{X_{ab}^2 + 4h^2}}{X_{ab}}\right) H/m \tag{7.32}$$

where, L_{gg} and L_{mg} are self and mutual inductances, r_g is radius of the generator wire and X_{ab} is distance between the generator and victim cables. Figure 7.12 shows the calculated and measured values of near and far end induced voltage for single core cable placed above a finite ground plane of dimensions 120 cm x 60 cm. Cables are routed at a height of 2.5 cm above the ground plane.

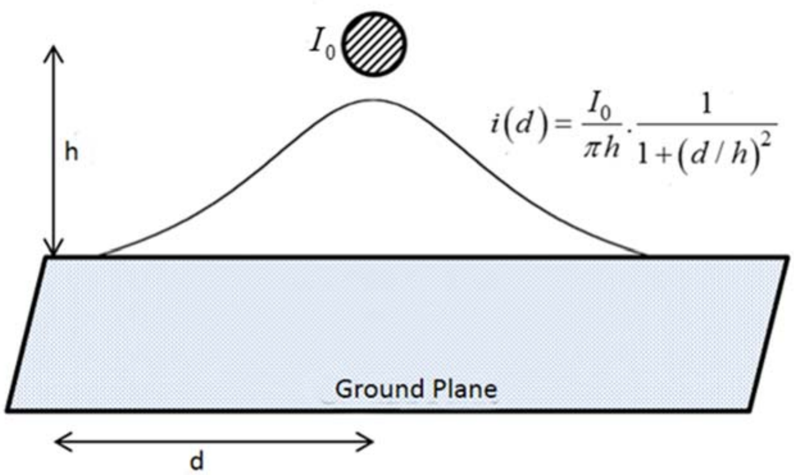

Figure 7.11: Current distribution in ground plane

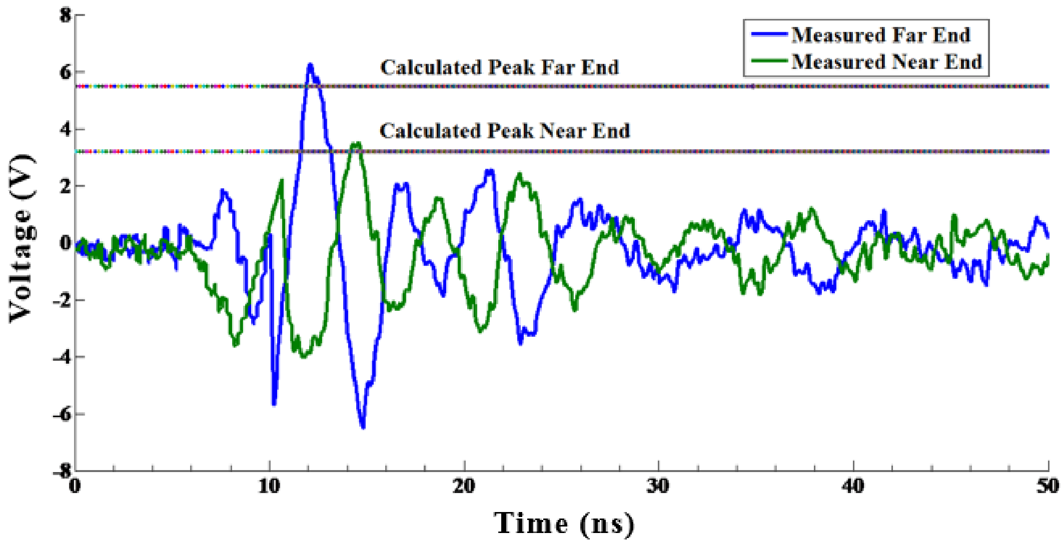

Figure 7.12: Near and far end crosstalk induced voltage under pulsed excitation in presence of ground plane

Simulation result for crosstalk induced voltage with transmission line matrix technique is shown in Figure 7.13. Crosstalk analyses based on analytical formulation and TLM method as presented above are in time domain.

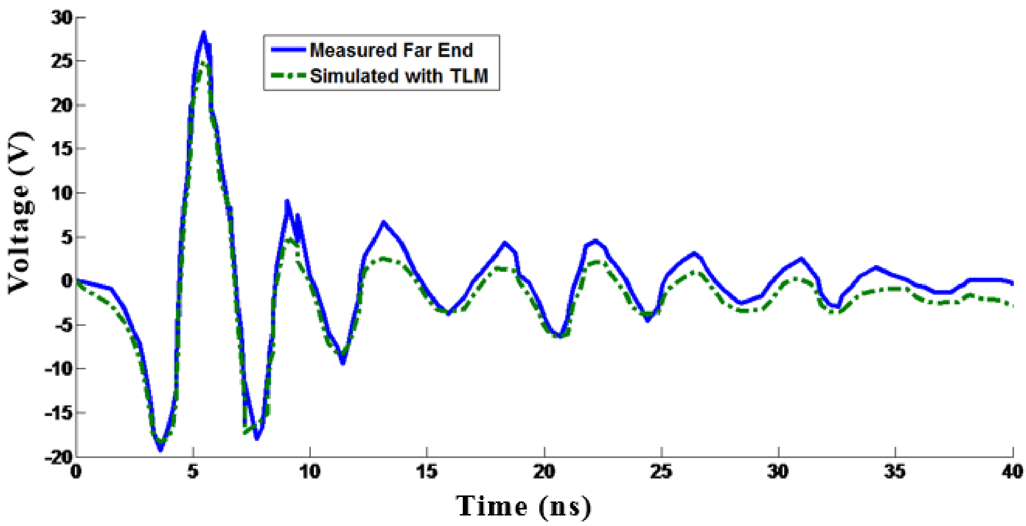

Figure 7.13: Crosstalk induced voltage simulated with TLM method

To further characterize the commonly used cables in laser power supply systems and ground planes, frequency domain analysis was carried out by two-port *S* parameter analysis. Scattering parameter (S-parameter) analysis is described earlier in section 5.3

of this dissertation for emission characterization of cables and terminations. S_{21} measurements were carried out at near and far end of the victim cable. S_{21} parameters at the near end in a victim cable with and without the ground plane are shown in Figure 7.14. Port 2 of a vector network analyzer excites an aggressor cable while port 1 is connected to near/far end of a nearby victim cable. Thus S_{21} is a measure of coupled voltage. Existence of a ground plane reduces the parasitic coupling. This is depicted as S_{21} parameter closer to zero dB axis in left half of Figure 7.14. In absence of a ground plane, the excited cable shows behavior of a dipole radiator. This results into a resonating structure and the crosstalk coupling increase at the radiated frequencies. Analytical and measurement results in frequency domain matches with those for single shot step excitations.

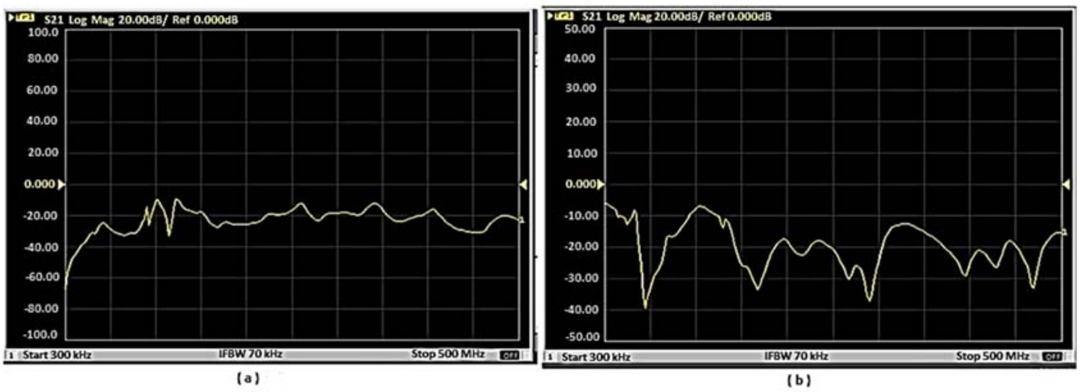

Figure 7.14: S_{21} measurement at near end (a) with ground plane (b) without ground plane

7.5 Shielding analysis

High power solid state laser chains consist of multiple electronic devices, electrical systems and conductors which are either good emitters of electromagnetic fields or are susceptible to external interference. It is a common electromagnetic compatibility practice to provide metallic shielding to noise emitters and sensitive components in intra-system setups. Shielding theory and practices are established subjects in electromagnetic compatibility and electrical engineering. However, investigations of shielding aspects of electro-optical components in high power laser systems requires different treatment because of the type of excitations which are transient and pulsed and also because of functional requirements of apertures for through passage of laser light. Shielding effectiveness of metallic enclosures is not linear under transient EM fields because of nonlinearities of electrical and magnetic properties [Croisant, 2003]. Apertures and enclosure resonance have significant negative effects on shielding effectiveness. Electromagnetic fields coupled through apertures induce voltage and surface currents which may result into false triggering of electro-optical devices and disturb laser synchronization and ultimately the laser quality. Fundamental studies on field couplings through apertures are attributed to Bethe [Bethe, 1944]. It deals with apertures of dimensions smaller than wavelengths and field is calculated in terms of electric and magnetic dipole moments [Mcdonald, 1972]. On a fundamental level the term electromagnetic shielding refers to means of reducing electromagnetic field in a prescribed region, aimed towards improvement of electromagnetic compatibility [Celozzi, 2008]. Electromagnetic shielding is achieved with the help of an electrically conducting material placed between source and victim systems. Shielding effectiveness (*SE*) is defined to quantify the effect of a shield. It is calculated as ratio of field intensity without the shield E_1 to field intensity with shield E_2 expressed on logarithmic scale [IEEE, 1983]. Mechanism of electromagnetic shielding is attributed to two different phenomena. These are due to polarization or magnetization of enclosure material and secondly due to generation of circulating eddy currents which opposes the incident fields. Calculations of shielding effectiveness are based on boundary value problem formulation, numerical electromagnetic techniques, approximate formulation or equivalent circuit methods [Thomas, 2001]. Intensity or power of electromagnetic field incident on a metallic barrier reduces either due to reflection at impedance discontinuity or attenuation in the bulk medium. Propagation constant of a plane wave travelling through a medium is given by,

$$\gamma = \sqrt{j\omega\mu\left(\sigma + j\omega\varepsilon\right)} \tag{7.33}$$

Where, ω is angular frequency of incident field, μ is permeability, σ is conductivity and ε is permittivity of the material. For a good electrical conductor, the conductivity term σ dominates and equation (7.33) reduces to,

$$\gamma = \sqrt{j\omega\mu\sigma} \tag{7.34}$$

Overall reduction of an incident field on a metallic enclosure is due to the sum of attenuation in the medium, reflection at the first interface and multiple reflections through shield plate [Schultz, 1998]. In terms of losses, shielding effectiveness for an enclosure can be expressed as,

$$SE\left(dB\right) = A\left(dB\right) + R\left(dB\right) + M\left(dB\right) \tag{7.35}$$

Terms *A*, *R* and *M* represent attenuation, reflection from the first interface and multiple reflections respectively. Expressions in simplified forms for these terms are derived as [Celozzi, 2008],

$$A = 20\log_{10}\left|e^{\gamma d}\right| 8.6\left(\frac{d}{\delta}\right) \tag{7.36}$$

$$R = 20\log_{10}\frac{1}{4\left|\zeta\right|} \qquad for\,\zeta \le 1 \tag{7.37}$$

$$M = 20\log_{10}\left|1 - \frac{\left(1-\zeta\right)^2}{\left(1+\zeta\right)^2}e^{-2\gamma d}\right| \tag{7.38}$$

where, d is enclosure thickness, δ is skin depth and ζ is ratio of impedance of medium of incidence to the impedance of shield medium, $\zeta = \frac{Z_0}{Z_s}$. Skin depth for a conductor is the distance at which field intensity reduces to *1/e*. It depends on electrical and magnetic properties of shield material and is given by,

$$\delta = \sqrt{\frac{2}{\mu\omega\sigma}} \tag{7.39}$$

For commonly encountered cases where EM fields travel from air to conducting enclosure and back to air, impedance of free space (Z_0) is 377 Ω. Intrinsic impedance of a medium Z_s depends on frequency of the incident field, permeability and conductivity and is given as $|Z_s| = \sqrt{\frac{\omega\mu}{\sigma}}$. Theoretical values of loss in intensity of an incident field due to attenuation and reflections by an aluminum enclosure of conductivity (σ) equal to 3.5×10^7 siemens/m and 3 mm thick is estimated and shown in Figure 7.15.

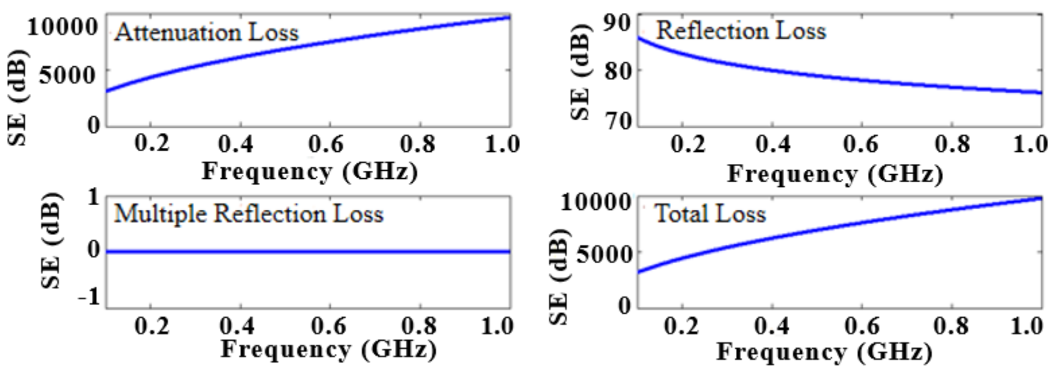

Figure 7.15: Calculated loss components in a shielding material

Apertures in an enclosure for ventilation, cable interfaces, connectors etc. reduce shielding effectiveness and the extent of deterioration depends on their shape and size [Masterson, 2001]. Metallic enclosures also exhibit resonant behavior at specific frequencies depending on enclosure dimensions at which shielding effectiveness reduces significantly. General analysis of apertures backed by metallic enclosures has been a topic of extensive research in the field of electromagnetic compatibility. Robinson [Robinson, 1998] adopted an equivalent circuit technique to compute shielding effectiveness of rectangular apertures. This technique has been widely used to analyze shielding related problems for different geometries and materials. An elaborate circuital approach is proposed by Azaro [Azaro, 2002]. Edrisi [Edrisi, 2000] has suggested an extension of modular decoupling methodology for enclosures with apertures. Coupling of specific frequency bands can be minimized by cylindrical or rectangular waveguide apertures. However, it is not always viable and practical to introduce waveguide type of structure in a compact system. Pockels cells are commonly used in applications involving fast switching of polarization to block or transmit laser light in high power laser systems. These are housed in metallic enclosures to reduce noise emissions from high voltage pulser circuits driving the cell and to minimize field couplings from external sources which may result in spurious switching. However, apertures are required to enable laser beam to be incident on Pockels cell and for onward transmission of the modulated beam. These are source of noise couplings generated by external components like flash lamp power supplies into Pockels cell housings and interference with synchronization circuits. Electromagnetic compatibility analysis of metallic enclosures housing large area electro-optic components pose a unique problem as they need apertures on two opposite faces for through passage of light. These apertures are in addition to slots for heat dissipation and for mounting connectors and feed through. There are very few reported studies to address this specific topic. Sharma [Sharma, 2007] has measured shielding effectiveness of a Pockels cell housing loaded with circular waveguide aperture. However, emphasis is on leakage of internal noise through waveguide apertures to nearby areas and the frequency is limited to 200 MHz. There is a need to understand the effect of apertures and to properly select their shapes and sizes such that noise couplings are kept to a minimum acceptable level. Apart from functional requirements of a reliable and noise free system operation, this issue is also important to meet growing and stringent demands of electromagnetic compatibility. Analysis and measurements presented in the following sections pertain to noise couplings from an external source into the enclosure through two differently shaped apertures i.e. rectangular and circular. For comparison purpose, planar areas are kept equal for each of the aperture shapes. A metallic enclosure with circular and rectangular apertures on two opposite faces and housing Pockles cell assembly is analyzed with the help of strip line equivalent circuit [Robinson, 1998]. Range of frequencies chosen for the present analysis is from 200 MHz to 2 GHz. This covers complete spectrum of radiated noise in high power laser systems as well as resonant frequencies of practical enclosures. For apertures of dimensions smaller than wavelength, the coupled fields depend on the electric and magnetic dipole moments [Bethe, 1944]. Electric and magnetic dipole moments in turn depend on respective polarizabilities which are shape and size dependent. Polarizability of a circular aperture of diameter D and of a rectangular aperture of width W and length L, such that $W/L=0.75$, are given by $0.16D^3$ and $0.1462L^3$ respectively [Mendez, 1978].

Following analysis pertains to typical enclosures in high power laser systems housing Pockels cell and drive circuitry. Circular and rectangular apertures of largest geometrical dimensions of 20 mm are considered for which the polarizabilities are equal. The classical analytical formula for shielding effectiveness with a rectangular aperture is attributed to Ott [Ott, 1998]. It calculates shielding effectiveness in terms of incident wavelength λ and maximum length l of the aperture as,

$$SE = 20\log_{10}\left(\frac{\lambda}{2l}\right) \quad (7.40)$$

This expression can be used for preliminary estimation of shielding effectiveness at different wavelengths and aperture lengths. To account for multiple numbers of apertures n the calculated SE is multiplied by $\sqrt{n}$. A circular aperture is treated as a square aperture of equal area [Turner, 1996]. Classical analysis of shielding structures based on Ott's formulation does not take into account resonant frequencies of the shield enclosures and apertures. Two different techniques are used in this thesis to simulate shielding effectiveness of an aluminum enclosure. These are based on equivalent circuit formulation proposed by Robinson [Robinson, 1998] and simulation based on finite difference time domain method [Bruns, 2007]. Calculated values are compared with the simulation results.

Robinson equivalent circuit method treats an aperture on one side of an enclosure as a coplanar strip-line. Width of the strip-line is taken as equal to enclosure height and strip-line separation distance is taken to be equal to aperture width. Figure 7.16 shows enclosure geometry. The equivalent circuit is shown in Figure 7.17. Rectangular enclosure is represented by a short-circuited waveguide. Coplanar strip lines X and X' represent the aperture. Voltage at observation point at a distance d from the aperture is a measure of the shielding effectiveness. Effective width h_e of the equivalent strip-line is given by,

$$h_e = h - \frac{5t}{4\pi}\left(1 + \ln\frac{4\pi h}{t}\right) \quad (7.41)$$

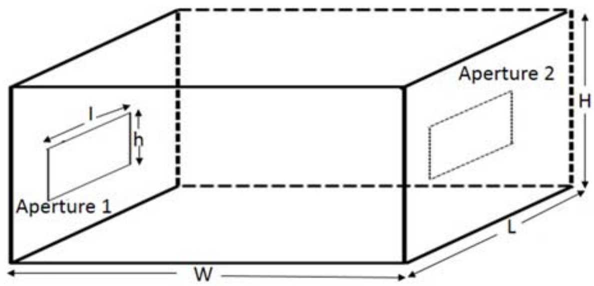

Figure 7.16: Enclosure geometry

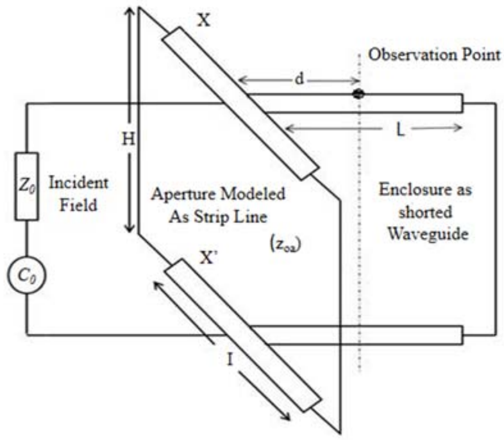

Figure 7.17: Equivalent circuit of enclosure and the apertures

Term t is thickness of enclosure plate and h is aperture width. Characteristic impedance of strip line is given by [Gupta, 1997] as,

$$Z_{oa} = 120\pi \left[\pi \ln \left(2 \frac{1+\sqrt[4]{1-(h_e/H)^2}}{1-\sqrt[4]{1-(h_e/H)^2}} \right) \right] \tag{7.42}$$

where, H represents the enclosure's height. Aperture impedance depends on geometrical dimensions and characteristic impedance as

$$Z_{ap} = \frac{1}{2}\frac{l}{L} jZ_{oa} \tan\frac{k_0 l}{2} \tag{7.43}$$

Where, l is aperture length and L is length of the enclosure and K_0 is propagation constant equal to $2\pi/\lambda$. In absence of the enclosure, load impedance at the observation point is Z_0 and voltage V_P is $V_0/2$. In presence of the enclosure and apertures, voltage V_{pe} at the observation point is derived by general circuit theory and the electrical shielding effectiveness is calculated as,

$$SE = -20\log_{10}\left|\frac{V_p}{V_{pe}}\right| \tag{7.44}$$

Circular aperture is treated as a square of equivalent area.

7.6 Simulation and measurement results

Measurements are carried out on an enclosure of size 170 mm x 130 mm x 175 mm. It is made up of 3 mm thick aluminum plates. The cuboid enclosure houses a Pockels cell, a DC to DC converter, PCB consisting of transistorized driver circuit, nylon mounting posts, a monopole antenna and wires. There are apertures on two opposite faces of the enclosure. These are aligned such that laser beams can pass un-hindered through Pockels cell. Analysis and measurement of shielding effectiveness for the following two types of apertures of equal surface area were carried out.

i) Rectangular apertures of dimension 20 mm x 15 mm
ii) Circular apertures of diameter 20 mm

Connectors for triggering the driver circuit and for AC mains are provided on one of the plates. A thin wire of 0.8 mm diameter and 80 mm length, configured as a monopole antenna is mounted through a connector and is used to monitor field at center of the enclosure. Figure 7.18 shows Pockels cell assembly, monopole receiver antenna and driver circuit placed inside the enclosure. Slots at enclosure edges were sealed by EMI copper tapes to minimize unintentional field coupling. A transmitting bi-conical antenna kept at a distance of 3 m is excited by a sweeping signal between the range 200 MHz to 2 GHz. Incident field on the aperture is vertically polarized and treated as a plane wave. Experimental set up is shown in Figure 7.19. Electric field coupled inside the enclosure is altered by presence of the electrical and electronic components, PCB and wires. Voltage induced at the monopole due to external field coupling was fed to a spectrum analyzer. Measurements were carried out under unexcited conditions of the Pockels cell to eliminate sources of noise inside enclosure. Measurement results for empty enclosure with rectangular and circular apertures are shown in Figures 7.20 and 7.21 respectively. An FDTD simulation is carried out for rectangular aperture only where the calculation regions are sharp and well defined. Finite difference time domain simulation on circular apertures does not converge easily due to curved surface and the results are quite erroneous.

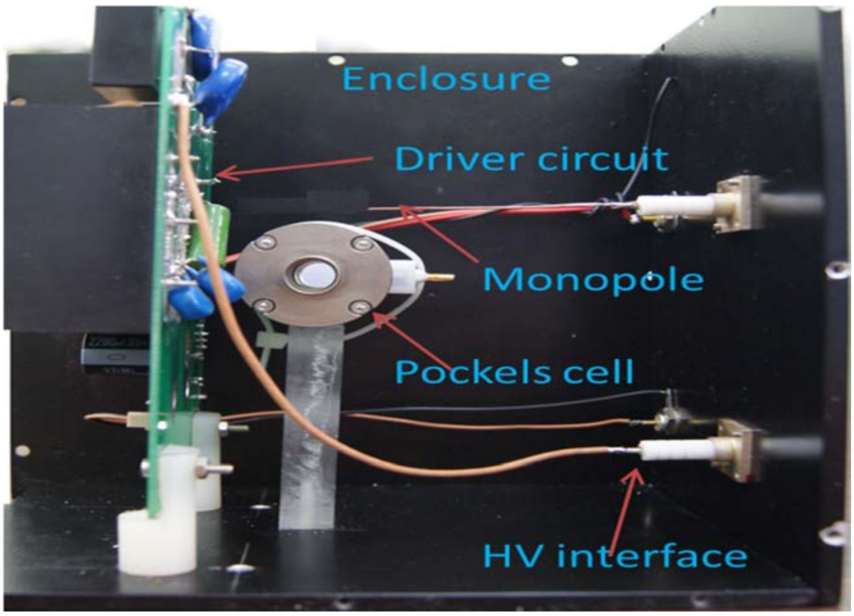

Figure 7.18: Location of Pockels cell and driver circuits

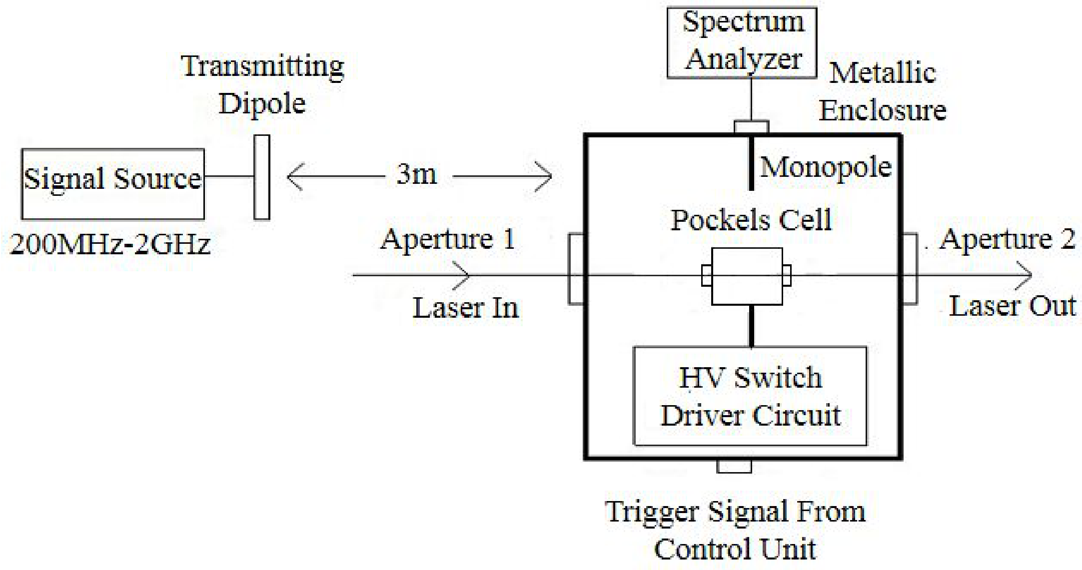

Figure 7.19: Experimental setup for measurement of shielding effectiveness

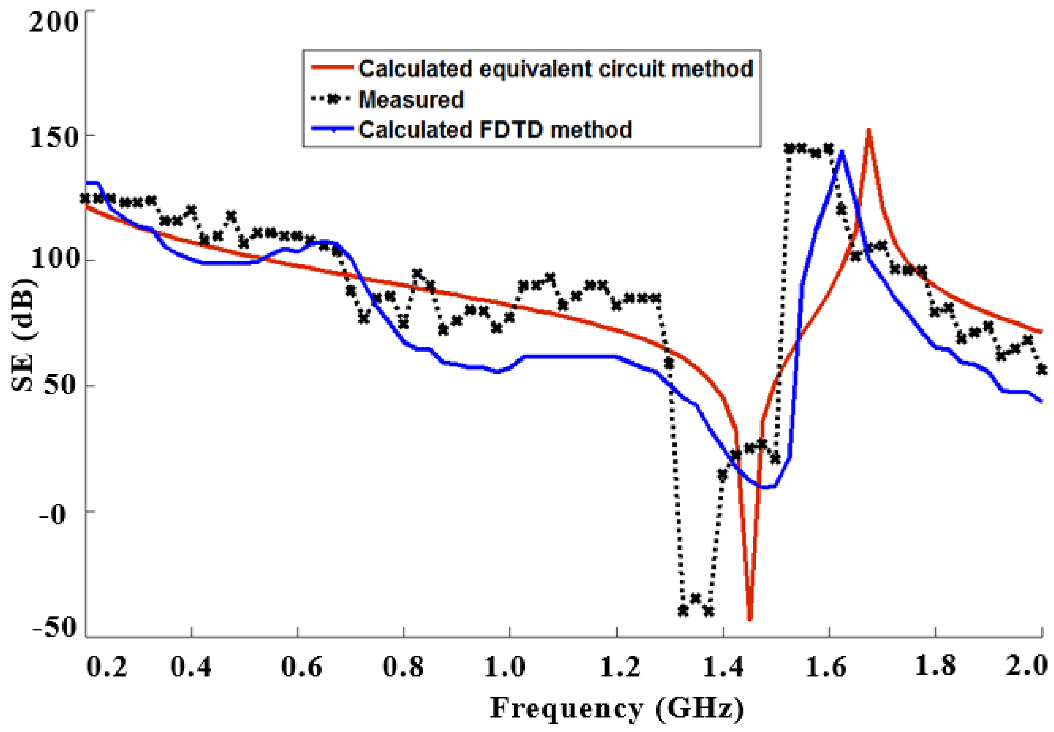

Figure 7.20: Calculated and measured *SE* for a pair of rectangular apertures

There is significant deterioration of shielding effectiveness at resonance frequencies of the shielding structure. Resonant frequency of TE_{110} mode of the cuboidal enclosure of dimensions, 170 mm (width) and 175 mm (height) is expressed by following expression,

$$f_{110} = \frac{c}{2}\sqrt{\left(\frac{1}{170}\right)^2 + \left(\frac{1}{175}\right)^2} = 1.23 \quad GHz \tag{7.45}$$

Equivalent circuit calculations show resonance effects at a slightly higher frequency. Variations between calculated and measured resonance frequencies are due to presence of Pockels cell and other devices inside the enclosure. These components change Q of the enclosure cavity and consequently resonant frequency shifts. In resonance regime, shielding effectiveness decreases considerably and attains negative values. Measurements were carried out for vertically polarized EM fields. Vertical polarization shows better shielding effectiveness for rectangular apertures in comparison to circular apertures. For vertical polarization, induced current gets obstructed by larger side of a rectangular aperture resulting into loss of the shielding effectiveness. Under similar conditions, obstruction length for induced current by a circular aperture of equal area will be lesser thereby reducing the shielding effectiveness. Results of shielding effectiveness studies carried out in this for different aperture shapes of equivalent areas are summarized below.

a) Shielding effectiveness data shows higher peaks for an enclosure with a pair of rectangular aperture as compared to a pair of circular aperture.
b) Resonance band of enclosure is slightly broader in case of circular apertures. For enclosure dimensions under study, pair of circular aperture shows deterioration of shielding effectiveness due to resonance in frequency band 1.20 to 1.40 GHz. Whereas, the same effect is seen in rectangular aperture pair in between 1.25 to 1.40 GHz.
c) Shielding effectiveness data with circular apertures has more oscillations between frequencies 1.5 to 2 GHz as compared to enclosure with rectangular apertures.

These observations, point to a marginally better shielding effectiveness for a pair of rectangular apertures under vertically polarized fields as compared to an enclosure with circular apertures.

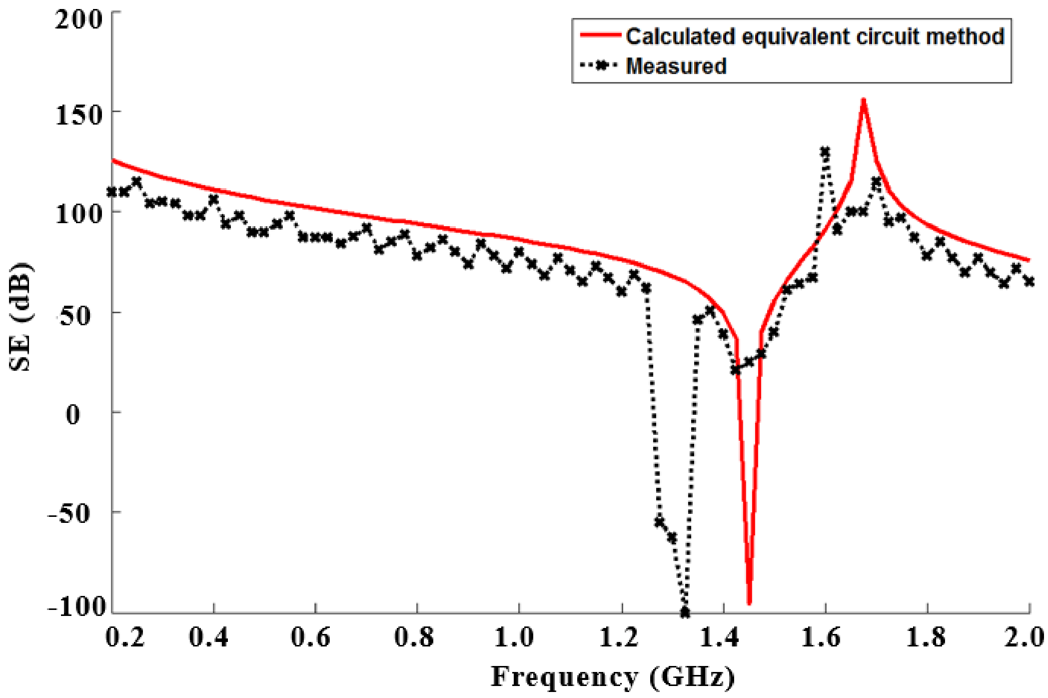

Figure 7.21: Calculated and measured *SE* for a pair of circular apertures

7. 7 Summary and conclusion

This chapter deals with measurement and analysis of electromagnetic crosstalk and shielding aspects the laser chains. A high power laser system consists of cable harnesses, which carry high peak pulsed currents as well as digital clock and control signals. Accurate estimation of crosstalk coupling due to parasitic impedances is essential to design a system with minimum induced noise. Ground planes tend to reduce the noise coupling by decreasing the overall inductance of current loop. Work presented in this chapter adopts conventional approach of analytical solutions as well as transmission line matrix based numerical techniques and frequency domain S parameter characterization for analysis of crosstalk induced voltages. Metallic enclosures are used to shield critical components in large electrical systems against external noise by the process of attenuation and reflections. Laser systems under discussion in this thesis consist of several devices such as Pockels cells and SCRs which are to be activated in time synchronized manner as discussed in previous chapters. The synchronization gets disturbed due to presence of external noise and its coupling into enclosures through slits, cables and connectors. Electro-optical systems have additional problem of noise coupling through intentional apertures, which are incorporated in enclosure plates to facilitate passage of laser light through optical components. Presence of apertures tends to shift the enclosure resonance frequency and reduces the overall shielding effectiveness. Intensity of field coupling through aperture depends on electric and magnetic polarizability, which is shape dependent. Shielding effectiveness of an aluminum enclosure for Pockels cell and consisting of a pair of circular and rectangular cross apertures of 20 mm largest dimensions are calculated. The calculation is based on strip-line equivalent circuit for apertures. Rectangular apertures are also analyzed with finite difference time domain method. Validation of the calculated result is carried out by measurement of coupled field for vertically polarized plane wave in the frequency range 20 MHz to 2 GHz. Deterioration in shielding effectiveness due to circular apertures is found to be more as compared to deterioration due to the presence of rectangular apertures.

Chapter 8
Conclusion

Research work described in this thesis investigates electromagnetic emissions from pulsed power supplies, effects of interference on signal integrity of synchronization circuits and electromagnetic shielding in flash lamp pumped high power solid-state laser chains. Electromagnetic emissions from pulsed power supplies constitute various aspects of electromagnetic interference and compatibility of electrical systems for high power solid state lasers. Deterioration in timing parameters of trigger signals due to radiated interference, corresponding timing jitter in synchronization circuits and development of less susceptible electrical circuits in a multi-stage high power laser unit are analyzed from signal integrity point of view. Electromagnetic interference and extent of loss of signal integrity in a system depend on several factors such as characteristics of interfering fields, types of components and their placements, timing parameters of high voltage high current switches, PCB design, cable routings, load terminations and electromagnetic shielding. Methodology for analysis, calculations and predictions of electromagnetic field coupling mechanisms and their effects on signal integrity parameters for large electrical systems in solid-state lasers using electromagnetic modeling and analytical techniques are important contributions of this work. Noise couplings, cross talk and shielding studies were done for two different types of laser chains namely 2- beams 800 J, 1.5 ns, Nd: phosphate and an ultra-high intensities (10^{18} W/cm^2) table top terawatt laser chain. These high power pulsed laser chains operate in an electromagnetically complex and non-homogeneous environment, where several stages are to be triggered, controlled and time synchronized. Each of these laser systems has its own unique functional and EMC requirements. The lasers consist of a low energy laser oscillator stage followed by successively increasing amplifier stages. Xenon flash lamps of varying arc lengths operating at maximum peak current of 6 kA are optical pump source for these amplifier stages. The 2-beam laser chain comprises of 200 flash lamps, which are excited in several combinations by energy storage capacitor banks with total energy handling capacity of 500 kJ. There are two different types of pulse forming networks for flash lamp operation, namely unipolar and bipolar. Peak current, pulse width and optical emission spectra depend on pulse forming components comprising of energy storage capacitors, trigger transformer inductance and flash lamp characteristics. Current discharge through flash lamp is initiated by a sharp trigger signal, which is main contributor of radiated emission. Other major sources of noise emissions are electro-optic Pockels cells, which are driven by high voltage, and high speed (~ 3kV, 5 ns rise time) biasing voltage and pulsed current flowing through Faraday isolator coils. High power laser chains operate under centralized control which generate charge, trigger and fire commands in specified sequence and set relative delays between firing of various stages. Low voltage control and synchronization electronics have to function in tandem with high voltage, high current power electronics and electro-optic switching devices. Apart from the high voltage and high current flash lamp power supplies and electro-optic components such as Pockels cell, the laser chains also consist of magneto-optic systems like Faraday rotators. Electromagnetic environment as seen by low voltage control, communication and synchronization circuits is polluted by noise emanating from flash lamp power supplies and other high voltage circuits. A distortion of the order of 2 ns due to timing jitter, is sufficient to introduce noticeable shot to shot variations in laser power because of jitter in round trips and amplification factor. Timing jitter is attributed to conducted and radiated noise generated by firing of flash lamps of laser amplifier stages at different instants of operation cycle. Development of timing and delay circuits with components having less susceptibility to transient electromagnetic interference is one of the aims of this dissertation. Towards this goal, a delay generator circuit based on emitter coupled logic family is developed, which significantly reduced the timing jitter to 800 ps. Large size of radiating structures and existence of different types of non-linear loads and discontinuities in a laser system, add to simulation and analysis complexities. A major portion of analysis in this work relies on actual on-site measurements. Extent of electromagnetic interference and its effects on signal integrity are estimated by in-situ measurements in near and far field.

Conventional techniques of calculating electromagnetic emissions from an excited conductor is extended to analyze radiated and conducted emissions from different types of flash lamp power supplies and Pockels cell driver circuits. Noise emissions are affected by various factors such as characteristics of cables, proximity to ground plane, and electromagnetic shielding. Results for measurements of radiated and conducted emissions from a single core and a coaxial conductor of length 2 m carrying flash lamp discharge current are presented. Shielded coaxial cable (RG-58) reduces noise level by at least 2 dB as compared to unshielded single core cable. Effects of ground planes and layouts on emission characteristics from electrically long cables are looked into.

The dissertation also presents digital signal processing, time-frequency domain measurements and analysis techniques in the EMI studies. Limitations of traditional techniques like Fourier transform are discussed and compared with short time Fourier and the wavelet transform. These are important tools for noise analysis and their applications in power supplies have been widely reported. Results of application of wavelet transform to characterize electromagnetic noise emitted by various components in the table top terawatt laser system are presented. Crosstalk and coupling studies between different types of cabling arrangements under pulsed excitations are carried out by transmission line equivalent models. Noise coupling depends on cable transfer impedance, which are calculated and measured for various configurations and geometries. Measurements are carried out for high voltage and low rise time Pockels cell driver signals (~ 3 kV and 5 ns rise time) and flash lamp current of around 5 kA peak value (300 to 500 μs pulse width). Laser power supply and control systems have multiple numbers of electrically long cables carrying control signals, high peak current and high voltage signals. Quite often these cables run in close proximity to each other. This affect signal integrity and consequent deterioration of laser operation. Studies of interaction of pulsed electromagnetic fields with cables, cross talk analysis and effects of ground planes on field coupling are important part of this thesis.

Electro-optical systems pose unique and interesting problems for electromagnetic shielding analysis because of presence of apertures of varying shapes and sizes from optical considerations. This thesis deals with the topic of electromagnetic shielding effectiveness of metallic enclosures under pulsed excitation. Focus is on the effects of intentional apertures for optoelectronic components on shielding effectiveness. Apertures for through passage of lasers are dominant in shielding effectiveness analysis carried out in this work. Analysis based on equivalent circuit (apertures modeled as strip lines) and finite difference time domain method for shielding effectiveness of metallic enclosures with cross apertures is carried out. Results of investigations of shielding effectiveness of an aluminum enclosure with rectangular and circular apertures on two opposite faces and housing Pockels cell and the driver circuit are discussed.

To summarize, the research work is focused on investigations of generation and interaction of electromagnetic fields produced by the power supplies and trigger circuits in flash lamp pumped high power laser systems. The methodical investigations and simulation of the process of electromagnetic emissions from different types of cables and structures and their interactions with other components have resulted into characterization and better predictability of electromagnetic interference in the laser system. These investigations have provided new and hitherto unreported information on the frequencies and types of radiated and conducted electromagnetic transients generated in flash lamp pumped high power solid state lasers. Application of computational electromagnetics and signal processing techniques in combination with measurement results have been applied to understand, estimate and mitigate electromagnetic interference and its negative effects on signal integrity in flash lamp pumped lasers. Apart from the contributions resulting into the betterment of high power laser performance, the dissertation work has provided theoretical insight into related topics like the electromagnetic pulse coupling to different types of structures and cables and susceptibility studies of digital ICs under transient electromagnetic fields.

8.1 Future directions

This thesis has limited its scope by investigating into electromagnetic fields due to pulsed excitations of cables and interconnects by high voltage and high peak current components in flash lamp pumped solid state laser chains. Work presented in this thesis may be extended to characterize and model electromagnetic and radio frequency interference because of plasma formation in flash lamps. Similarly, the electromagnetic pulses generated during laser-matter interaction experiments by terawatt and peta-watt class of high power lasers need investigations from EMI point of view. It will be interesting to understand their interaction with electronic sensors, trigger circuits and systems in near and far field regions. Electromagnetic pulses generated from flash lamp arc discharge and laser-matter interactions are transient and non-stationery. Time evolution of these pulses can be investigated by using wavelet transformation of compatible basis function. There is scope of formulating accurate wavelet functions for application in the area of laser produced electromagnetic pulses. Effects of laser-plasma produced EMPs on biological systems in terms of models for absorption rate can be another field of future research. EMI produced as a result of triggering of flash lamps and semiconductor devices have a certain degree of randomness and statistical variation. Statistical and probabilistic techniques can be applied to predict the jitter window in generated fields, their interactions with nearby systems and effects on mixed signal circuits. At present no separate guideline is available for EMC/EMI in high power laser chains. Experimental results, measurement techniques and information provided in this work can be used to formulate guidelines for EMC standards in flash lamp pumped high power laser chains.

REFERENCES

Abry P., "Ondelettes et turbulences: Multiresolutions, algorithms de décomposition, invari- ance d'échelle et signaux de pression," *Diderot Editeur Arts et Sciences*, Paris, 1997.

Achar R., Nakhla M. S., "Simulation of high-speed interconnects," *Proceedings of the IEEE,* vol. 89, issue 5, pp. 693-728, 2001.

Agrawal A. K., Price H. J., Gurbaxani S., "Transient response of a multiconductor transmission line excited by a nonuniform electromagnetic field," *IEEE Transaction on Electromagnetic Compatibility*, vol. EMC-22, issue 2, pp.119 -129, 1980.

Anderson R. A., Clancy T. J., Fulkerson S., Petersen D., Pendelton D., Hulsey S., Ullery G., Tuck J., Polk M., Kamm R., Newton M., Moore W.B., Arnold P., Ollis C., Hinz A., Robb C., Fornes J., Watson J., "Measurements of the radiated fields and conducted current leakage from the pulsed power systems in the national ignition facility at LLNL," *Digest of technical papers 14th IEEE international pulsed power conference,* vol. 2, pp. 793-796, 2003.

Ansari M. S., Singh B., Navathe C. P., "A low jitter variable delay generator for regenerative amplifier in a table top terawatt femto second laser system," *Indian Journal of Engineering and Material Sciences,* vol. 13, pp. 269-274, 2006.

Antonini G., Orlandi A., "Wavelet packet-based EMI signal processing and source identification," *IEEE Transactions on Electromagnetic Compatibility*, vol. 43, issue 2, pp. 140-148, 2001.

Ari, N., Blumer. W., "Analytic Formulation of the Response of a Two-Wire Transmission Line Excited by a Plane Wave," *IEEE Transactions on Electromagnetic Compatibility*, vol. 30, issue 4, pp. 437-448, 1988.

Arnold P. A., Barbosa F., Cook E.G., Hickman B.C., "A high current, high voltage solid-state pulse generator for the NIF plasma electrode Pockels cell," *16th IEEE International Pulsed Power Conference* vol. 2, pp. 1468-1472, 2007.

Azaro R., Caorsi, S., Donelli, M., Gragnani G.L., "A circuital approach to evaluating the EM field on rectangular apertures backed by rectangular cavities," *IEEE Transaction on Microwave Theory and Techniques,* vol. 50, pp.2259-2266, October 2002.

Baker R. J., "High voltage pulse generation using current mode second breakdown in a bipolar junction transistor," *Rev. Sci. Instrum.* vol. 62, issue 4, pp. 1031-1036, 1991.

Baum C. E., Breen E. L., Giles J. C., O'Nelll J., Sower G.D., "Sensors for electromagnetic pulse measurements both inside and away from nuclear source regions," *IEEE transactions on antennas and propagation*, vol. ap-26, no. 1, 1978.

Balanis C. A., *Antenna theory analysis and design*, Wiley Interscience, New Jersey 2005.

Bartlett M. S., "Smoothing periodograms from time series with continuous spectra," *Nature*, Vol. 161, pp. 686-687, 1948.

Becker K., Johnson J. B., Edward G., "Broadband Pockels cell and driver for a Mark III-type free electron laser," *Rev. Sci. Instrum.,* vol. 65, Issue. 5, pp 1496-1501, May 1994.

Benson F. A., Cudd P. A., Tealby J. M., "Leakage from coaxial cables," *IEE Proceedings on Science, Measurement and Technology*, vol. 139, issue 6, pp. 285–303, 1992.

Berenger J. P., "A perfectly matched layer for the absorption of electromagnetic waves," *Jour. Comp. Phys.,* vol. 114, issue 2, pp. 185-200, 1994.

Berghe S. V., Zutter D. D.; "Study of ESD signal entry through coaxial cable shields," *Journal of electrostatics*, vol. 44, issue 3-4, pp. 135-148, 1998.

Bethe H. A., "Theory of diffraction by small holes," *The physical review*, vol. 66, nos. 7 and 8, 1944.

Bhadani P. K., "Capacitor charging power supply for laser pulsers using a boost converter," *Rev. Sci. Instrum.*, vol. 60, issue 4, pp.605 -607, 1989.

Bhatia M. S., Kumar G., "On the EMI potential of various laser types," *Proceedings of the International Conference on Electromagnetic Interference and Compatibility*, pp. 3-5, 2002.

Boyer A., Bendhia S., Sicard E., "Characterisation of electromagnetic susceptibility of integrated circuits using near-field scan," *Electronics Letters*, vol. 43, issue 1, pp. 15-16, 2007.

Braun S., Al-Qedra M., Russer P., "A novel real time time-domain EMI measurement system based on field programmable gate arrays," *17th International Symposium on Electromagnetic Compatibility*, pp. 501-504, Zurich, 2006.

Brown D. C., *High peak power Nd: glass laser systems*, Springer Series in Optical Sciences, 1981.

Brown G., Ayers J., Felker B., Ferguson W., Holder J. P., Nagel S. R., Piston K.W., Simanovskaia N., Throop A. L., Chung M., Hilsabeck T., "Assessment and mitigation of diagnostic generated electromagnetic interference at the National Ignition Facility," *Rev. Sci. Instrum.*, vol. 83, issue 10, 2012.

Bruns H., Schuster C., Singer H., "Numerical electromagnetic field analysis for EMC problems," *IEEE Transactions on Electromagnetic Compatibility*, vol. 49, issue 2, pp. 253-262, 2007.

Burrus C. S., Gopinath R. A., Guo H., Odegard J. E., *Introduction to wavelets & wavelet transforms, a primer*, Prentice-Hall international Inc., 1998.

Caignet F., Bendhia S. D., Sicard E., "The challenge of signal integrity in deep-submicrometer CMOS technology," *Proceedings of the IEEE*, vol. 89, issue 4, pp. 556-573, 2001.

Carder B. M., "Driving Pockels cells in multi-arm lasers," *13th pulse power modulator symposium*, New York, 1978.

Celozzi S., Araneo R., Lovat G., *Electromagnetic shielding*, John Wiley & Sons, 2008.

Cervens de D. R., Gomme J. C., Raimbourg J., Baggio J., "EMC protections for high voltage and high power on a wide facility — The mégajoule laser," *IEEE International Symposium on Electromagnetic Compatibility*, pp. 109-114, Austin, 2009.

Chen G. K. C., Whalen, J. J., "Macromodel predictions for EMI in bipolar operational amplifiers," *IEEE transaction on Electromagnetic Compatibility,* vol. EMC-22, no.4, pp.262-265, Nov. 1980.

Chen Zhang et al., "Experimental parametric study of the parasitic inductance influence on MOSFET switching characteristics*," International Power Electronics Conference (IPEC),* 2010.

Christopoulos C., *The transmission-line modeling method*, Institute of Electrical and Electronics Engineers, Oxford, 1995.

Christopoulos C., *Principles and techniques of electromagnetic compatibility*, CRC press, 2007.

CISPR Publication, *Information technology equipment-radio disturbance characteristics limits and methods of measurement*, 1997.

Coppola L., Buso S., Qian L., Boroyevich D., "Application of Fourier and wavelet transforms to the identification of EMI noise sources in SMPSs," *International Symposium on Electromagnetic Compatibility*, vol. 2, pp. 584 – 589, Chicago, 2005.

Croisant W. J., Feickert C. A., McInerney M. K., "Numerical investigation of the nonlinear penetration of pulsed electromagnetic fields into a ferromagnetic shield with a simple exponential permeability model," *IEEE International Symposium on Electromagnetic Compatibility*, vol. 2, pp.765-770, 2003.

Daga J. M., Auvergne D., "A comprehensive delay macro modeling for sub micrometer CMOS logic," *IEEE Journal of Solid State circuits*, vol.34, issue 1, pp. 42-45, 1999.

Daubechies I., "Orthonormal bases of compactly supported wavelets," *Communications on Pure and Applied Mathematics*, vol. 41, issue 7, pp. 909-996, 1988.

Daubechies I., "The wavelet transform, Time-frequency localization and signal analysis," *IEEE Trans. Info. Theory*, vol. 36, issue 5, pp. 961-1005, 1990.

Daubechies. I., “Ten Lectures on Wavelets,” *SIAM* ,1992.

Dhia S. B., Ramdani M., Sicard E., *Electromagnetic compatibility of integrated circuits*, Springer Science Inc., 2006.

Dishington R. H., Hook W. R., Hilberg R. P., “Flash lamp discharge and laser efficiency,” *Applied Optics*, vol. 13, issue 10, 1974.

Dockey R.W., Camas W. A., German R. F., “New techniques for reducing printed circuit board common mode radiation,” *IEEE International Symposium on Electromagnetic Compatibility*, pp. 334-339, 1993.

Edrisi M., Chan W. K., Nafalski A., “An extension of modular decoupling methodology for EMC to enclosure with aperture and some contents,” *International Journal of Applied Electromagnetics and Mechanics,* vol. 12, no. 3-4, pp. 211-221, 2000.

EIA-656 standard, *I/O Buffer Information Specifications (IBIS),* 1996.

Fan H., Schlagenhaufer F., “Far field approximation of electrically moderate-sized structures by infinitesimal electric and magnetic dipoles,” *IEEE transactions on EMC*, vol. 52, issue 1, 2010.

Fang T. F., Whalen J. J., Chen G .K. C., “Using NCAP to predict effects in linear bipolar integrated circuits,” *IEEE transaction on Electromagnetic Compatibility,* vol. EMC-22, no. 4, pp.256-262, 1980.

Gabor D., “Theory of communication,” *Journal of the Institution of Electrical Engineers - Part III: Radio and Communication Engineering*, vol. 93, issue 26, pp. 429-457, 1946.

Gagnon W., Albrecht G., Trenholme J., Newton M., *Pulsed Power for Solid-State Lasers*, LLNL-BOOK-400175, 2008.

Gargoom A. M., Ertugrul. N, and Soong. W. L., “Comparative study of using different mother wavelets on power quality monitoring,” *Australasian Universities Power Engineering Conference (AUPEC)*, Brisbane, 2004.

Geetha S., Satheesh K. K. K., Chepuri R. K. R., Vijayan M., Trivedi D C., "EMI shielding: Methods and materials—A review," *Journal of Applied Polymer Science*, vol. 112, issue 4, pp. 2073-2088, 2009.

Green L., "Understanding the importance of signal integrity," *IEEE Magazine Circuits and Devices*, vol. 15, issue 6, 1999.

Gupta K. C., Garg R., Bahl I. J., *Microstrip Lines and slot lines*. Norwood, Artech House, 1997.

Gusinow M. A., "Spectral enhancement of near uv xenon flashlamps," *Applied Optics*, vol. 14, issue 11, pp. 2645-2649, 1975.

Hall S. H., Hall G. W., *High-Speed Digital System Design-A Handbook of Interconnect Theory and Design Practices*, John Wiley & Sons, 2000.

Hiebel M., "*Fundamentals of vector network analysis*" Rohde & Schwarz, Germany, 2007.

Hoefer W. J. R., "The Transmission-Line Matrix Method - Theory and Applications," IEEE Trans. on Microwave Theory and Techniques, vol. MTT-33, no. 10, 1985.

Holland R., Williams J. W., "Total-field versus scattered-field finite-difference codes: A comparative assessment," *IEEE Trans. Nuclear Science*, vol. 30, issue 6, 1983.

Houtman H., Meyer J., "Synchronizable Q-switched, mode-locked, and cavity-dumped ruby laser for plasma diagnostics," *Journal of Applied Physics*, vol. 57, issue 11, pp. 4892-4896, 1985.

Huang Shyh-Jier, Hsieh Cheng-Tao, Huang Ching-Lien, "Application of Morlet Wavelets to Supervise Power System Disturbances," *IEEE Transactions on Power Delivery*, vol. 14, No. 1, 1999.

IEC standard 62014-1, *IEC Input/output buffer information specifications*, 2001.

IEC standard 61000-4-4, *IEC Testing and measurement techniques-Electrical fast transient/burst test*, 2004.

IEEE standard 145, *IEEE standard definitions of terms for antennas, 1983.*

IEEE standard 299, *IEEE standard method for measuring the effectiveness of electromagnetic shielding enclosures, 1997.*

Jennings H. K., "Charging large capacitor banks in thermonuclear research," *Electrical Engineering*, vol. 80, pp. 419-421, 1961.

Johns P. B., O'Brien M., "Use of the transmission-line modelling (t.l.m.) method to solve non-linear lumped networks," *Radio and Electronic Engineer*, vol. 50, issue 1-2, pp. 59-70, 1980.

Johnson H., Graham M., *High speed digital design*, Prentice-Hall Inc., 1993.

Joshi A. S., Kamath M. P., Sharma A. K., M.R. Raghuramaiah M. R., Patidar R. K., Ansari M. S., Sreedhar N., Chandra R., Navathe C. P., Naik P. A., Gupta P. D., "Development of a two arm, high energy, high power laser for plasma research in India," *Proc. 7th Conf. IFSA*, Bordeaux-Lac, 2011.

Kaiser G., A Friendly Guide to Wavelets*, Birkhauser*, Boston, 1994.

Kanda M, "Standard antennas for electromagnetic interference measurements and methods to calibrate them," *IEEE Transaction on Electromagnetic Compatibility*, vol. 36, issue 4, 1994.

Kao W. H., "Parasitic extraction: current state of the art and future trends," *Proceedings of the IEEE*, vol.89, issue 5, pp. 729 – 739, 2001.

Keshwani V. R., Kant N., Roy K., "Modeling, simulation and signal processing for Control room EMI problem using frequency domain Approach and Bayesian estimation," *International Journal of Computer Applications*, vol. 1, issue 15, pp. 112-119, 2010.

Kelly John H., et al., "Time resolved spectroscopy of large bore Xe flash lamps for use in large aperture amplifiers," *Applied Optics*, vol. 19, Issue 22, 1980.

Kley T., "Optimized single-braided cable shield," *IEEE Transactions on Electromagnetic Compatibility*, vol. 35, no. 1, 1993.

Koechner W., *Solid-State Laser Engineering*, Springer Series in Optical Sciences, 2006.

Koga R., Wada O., Toyota Y., Fujimori K., Miyashita T., Kagawa N., Watanabe T., Wang Z. L., Namba1 A., “Control of unintentional electromagnetic waves from digital circuits efficient modelling of devices and PCB,” *int. Symp. on EMC,* Sendai, pp. 197-200, 2004.

Krug F., Russer P., “Ultra-fast broadband EMI measurement in time-domain using FFT and periodogram,” *IEEE International symposium on electromagnetic compatibility*, pp. 577-582, Minneapolis, 2002.

Kumar R., Gupta K. K., Manjunath H. V., “Wavelet based MOSFET switching loss analysis,” *International Power Engineering Conference*, pp. 672 – 676, Singapore, 2007.

Laurin J., Zaky S. G., Balmain K. G., “On the prediction of digital circuit susceptibility to radiated EMI,” *IEEE Transactions on Electromagnetic Compatibility*, vol. 37, issue 4, pp. 528-535, 1995.

Laurin J., Zaky S. G., Balmain K. G., “Prediction of delays induced by in-band RFI in CMOS inverters,” *IEEE Transactions on Electromagnetic Compatibility*, vol. 37, issue 2, pp. 167-174, 1995.

Lee S., Hayakawa M., “A study on the radiation loss from a bent transmission line,” *IEEE Transactions on Electromagnetic Compatibility*, vol. 43, issue 4, pp. 618-621, 2001.

Lee D. T. L., Yamamoto A., “Wavelet analysis theory and applications,” *Hewlett-Packard Journal*, pp. 44-52, 1994.

Li L. Z., Liu L. L., Gu C. Q., Generalized equivalent cable bundle method for modeling EMC issues of complex cable bundles terminated in arbitrary loads,” *Progress In Electromagnetic Research*, vol. 123, pp. 13–30, 2012.

Lin Y. H., Wu T. L., “Investigation of signal quality and radiated emission of microstrip line on imperfect ground plane: FDTD analysis and measurement,” *IEEE International Symposium on Electromagnetic Compatibility*, vol. 1, pp. 319-324, Montreal, 2001.

Liu E. X., Li Ping., Li Le-Wei., Shen Zhongxiang., “Finite-difference time-domain macromodel for simulation of electromagnetic interference at high-speed interconnects,” *IEEE Transactions on Magnetics*, vol. 41, issue 1, pp. 65-71, 2005.

Liu C., Wang L., Zhang G., “Analysis of Transient Electromagnetic Field Coupling to Shielded Twisted-Pairs,” *3rd International Joint Conference on Computational Science and Optimization (CSO),* vol. 1, pp. 95-98, Huangshan, 2010.

Liu L., Li Z., Yan J., Gu C. Q., “Simplification method for modeling crosstalk of multi coaxial cable bundles,” *Progress In Electromagnetics Research*, Vol. 135, pp. 281–296, 2013.

Mallat S. G., “Multiresolution approximations and wavelet orthonormal bases of $L^2(R)$,” *Transcation of the American mathematical society*, vol. 315, issue 1, pp. 69-87, 1989.

Markiewicz J. P., Emmett J., “Design of flash lamp driving circuits,” *IEEE Journal of Quantum Electronics*, vol. QE-2, issue 11, pp. 707-711, 1966.

Marlier C., Videt A., Idir N., Moussa H., “Modeling of switching transients for frequency-domain EMC analysis of power converters,” *15th International Power Electronics and Motion Control Conference (EPE/PEMC)*, Novi Sad 2012.

Marshak I. S., *Pulsed light sources*, Consultants Bureau, New York, 1984.

Masterson K. D., Novotny D. R., “Electromagnetic shielding characteristics of optical-fiber feedthroughs,” *IEEE Transactions on electromagnetic compatibility*, vol. 43, issue 2, pp. 177-186, 2001.

Masugi M., “Multi-resolution analysis of Electrostatic Discharge Current From Electromagnetic Interference aspects,” *IEEE Transaction on Electromagnetic Compatibility*, vol. 45, issue 2, pp. 393-403, 2003.

Matsushima I., Kasai T., Yano M., "Single pulse switch out system for a passively mode-locked Q-switched Nd: YAG laser," *Rev. Sci. Instrum.*, vol. 52, issue 12, pp. 1860-64, 1981.

McDonald N. A., "Electric and magnetic coupling through small apertures in shield walls of any thickness," *IEEE Trans. Microwave Theory Tech*., vol. 20, pp. 689-695, 1972.

Mead M. J., Neely D., Gauoin J., "Electromagnetic pulse generation within a peta-watt laser target chamber," *Rev Sci. Instrum.*, vol. 75, issue 10, pp. 4225-4227, 2004.

Mead M. J., Moncho-Banulsb S., Pottierb S., Brasile J. P., "Pulsed Power System for the Orion High Power Laser," Acta Physica Polonica A, vol. 115, issue 6, pp. 978-979, 2009.

MECL integrated circuits, *Motorola,* 1993.

Mendez H. A., "Shielding Theory of Enclosures with Apertures," *IEEE Transactions on Electromagnetic Compatibility,* vol. 20, issue 2, pp. 296-305, 1978.

Morgan D., *A handbook for EMC testing and measurements*, IET, UK, 2007.

Moses E. I., Boyd R. N., Remington B. A., Keane C. J., R. Al-Aya R., "The National Ignition Facility: Ushering in a new age for high energy density science," *Physics of plasmas*, 16, 041006, 2009.

Muot N., Girard C., Bachelier E., Ferrieres X., "Lightning effects on interconnected ground installations: Hybrid 3D-1D numerical approach in time domain," *International Conference on Lightning Protection (ICLP)*, pp. 1-6, Vienna, 2012.

Naik P. A., Gupta P. D., Navathe C. P., Sharma A. K., Ansari M. S., Raghuramaiah M, Kumbhare S. R., Upadhyay J., Bundel H. R., Mishra K. K., Kushwaha R. P., Joshi R. A., "Development of a chirped pulse amplification based Table Top Terawatt Nd: glass laser system," *CAT/2003-28, CAT Internal report*, CAT, Indore, December 2003.

Navathe C. P., Ansari M. S., Nigam, S., Sreedhar N., Singh B., Chandra R., "Control system for a bipolar capacitor bank of a high-power Nd:glass laser chain," *IEEE transactions on plasma science*, vol. 40, No. 7, pp. 1898-1906, 2012.

Nicholson J. R. and Malack J. A., "RF Impedance of Power Lines and Line Impedance Stabilization Networks in Conducted Interference Measurements," *IEEE Transactions on Electromagnetic Compatibility*, emc-15, issue 2, 1973.

Oak S. M., Bindra K. S., Narayan B. S., Khardekar R. K., "A fast cavity dumper for a picosecond glass laser," *Rev. Sci. Instrum*. vol. 62, issue 2, pp. 308-312, 1991.

Olsen S. L., "Asymptotic Conical Dipole D-dot Sensor Development," *AFWL-TR-75–263*, 1976.

Ott H. W., *Noise reduction techniques and electronic systems*, Wiley Inter science, 1998.

Paasschens J. C. J et al. "Modelling the excess noise due to avalanche multiplication in (Hetero-junction) bipolar transistors," *Proceedings of the bipolar/BiCMOS circuits and technology*, 2004.

Paul C. R., "Prediction of crosstalk in ribbon cables: comparison of model predictions and experimental results," IEEE Transactions on Electromagnetic Compatibility, vol. emc-20, no. 3, pp. 394-406, 1978.

Paul C. R., Bush D. R., "Radiated fields of interconnect cables," *Proceeding International conference on Electromagnetic Compatibility,* London, 1984.

Paul C. R., "A comparison of the contributions of common-mode and differential-mode currents in radiated emissions," *IEEE Transactions on Electromagnetic Compatibility*, vol. 31, issue 2, 1989.

Paul C. R., *Analysis of Multi-conductor Transmission Lines*, Wiley Interscience, New York, 1994.

Paul C. R., *Introduction to electromagnetic compatibility*, John Wiley and Sons Publications, 2006.

Paul J., Christopoulos C., “Time-domain modeling of electromagnetic wave interaction with thin-wires using TLM,” *IEEE Transactions on Electromagnetic Compatibility*, vol.47, issue 3, pp. 447-455, 2005.

Rachidi F., “Formulation of the field-to-transmission line coupling equations in terms of magnetic excitation field,” *IEEE Transactions on Electromagnetic Compatibility*, vol. 35, issue 3, pp. 404-407, 1993.

Rachidi F., Janischewskyj W., Hussein A. M., Nucci C. A., Guerrieri S., Kordi B., Chang Jen-Shih., "Current and electromagnetic field associated with lightning-return strokes to tall towers," *IEEE Transactions on Electromagnetic Compatibility*, vol. 43, issue 3, 2001.

Raimbourg J., “EMC Management in a High Power Pulse Laser,” *IEEE International Symposium on Electromagnetic Compatibility*, pp. 1-5., Honolulu, 2007.

Redl R., “Power electronics and electromagnetic compatibility,” 27th *IEEE Power Electronics Specialists Conference*, vol. 1, pp. 15-21, Baveno, 1996.

Robinson M. P., Benson T. M., “Analytical formulation for the shielding effectiveness of enclosures with apertures,” *IEEE Transactions on Electromagnetic Compatibility,* vol. 40, pp. 240-247, 1998.

Robinson M. P., K Fischer K., Flintoft I. D., “A simple model of EMI-induced timing jitter in digital circuits, its statistical distribution and its effect on circuit performance,” *IEEE Transactions on Electromagnetic Compatibility*, vol. 45, issue 3, pp. 513-519, 2003.

Roy A., Ghosh S., Chakraborty A., “Simple crosstalk model of three wires to predict near end and far end crosstalk in an emi / emc environment to facilitate emi / emc modeling,” *Progress In Electromagnetics Research B*, vol. 8, pp. 43-58, 2008.

Russer P., “EMC measurements in the time-domain,” *Proceedings xxxth General Assembly and Scientific Symposium*, 2011.

Safavian, L.S., Kinsner W., Turanli H., “A quantitative comparison of different mother wavelets for characterizing transients in power systems,” *Canadian Conference on Electrical and Computer Engineering*, 2005.

Sali S., *Transfer impedance of braided coaxial cables at radio and microwave frequencies*, M. Eng. Thesis, University of Sheffield, UK, 1979.

Sali S., Benson F. A., Sitch J. E., “Coupling between multi-coaxial cable systems. Part I: General considerations and efficient numerical method for crosstalk,” *IEE Proc*., Vol. 129, No. 3, pp. 162–166, 1982.

Schultz R. B., Plantz V. C., Brush D. R., “Shielding theory and practice,” *IEEE Transactions on electromagnetic Compatibility*, vol. 30, no. 3, pp. 187-201, 1988.

Sharma A. K., Mishra K. K., Raghuramaiah M., Naik P. A., Gupta P. D., “Design and performance characteristics of an EMI shielded enclosure for high voltage Pockels cell switching system,” *Sadhana*, vol.32, part 3, pp 235-242, 2007.

Singh B., Ansari M. S., Navathe C. P., “Electronic Control Unit for Optical Parametric Chirped Pulse Amplification based Laser System,” *Proc. Sixth DAE-BRNS national laser symposium*, Indore, pp.25, 2006.

Souda M., Yamazaki C., Okamura K., Fukushima K., “Development of high power capacitor charging power supply for pulsed power applications," *Proc. IEEE Pulsed Power Conf*., vol. 2, pp.1414 -1416 1999.

Stahl J., Kuebrich D., Bucher, Alexander; Duerbaum, T., “Characterization of a modified LISN for effective separated measurements of common mode and differential mode EMI noise,” *IEEE Energy Conversion Congress and Exposition (ECCE)*, Atlanta, 2010.

Stathis P., “Radiation and EMI effects in the NIF environment,” *Lawrence Livermore National Laboratory Report UCRL-1D-118202*, 1994.

Stutzman W. L., Antenna *theory and design*, New York: John Wiley & Sons Inc., 1981.

Taflove A., "Review of the formulation and applications of the FD-TD method for numerical modeling of EM wave interactions," Wave Motion, vol. 10, 1988.

Taflove A., Hagness S. C., *Computational electrodynamics: The Finite-Difference Time-Domain Method*, Artech House, Norwood, MA, 2005.

Takahata Y., Watanabe A., Wada O., Koga R., “Power Current Model of IC with Internal Impedance,” *IEICE Tech. Rep*., EMCJ 99-104, pp. 21-26, 1999.

Taylor C., R. S. Satterwhite R. S., Harrison C. W., “The response of a terminated two-wire transmission line excited by a non-uniform electromagnetic field,” *IEEE Transactions on Antennas and Propagation*, vol.13, issue 6, pp. 987-989, 1965.

Tealby J. M., “Coupling between jacketed braided coaxial cables,” *IEE Proceeding*, vol. 134, issue 10, pp. 793–798, 1987.

Tesche F. M., “Numerical Modeling for EMC,” *12th international symposium on Electromagnetic Compatibility*, pp.269-274, Zurich, 1997.

Thomas D. W. P., Christopoulos C., “Calculation of radiated electromagnetic fields from cables using time-domain simulation,” *IEEE transactions on electromagnetic compatibility*, vol. 36, no. 3, pp. 201-205, 1994.

Thomas D. W. P., Denton A. C., Konefal T., Benson T., Christopoulos C., Dawson J. F., Marvin A., Porter S.J., Sewell P., “Model of the electromagnetic fields inside a cuboidal enclosure populated with conducting planes or printed circuit boards,” *IEEE Transactions on Electromagnetic Compatibility*, vol. 43, issue 2, pp. 161-169, 2001.

Torrence C., Compo G. P., “A Practical Guide to Wavelet Analysis,” *Bulletin of the American Meteorological Society*, vol. 79, pp. 61–78, 1998.

Tront J. G., “Predicting URF Upset of MOSFET Digital IC's,” *IEEE Transactions on Electromagnetic Compatibility*, vol. EMC-27, issue 2, pp. 64-69, 1985.

Tsaliovich A., “Cable Shielding for Electromagnetic Compatibility,” *Van Nostrand Reinhold*, 1995.

Ward D A and J La T Exon: “Using Rogowski coils for transient current measurements” IEE Science and Engineering Journal, vol. 2, no. 3 June 1993.

Turner J. D., Benson T. M., Christopoulos C., Thomas D. W. P., Robinson M. P., Dawson J. F., Ganley M. D., Marvin A. C, Porter S. J., “Characterization of the shielding effectiveness of equipment cabinets containing apertures,” *International Symposium on Electromagnetic Compatibility*, pp. 574-578, Rome, 1996.

Uman M. A., McLain D. K., Krider E. P., “The electromagnetic radiation from a finite antenna,” *American Journal of physics*, vol. 43, issue 33, 1975.

Uman M. A., Master M. J., Krider E. P., “A Comparison of Lightning Electromagnetic Fields with the Nuclear Electromagnetic Pulse in the Frequency Range 104-107 Hz,” *IEEE Transactions on Electromagnetic Compatibility*, vol. EMC-24, issue 4, pp. 410-416, 1982 .

Vance E. F., *Coupling to shielded cables*, Wiley interscience publication, 1978.

Wada O., “Power current model of digital IC with internal impedance for power decoupling simulation,” *4th European Symposium on Electromagnetic Compatibility,* pp. 315-320, Brugge, 2000.

Walsh P. J., William L., Hammond T. J., “Voltage-current relationship for pulsed arc discharge,” *Journal of Applied physics*, vol. 52, issue 9, pp.5476-5482, 1981.

Wang Jianjing et al. “Characterization and experimental assessment of the effects of parasitic elements on the MOSFET switching performance,” *IEEE transactions on power electronics*, vol. 28, no. 1, 2013.

Weber T., Ter Haseborg J. L., “Measurement techniques for conducted HPEM signals,″ *IEEE Transactions on Electromagnetic Compatibility*, vol. 46, no. 3, 2004.

Welch P. D., "The Use of Fast Fourier Transform for the Estimation of Power Spectra: A Method Based on Time Averaging Over Short, Modified Periodograms," *IEEE Trans. Audio Electroacoust*., vol. AU-15, pp. 70-73, 1967.

Yazdani M. R., Farzanehfard H., Faiz J., “Conducted EMI modeling and reduction in a flyback switched mode power supply,” *2nd Power Electronics, Drive Systems and Technologies Conference*, pp. 620-624, Tehran, 2011.

Yee K., Numerical solution of initial boundary value problems involving Maxwell's equations in isotropic media," *IEEE Trans. Antennas and Propagation,* vol. 16, issue 3, pp. 302-307, 1966.

Young B., *Digital Signal Integrity: model and simulation with interconnects and packages*, Prentice Hall, NJ, 2001.

Appendix A

Pulse selector circuit and susceptibility tests for integrated circuits

Pulse selector and delay generator circuit for table top terawatt laser unit and EMI test procedures for integrated circuits are discussed in this appendix. Schematic of the pulse selector and delay generator circuit is shown in Figure A.1. It generates a trigger signal which is synchronized with 100 MHz clock and with an external trigger pulse. ECL (Emitter couple logic) ICs with propagation delay of the order of pico-second are used for selector circuit to process 100 MHz clock signal. This family of ICs has differential output signals with capability to drive longer cables. Lower propagation delay of these devices helps in reducing the timing jitter and maintain signal integrity.

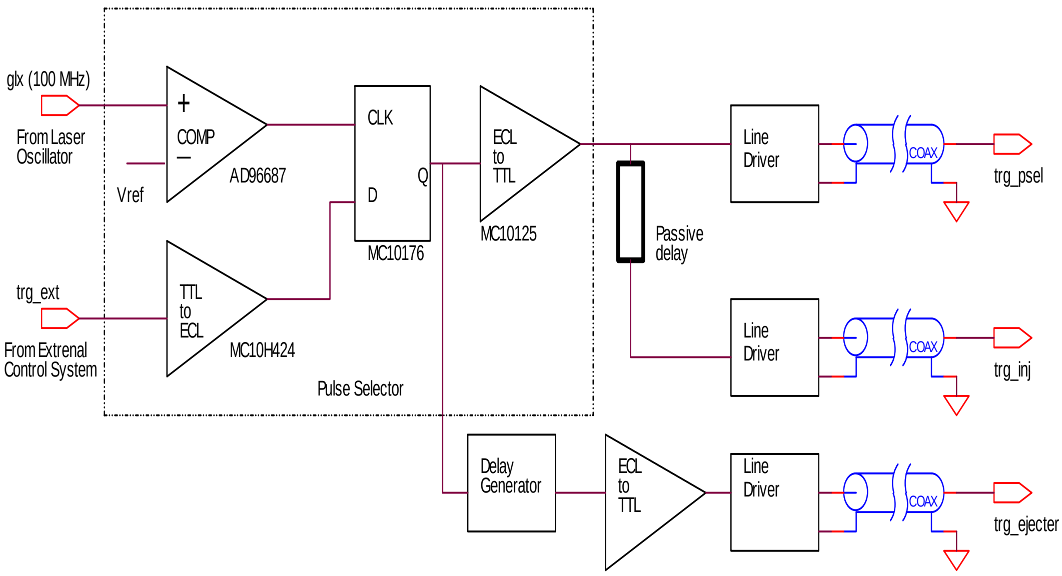

Figure A.1: Pulse selector circuit for TTT laser

The 100 MHz signal is shaped by an ultra-fast comparator (AD96687) and fed as clock to the D- flip-flop (MC10176). External trigger pulse, *trg_ext*, is converted to ECL logic by (MC10H424) and fed to the D input of the flip-flop. Output, 'Q' of the flip-flop is synchronized with external trigger and with rising edge of one of the pulses in 100 MHz pulse train from the laser oscillator. This synchronized pulse**,** *trg_psel*, is used to trigger a high voltage MOSFET switch, which in turn generates a 5 ns FWHM pulse of 3.5 KV to bias a Pockels cell used as an optical gate. The *trg_psel* signal is delayed by a passive delay circuit and the delayed signal *trg_inj* is used to trigger a Pockels cell for injection of the pulse in the regenerative amplifier stage. The passive delay generator is based on signal propagation delay in co-axial cables. Ejection trigger signal, *trg_ejecter* ejects out the amplified laser pulse after several round trips in regenerative amplifier stage. The delay provided to this signal with respect to the injection pulse is variable in the range 5 to 800 ns. One of the objectives of signal integrity design in the reported work is to provide low timing jitter in set delay between injector and ejector signals. This ensures gain stability in regenerative amplifier stage and consequently the shot to shot variation in laser energy and beam quality is minimized. Features of the devices which are relevant for design of low jitter and low noise susceptible laser pulse selector and synchronization systems as used in the circuit shown in Figure A.1 are given in table A.1.

There are several methods for modeling of electromagnetic emission and susceptibility of digital ICs. One of the widely used techniques is IBIS (I/O Buffer specifications information) [EIA, 1996], [IEC, 2001]. It comprises of an input/output buffer description standard based on non-confidential data for IC interfaces. IBIS is recognized by semiconductor manufacturers as a standard for describing integrated circuit interfaces to printed circuit boards. It simulates overall system behavior by developing appropriate models for behavior of the systems that employ these ICs. IBIS models were primarily developed for modeling signal integrity. For this reason, many parameters that are necessary for EMC modeling are not included in the IBIS specification.

Table A.1 Electrical specifications of ICs for laser pulse selector circuit

1. AD96687: Low propagation delay comparator	
Propagation delay	2.5 ns
Delay dispersion	50 ps
Logic compatibility	ECL
Power supply	+5 V, -5.2 V
2. MC10176: Master/slave Flip-Flop	
Toggle frequency	150 MHz
Propagation delay	1.6 ns
Rise time	1.1 ns
Fall time	1.1 ns
Setup time	2.5 ns
Hold time	1.5 ns
3. MC10H424: TTL to ECL translator	
Propagation delay	1.5 ns
Noise margin	150 mV
Rise time	2.2 ns
Fall time	2.2 ns
4. MC10125: ECL to TTL converter	
Propagation delay	1 ns
Rise time	3.3 ns
Fall time	3.3 ns

An integrated circuit electromagnetic model, ICEM [Dhia, 2006], [IEC, 2001] was proposed later on. Goal of ICEM is to provide a relative simple, yet accurate model for parasitic electromagnetic emission prediction from 1 MHz to 1 GHz. Signal integrity analysis may be performed by combining IBIS data and PCB routing information. Adding an EMC core model could give system designers the ability to simulate parasitic electromagnetic emissions and immunity to radio frequency interference. Prediction of the immunity behaviour of an integrated circuit is more difficult than the parasitic emission simulation because it requires the definition of a failure criterion. It also needs considerable post-processing that must be in agreement with the chosen failure criterion. Different failure criterion in an IC are due to power supply stress and over current conditions [Dhia, 2006]. Daga presented a study to show the effect of reduced V_{dd} on the signal delay [Daga, 1999]. The simulation was carried out on a CMOS inverter designed in 0.25 um technology with typical load conditions. It shows that a decrease of 30% of the power supply voltage (from 2.5V to 1.75V) corresponds to an increase of the switching delay of about 60%. A decrease of 50% of the voltage V_{DD} generates a switching delay of 150%. The delays cause some functional blocks to be no longer operational or correctly synchronized and thus generate faults at the component level.

LECCS (Linear equivalent circuit and current source) is macro-model of an integrated circuit for noise immunity analysis [Takahata, 1999], [Wada, 2000]. LECCS models represent the impedance between power pin and ground in terms of equivalent *RLC* circuits. Complete model of an IC consists of LECCS core for internal core model and the LECCS I/O model for the output buffer circuit. Figure A.2 shows simplified LECCS I/O model for a CMOS driver.

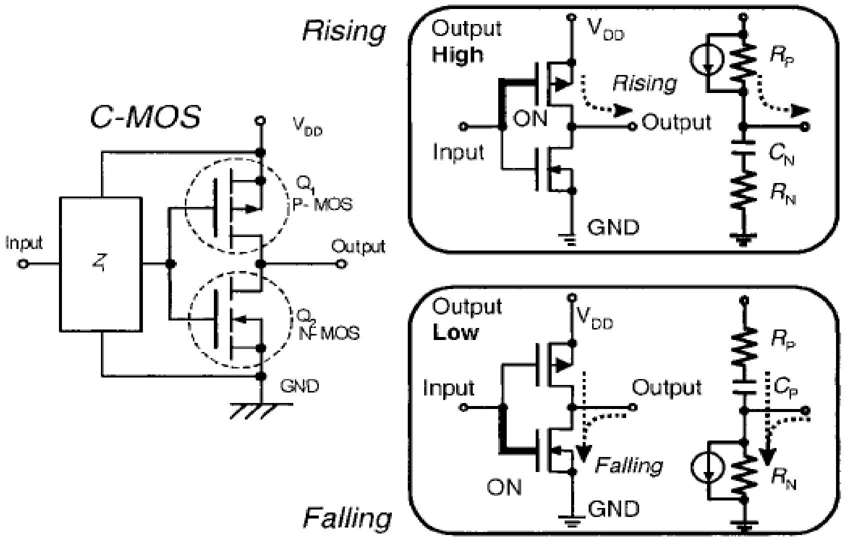

Figure A.2: LECCS I/O model of CMOS driver [Dhia, 2006]

Koga et al. [Koga, 2004] have used LECCS-core model to simulate EMI from practical PCB with good agreement between the simulation and measurement results. It includes decoupling simulation with on-package and on-board capacitors, and EMI simulation with a power bus resonance model of a multi-layer PCB. Operational amplifiers are main building blocks of a front end data acquisition system. They are subjected to EMI from various sources. Noise is coupled through sensors and cabling. Non-linear characteristics of the input differential stage modulate the EMI signal. This leads to appearance of the EMI effect as generation of a RF, DC and low frequency components. The RF component is attenuated by the OPAMP. However, the DC and the low frequency components fall in pass band of the OPAMP and usually cannot be separated from the true signal. This causes offset errors which can be predicted by simulation in time domain. Various analytic models to predict susceptibility in operational amplifiers are reported [Fang, 1980]. These models use whole internal structures of the OPAMP, and each individual transistor is modeled with precise equivalent circuit. This method is complex and time consuming. In recent approaches the OPAMPs are analyzed by macro-models. Under this technique only the input stage is considered in details [Chen, 1980]. Literature survey in this area points towards the need for modification or extension of the existing Gummel-Poon model to take into account the distributed phenomena under high frequency excitation. Several measurement procedures have been proposed for evaluating the electromagnetic immunity (or susceptibility) of integrated circuits. Some of the popular measurement techniques for IC immunity tests are bulk current injection, direct power injection and field coupled. The Bulk current injection techniques intentionally couple a noise current onto one or more traces or wires connected to the pins of the IC. Currents are normally coupled via a magnetic field as illustrated in the Figure A.3.Level of injected current is measured by a second current probe and can be specified for any pin of an IC including output pins. For differential inputs, where the signal is defined as the voltage on one pin relative to the voltage on another pin, bulk current injections testing can be done on both input pins simultaneously to measure the ability of the device to reject common mode noise. Direct power injection measurements couple voltages to an input though an electric field as shown in Figure A.4. Typical value of the decoupling capacitor is 6.8 nF and the source impedance R_s is set to 50 Ω. Amplitude of the input voltage V_s depends on required power to be injected P_{inj} and is given by,

$$V_{inj} = 2\sqrt{2.P_{inj}R_s} \qquad (A.1)$$

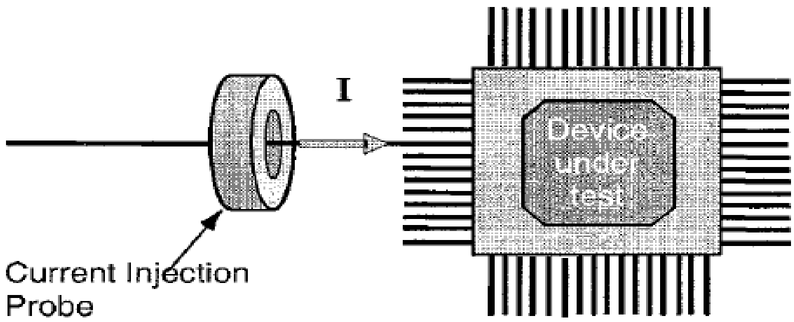

Figure A.3: Bulk current injection testing [Dhia, 2006].

Direct power injection measurement is easier to perform because it does not require a probe that must wrap around the injection point. Power injection can be accomplished by placing an electric field probe up against a trace on a printed circuit board or even against a package pin while the device is operating in its normal environment. IEC standard sets the measurement frequency band for direct current and power injection in the range 100 kHz to 1 GHz. Third category of susceptibility measurements known as field coupled exposes the entire device to strong electric or magnetic fields rather than trying to couple to individual pins. One example of this type of measurement is the Workbench Faraday Cage Measurement, in which the IC is mounted to a printed circuit board and placed in a metal enclosure.

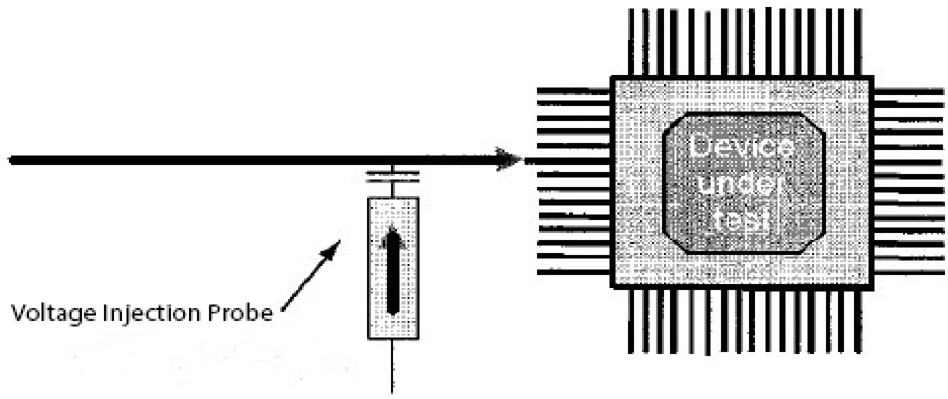

Figure A.4: Direct power injection testing [Dhia, 2006]

A. 1 Summary and conclusion

This appendix describes a pulse selector circuit designed to operate under transient electromagnetic field produced from flash lamps and high voltage switches. It generates trigger signal which is synchronized with a high frequency digital clock and an external signal. It also consists of delay generator sections for two separate pulses, which are delayed with respect to the synchronized signal. Operational requirements of the table top terawatt laser unit, as explained in chapter 6 demand uses of components having low propagation delay and good immunity to electromagnetic interference so that timing jitter in the set delay is minimized. ICs belonging to TTL, CMOS and ECL logic families were tested for pulse selector circuit. Emitter coupled logic ICs provided very low jitter due to low propagation delay and differential input/output signal. Although, these ICs have low noise margin, they are less susceptible to common mode noise which is an important requirement for glitch free operation in pulsed interference environment. Later part of the appendix describes modeling and measurement techniques for electromagnetic emission and susceptibility of integrated circuits. IBIS, ICEM and LECCS are circuit models provided by IC manufacturers to estimate electromagnetic emissions and power supply integrity. Commonly used procedures for measurement of susceptibility of integrated circuits are bulk current injection, direct power injection and field coupled methods.

Appendix B

Sensors for time domain EMI measurements

B. 1 Antennas for EMI measurements

An antenna is a device for radiating or receiving electromagnetic waves. The IEEE 145 Standard [IEEE, 1983] defines an antenna or aerial as “a means for radiating or receiving radio waves.” In other words, the antenna is the transitional structure between free-space and a guiding device. In EMC applications, antennas are primarily used for radiated emissions measurements, radiated immunity testing, site qualification testing or other applications such as exciting a reverberation chamber. In a specific application, one set of parameters may be more important than another. The functional attribute of an antenna refers to realizing desired field strength (specified in terms of ***E*** and/or ***H*** field intensities) in specified directions. The map of this spatial field strength distribution is known as the antenna pattern. In terms of circuit attributes, a corresponding power delivery at the antenna can be identified as the “radiated power” from the antenna as excited by the source into the medium or vice versa. The source exciting an antenna (represented either in Thevenin’s or Norton’s form) has an internal impedance. Correspondingly, an input impedance (or driving-point impedance) can be specified to characterize the extent that a source excites an antenna in terms of power transfer considerations. The maximum transfer of power from the source to the antenna (or from the medium through the antenna into a receiver) corresponds to impedance matching (as governed by the maximum power transfer theorem) between the source and the load. In general, the radiating structure, namely the antenna, has a specified bandwidth. Ratio of power radiated to the total power supplied by source refers to the radiation efficiency. This efficiency results from the fact that, the total power supplied by a source to the antenna structure is divided into a radiated power component and a non-radiated dissipation part. Phenomenon of radiation or the excitation of electromagnetic energy as waves into (or from) the surrounding medium is subject to supporting the ***E*** and ***H*** fields at the antenna structure in accordance to the associated Maxwell's equations with the relevant boundary conditions. The guiding device or transmission line may take the form of a coaxial line or a hollow pipe (waveguide), and it is used to transport electromagnetic energy from the transmitting source to the antenna, or from the antenna to the receiver. An antenna in receiving mode is shown in the following Figure. Incident wave impinges upon the antenna, and it induces a voltage V_T. The equivalent circuit, Thevenin's equivalent and Norton's equivalent of a receiving antenna is shown in Figure B.1.

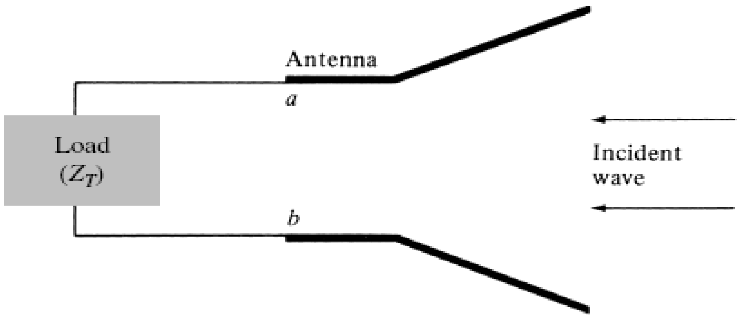

(a)

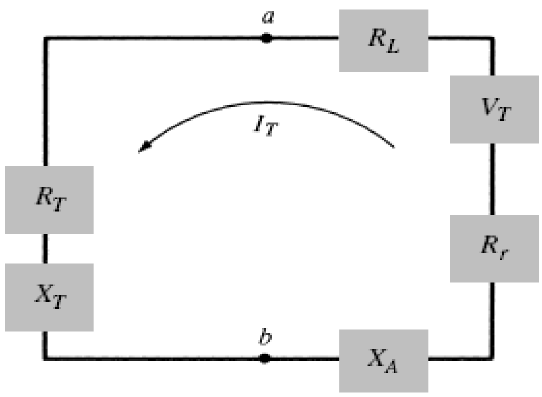

(b)

Figure B.1: (a) Antenna in receiving mode (b) Equivalent circuit of antenna [Balanis, 2005]

Terminal a-b represents input terminal of the antenna. Ratio of the voltage to current at these terminals under no load conditions defines antenna impedance,

$$Z_A = R_T + JX_A \tag{B.1}$$

R_A is real part of the antenna impedance. It consists of two parts namely radiation resistance (R_r) and loss resistance (R_L).

$$R_T = R_r + R_L \tag{B.2}$$

$$X_A = - X_A \tag{B.3}$$

The induced power is given by,

$$P = \frac{|V_T|^2}{4}\left(\frac{1}{R_r + R_L}\right) \tag{B.4}$$

Antenna type depends on frequency of operation. Table A2. 1gives a list of commonly used antennas and approximate useful frequency range up to 1 GHz.

Table B.1 Antennas for EMC measurements

Antenna Type	**Frequency, MHz**
Dipole Antenna	30-1000
Loop Antenna	0.01-30
Bi-conical Antenna	30-220
Log periodic Antenna	200-1000

Important antenna characteristics are,

a) Antenna Factor (AF): It is defined as the ratio of the electric field strength ***E*** of a plane wave incident on the antenna to the induced voltage.

b) Gain: It is the ratio of the radiation intensity, in a given direction, to the radiation intensity of a lossless isotropic radiator.

c) Directivity: It is the ratio of the radiation intensity, in a given direction, to the radiation intensity averaged over all directions. If an antenna has no dissipation loss, the gain and directivity are equal. With dissipative losses, the gain is less than the directivity.

d) Beam-width: It is the angle between the two directions in which the radiation intensity is one-half the maximum value (3 dB down) of the beam in a principal plane of the radiation.

e) Polarisation: Polarisation of an antenna is the orientation of the electric field vector in the direction of maximum radiation.

f) Effective area: The effective area in a given direction is the ratio of the available power at the terminals of the antenna to the incident power density of a plane wave from that direction polarised coincident with the polarisation that the antenna radiates.

g) Input impedance: It is the impedance seen at the input terminals of the antenna. It consists of a real and an imaginary part.

h) Radiation resistance: It is the real part of the input impedance. It can be also defined as the ratio of the power radiated by the antenna to the square of its input current.

i) Bandwidth: Bandwidth of an antenna is defined as “the range of frequencies within which the performance of the antenna, with respect to some characteristic, conforms to a specified standard. Bandwidth can be considered to be the range of frequencies, on either side of a centre frequency, where the antenna characteristics (input impedance, pattern, beam-width, polarization, side lobe level, gain, beam direction, radiation efficiency) are within an acceptable value of those at the centre frequency. For broadband antennas, the bandwidth is usually expressed as the ratio of the upper-to-lower frequencies of acceptable operation. For example, a 10:1 bandwidth indicates that the upper frequency is 10 times greater than the lower. For narrowband antennas, the bandwidth is expressed as a percentage of the frequency difference over the centre frequency of the bandwidth. For example, a 5% bandwidth indicates that the frequency difference of acceptable operation is 5% of the centre frequency of the bandwidth. Because the characteristics (input impedance, pattern, gain, polarization, etc.) of an antenna do not necessarily vary in the same manner or are even critically affected by the frequency, there is no unique characterization of the bandwidth. The specifications are set in each case to meet the needs of the particular application. Usually there is a distinction made between pattern and input impedance variations. Accordingly, pattern bandwidth and the impedance bandwidth are used to emphasize this distinction. Associated with pattern bandwidth are gain, side lobe level, beam width, polarization, and beam direction while input impedance and radiation efficiency are related to impedance bandwidth. For example, the pattern of a linear dipole with overall length less than a half-wavelength $(l < \lambda/2)$ is insensitive to frequency. The limiting factor for this antenna is its impedance, and its bandwidth can be formulated in terms of the quality factor Q or in terms of beam-width, side lobe level, and pattern characteristics. For intermediate length antennas, the bandwidth may be limited by either pattern or impedance variations, depending upon the particular application. It is possible to increase the acceptable frequency range of a narrowband antenna if proper adjustments can be made on the critical dimensions of the antenna and on coupling networks as frequency is changed.

A dipole antenna is a straight electrical conductor measuring *1/2* wavelength from end to end and connected at the center to a feed line. This antenna, is one of the simplest types of antenna, and constitutes the main RF radiating and receiving element in various applications. The dipole is inherently a balanced antenna, because it is bilaterally symmetrical. A dipole and the field configuration are shown in Figure B.2. Wire in a dipole structure is taken to be very small and thin i.e. length $l << \lambda$ and diameter $a << \lambda$. The spatial variation of the current is assumed to be constant and is given by $I(Z) = \hat{a}_z I_0$, where I_0 is a constant.

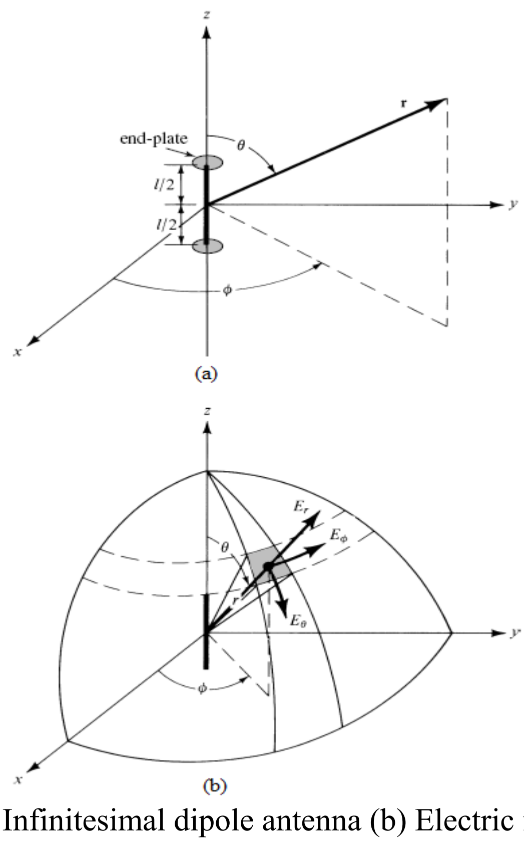

Figure B.2: (a) Infinitesimal dipole antenna (b) Electric field orientation [Balanis, 2005]

Net charge on the dipole system is zero. A punctiform electric dipole is the limit as either charge goes to infinity and the separation distance goes to zero, while the product (dipole moment) remains constant. For a dipole wire antenna to be classified as an infinitesimal dipole, its overall length must be very small ($l \leq \lambda/50$).The electric and magnetic field strengths of an infinitesimal dipole antenna is given by the following equations.

$$E_r = \eta \frac{I_0 l Cos\theta}{2\pi r^2}\left[1+\frac{1}{jkr}\right]e^{-jkr} \qquad (B.5)$$

$$E_\theta = j\eta \frac{kI_0 l Sin\theta}{4\pi r}\left[1+\frac{1}{jkr}-\frac{1}{(kr)^2}\right]e^{-jkr} \qquad (B.6)$$

For infinitesimal dipole the radiated power is given by the expression,

$$P_{rad} = \eta\left(\frac{\pi}{3}\right)\left|\frac{I_0 l}{\lambda}\right|^2 = \frac{1}{2}\left|I_0\right|^2 R_r \qquad (B.7)$$

The term R_r represents the radiation resistance given by,

$$R_r = \eta\left(\frac{2\pi}{3}\right)\left(\frac{l}{\lambda}\right)^2 = 80\pi^2\left(\frac{l}{\lambda}\right)^2 \qquad (B.8)$$

A bi-conical antenna is constructed from a dipole antenna when the conductors are flared to form a bi-conical structure. There are two practical forms of a bi-conical structure namely finite bi-conical antenna and infinite bi-conical structures. An infinite bi-conical structure has two infinite conical conducting surfaces end-to-end with a finite gap at the feed point. With time varying voltage applied across the gap, current flows radially along the surface conductor as shown in Figure B.3.Since the structure is infinite, it can be analysed as a transmission line. A practical finite bi-conical antenna is made by terminating two cones of the infinite bi-cone as shown in Figure B.4.Ends of the cones cause reflections that set up standing waves leading to complex input impedance. Resulting modes of H_φ can be obtained for a given voltage excitation [Stutzman, 1981]. Boundary conditions lead to derivation of current and subsequently the expression for impedance. Input impedance of a finite bi-conical antenna is shown in Figure B.5.

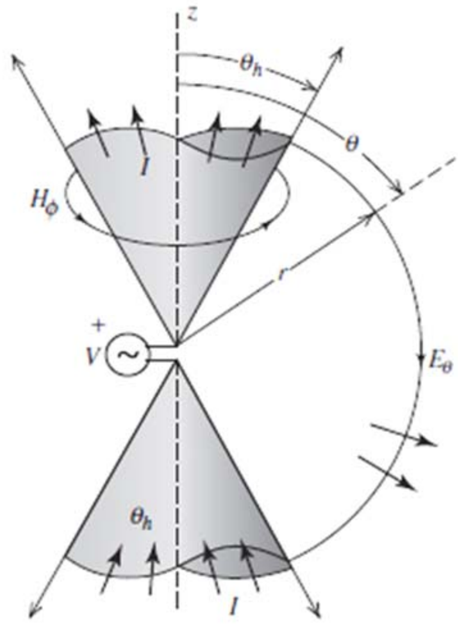

Figure B.3: Infinite bi-conical antenna [Stutzman, 1981]

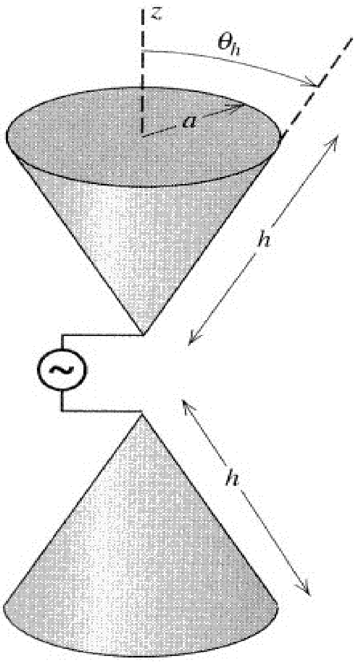

Figure B.4: Finite bi-conical antenna [Stutzman, 1981]

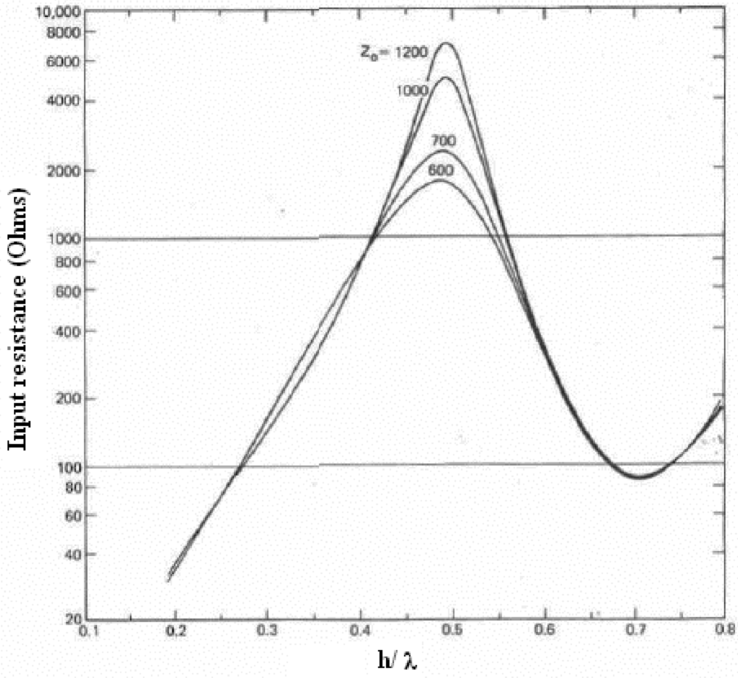

Figure B.5: Input impedance of a finite bi-conical antenna [Stutzman, 1981]

Input resistance becomes very large and input reactance very small for an overall antenna length *2h* of slightly less than one wavelength.

B. 2 D-dot and B-dot sensors for EM field measurements

Electromagnetic sensors are analog devices which converts electrical or magnetic fields of interest to equivalent voltage or current at a terminal pair for driving a load impedance [Baum, 1978] Research interests in broad band sensors were initially driven by measurement requirements of transient fields generated by nuclear explosion, plasma experiments and lightening. Later on it encompassed the domain of electrostatic discharges and electromagnetic interference. D-dot and B-dot are two important class of sensors for measurements of time rate change of electric and magnetic fields.

D-Dot sensors are electric field sensors which generate time derivative of the incident electric field. These sensors have been widely used for high-power electromagnetic measurements [Weber, 2004]. It works on the principle of Gauss's law in a closed volume. Consider an electric field directed normally towards a conducting surface. Gauss's law for electric field is written as,

$$\int D.dA = \int \rho.dV \qquad (B.9)$$

Whereas, *D* is the electric field displacement, *dA* is the differential element area, ρ is the charge density and *dV* is the volume element enclosed by the surface. This equation leads to,

$$D.A = \rho.V = Q \qquad (B.10)$$

The term *V* is the total volume contained within the surface and *Q* is total charge on the conducting surface.

$$A.\frac{dD}{dt} = I \qquad (B.11)$$

Where, *I* is the current flowing through the conducting surface to ground. Thus the time rate of change of electric displacement is directly proportional to the sensor current. Equivalent circuit of a D-Dot sensor is shown in Figure B. 6. Transfer function of a D-Dot sensor is given as,

$$\frac{V(s)}{D(s)} = \frac{AsR}{1 + RCs} \qquad (B\ .12)$$

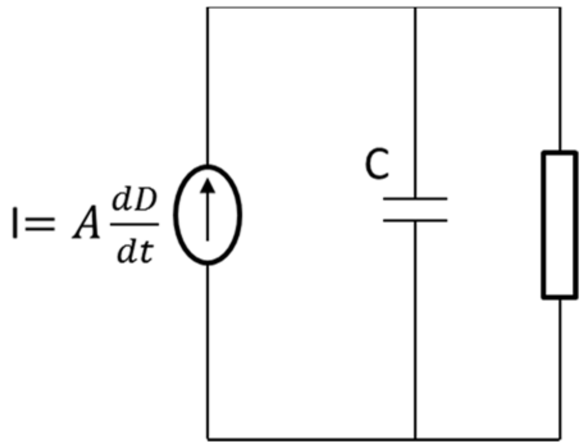

Figure B.6: Equivalent circuit of D-dot sensor [Olsen, 1976]

B-Dots are magnetic field sensors used for measurement of high frequency magnetic fields. These sensors basically consist of a conducting loop with a pair of terminal. The basic construction and equivalent circuit of a magnetic field sensor is shown in Figure B.7 [Baum, 1978]. The terms A_e and L_e are loop equivalent area and length respectively. L is the loop inductance and V is the voltage induced across load. The term μ is the magnetic permeability. A conventional loop for magnetic field measurements may exhibit resonant characteristics due to loop inductance and the cable capacitance. It may further exhibit multiple reflections due to termination impedance mismatch. These limitations restrict their use for high frequency fields. Multi-gap loop (MGL) B-dot sensor constructed in the form of circular cylinder is designed to overcome these limitations. The overall inductance is lowered by extending vertical dimensions of the loop. A multi-gap loop B-dot sensor is shown in Figure B.8.

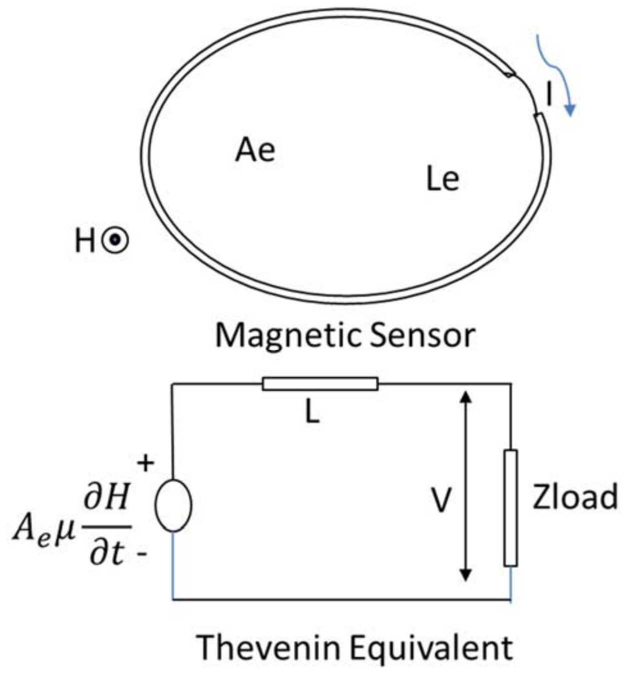

Figure B.7: Magnetic field sensor

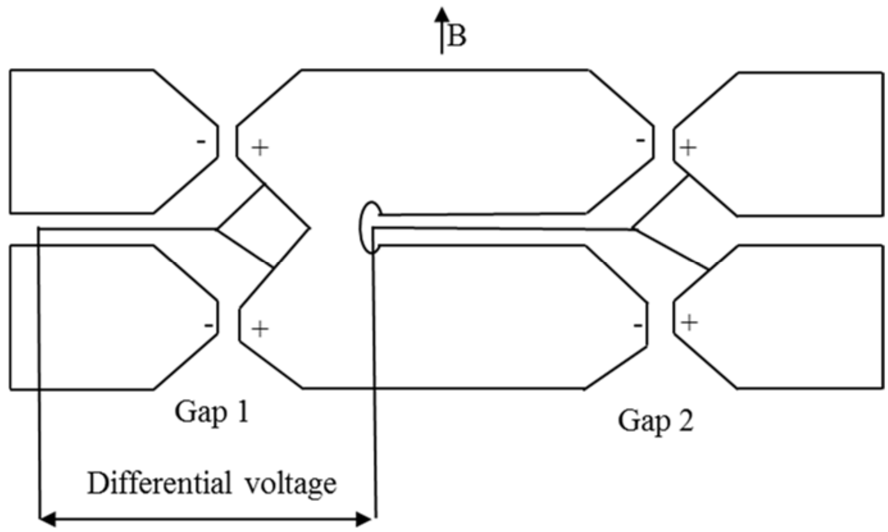

Figure B.8: Multi-gap Loop (MGL) B-dot sensor

B. 3 Rogowski current sensor

Rogowski coils are used for detection and measurement of pulsed currents [Ward, 1993]. These are commonly used sensors for measurement of flash lamp and Faraday isolator currents in solid state high power laser chains. It consists of an air cored coil placed around current carrying conductor. Current through the conductor induces magnetic field which in turn generates a voltage. Integration of output voltage, thus generated is proportional to current through the conductor. Main components of a Rogowski coil are shown in Figure B. 9

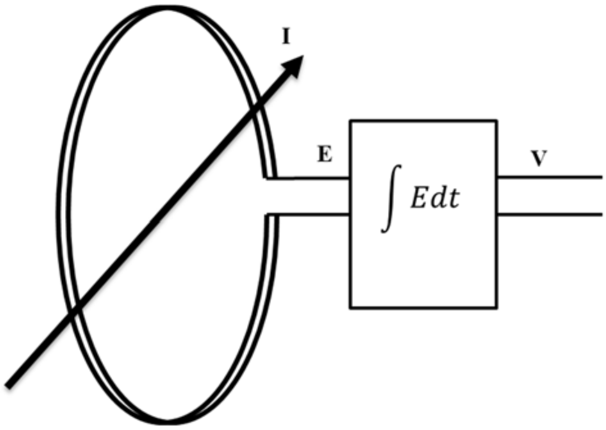

Figure B.9: Rogowski current sensor

Voltage E from a Rogowski coil depends on rate of change of magnetic flux Φ, permeability μ_0 , number of turns per unit length n, cross sectional area of the coil A and rate of change of current I,

$$E = -\frac{d\emptyset}{dt} = -\mu_0 nA\frac{dI}{dt} \qquad (B.13)$$

The sensor output is integration of the coil voltage,

$$V = -\frac{1}{\tau}\int Edt = \frac{\mu_0 nAI}{\tau} \qquad (B.14)$$

Where the term τ is the integrator time constant. Consequently sensitivity of the sensor is given by,

$$\frac{V}{I} = \frac{\mu_0 nA}{\tau} \quad \frac{V}{A} \qquad (B.15)$$

Since it does not depend on ferromagnetic cores, Rogowski coils exhibit linear operation over wider range of operation. Furthermore, there is no effect from saturation and the mutual inductance is independent of the magnitude of current pulse under observation.

B. 4 Line Stabilization Network (LISN)

Line impedance stabilization network (LISN) is used to carry out conducted emission testing on AC mains. It establishes fixed impedance between the device under test and power line for measurement of common mode conducted noise. Impedance of unfiltered AC power line varies between 2 to 450 Ω over a frequency of 100 kHz to 30 MHz [Nicholson, 1973]. Circuit diagram of a LISN is shown in Figure B.10

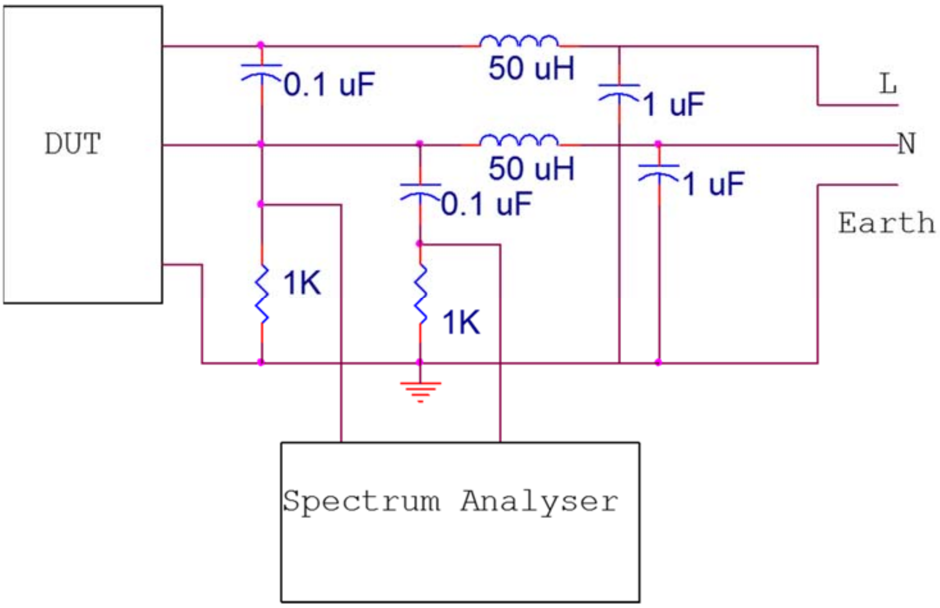

Figure B.10: Line impedance stabilization network

The 50 mH inductors block external high frequency noise on commercial power supply lines. At higher frequencies, LISN presents 50 Ω load through 0.1 µF capacitors and 50 Ω impedance of the measuring device. Noise measurements for peak and quasi peak values are carried out by a receiver consisting of spectrum analyser. A line impedance stabilization network also electrically isolates an equipment from the mains line at higher frequency and presents low impedance conducting path at line frequency. For conducted EMI measurements FCC and CISPR regulations set the frequency range to be between 150 kHz to 30 MHz. FCC regulation limits the average voltage of conducted emission for equipments operating in industrial environment (Class A) as 66 dBμV in frequency range 150 kHZ to 500 kHz and 60 dBμV in frequency range 500 kHz to 30 MHz [Federal Communications Commission. FCC Rules and Regulations Part 15, 2003].

B. 5 Vector Network Analyzer (VNA)

Vector network analysers (VNA) is used to characterize magnitude and phase characteristics of passive and active devices at radio to sub-millimeter wave frequencies [Hiebel, 2007]. At increased frequencies, devices are analysed in terms of incident and reflected waves. Measurement of scattering matrix (S-parameters) is an important function of vector network analysers. The number of S-parameters for a given device is equal to square of the number of ports. Thus four scattering parameters namely S_{11}, S_{12}, S_{21}, S_{22} can be measured for a two port network. Some of the devices which are characterized with the help of vector network analysers are antennas, filters, baluns, power amplifiers and mixers. Vector network analysers measure complex reflection coefficient in frequency domain by transmitting a sweep of sine waves. Commercial vector network analysers are available with multi-port capabilities. Block diagram of a vector network analyser is shown below in Figure B. 11.

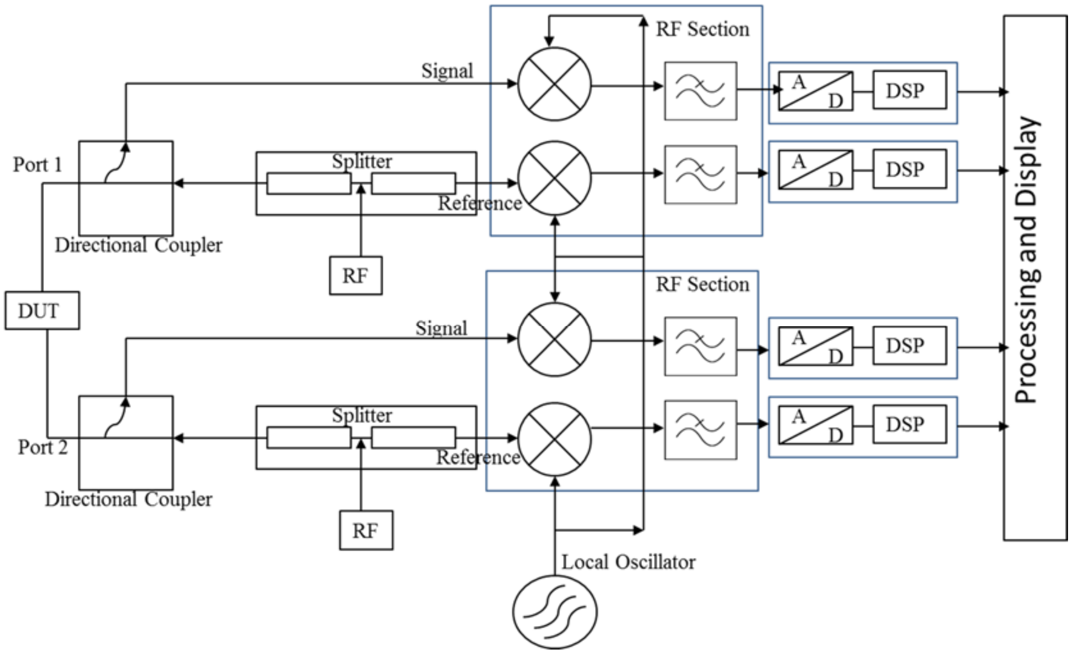

Figure B.11: Block diagram of a vector network analyzer

A tuned source with calibrated impedance and voltage generates a stimulus sinusoidal wave. The stimulus signal is split in two parts. One part acts as a reference signal and the other is incident on the port of measurement. A directional coupler feeds the reflected and incident waves to the receiver section. Receiver section consists of measurement and reference channels. Each of these channels consist of a RF signal section consisting of a mixer stage for frequency down conversion and a digital signal processing stage which carries out the digitization, processing and display functions. The signal processing stage generates measurement data in the form of complex numerical values.

B. 6 Co-axial cable RG-58

RG-58 is a type of braided coaxial cable used for low-power signal and RF connections [Tsaliovich, 1995]. The cable has a characteristic impedance of 50 Ω. It is used in moderate to high frequency applications. It has distributed inductance and capacitance 0.2 μH/m and 100 pF/m respectively. The signal attenuation is frequency dependent from 3.3 dB/100feet at 50 MHz to 21.5 dB/100 feet at 1 GHz. Insulator material consists of solid polythene. Maximum operating voltage is 1900 V. It has a solid central conductor made of copper or tin. However, some versions of RG58 has 7 to 19 strands central conductor. Outside diameter of the cable is around 5 mm. Braid material consists of tinned copper.

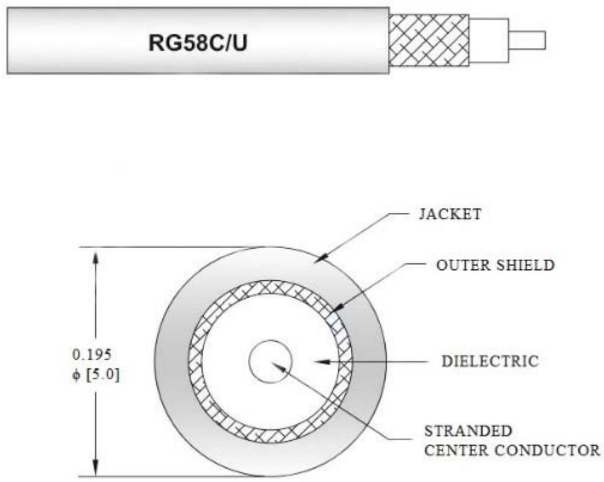

Figure B.12: Co-axial cable (RG58) geometrical dimensions

B. 7 Summary and conclusion

As mentioned in earlier chapters, electromagnetic interference specific to the high power laser systems are pulsed and non-stationary. Time domain measurements are suited for this type of applications. Antennas and probes are fundamental sensors for field measurements in EMC investigations. This appendix discusses main specifications and theoretical aspects of the antennas, field sensors, Rogowski coil based current sensors, line impedance stabilization network and vector network analyzer used in this research work. Bandwidth, antenna factor, gain, directivity and polarization are some of the important characteristics of an antenna. CISPR specifications for EMC antennas require low directivity, linear polarization and maximum VSWR of 2:1. It allows measurement overall uncertainty of ±3 dB. Bi-conical and dipole antennas operating in the frequency range of 20 - 330 MHz and 25 MHz – 1 GHz respectively are used in the measurement setups. These antennas have calibration uncertainty of ±1 dB and antenna factor of 10 dB/m at central frequency. B-dot and D-dot sensors measure rate of change of magnetic and electric fields respectively. Line impedance stabilization network provides a fixed 50 Ω line impedance to the device under test for measurement and testing of conducted EMI. A vector network analyzer is used to measure radiated power from cables and antenna by calculating scattering parameter matrix.